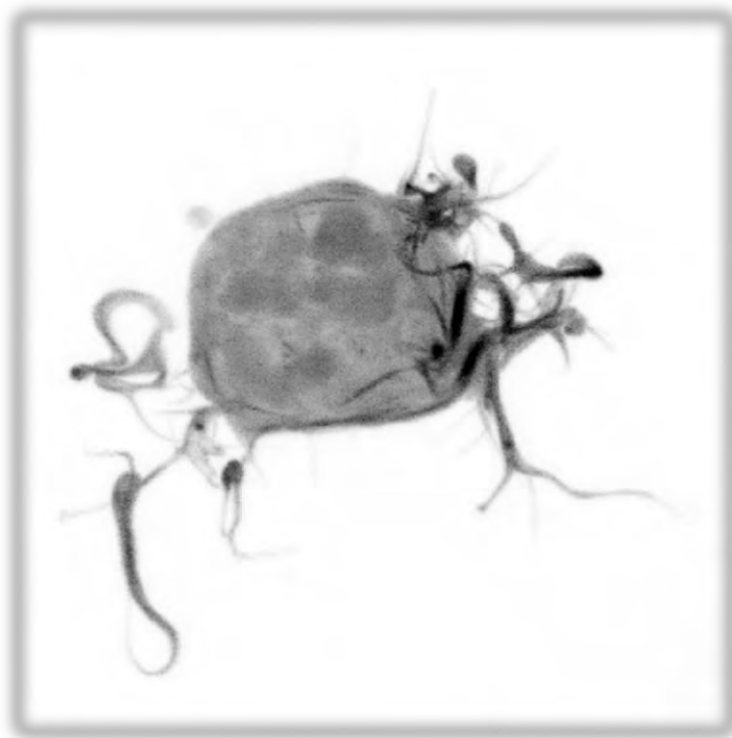




PhD Thesis

Investigation of cancer cell dynamics during division and migration

Ann-Katrine Vransø West



Academic supervisors:

Lene B. Oddershede (main supervisor)

Janine T. Eler (co-supervisor)

Submitted on: 9. January 2018

Preface

This thesis covers the primary projects I have worked on during my PhD at the Niels Bohr Institute in the group of Prof. Lene Oddershede. From the beginning the overall project has been a collaboration with Prof. Janine Eler from the Biotech Research Institute Center also from University of Copenhagen, and her PhD student Lena Wullkopf (joint PhD with our group). Lena and I embarked on this project together, supervised by post doc Natascha Leijnse. As the project unfolded we drew in new collaborative partners from the Biocomplexity group at the Niels Bohr Institute, and I had a stay in the group of Prof. Julia Yeomans at Rudolf Peierls Institute for Theoretical Physics in Oxford, England. Both of these two groups supplied us with theoretical knowledge on the biological systems we have worked on. It has been a pleasure to work with all of these inspirational scientists. A special thank you to my wonderful and always supportive husband.

List of publications

Publications in peer-reviewed journals:

A-K. V. West, A. Christensen, J. M. Tarp, L. Wullkopf, J. T. Erler, L. B. Oddershede. (2017). "Dynamics of cancerous tissue correlates with invasiveness". Scientific Reports 7: 43800. DOI: 10.1038/srep43800

Submitted:

A. Christensen, A-K. V. West, L. Wullkopf, J. T. Erler, L. B. Oddershede, and J. Mathiesen. (under review). "Quantifying Cell Motility and Division Processes in Tissue by a Mechanical Continuum Model". Preprint for Biophysical Journal.

Attached preprints:

L. Wullkopf, A-K. V. West, N. Leijnse, L. B. Oddershede, J. T. Erler. "The ability of cancer cells to mechanically adjust to their matrix correlates with their invasive potential". Preprint for PNAS.

C. D. Florentsen, A-K. V. West, J. N. Clausen, P. M. Bendix, L. B. Oddershede. "Quantification of loading and laser assisted release of siRNA from single gold nanoparticles ". Preprint for Langmuir.

In preparation:

A-K. V. West, L. Wullkopf, J. T. Erler, L. B. Oddershede. "Correlation between cancer cell shape and deformability". Preparing for Physical Review X.

Contents

Preface	i
List of Publications	ii
1 Introduction	1
2 Biological and Theoretical Background	3
2.1 Cell biology	3
2.1.1 Cell division	4
2.2 Cancer Pathogenesis	5
2.2.1 Migration and invasion	5
2.2.2 Microenvironment and cell cultures	6
2.2.3 Cancer cell lines	8
2.3 Modelling biomechanics of cells	8
2.3.1 Simple continuum model	9
2.3.2 Nematics of cells	10
3 Methods	13
3.1 Microscopy techniques	13
3.2 Optical tweezers	15
3.2.1 Trapping setup	15
3.2.2 Theory and method	16
3.3 Particle image velocimetry	17
3.4 Real-time deformability cytometry	18
3.4.1 Experimental setup and data acquisition (ShapeIn)	18
3.4.2 Data output (ShapeOut)	21
3.5 Orientation analysis	22
4 Dynamics of cancerous tissue correlates with invasiveness	25
4.1 Introduction	25
4.2 Methods	26
4.2.1 Particle image velocimetry analysis	26
4.3 Results	28

4.3.1	Speed distributions and velocity profile	28
4.3.2	Vorticity and divergence	30
4.3.3	Controls	30
4.4	Continuum model	33
4.4.1	Theory	33
4.4.2	Comparing theory and experimental	34
4.4.3	Quantifying force	35
4.5	Conclusion	37
5	Correlation between cancer cell shape and deformability	39
5.1	Introduction	39
5.2	Method	40
5.2.1	Acquisition software: Shapeln	40
5.3	Results	40
5.3.1	Deformability versus cell area	40
5.3.2	Prior shape perturbations	45
5.3.3	Young's elastic modulus	46
5.3.4	Statistical significance	47
5.3.5	TGF-beta	48
5.4	Investigating cell shape	49
5.5	Conclusions	50
6	Mechanosensitivity of cancer cells	53
6.1	Introduction	53
6.2	Method	54
6.3	Results	54
6.3.1	Matrix stiffness	54
6.3.2	Mechnosensitivity of cancer cells	55
6.4	Summary	58
7	Nematic kenotaxis	59
7.1	Introduction	59
7.2	Methods	60
7.3	Results	61
7.3.1	Velocity field analysis	61
7.3.2	Orientation analysis	63
7.3.3	Investigating divisions during kenotaxis	65
7.4	Summary & perspective	66
8	Conclusion	67

A	Experimental details	69
A.1	Cell cultures	69
A.1.1	Growth medium requirements	69
A.1.2	Passaging	69
A.2	Sample preparation	70
A.2.1	Confluent 2D monolayers (chapter 4)	70
A.2.2	Cells in solution for RT-DC (chapter 5)	70
A.2.3	Calcein treatment (chapter 5)	71
A.2.4	3D collagen gels (chapter 6)	71
A.2.5	Wound assays (chapter 7)	71
B	Figures	73
B.1	Division study	73
B.2	RT-DC study	74
B.3	Nematics of migrating monolayers study	77
C	Publications and manuscripts	79
C.1	Dynamics of cancerous tissue correlates with invasiveness	79
C.2	Quantifying Cell Motility and Division Processes in Tissue by a Mechanical Continuum Model	91
C.3	The ability of cancer cells to mechanically adjust to their matrix correlates with their invasive potential	108
C.4	Florentsen et al. preprint	137
	References	145

Chapter 1

Introduction

Biological tissues need to display a robust architecture and resistance towards stress, but at the same time they exhibit great compliancy during morphogenesis[1]. These seem like contradictory properties, but are the basis of cell homeostasis. Collective cell motion underlies the development of tissues within both plant and animals, and is necessary for embryonic organization and organ formation. Cancer migration and invasion has been found to occur in different ways, with both collective and individual invasion possible[2]. Metastasis is responsible for 90% of all cancer related death[3], but our knowledge on the subject is still lacking. It is not known why some cells are metastatic and invasive while others are not, and whether this property is in fact reversible[4].

The projects to be presented in this thesis concern flow dynamics in confluent monolayers, with focus on divisions; mechanical properties of cells in suspension; viscoelastic properties within the cell, and nematics of migrating cancer cell tissue. The primary focus has been on cancerous breast epithelial cells, but with supporting results from pancreatic and colorectal cancers. All of the mentioned projects have been put in relation to the invasive potential of the cancer cells, and their morphology. Together with theoretical models, we have tried to give insight into distinguishable features of benign cancers versus malignant cancer. Though chemical signalling pathways are significant in relation to migration and division, we have primarily focused on the mechanical aspects.

This thesis is intended as a summary of the main results of the research projects. The biological background is introduced in chapter 2, chapter 3 describes the main methods, while chapters 4-7 are the respective research projects previously mentioned. Each chapter contains an introduction to the methods, an overview of the results, and concluding remarks or a discussion on future directions of the project. An overall summary of conclusions and future outlook of the project is given in Chapter 8.

Chapter 2

Biological and Theoretical Background

The primary focus of this thesis is on cancer cells of different invasive potential, and characterization of inherent properties that differ between non-invasive and invasive strains of similar origin. To understand our motivation we will outline some of the main aspects of cancer cells, especially in respect to their survival and spreading. This background introduction will briefly recap important knowledge regarding cancer dynamics as a classical biological system, but also in relation to computational models present in literature.

2.1 Cell biology

Cells are the building blocks of all living organisms, and in order to understand cancer we have to start off with its precursor; the normal healthy mammalian cell. The mammalian cell is eukaryotic, which means that it has membrane encased organelles. Major features of the cell can be seen in Figure 2.1. The fluid-like cytosol and the internal organelles comprise the cytoplasm. This is separated from the surrounding environment by the plasma membrane. Inside the cell and lining the plasma membrane is a complex system of proteins (filaments and molecules) known as the cytoskeleton, and they extend throughout the cytoplasm. The three most common types of cytoskeletal filaments are the intermediate filaments (mechanical strength), microtubulus, and actin filaments. They control cell shape, internal transportation, and interaction with the external environment. The actin network is abundant near the plasma membrane, and can remodel and create protrusions. This is done in cooperation with extra cellular matrix (ECM) proteins, from which collagen is the most common in human tissue. The cell uses protrusions, called filopodia, to investigate surrounding areas and for guidance during migration. The cytoskeleton is also responsible for intracellular transport and drives chromosomal separation during division. Besides generating stability in the cell, the cytoskeleton also controls polarity. This is important in cell migration, as polarity can direct cell motion[5]. Eucaryotic cells store their hereditary information, DNA, within the internal compartment called the nucleus. DNA is transcribed into RNA and translated into proteins which regulate processes within the cell. Inheritance of the genetic code is ensured by DNA replication.

The flow of genetic information within the cell (transcription and translation), is known as the central dogma.[3]

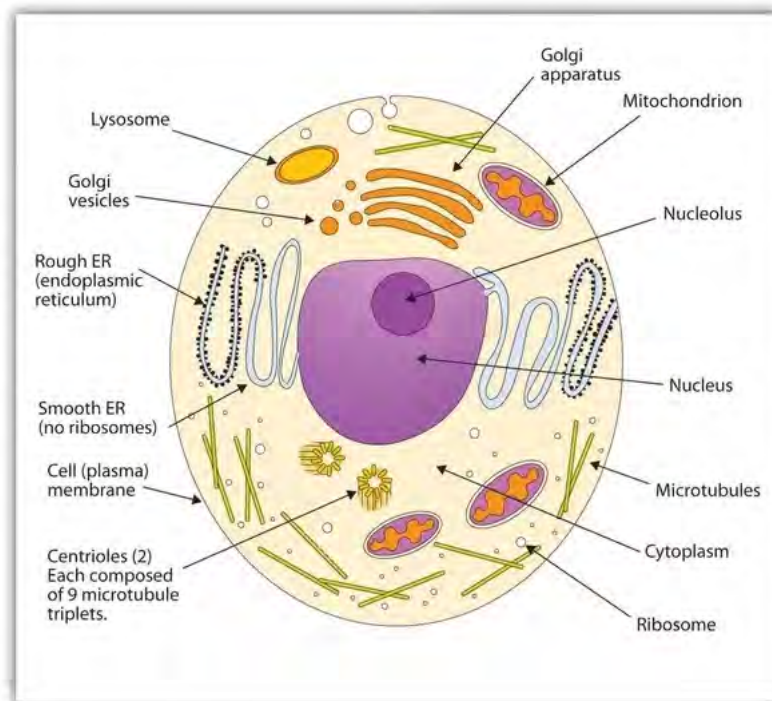


Figure 2.1: The major features of mammalian cell. Adapted from Ball et al. [6].

The two major types of cells in the human body are the epithelial and endothelial cells. Endothelial tissues line our vasculature and are exposed to intracellular stresses due to the laminar blood flow[7]. The fluid shear results in endothelial cell body alignment. Epithelial cells line all other exposed surfaces in the body both within (mouth, lungs) and externally (skin). Their tight intercellular interactions and adhesions ensure mechanical support of the enclosed tissue.[3]

2.1.1 Cell division

Cells grow and divide by mitosis, which is the process in which one cell splits (cytokinesis) into two daughter cells. Division entails a complete reorganization of the cell cytoskeleton, which for fibroblast can take up to an hour[3], while *Drosophila* embryo have been shown to undergo rearrangement within less than five minutes. The main features of the cell cycle are essentially the same in all eucaryotes. For different phases there are distinct biochemical signals that have made it possible to analyze specific time-points of the cell cycle[8].

A study from 2014 by Rossen *et. al.*, revealed long distance correlations in endothelial tissue movement around dividing cells[9]. They found that a single aligned division created rotational patterns (vorticity, see section §3.3) detectable up to three cell diameters away from the site of mitosis, as can be seen on the images in Figure 2.2. This is a testament to the tight cooperative function that exists within our cell tissue, and is

relevant for the project described in [chapter 4](#).

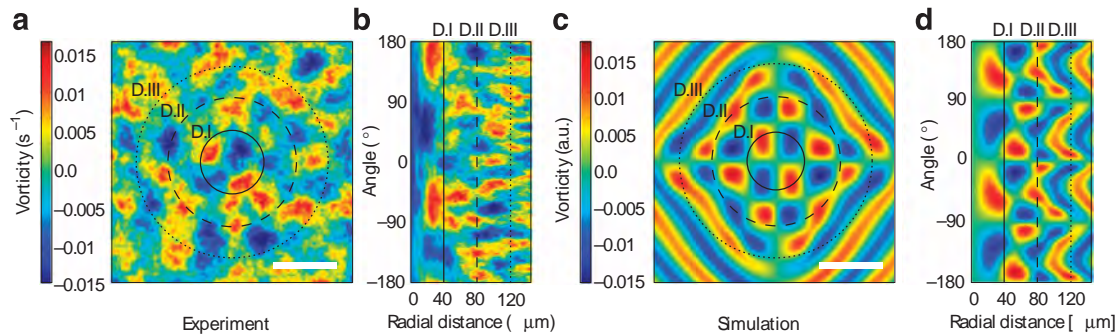


Figure 2.2: Long distance patterns induced by divisions in endothelial tissue as discovered by Rossen et al. [9]. 100 images have been averaged with a centered aligned division, and fields depicted are 30 minutes after division in (a) cartesian coordinates and (b) polar coordinates. (c,d) show the corresponding fields as found via simulations, (c) in cartesian coordinates and (d) in polar coordinates. The solid line and dashed lines denote the distances of one, two and three cell diameters away. The scale bar is $80 \mu\text{m}$. Adapted from Rossen et al. [9]

2.2 Cancer Pathogenesis

Cell homeostasis is upheld by certain pathways that ensure that cells with severe malfunctions are terminated (apoptosis). Mutations are a natural phenomenon in the DNA, but are most often repaired or are not critical to the overall cell function. Accumulation of multiple mutations or mutations in significant coding regions can lead to terminal malfunctions. Cells with uncontrolled proliferation are known as cancers. Malignant cells have the ability to disseminate to secondary sites, and create new tumors[10]. Carcinomas are by far the most common types of cancer in humans, and stem from epithelial tissue[11]. Cancers originating from different cell types give rise to fundamentally different diseases, as they retain traits from their original state. Metastasis is rare in some tissues while prevalent in others. Besides uncontrolled proliferation, cancer cells are often also more resistant to apoptosis allowing the cells to have abnormal survival capabilities[3].

2.2.1 Migration and invasion

Though the abnormal proliferation rate of cancer cells is destructive to surrounding tissue and organs, a solid tumor can most often be easily removed when detected. The risk of mortality is highly related to whether the cells can metastasize to secondary tumor sites, and if they have done so prior to detection of the primary tumor. It has been a common conception, that the invasive potential is an evolutionary step in cancer progression. In recent studies it has become increasingly clear that invasive cells are present from early stages of cancer, and that the property is possibly prevalent in specific subgroup of the tumor cells[4]. The first step in metastasis, is for the cells to break free from the constraints that keep normal tissue in place. Though the underlying mechanisms are not well understood, it is quite certain disruption of normal cell adhesion is necessary. In gen-

eral, normal healthy cells are highly connective and cooperative, while cancer cells have been shown to have lower intercellular adhesion. Modes of migration, whether single cell or collective[12, 13, 2], were originally defined according to observed morphological patterns[14]. Transition from round epithelial to elongated mesenchymal (EMT) is often associated with loss of adhesion and thereby greater motility. This is a dynamic transition known to occur during embryonic development, but also classically related to invasive cancer cells[15]. Nowadays, it is clear that single cell mesenchymal invasion, single cell amoeboid invasion, and collective invasion are among some of the possible pathways observed in tumor progression[2]. When chemical gradients (fx growth factors) guide cell migration and invasion[16], it is called chemotaxis. Kenotaxis is the general collective migration of cells into a cell-free void[17]. Biochemical signaling pathways related to cancer cell migration have been reported, but it is also becoming apparent that mechanical cues may play a role as cells have been observed to migrate in the direction of minimal stress [18, 19]. An interesting hypothesis regarding collective motility concerns whether there are leader cells directing the cell colony motility. Poujade et al. [20] found within a colony of migrating kidney cells (MDCK cells), that leader cells were identifiable at the rim of migrating monolayers. Leader cells are believed to actively drive the migratory movement within cell colonies[21].

There are different ways to investigate the kenotaxis of cell colonies. A simple way is by using wound assays which can be performed in different ways. In a classical wound scratch assay, one grows a confluent tissue, in which a scratch is created mechanically using a pipette tip, see Figure 2.3 (a). Creating the scratch damages cells at the border, and quite likely triggered stress pathway responses, which might affect the migratory properties of cells. Other motility assays include transmembrane assays and exclusion zone assays[22]. The latter is a way of minimizing the traumatic side effects from scratch assays. Together with other approaches using stensil, the exclusion assay, allows cell migration into cell free areas without directly triggering biochemical pathways. Another such approach is with the use of removable culture inserts. The insert is easily attached to the surface of the plastic well, and is constructed with a well-defined 500 μm cell-free gap between two reservoirs for cell seeding, see Figure 2.3 (b). After insert removal, the cells migrate to close the gap.

2.2.2 Microenvironment and cell cultures

In mammalian cells, growth is dependent on extracellular signals from other cells (growth factors), and is often also coordinated within the tissue. The development of a tumor *in vivo* is highly dependent on the supporting connective tissue as the vasculature is significantly different than in normal tissues. Tumors stimulate blood vessel growth (angiogenesis), and the resulting increased flow of nutrients promotes tumor growth. Scientists often study cells by harvesting normal tissue or tumors and growing them in plastic culture dishes. This has to be done under the right conditions in respect to nutrients, temper-

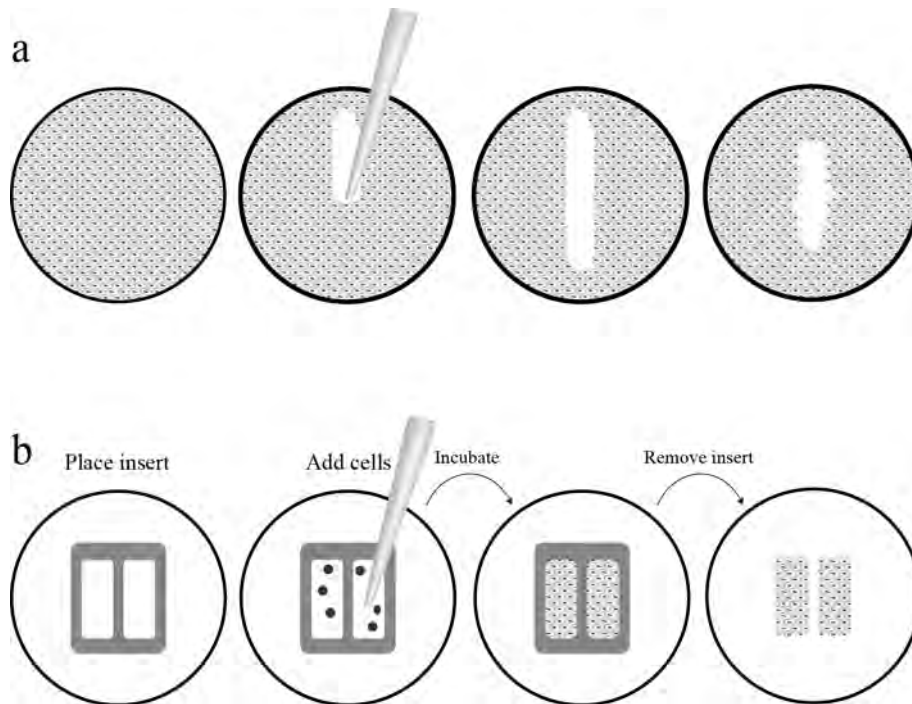


Figure 2.3: Illustration of two different approaches to a wound healing assay. (a) Scratch wound healing assay. You mechanically create a scratch in the confluent cell monolayer using a pipette tip or razor. (b) Wound healing assay using a culture insert. Cells are seeded using into an insert with two reservoirs, which creates a cell-free gap of 500 μm .

ature, and CO_2 concentration. When normal cells are grown in culture dishes they will create adhesions to the surface, and proliferate until they form a confluent monolayer. At this point, density-dependent inhibition of cell division typically occurs. This is most likely due to depletion of nutrients. Normal cells are highly collaborative and coordinated in their behavior via controlled cell death and timed proliferation. The self sacrifice and cooperative behavior ensures survival of the whole organism as cells compete for nutrients in the microenvironment. This holds true both in cultures and tissues. In contrast cancer cells reproduce without restraint, and do not have an inherent limitation to cell proliferation[3]. One should though be aware that immortalized cells can, in some cases, stop proliferating or undergo mutations, rendering them with different features than in the original tumor[23]. Immortalized cell lines have widely been used for general studies, as they provide an unlimited source of genetically homogeneous cells. Though they are in fact not normal, such studies have provided great insight into gene expression and for example the loss-of-function in cancer cells[24, 25]. The first immortalized cell line[26] came from a cervical cancer patient called Henrietta Lacks. Her cells have since been used during the 50's by Jonas Falk to test the first polio vaccine[27], and have increased our knowledge concerning human papillomavirus (HPV)[28].

2.2.3 Cancer cell lines

There are different ways of defining cancer subgroups, and they can often be of little clinical relevance. Most relevant in clinical diagnosis is whether certain therapeutics will be effective, and to this end certain receptors are needed intact. Typical markers in breast cancer are the estrogen receptor (ER), progesterone receptor (PR) and the human epithelial growth factor receptor2 (HER2). A triple negative breast cancer is lacking all three markers, and does not respond to endocrine treatments or therapies targeting HER2, which means the primary approach is chemotherapy[29]. In relation to research regarding migratory properties cell adhesion proteins, such as E-cadherin and vimentin, are of high interest[30, 31]. E-cadherin expression is frequently lost during cancer progression.

2.2 Breast cancer cells

The main subject of this thesis concerns breast cancer cells from human and murine origin. The invasive cell lines 4T1 (mouse) and MDA-MB-231 (human) are both triple negative, while the non-invasive 67NR (mouse) and MCF7 (human) are ER positive[32, 33]. Differences in gene-expression are reflected in the morphological phenotypes observed for the different cell lines (mesenchymal versus epithelial). The invasive human breast cancer cell line, MDA-MB-231, have a significant downregulation of the classic epithelial marker, E-cadherin. Invasive murine 4T1s display constant high levels of E-Cadherin. For the non-invasive cell lines, the human MCF7 exhibit high E-Cadherin levels, while the murine 67NR does not[34].

2.2 Colorectal and pancreatic cancers

To compare with other cancer types, experiments were also done with colorectal and pancreatic invasive pairs. Murine pancreatic cell lines; KPC (invasive) and KPflC (non-invasive). Human colorectal cell lines; SW620 (invasive) and SW480 (non-invasive). For colorectal lines, E-cadherin is highly expressed, and they display a round epithelial morphology[35], while the pancreatic cancers show lowered expression and have a elongated mesenchymal morphology[36].

2.3 Modelling biomechanics of cells

Coordinated motion of cells is of high importance during biological processes such as morphogenesis, tissue growth, and tumor invasion. Though cell motility is an interplay between biochemical signalling and mechanical forces, it is possible to simulate tissue dynamics using mathematical models. In literature, a variety of different approaches have been used to model collective cell migration. Among some are cellular Potts models[24, 37], vertex models[38, 29], and continuum models[39, 40, 41, 9]. In the following I will introduce continuum and liquid crystal theory models in relation to tissue

dynamics. In all our studies we have experimental velocity field data, which was the basis for comparison with the computational models.

2.3.1 Simple continuum model

Biological tissues can be modelled as a continuous viscoelastic material. Such a material will respond as an elastic to short term mechanical stress, while long term exposure will deform the material as a viscous fluid. Since we are looking at large timescales (hours), the tissue response will primarily be that of a viscous material. The simplest model within rheology is a pure Maxwell fluid, but this is not recapitulate division induced dynamics within the velocity fields. We instead use the Oldroyd B model, which is often imagined as the result of dissolving a Maxwell fluid into a Newtonian fluid.

$$\sigma + \lambda_1 \overset{\nabla}{\sigma} = 2\eta_0 \left(\gamma + \lambda_2 \overset{\nabla}{\gamma} \right), \quad (2.1)$$

where σ is the stress tensor, $\gamma = \frac{1}{2} [\nabla v + (\nabla v)^T]$ is the strain rate tensor, λ_1 is the relaxation time, λ_2 the retardation time, and η_0 the total viscosity. The models can be visualized as elastic springs and viscous dash-pots as depicted in Figure 2.4.

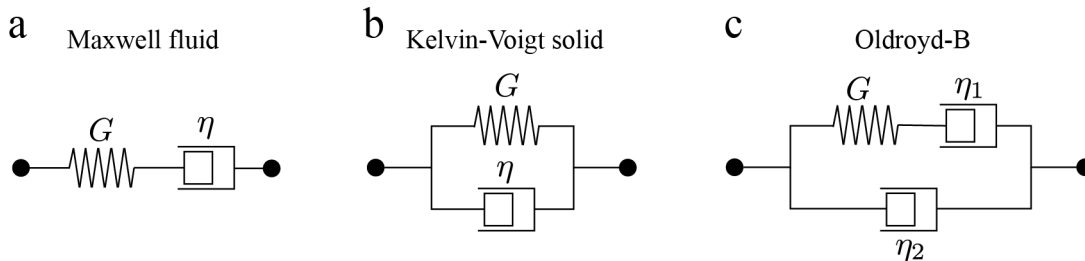


Figure 2.4: Spring and dash pot diagrams of rheological models. Elastic springs (elastic modulus, G) coupled with viscous dash pots (viscosity, η). Elements in series have an additive strain, while the stress is additive for elements in parallel. (a) Maxwell fluid: When under stress the spring will deform instantly like a spring, while the dash pot will deform at a constant rate like a fluid. Upon relaxation irreversible deformation will occur due to the dash pot. (b) Kelvin-Voigt solid: Under stress the Kelvin-Voigt solid deforms with the characteristic time scale G/η . The deformation is reversible, and when released from the stress the solid regains its original shape. (c) Oldroyd-B: The stress applied to this system will decay towards zero with a timescale of G/η_1 .

Important elements in modelling cell tissue are rheology, friction and motility. We have covered the rheology, and now need to introduce the friction with the substrate. In literature, this is typically represented by a Stokes-like drag term (equation (2.2)), but this gives a Gaussian tail on the speed distributions[42]. For distributions with exponential tails, as will be seen in the next chapters, the friction can be modelled as a dry Coulomb kinetic friction between two solids in contact, equation (2.3).

$$f_{drag} = -\alpha_{drag} \cdot v \quad (2.2)$$

$$f = -\alpha \cdot \hat{v} \quad (2.3)$$

The motility of cells is often modelled as the result of an Ornstein-Uhlenbeck process, in which they are assumed to be non-interacting.

$$\frac{\partial m}{\partial t} + (v \cdot \nabla)m = -\frac{1}{\lambda_m} + \Phi(x, t) \quad (2.4)$$

, where $m(x, t)$ is the forcing from cell motility, λ_m is the persistence time, and $\Phi(x, t)$ is a white Gaussian noise. Since the cells have a finite length scale, we impose such a parameter on the random forcing by filtering the noise with a Gaussian function ($\xi(x', t)$) of width l_m .

$$\Phi(x, t) = \frac{1}{2\pi l_m^2} \xi(x', t) \exp\left(-\frac{|x - x'|}{2l_m^2}\right) dx' \quad (2.5)$$

The final model and simulation results can be seen in section §4.4.

2.3.2 Nematics of cells

Nematics is a term related to liquid crystal theory. A nematic material consists of anisotropic molecules, which display a crystal-like behavior in the sense that there is an order in the molecular orientation. The orientation of the oval particles depicted in Figure 2.5 can be depicted as headless vectors, known as directors. The local nematic director is given by the long molecular axes of the registered cell contour, and is similar to the classical direction vector. In contrast to the direction vector, a director portrays an orientation without directional quantity. Hence, the director \mathbf{n} is indistinguishable from the director $-\mathbf{n}$. (For more on the physics of liquid crystals, De Gennes and Prost [43]). Though the molecules within a nematic material will tend to align with their neighbors, their general position is random as in an isotropic fluid. The conflicting liquid-crystal material properties can result in singularities. The two fundamental energy excitations when in a two dimensional system are bend and splay as seen in Figure 2.5 for a two dimensional system.

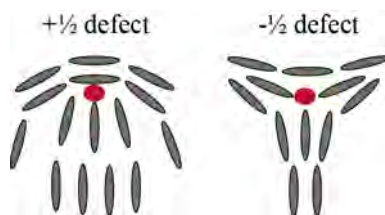


Figure 2.5: Topological defects within an orientation field in two dimensions. $+1/2$ (left) and $-1/2$ (right) defects. The red dot illustrates the defect core.

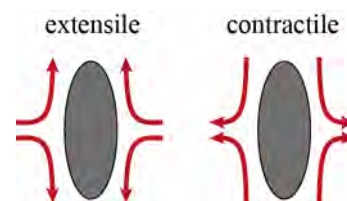


Figure 2.6: Activity in a nematic liquid crystal dipole. Arrows indicate the flow field created by the cell; extensile (left) and contractile (right).

The defects are identified as $\mp 1/2$ defects corresponding to the $\mp \pi$ rotation of the molecular orientation around the defect. They occur due to the inherent instability of the system, which results in turbulent flow fields within the material[44]. Defects occur due to energy perturbation in the system, and are very important in relation to tissue dynamics. It has been found that defects play a role in cell extrusion [45], division[46], and can drive migration patterns. The latter has not yet been reported in mammalian cell

lines, but was clear for bacterial growth patterns[47]. It has also been observed in previous studies on bacteria, that $-1/2$ defects are immobile while $+1/2$ defects are persistently motile[48, 49, 50]. The motility of the cell gives rise to turbulent flow, which in nematics is expressed as an activity parameter. The activity of nematic cells can be approximated as a force dipole[51] and is either extensile or contractile. An extensile or contractile nematic material creates flow fields as shown in Figure 2.6.

Chapter 3

Methods

Methods used in the different projects of this dissertation are explained in the following sections; Microscopy techniques- section §3.1, Optical tweezers - section §3.2, Particle image velocimetry (PIV) - section §3.3, Real-time deformation cytometry - section §?? (3.4), and Orientation analysis - section §?? (3.5).

3.1 Microscopy techniques

Since the discovery of the microscope, methods for observing biological systems have expanded vastly. Confocal microscopy allows imaging of biological samples using reflection and fluorescence[52], while long term imaging is acquired with a time-lapse microscope. For a general introduction to the basic microscopy techniques (confocal, bright field, and fluorescence microscopy) an overview can be gained from the two review papers by Stephens and Allan [53] and Webb [54].

3.1 Confocal microscopy

In this project, confocal images were acquired using a Leica TCS SP5 laser scanning confocal microscope (3.1), which allowed multispectral imaging by detection of emission across the whole visible region. The setup is illustrated in Figure 3.1. It is equipped with three lasers; an argon ion laser with five excitation lines from 458 nm to 514nm, and two Helium Neon (HeNe) lasers with lines at 594 nm and 633 nm. The confocal lasers pass through an acousto-optical tunable filter, allowing regulation of individual laser intensity (AOTF). An acousto-optical beam splitter (AOBS) separates emission and excitation light in the pathway to and from the scanner located before the sample, as seen in 3.1. The focused laser beam spot is scanned through the biological sample, allowing light emitted from the sample to pass back through the scanner, AOBS, through a pinhole (removing out-of-focus light), and collected in photomultiplier tubes (PMTs). Images are acquired via the charge coupled device (CCD) camera. A piezo stage allows for precise control in the x and y direction, either manually or via Labview programs. The objective constricts

the laser beam to a diffraction limited spot. Samples have been imaged using a 63x water immersion objective (Leica, HCX PL APO, 63x, NA=1.2, COR R CS, water), and image acquisition was done using bidirectional scanning at 700 Hz, with an 8 bits resolution, a pinhole size of 111.5 μm , format of 1024 x 1024 pixels, line average 2, and a zoom of 3.

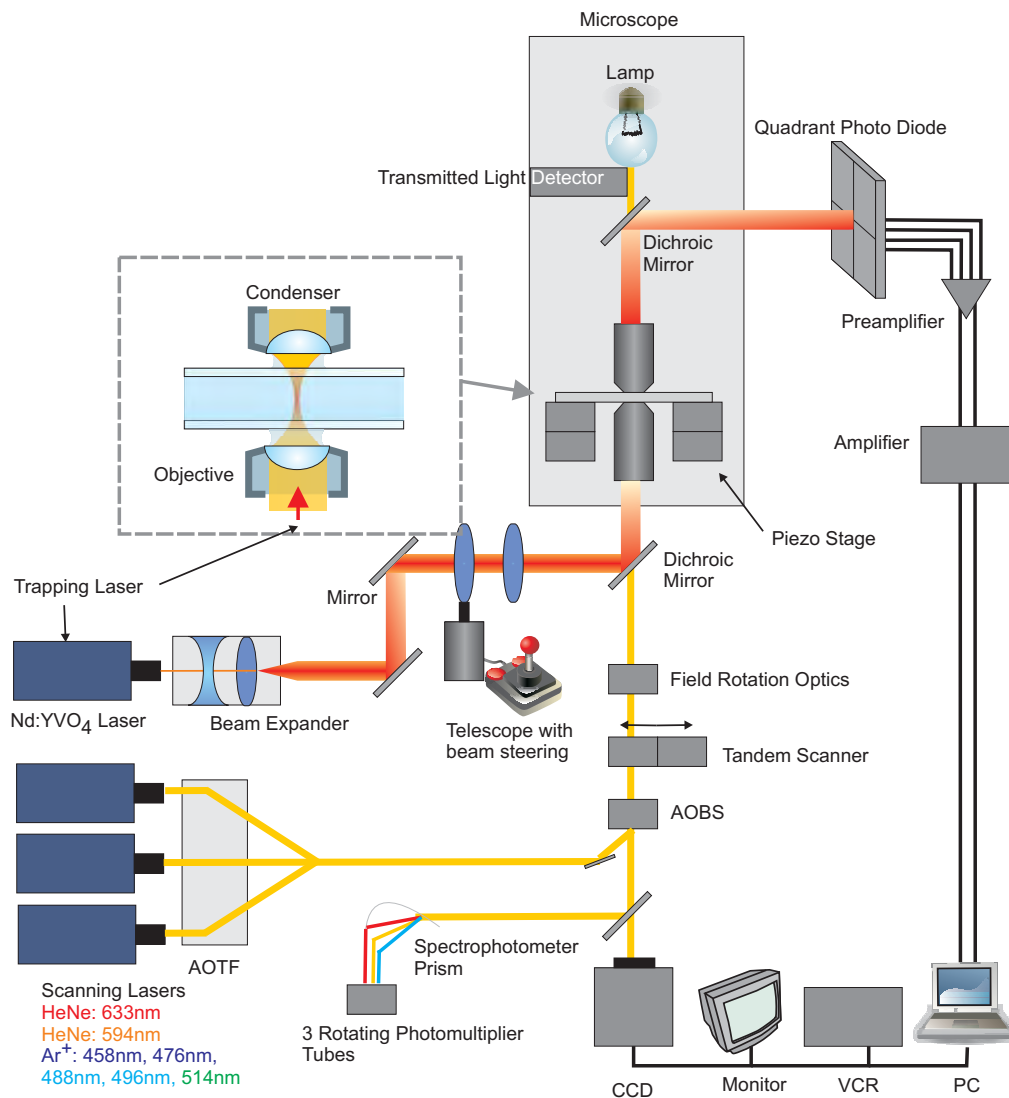


Figure 3.1: Confocal microscope with focused trapping laser. The figure has been adapted from Richardson et al. [55] in which the setup has been described.

3.1 Time-lapse microscopy

A Nikon Eclipse Ti-E microscope system was used for overnight imaging (Figure 4.1, Figure 2.3) and experiments with large areas of interest (Figure 5.10). The microscope has a wide range of observation methods (for example, brightfield, fluorescence, and phase contrast). It is equipped with a Perfect-Focus-System (PFS), which limits axial focus fluctuations during long term imaging. Images were acquired with either a 10x air objective (CFI Plan Fluor DLL, 10x, N.A. 0.30, W.D. 16.0 mm, Ph1, Nikon), or a 20x air objective (CFI Plan Fluor DLL, 20x, N.A. 0.50, W.D. 2.1 mm, Ph1, Nikon). The stage is located inside a plexiglass box, which constitutes a nearly closed system supplied with CO₂ and a heat control. The acquisition and analysis software contains image stitching algorithms. The large field of view of the microscope is often subject to a significant and undesired light gradient, which is clearly visible when multiple images are stitched. The gradient was minimized by choosing a smaller region of interest (800x800 μm instead of the full 1105x1105 μm). Post process light correction was done by filtering out large (shading correction) and small structures (smoothing) of a specified size using Gaussian filters in fourier space (ImageJ/FFT/Bandpass Filter). The bandpass filter thresholds were 30 μm and 2 μm , respectively.

3.2 Optical tweezers

3.2.1 Trapping setup

The confocal setup explained in section §3.1 is equipped with a 1064 nm focused trapping laser (5W Spectra Physics BL106C, TEM(0,0)). Near infrared lasers (850-1064nm) minimize damage to biological specimens as absorption of biological tissue in this range is low. The near infrared laser is implemented in the confocal setup illustrated in Figure 3.1. The setup has been described in Leijnse et al. [56]. The light beam is expanded and sent through telescopic lenses with beam steering, allowing adjustment of the trap focus position within the sample plane. The trapping laser enters the setup after the scanner, allowing scanning of the sample without altering the trap position. The dichroic mirror reflects the laser beam into the setup. Illumination of the sample results in forward scattered light, which is collected by adding a condenser (Leica, P1 1.40 oil S1). The condenser images the light onto a quadrant photodiode (QPD), that is subsequently amplified.

3.2.2 Theory and method

An optical trap is formed by a tightly focused laser beam, and has been successfully used for force measurements of objects from micron to nanometer size. A microscopic object near the focus will experience scattering and gradient forces driving it towards the center, and thereby stably trapping it. A wide range of objects can be trapped from silver nanoparticles[57], lipid vesicles[58], organelles[59], and to whole cells[60]. There are three distinct regimes in scattering theory depending on the diameter, d , of the particle in relation to the wavelength, λ , of the light. In the Mie regime, $d \gg \lambda$, where the particle is much larger than the wavelength, the scattering is greater in the forward direction, and forces can be calculated using ray optics[61]. If the particle is much smaller than the wavelength of the incident light, $d \ll \lambda$, then there is Rayleigh scattering where scattering is equally distributed in forward and reverse direction. The optical forces can be calculated by treating it as an induced dipole behaving according to simple electromagnetic laws[62]. The two forces at play, are the scattering forces and gradient forces. An illustration on the principles behind the balancing forces can be seen in Figure 3.2. In order to trap a particle in the Gaussian beam, we need a stable equilibrium, and this is achieved by changes in momentum of the laser light which counteracts the movement of the particle. We typically work with particles in the intermediate regime, $d \approx \lambda$, where forces have to be calculated using electromagnetic theory of light.

The forces exerted on a trapped particle are assumed to be Hookean. The trap force is thereby given as:

$$F_{trap} = -\kappa \cdot x. \quad (3.1)$$

The trapping force, F_{trap} , acts as a spring, pulling the particle back towards the center of the trap upon displacement, x . The stiffness of the trap is given by the constant, κ , which can be found by calibrating the optical trap[63]. The basics of optical trapping have been reviewed by Neuman and Block [64].

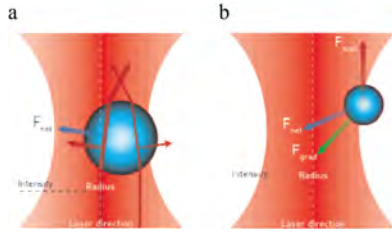


Figure 3.2: Illustration of forces in an optical trap. (a) Mie regime, $d \gg \lambda$: Reflective and scattering forces transfer momentum to the particle in the direction of light propagation. The cells refractive index determines the direction of the scattering. The trap is stable when scattering and gradient forces cancel out. (b) Rayleigh regime, $d \ll \lambda$: Balance is also upheld by scattering and gradient forces, but the scattering is a result of absorption and re-radiation. Figure adapted from Coffey [65].

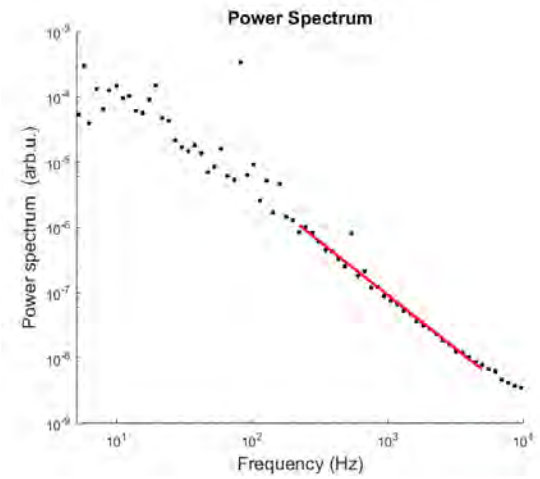


Figure 3.3: Example of linear fit to power spectrum of measured lipid granules within a cell.

Time series of measured displacements (QPD) can be Fourier transformed to calculate the power spectra, Figure ??(3.3), and recorded timeseries, $\vec{r}(t)$, are analyzed in terms of the time averaged mean square displacement. Imposing a linear fit at high frequency values one can find the scaling exponent α . The movement of a particle (diffusion) can be classified in terms of the scaling of the mean square displacement

$$MSD = \langle [\vec{r}(t + \nabla) - \vec{r}(t)]^2 \rangle \propto t^\alpha, \quad (3.2)$$

where t is the time, and α is the scaling exponent characterizing the type of diffusion. When $\alpha=1$ normal Brownian diffusion is dominant, while $\alpha < 1$ indicates super diffusion in which motion is driven and has directionality (internal transport mechanisms). When α is between 0 and 1 the particles are moving in a confined manner (sub-diffusive behavior), motion consistent with a more viscous media (crowding from intercellular constituents). This method has been described in detail by Jeon et al. [66], Norregaard et al. [63].

3.3 Particle image velocimetry

As introduced in section §2.3, it is possible to use classical hydrodynamic approaches to model tissue dynamics. A way of mapping experimental flow dynamics of a continuous material is by using particle image velocimetry (PIV). It uses cross correlation algorithms to measure space- and time-resolved flow velocities. By dividing an image into a grid with a chosen grid size (interrogation area), the PIV algorithm cross-correlates two sequential images to obtain displacement vectors for each grid point. The technique is illustrated in Figure 3.4 (a). Cross correlation algorithms measure space- and time-resolved flow velocities, and enhances signal-to-noise and vector resolution by applying multiple rounds of displacement analysis to offset the following rounds. These multiple rounds are known as passes.

From the vector field it is possible to investigate motility patterns such as vorticity and divergence, see Figure 3.4 (b,c). Vorticity (σ) is the local rotational motion, and divergence (d) is the contraction or expansion within the field, and they are given by the following equations:

$$d = \frac{\partial}{\partial x}v_x + \frac{\partial}{\partial y}v_y = \sum \frac{v_x(\mathbf{r})\mathbf{r}_x - v_y(\mathbf{r})\mathbf{r}_y}{A}. \quad (3.3)$$

$$\sigma = \sum \frac{v_x(\mathbf{r})\mathbf{r}_y - v_y(\mathbf{r})\mathbf{r}_x}{A}. \quad (3.4)$$

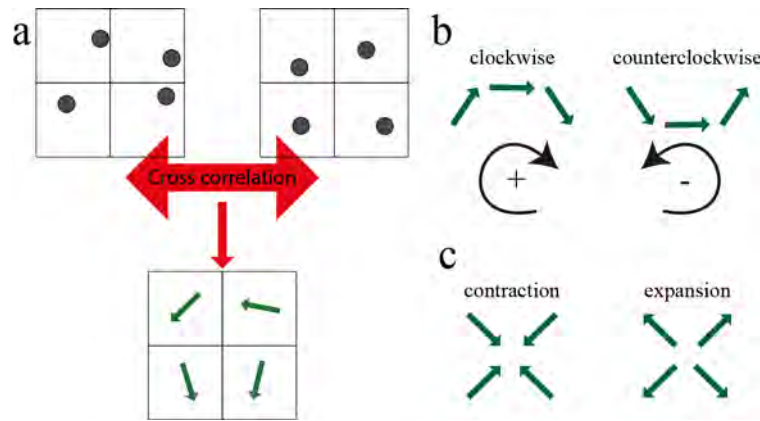


Figure 3.4: Particle image velocimetry analysis. (a) Cross correlation analysis of particle displacement resulting in velocity field vectors. (b) Vorticity of a vector field is the clockwise and counterclockwise motion determined as shown. (c) Divergence is the contraction and expansion within the field, and evaluated in relation to neighboring vectors.

3.4 Real-time deformability cytometry

3.4.1 Experimental setup and data acquisition (Shapeln)

Real time deformability cytometry (RT-DC) is a fairly new system developed in the group of Prof. Jochen Guck (Biotechnology Center of the TU Dresden) and is detailed in the article by Otto et al. [67]. The commercial product is called an AcCellerator, and is manufactured and distributed by the company ZellMechaniks located in Dresden. It is a flow cytometry system with an integrated complementary metaloxide semiconductor (CMOS) camera, and a camera-triggered LED pulse illumination. The experiments require a special microfluidic chip, FLICXX (produced by ZellMechaniks). You can see an illustration of the internal chip structure in Figure 3.5. Inside the microfluidic chip the cells flow through a confining channel, where the deformed cells are imaged. It is possible to purchase chips with different channel sizes (customizable), and the diameter of the analyzed cells should fall between 20-95% of the channel size. Prior to the reservoir, the cells flow through two rows of pillars. These pillars will prevent possible cell debris from continuing on in the system. This minimizes the probability of something getting stuck and blocking the flow through the channel. In some cases a blockage of the channel can not be prevented, and then the flow chip is exchanged. From classic flow cytometry systems, the

running fluid is known as the sheath[68]. Since the viscosity of the fluid is of high importance to the flow dynamics, the system comes with special measurement buffer known as CellCarrier (1xPBS with <1% methyl cellulose and adjusted viscosity).

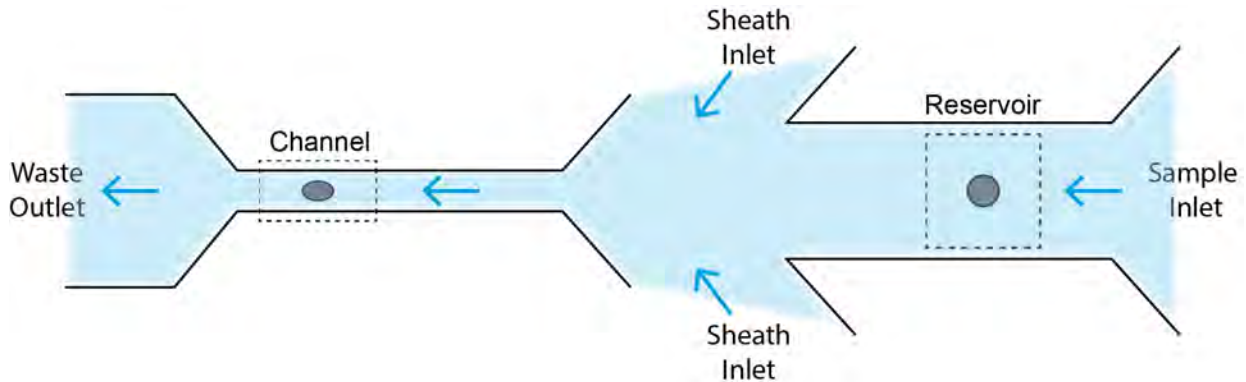


Figure 3.5: Internal structure of the FLICXX microfluidic chip. The dotted squares are the two acquisition areas. Cells are measured unperturbed in the reservoir prior to entering the channel, and near the end of the channel, where the deformation occurring due to strains in the channel are assumed to have reached a steady state.

The experimental setup comes with complimentary software. In the measurement software, ShapeIn, it is possible to change between two different imaging windows, reservoir or channel, which basically is changing the size of your imaging area. Examples of acquired images are given in Figure 3.6. You can see how the cell is unperturbed in the reservoir, while a shear stress and pressure gradient from the confining channel deforms the cell into a bullet shape. Image acquisition can be automated to stop after a specified amount of time or after a certain amount of cells have been measured.

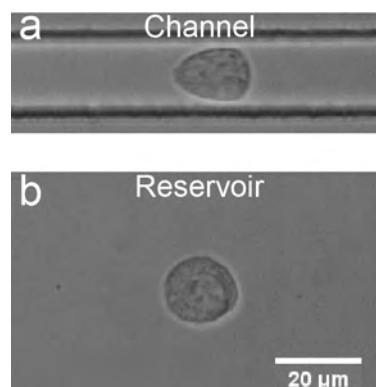


Figure 3.6: Examples of images acquired using RT-DC . (a) Bullet shaped cell in the confinement of a 20 μm channel. (b) Spherical cell in the reservoir. The reservoir image has been cropped to approximately 35% of its original size. The flow direction is from right to left. Scale bar is 20 μm .

The acquisition software registers cells in real time. It runs an algorithm which calculates the cells deformation and size (cross-sectional area), and displays results in a scatter plot as data is collected. The deformation, D , is defined as $D = 1 - \text{circularity}$,

where circularity is a parameter that evaluates the roundness of a shape and is given as seen in equation (3.5).

$$C = \frac{2\sqrt{\pi A}}{P} \quad (3.5)$$

From this definition, the circularity parameter is 1 for an ideal circle and decreases towards 0 for any deformations. This means deformation values will span values from 0 (circular) to 1 (highly deformed). Figure 3.7 depicts an example of typical deformability versus cell size plots for channel and reservoir measurements (non-invasive mouse breast cancer, 67NR). The stress within the constriction of the channel, increases closer to the wall, which means larger cells will experience a greater deformation. To allow users to evaluate the deformation of cells with different sizes, the plots also depict isoelastic lines which decouple size and deformation. The lines are based on an analytical model by Mietke et al. [69]. Through hydrodynamic equations, the stress distributed over a spherical cell's surface have been calculated, assuming deformation is of an isotropic and linearly elastic sphere. Cells of similar Young's elastic modulus, but varying size will fall on the same line in the deformation versus cell area plot. The isoelastic lines are universal, but scaled depending on the settings used in the program, ie. flow speed, channel size and viscosity of sample buffer. The lines are used during experimentation to evaluate material properties between different cells. The color scale seen in Figure 3.7 (a) and (b) indicates a linear density scale, allowing one to assess the location of the majority of the data points. In Figure 3.7 (c) contour plots of the two measurements are compared, red=channel and green=reservoir. The solid line marks 50% maximum density and the dashed line is at 95% maximum density.

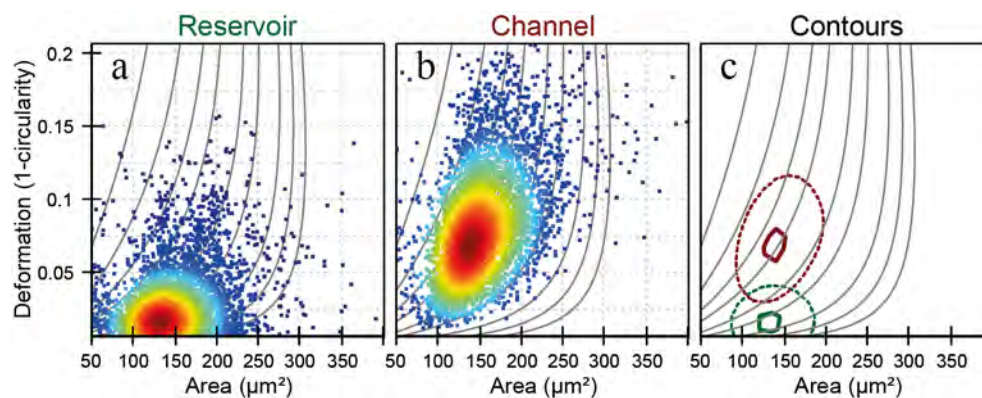


Figure 3.7: Sample of experimental data acquired with RT-DC and recalled with the analysis software Shapeout. The scatter plots depict deformation versus cell area (cross-sectional area) measured within a narrow channel (a) and an open reservoir (b). (c) Density contour plots comparing the two data sets from a and b (reservoir=green, channel=red). The solid line marks 50% maximum density and the dashed line is at 95%.

3.4.2 Data output (ShapeOut)

Post acquisition, data is recalled using the software ShapeOut. Data is depicted in deformation versus cell area plots, as described for ShapeIn above. Within ShapeOut, a variety of filters are at ones disposal (see screenshot in Figure B.3). Minimum and maximum values can be set for cell size and deformation, while also position within the channel can be defined. These are just some of the filters, and since we only apply one filter to our data, this will be the only to be expanded on. The parameter we limit is “Range area ratio”, which defines the relative difference between the convex hull and the cell contour, as depicted in Figure 3.8. The convex hull is the outline of the cell in which the line segments that connect any two points within the shape are also part of the shape. For the cell contour presented in Figure 3.8, the area ratio will thus be the difference between the area of the convex hull, and the registered cell contour area. Defining this parameter limits the allowed difference between the two shapes, ie. odd cell shapes are eliminated.

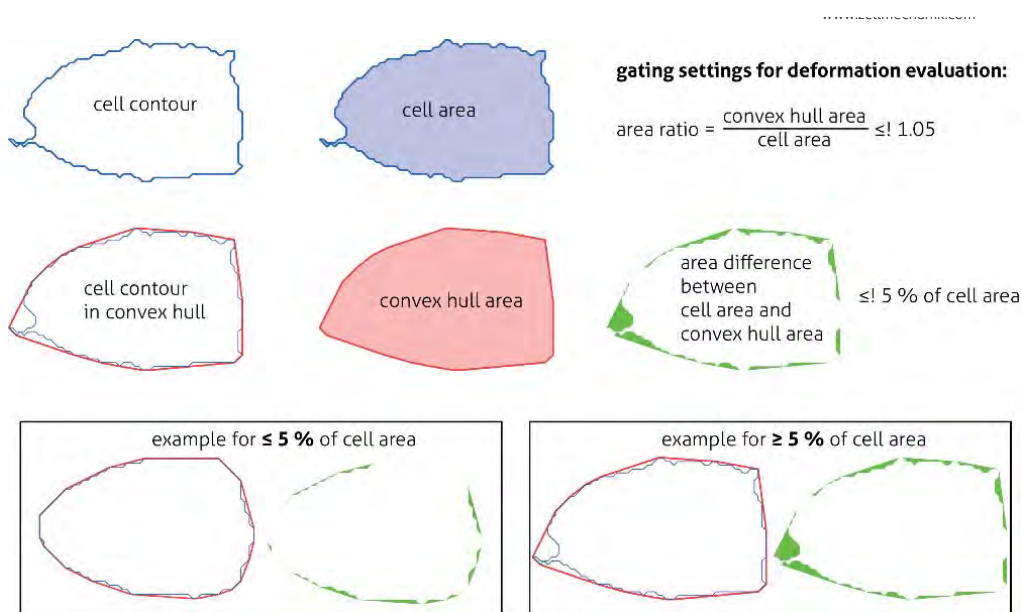


Figure 3.8: Illustration of how the “range area ratio” parameter is defined. Figure adapted from instruction manual delivered with RT-DC setup from ZellMechaniks.

3.4 Young's elastic modulus

The elastic properties of a solid material undergoing compression is described by the material property Young's elastic modulus. It represents the relationship between stress and strain, equation (3.6), and is a numerical constant. Young's modulus is essentially the stiffness of a material, and represents how easily it bends or stretches. It is only valid in the range where the stress is proportional to the strain (linear elastic), and the material returns to its original shape after the external force has been removed. It is a fundamental property of every material which cannot be changed, and is therefore a good measure for comparative studies.

$$Y = \frac{\text{stress}}{\text{strain}} \quad (3.6)$$

From the measured deformability values, it is possible to calculate Young's elastic modulus (via ShapeOut) based on numerical simulations for fully elastic spheres by Mokbel *et al.*[70]. The model quantitatively relates cell deformation to mechanical parameters. The model is valid for a wide range of deformations, and allows extraction of the cells stiffness. The conversion is possible for a valid region, which is limited by certain sizes and high deformability values.

3.5 Orientation analysis

The algorithms used to calculate the orientation of cells were written by Dr. Thuan Saw (Singapore University). The software was developed for kidney cells (MDCK cells), and results using this approach were recently published[45, 71, 72]. Simply stated; the orientation field algorithms calculated the orientation vector of defined interrogation areas within the cell layer (similar to PIV approach), by analyzing the contours and orientation profiles obtained from image analysis. Expanding on this, first, phase contrast images were processed in ImageJ with automated macros built using imbedded/native functions (smoothing and threshold filters). The processing was done to outline single cells in the monolayer. To minimize the effect of the interphase between the two advancing cell fronts (closing gap), a mask was applied in the gap area. Figure 3.10 depicts a typical set of images processed in ImageJ. Phase contrast images (Figure 3.10 (a)) have been inverted (I), contrast changed (C), smoothed (S), and an auto local threshold (ALT) has been applied, resulting in images termed ALT_SIC (Figure 3.10 (b)). Smoothing was done using a customized macro that applies a bandpass filter, similar to the one used for light gradient smoothing as mentioned in section §3.1. The image sequence in Figure 3.10 (c) are the result of applying OrientationJ analysis (ImageJ function) to inverted images and visualizing as grey level. The OrientationJ approach in ImageJ (plugin) functions similarly to PIV with a chosen interrogation window (Gaussian shaped for smoothing), which is used to calculate the structure tensor for each pixel. The local orientation properties were computed and visualized using gray scale[73].

The segmentation and alignment information stored in the analyzed images, Figure 3.10(b,c), was used in customized Matlab scripts (developed by Dr. Thuan Saw) to find the local orientation of the tissue. The algorithm identifies the orientation angle within local segmented structures, and plots a representative headless vector, director, to indicate alignment. An example of the director field (red arrows) overlaid an image of the cells can be seen in Figure 3.9.

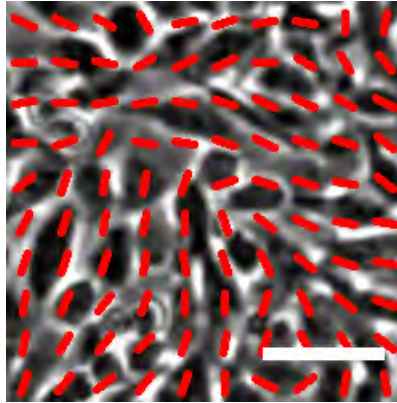


Figure 3.9: Director field of cell tissue. Phase contrast images of cell monolayer with headless orientation vectors, directors, overlaid. Scale bar, 50 μm .

Further information about the analysis can be found in [chapter 7](#).

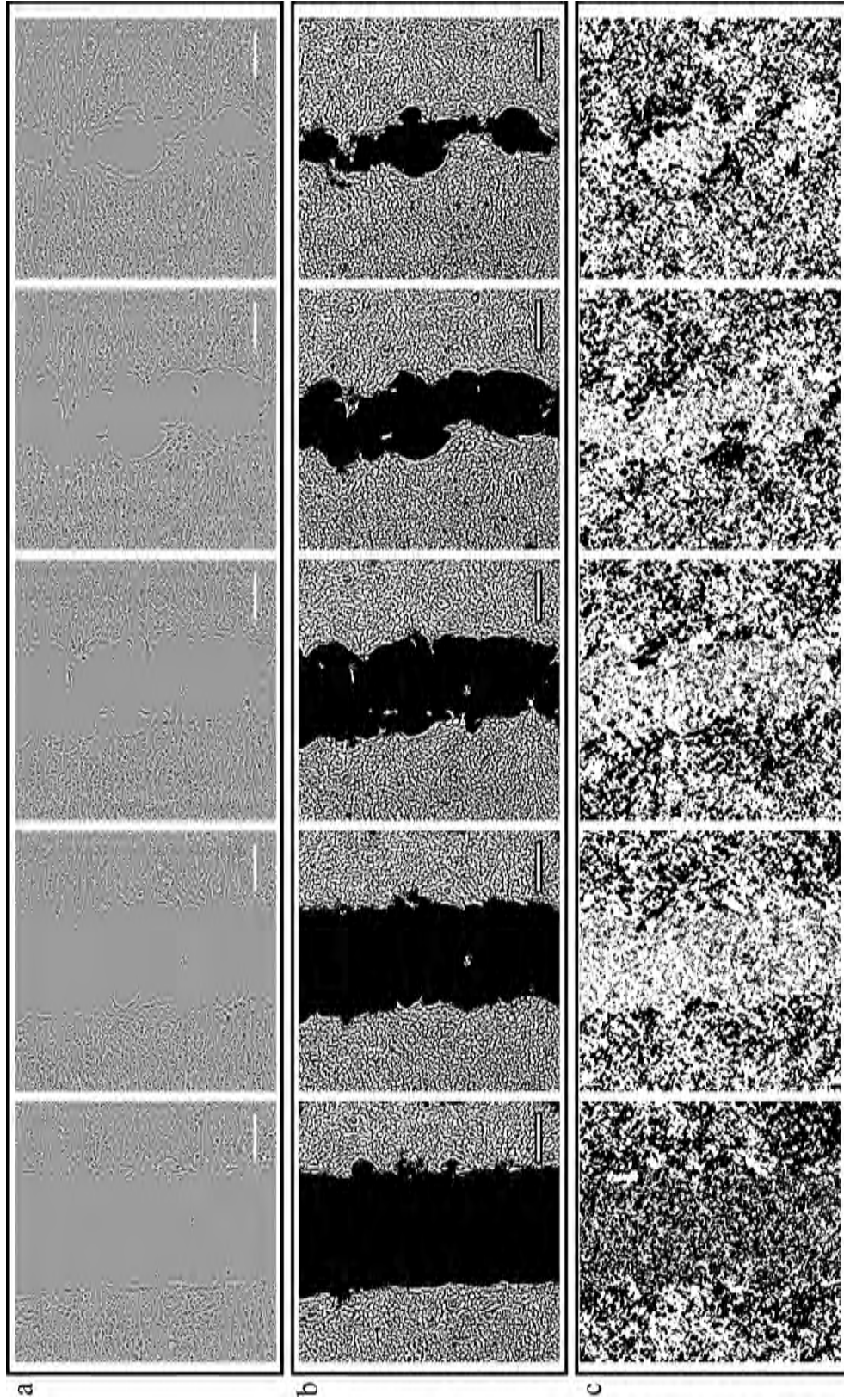


Figure 3.10: Sample images of orientation field analysis work-flow. (a) phase contrast image sequence with an interval of 3h and 20 min (20 frames) between each depicted frame, and first frame at the onset of imaging ($t=0$). (b) ALT-SIC (auto-local-threshold, smoothed, inverted, contrast) images overlaid with a mask to remove the gap area (black). (c) Local orientation visualized as grey level using OrientationJ in ImageJ. The cell line in the experiment is invasive murine breast cancer, 4T1. Scale bar, 200 μm .

Chapter 4

Dynamics of cancerous tissue correlates with invasiveness

In this chapter we present our work done on 2D cancer tissues using continuum mechanics. Methods described in the previous chapter were applied to study the dynamics and cellular forces within a 2D confluent cell monolayer for cells of different invasive potential. It was inspired by previous work done with endothelial cells, where Rossen et al. [9] revealed that cell divisions induce long range correlated motion in endothelial tissue. The experimental results prompted a collaboration with theoreticians, Dr. Jens Tarp, Dr. Amalie Christensen, and Associate Prof. Joachim Mathiesen, from the Biocomplexity group at the Niels Bohr Institute. The combined work was published in Scientific Reports[74], section §C.1, and a second paper with focus on the theoretical model is submitted, section §C.2.

4.1 Introduction

Cancer cells arise from malfunctioning healthy cells. The diseased cells divide uncontrollably and can be highly invasive into adjacent tissues, thereby posing a large threat to the patient they reside in. Characterizing the dynamics of cancer tissue may lead to a better understanding of the metastatic process, which is one of the main challenges in today's cancer treatment. Many different types of invasion have been revealed in the last decades, including single cell migration, but also collective migration of cell groups or sheets[17, 20, 75, 76]. Although these mechanisms are studied in detail, it remains unclear to which extent collective behavior is influenced by flow dynamics and mechanical stimuli. Moreover, it has not been reported yet if less adhesive cells cooperate via the same mechanisms as tightly connected cells. Many processes involve the remodelling of multicellular tissue, an cells posses the ability to respond to biomechanical stresses over significant length scales[1, 77]. Cells in tissues have been found to behave as fluids and be well described by continuum models, and within such frameworks cell divisions have been found to induce stress patterns[78], which have also been seen in experimental

studies[9].

In this study particle image velocimetry, a non-intrusive optical technique for quantitative flow measurements, was used in order to investigate the dynamics of two-dimensional breast epithelium and cancer cell sheets. In special focus are the cellular dynamics induced by a cell division within these confluent cell monolayers. We have focused on the mechanical aspects of cancer tissue dynamics and formulated a hydrodynamic continuum model in which we regard the tissue as an active material.

4.2 Methods

Invasive and non-invasive breast cancer cells from both human and murine lines were investigated; 67NR (mouse, non-invasive), 4T1 (mouse, invasive), MCF7 (human, non-invasive), and MDA-MB-231 (human, invasive). The cells were cultured as explained in A.1, and samples prepared using the protocol given in ???. Experimental images were collected using the Nikon Eclipse Ti-E microscope system described in section §3.1.

Phase contrast images of the confluent monolayers were acquired over 6-12 hours with 2 min between each image. The majority of the data was collected using a 10x air objective. To increase spatial and temporal resolution, imaging was repeated with a 20x objective, and an imaging interval of 0.5 min. Dividing cells were manually identified in the images, and only those without another division within 150 μm were used for further analysis. The point of division was defined to be when it was optically possible to distinguish two emerging daughter cells (cytokinesis). Images sequences of the centered dividing cells were rotated so the daughter cells moved along the horizontal axis, and cropped to a 300x300 μm^2 frame. Examples of these images are given in Figure 4.1, for mouse lines and human lines, respectively. The analyzed image sequences extracted were taken 40 minutes before division to 40 minutes after division. Particle image velocimetry, section §3.3, a non-intrusive optical technique for quantitative flow measurements, was used to investigate the dynamics of two-dimensional cancer cell sheets.

4.2.1 Particle image velocimetry analysis

Acquired images were analyzed using the PIVlab version 1.41 for Matlab as explained in section §3.3. The multi-pass window deformation technique was used to calculate the image correlations (FFT window deformation setting). Three passes were used and final interrogation areas of 15.6 μm for the 10x experiments and 7.8 μm for the 20x experiments, respectively. Both with an overlap of 50%. Interpolation was done in post processing with a standard deviation filter threshold of 7. An example of the analysis can be seen in Figure 4.2. To increase the signal-to-noise ratio, the velocity fields were averaged over at least 30 (for 10x) or 50 (for 20x) data sets, deriving from at least 4 individual experiments. Analysis of the velocities was performed with custom made Matlab scripts.

Results shown in the following are for 10x experiments. Experiments were repeated with a 20x objective, to increase the amount of data points and better resolve the division

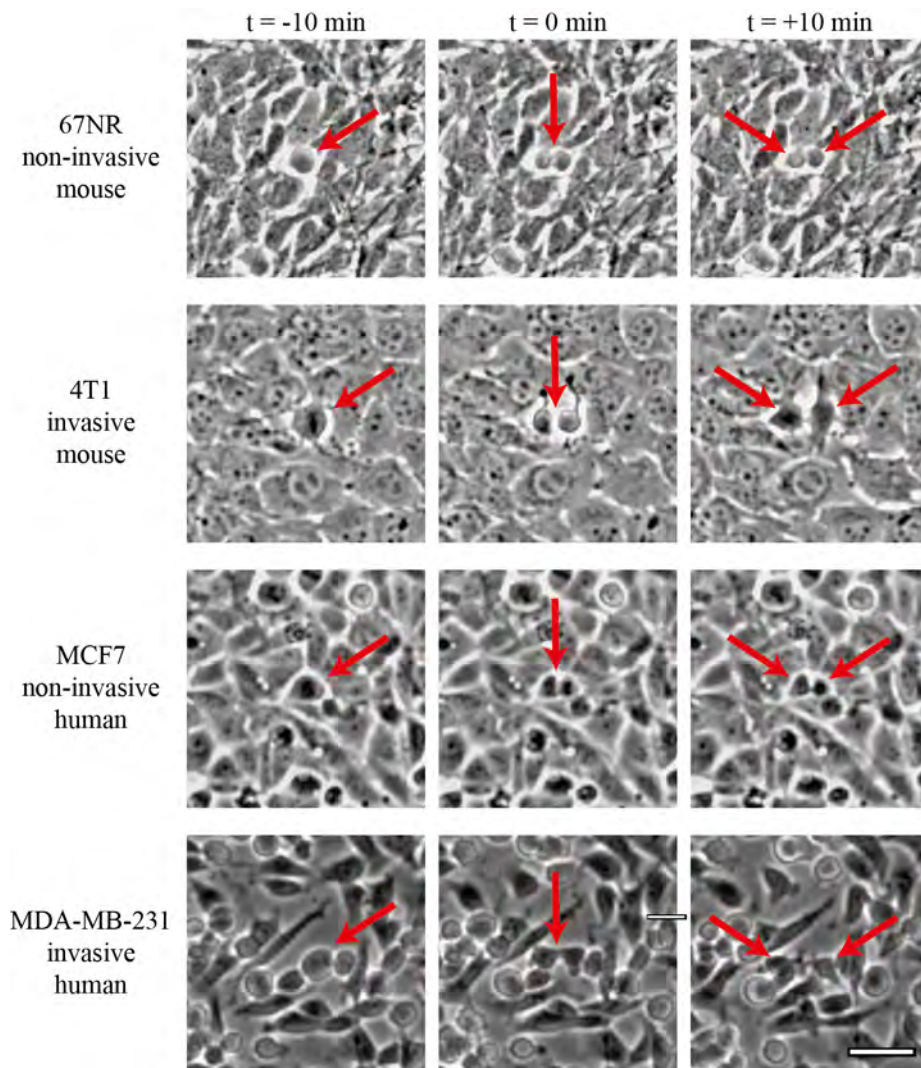


Figure 4.1: Isolated divisions within confluent breast cancer monolayers. Sample images of experimental data with murine and human breast cancer cell lines; 67NR (mouse, non-invasive), 4T1 (mouse, invasive), MCF7 (human, non-invasive), and MDA-MB-231 (human, invasive). The red arrows point to the site of cell division and at the resulting daughter cells. Time zero is defined as the point where two distinct daughter cells are visible (cytokinesis). The dividing cell is centered in the image and rotated so that the daughter cells move in the horizontal plane after cell division. The scale bar is $40\ \mu\text{m}$ and applies to all images.

dynamics, as these occur over just a few points in the grid. This was necessary for a better comparison with the theoretical model which will be introduced in section §4.4. The higher magnification did not change the patterns and dynamics on which we report in the following.

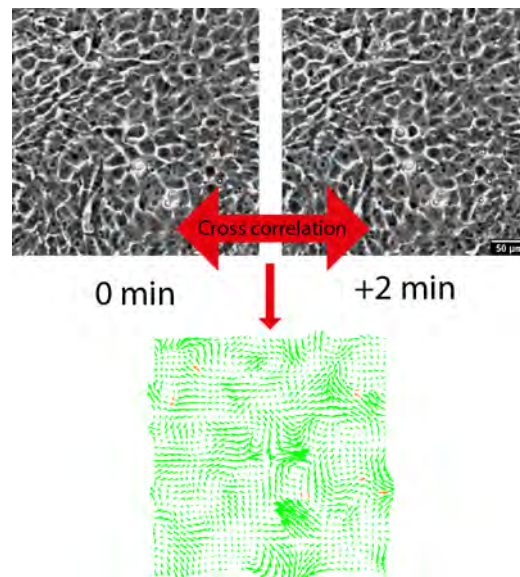


Figure 4.2: PIV analysis of cancer monolayer motility. Resulting displacement vector field from cross correlation calculations done using PIV on consecutive bright field images of confluent cancer monolayers. The orange vectors have been interpolated.

4.3 Results

With the chosen grid size our vector field was 37×37 , which gives 1,369 velocity vectors per image and 109,520 per division. This is in total 3,285,600 velocity vectors for each cell type.

4.3.1 Speed distributions and velocity profile

From the velocity fields, we calculated the speed distributions of all investigated cell types for the whole imaging period (80 min). These are depicted in Figure 4.3 for the murine (a) and human cells (b), respectively. Figure 4.3 (c) shows the time evolution of the average speed during the imaging period. The above average speeds were only observed within 1-2 cell diameters from the division site, consistent with the movement of the two emerging daughter cells. Around the site of division we observed an amplification in velocity compared to the general average tissue velocities. The increase is highly localized and short term (± 6 min from cytokinesis), and resulting perturbation in the measured velocity field are negligible in relation to the overall motility. The overall tissue velocity, Figure 4.3, is constant throughout the imaging period. The average speed distributions therefore characterize the motion of the entire monolayer. The murine cell lines showed an average speed of $0.13 \pm 0.03 \mu\text{m}/\text{min}$ for the non-invasive 67NR cells, while the invasive 4T1 cells had an average velocity of $0.27 \pm 0.06 \mu\text{m}/\text{min}$. For the human cell lines, the non-invasive MCF7 cells display a mean velocity of $0.23 \pm 0.02 \mu\text{m}/\text{min}$, while the invasive MDA-MB-231 cells had an average speed of $0.7 \pm 0.2 \mu\text{m}/\text{min}$. The reported errors were found as the standard deviation of the average speeds (SEM), calculated for 30 random areas from at least 3 independent experiments. For both the murine and human cell lines, the invasive cells display a significantly larger average speed than their

non-invasive counterparts. From the speed profiles it is also apparent that the invasive human cells, MDA-MB-231, have a heavy-tailed distribution (see Figure 4.3(b)). It indicates that a significant amount of cells move at a greater speed, which was also our observation during imaging. The MDA-MB-231 cells move generally in a more chaotic and aggressive way than the other cell lines.

Cell speeds reported in literature correspond well with our observed values for the human cell lines, though it should be noted that the studies were with cells migrating into vacant space [79, 80, 81, 82]. For the murine cell lines, we have only found a reported value for the non-invasive 67NR[83]. With an average speed of $0.03 \mu\text{m}/\text{min}$, this is considerably lower than what we have registered. This can maybe be attributed to the different assays resulting in different expressions of growth factors and cytokines (molecules that affect proliferation).

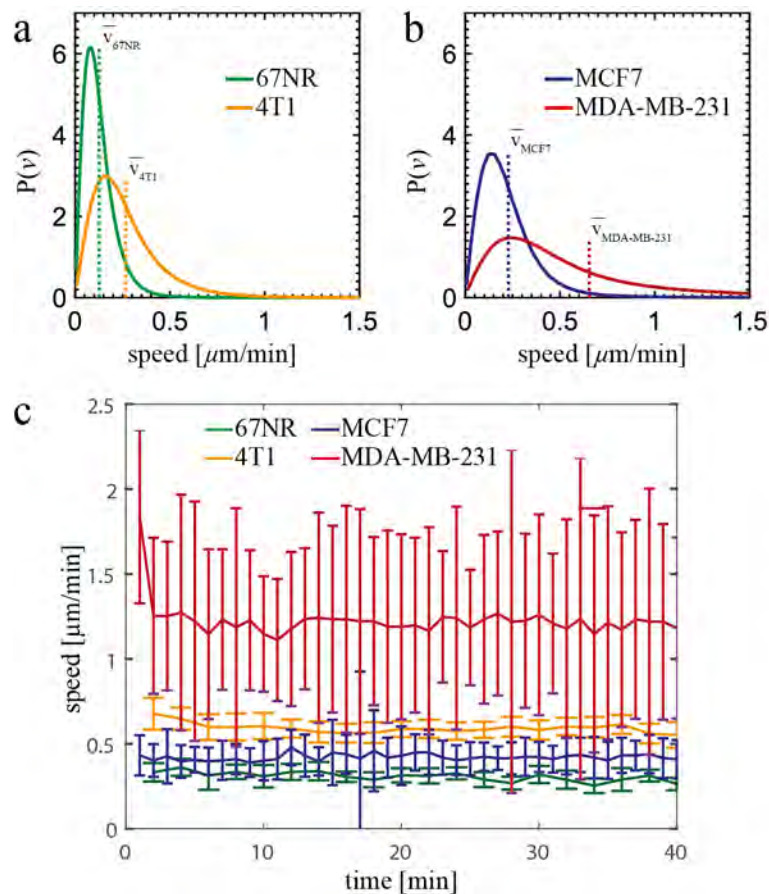


Figure 4.3: Velocity profiles for confluent breast cancer monolayers of different invasive potential. Probability density of normalized speed distributions for murine cell lines (a) and human cell lines (b). The dotted vertical lines mark the average speed for each cell type. (c) depicts the time evolution of the average velocity from the point of division ($t=0$). Parts of the figure have been published in West et al. [74].

4.3.2 Vorticity and divergence

From the velocity fields it is possible to map the divergence and vorticity fields as explained in section §3.3. By averaging over 30 different divisions, we increase the signal-to-noise ratio. This allows us to remove signals which are random noise and reveal what is perpetual throughout different samples.

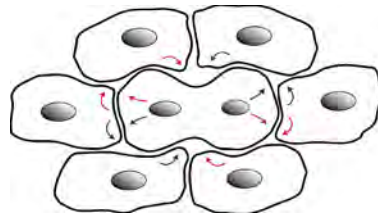


Figure 4.4: Illustration of rotational motion created by a dividing cell.

Figure 4.4 depicts how the dividing cell creates vorticity (swirling) in the motion of the surrounding cells. The dividing cell expands to make room for the two emerging daughter cells, creating a push on the neighboring cells in a clockwise (red) and counterclockwise (blue) motion. The time evolution of the averaged vorticity field is given for 5 frames in Figure 4.5, for all 4 cell lines: the non-invasive and invasive murine and human cell lines respectively. For all investigated cell lines, at the time of division ($t=0$), both daughter cells were flanked by a pair of vortices, and these ordered hydrodynamic structures sustained for up to 6 minutes after cytokinesis. This was found to be unique for the time point and site of division. Interestingly, the intensity of the vorticity patterns is generally higher for the invasive cell lines, consistent with the higher velocities observed in these tissues.

From the averaged velocity fields we also calculated the corresponding divergence fields. Values are portrayed using a color map with contractions in blue, and expansions in red in Figure 4.6 (b). The color green signifies an average value close to zero, and is a sign of purely random motion within the cell layer, since stochastic noise averages to zero. At the center of the division site is a recognizable expansion pattern flanked by slight contraction. Figure 4.6 (a) illustrates the way the emerging daughter cells expand into the surrounding by pushing the neighbors away.

4.3.3 Controls

To control whether observed patterns are unique for cell division in the monolayer, we performed a few controls. In line with the study from 2014, we treated our cells with the drug, aphidicolin (see protocol in ??(Appendix A.2). Aphidicolin (Sigma Aldrich) is a known antimetabolic agent, and we applied it to see how the flow dynamics changed when cell division was blocked. The cells did not respond well to aphidicolin treatment, as they became multinucleated and swollen, leading us to doubt the validity of this as a proper control. We chose to perform another type of control where we did the exact same analysis, but of random areas in the cell layer without a division. The previously observed double dipole pattern visible in Figure 4.5, is not present in the vorticity field of

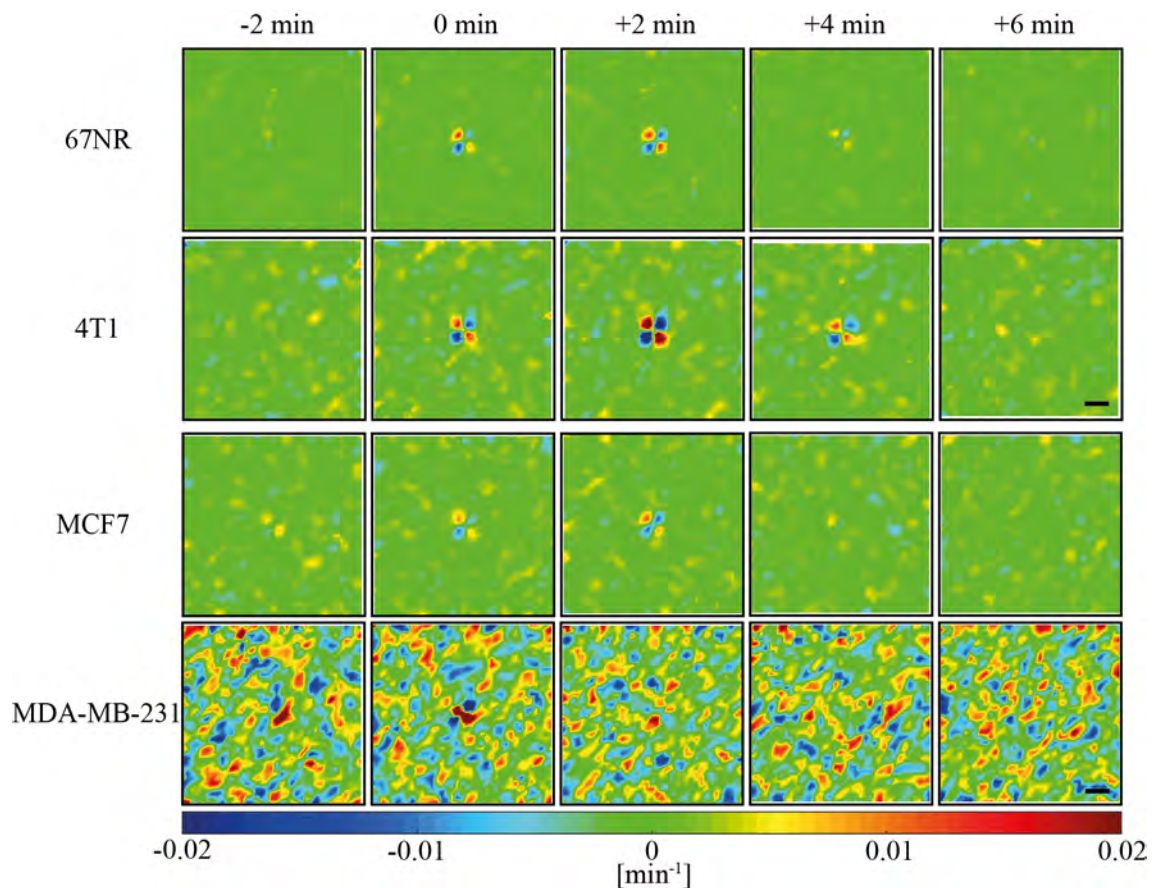


Figure 4.5: Cell divisions induce ordered vorticity patterns in a confluent monolayer of breast cancer cells. Timeseries of average vorticity fields ($300 \times 300 \mu\text{m}$ frame, $n = 30$), in which a dividing cell is centered, and the daughter cells are moving in a horizontal direction after cytokinesis. Time zero was defined as onset of cytokinesis. The columns are different timepoints denoted at the top, while rows are the different cell lines. Two top rows are vorticity fields of murine cell lines (non-invasive 67NR, invasive 4T1). Two bottom rows are vorticity fields of human cell lines (non-invasive MCF7, invasive MDA-MB-231). The colorscale and arrow color displays the vorticity (counterclockwise motion=blue, and clockwise motion=red). The scalebars are $40 \mu\text{m}$ and apply to all images. Figure adapted from West et al. [74].

the control areas without division, in Figure 4.7 (a). Neither are any protruding expansion or contraction patterns in the divergence field of the control in Figure 4.7 (b).

As a control of the effect of microenvironment, similar analysis was done for cells seeded onto collagen (4mg/mL), see protocol in ???. The color maps shown in Figure 4.8 have only been averaged over 5 different samples, and are therefore more noisy than our main results. The vorticity (a) and divergence (b) patterns previously observed at the division site are still recognizable.

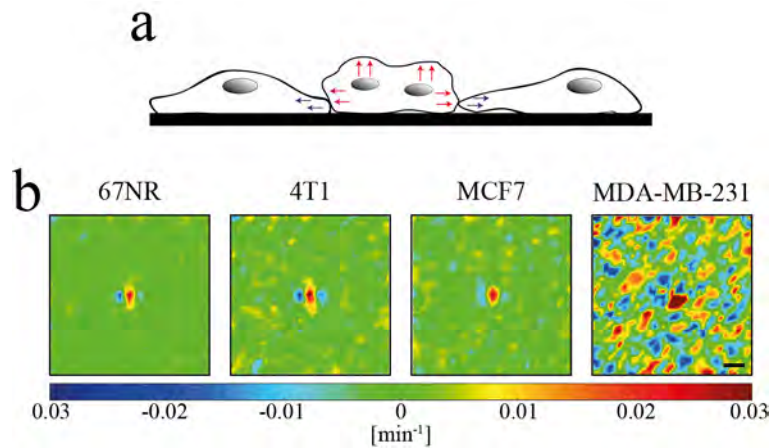


Figure 4.6: Divergence field of confluent breast cancer monolayers with a centered cell division site. (a) Illustration of the contraction (blue arrows) and expansion (red arrows) of cells undergoing or neighbouring cell division. (b) Divergence field during cytokinesis around a dividing cell located in the center of each image. The daughter cells move in a horizontal direction after cytokinesis. Each image is $300 \times 300 \mu\text{m}^2$ and is an average of at least 30 data sets. The scalebar is $40 \mu\text{m}$ and applies to all images. The color scale displays the degree of divergence with blue denoting contraction and red expansion. The two invasive tissue types (mouse 4T1 and human MDA-MB-231) exhibit a higher degree of contraction and expansion than their non-invasive counterparts (mouse 67NR and human MCF7). Figure adapted from West et al. [74].

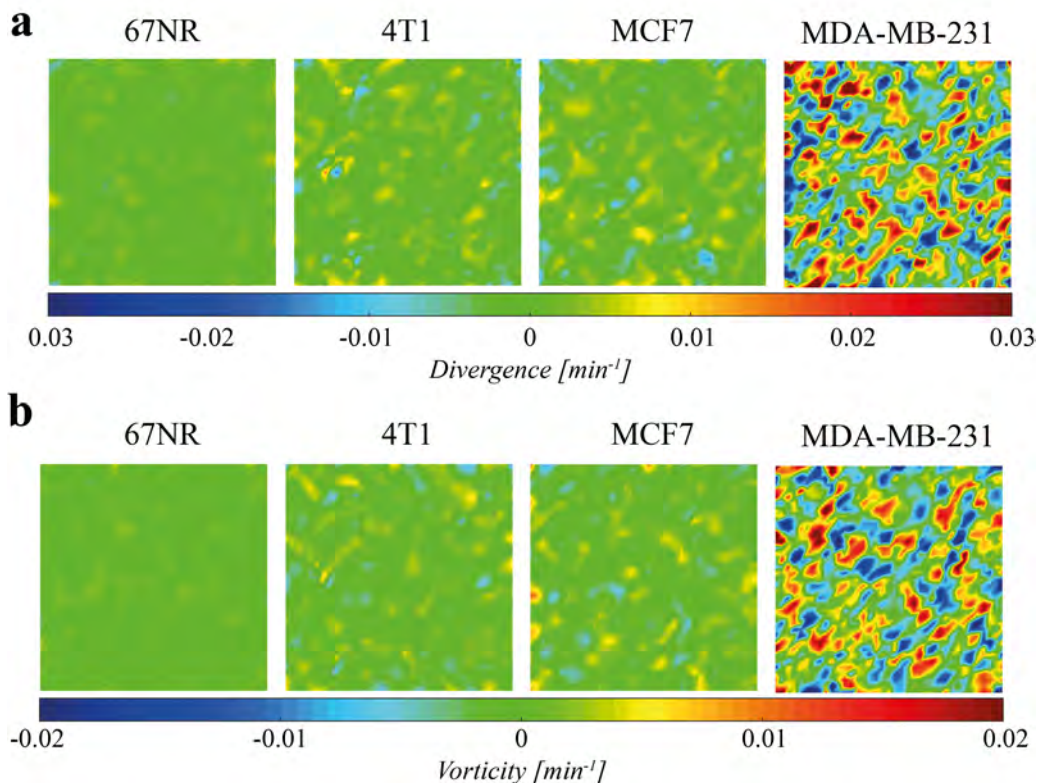


Figure 4.7: Control analysis of random areas in confluent breast cancer monolayers. Each image is $300 \times 300 \mu\text{m}^2$ and is an average of at least 30 data sets. The scalebar is $40 \mu\text{m}$ and applies to all images. (a) depicts the vorticity fields (counterclockwise motion=blue, clockwise motion=red). (b) portrays the divergence fields (contractions=blue, expansion=red).

4.4 Continuum model

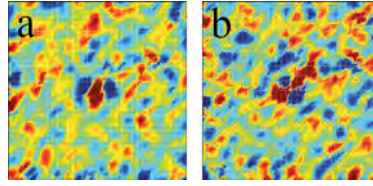


Figure 4.8: Flow patterns of dividing cell on collagen. Divergence (a) and vorticity (b) patterns also apparent in cells grown on collagen ($n=5$). Cells depicted are 4T1s. Images are 2 min after cytokinesis, and the frame is $300 \times 300 \mu\text{m}$.

The following model was inspired by Prof. Julia Yeoman's work and formulated as summarized below by Dr. Amalie Christensen & Associate Prof. Joachim Mathiesen.

4.4.1 Theory

The collective motion of cells was reproduced by a continuum-scale model integrating the mechanical interaction between the cells, the Coulomb-like friction with the substrate and the self-propelling forces of the cells. It has been based on one of the most simple models of viscoelastic behavior, known as the Oldroyd-B model (section §4.4). With this model we achieve a system which acts as an elastic material on short time scales, while displaying viscous behavior on larger time scales. In the limit of small velocity gradients this model is based on the constitutive relation:

$$\sigma + \lambda_1 \frac{\partial \sigma}{\partial t} = 2\eta_0 \left(\gamma + \lambda_2 \frac{\partial \gamma}{\partial t} \right), \quad (4.1)$$

where σ is the derivative stress tensor, $\gamma = \frac{1}{2} [\nabla v + (\nabla v)^T]$ is the strain rate tensor, λ_1 is the relaxation time, λ_2 the retardation time, and η_0 the total viscosity. A characteristic of a viscoelastic fluid is that it retains memory of the past stress states, which is included in the constitutive equation as time derivative of the stress tensor σ . We include the self-propelling of individual cells by adding mass and momentum balance equations. The mass balance is guaranteed by the incompressibility condition $\nabla \cdot v$, and the momentum balance equation assumes the form

$$0 = -\frac{1}{\rho} \nabla p + \frac{1}{\rho} \nabla \sigma - \alpha \hat{v} + m, \quad (4.2)$$

where ρ is the mean density, p is the pressure, $\hat{v} = v/|v|$ is the direction of the local mean velocity of the tissue, α is a positive friction constant and m is the motility term. Since the dynamics are assumed to be fully overdamped, the momentum balance, equation (4.2), contains no inertial terms.

4.4.2 Comparing theory and experimental

Numerical simulations were done using the continuum model described by equation (4.1) and equation (4.2). The self-propelling of the cells was taken to be the result of an Ornstein-Uhlenbeck process with a noise persistence time λ_m , strength β_m and a chosen characteristic length scale m (see Appendix B Figure B.1). From the simulations we calculated the speed probability density function $P(v)$, the spatial velocity correlation function $C_r(r)$, and the temporal velocity correlation function $C_t(t)$. Figure 4.9 shows the speed distributions returned by the continuum model for the different cell types. The model (dotted lines in Figure 4.9) recapitulates the experimental data (full lines) well, and even captures the fat high-velocity tail of the human invasive MDA-MB-231 in the speed distributions. Through the model it was possible to simulate the horizontal and vertical velocity field components ($v_{mod,x}, v_{mod,y}$) in a cell layer with a local centered division. The resulting velocity maps can be seen in Figure 4.10, and they are in agreement with the experimental data also shown (v_x, v_y).

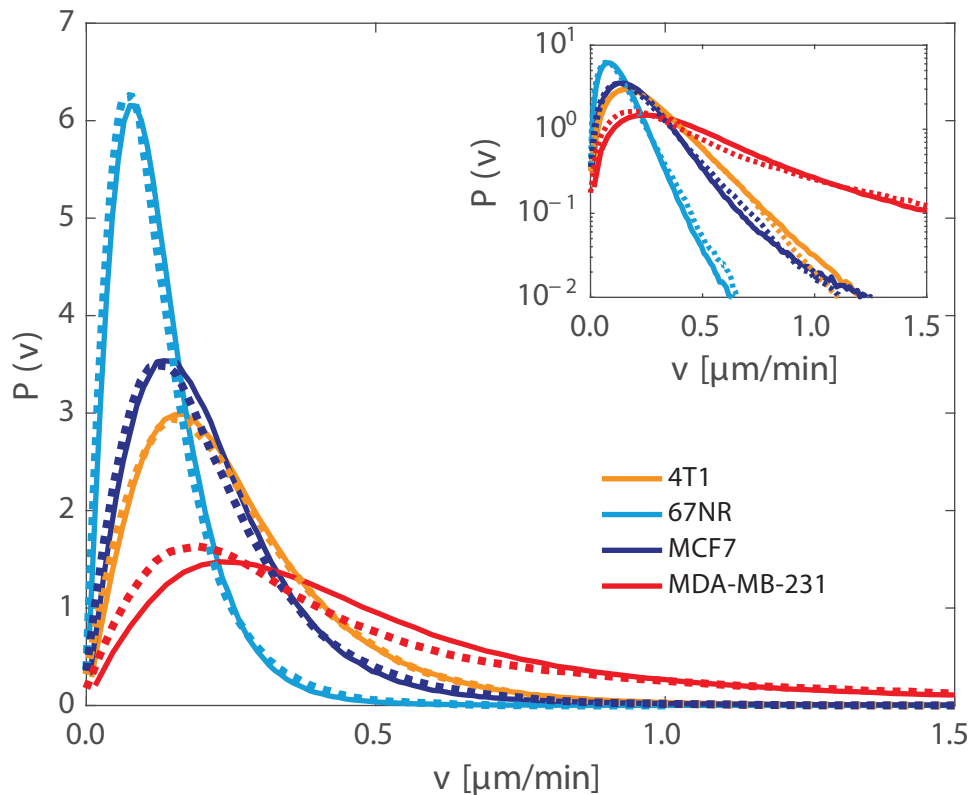


Figure 4.9: Comparison of experimental speed distributions and model predictions. Normalized probability density speed distributions from whole imaging period (80 min). Full lines depict experimental data, and dashed lines are theoretical predictions. The inset shows the speed distributions on a semi-logarithmic scale. The model fits well with experimental data, and even captures the fat high-velocity tails. Figure adapted from West et al. [74].

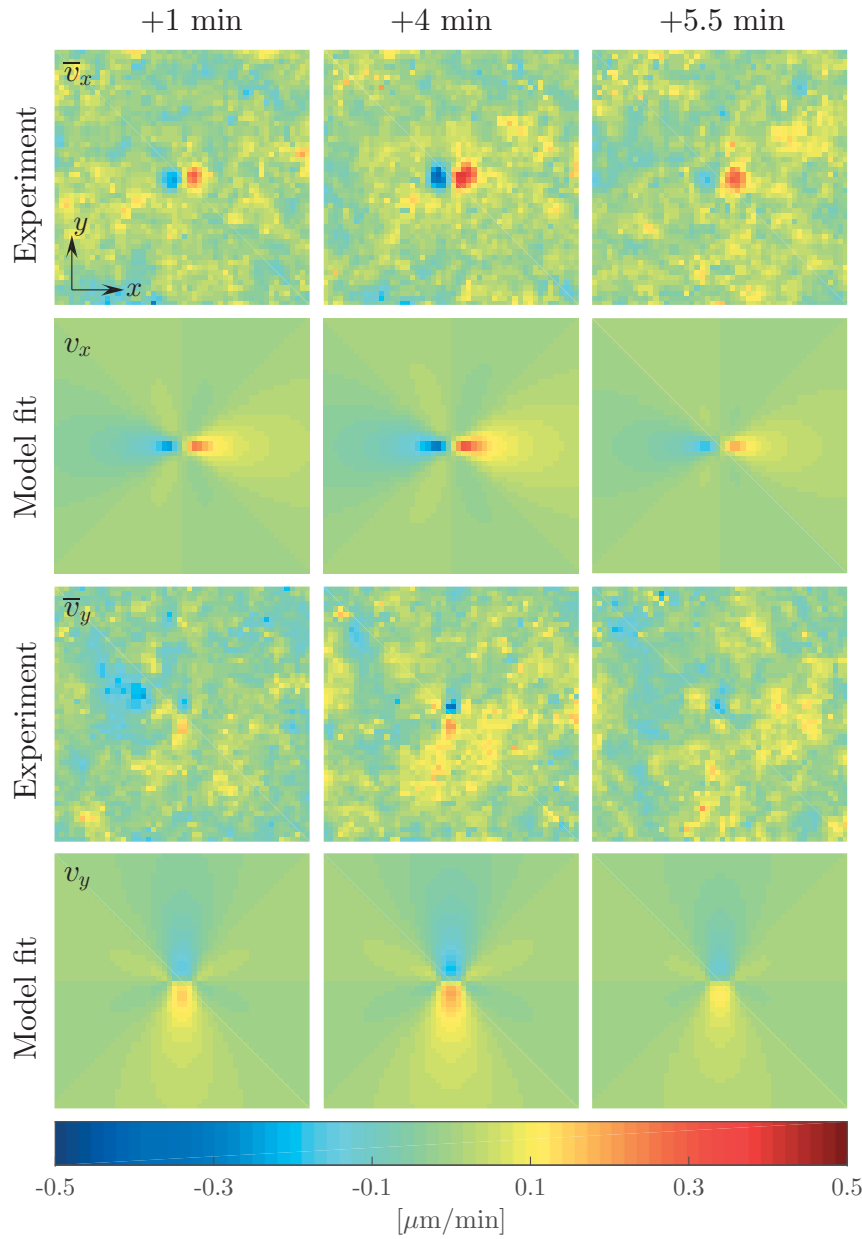


Figure 4.10: Cell division induced flow field at different timepoints. Comparison of experimental velocity fields (v) and a fit of the model (v_{mod}) given by equation (4.3). Experimental data is of MCF7 cells with a centered division in a frame of $200 \times 200 \mu\text{m}$, and the model predicts equally well for the 3 other cell lines. Time zero is defined as the point of cytokinesis. Figure adapted from Christensen [84].

4.4.3 Quantifying force

We were able to extract the forces exerted by a dividing cell via the active stress, σ , in the constitutive model, equation (4.1). The active stress consisted of two point forces, which are equal in size and in opposite direction, with center at the division site. Since we were interested in the division-induced effect we neglected the general noise term m , which represented the cells' intrinsic motility, and the friction term $-\alpha\hat{v}$. In the absence of noise and friction we solved equation (4.1) analytically. The obtained velocity field was

a Stokeslet dipole $v_{sto}(\mathbf{x})$ in space multiplied by a time dependent function $h(t)$, (see ??):

$$\mathbf{v}_{mod}(\mathbf{x}, t) = v_{sto}(\mathbf{x}) \cdot h(t). \quad (4.3)$$

The velocity field in equation (4.3) was fitted to the timeseries of experimental flow fields both with and without a timeseries dependence in Figure 4.11. We defined the expression for force as force divided by viscosity, since we did not know the absolute value of the viscosity, but we assumed that the viscosity did not change much between cell types. When fitting to the timeseries, one forcing (f_0/η_0) and one retardation (λ_2) value was returned, while fitting to each frame returned a timeseries of forcing and retardation values. The model predictions show that for both murine ($p < 10^{-8}$) and human ($p < 10^{-3}$) breast cancer cell lines, the invasive cell types, 4T1 and MDA-MB-231, respectively, exerted a higher forcing during division.

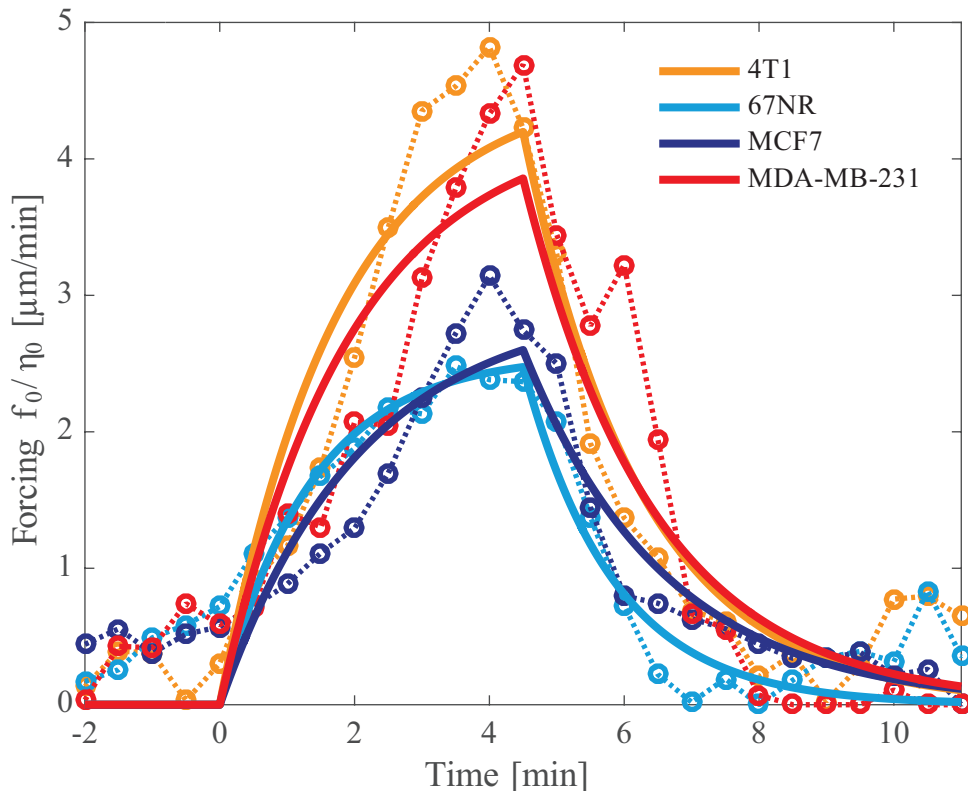


Figure 4.11: Theoretically predicted forcing exerted by a dividing cell as a function of time. Forcing is given as the force divided by the viscosity for four different breast cancer cell lines; 4T1 (invasive, murine), 67NR (non-invasive, murine), MCF7 (non-invasive, human), and MDA-MB-231 (invasive, human). Solid lines represent result from fitting equation (4.3) to the experimental velocity timeseries returning one value for forcing (f_0/η_0) and retardation time (λ_2). The dashed lines represent fits to the same experimental data, when each time frame is fitted with a Stokeslet dipole $v_{sto}(\mathbf{x})$. The invasive cell lines, in both human (red) and murine (orange) breast cancers, have a larger forcing on the surrounding when dividing. Figure adapted from West et al. [74].

4.5 Conclusion

We have investigated tissue dynamics of invasive and non-invasive breast cancer cancer tissue on the basis of displacement velocity fields of 2D tissues. We have two major findings. First, we have found that cell divisions induce motility of the adjacent cells with ordered divergence and vorticity fields. Second, the magnitude of the whole monolayer velocity and flow fields were found to be higher in the invasive cell lines relative to their non-invasive counterparts. We proposed a viscoelastic continuum model which recapitulates the coordinated motion of the cancer cells. It even catches the fat exponential tails of the velocity distributions. The model was formulated in a mechanical framework allowing quantification of forces in the tissue. The extracted forcing values confirmed a higher stress within the aggressive cell layers. The model differs from previously reported models in literature in two significant ways. First, the friction term is not a classical drag-like friction[85, 40, 46], but rather a friction from lateral motion of two solid surfaces in contact (dry Coulomb friction). This term is responsible for our ability to reproduce the experimentally observed exponential tails of the speed distributions. Second, the model is formulated on the basis of the tissue velocities and the material is treated using microrheological terminology. The model might be too simple in its coarse-graining of cell interactions. Recent studies have found that when treating cell tissues as an active nematic material, one can account for features, such as cell extrusion, in relation to defects within the layer[45]. Nematic properties cannot be reproduced using our proposed model. The model was designed to reproduce bulk properties, which we have found it does very well, however it might be improved by introducing a nematic contribution.

Chapter 5

Correlation between cancer cell shape and deformability

During this PhD project we bought a newly developed cell deformation analysis setup, as described in section §??(3.4) and in Otto et al. [67]. In the following we will present results from our study on cell deformation, and set it in relation to observed shape morphologies of the chosen cell lines. For these experiments we expanded our set of cell lines from the previous 4 breast cancer lines to also include pancreatic and colorectal lines, both with a non-invasive and invasive variants. See more information regarding cell lines in [chapter 3](#). The results presented in this chapter are under preparation for publication.

5.1 Introduction

Recent years there has been an effort to use mechanical cues to distinguish cancer cells from normal tissue. Multiple studies have reported a loss of cytoskeletal rigidity during cancer progression, and observed a proportionality with metastatic potential[86, 87, 88]. Malignant cells have the ability to detach from the primary tumor, cross normal tissue barriers, and metastasize to other areas of the body[10]. To do this, they need some degree of adaptability, which could be consistent with a compliant outer structure. Modes of migration, whether single cell or collective, were originally defined according to observed morphological patterns[14]. Transition from round epithelial to elongated mesenchymal (EMT) is often associated with a loss of adhesion, and related to more motile and invasive behavior. This is a dynamic transition known to occur during embryonic development, but also classically related to invasive cancer cells[15]. Previous studies using AFM[86], optical stretchers[88], and microfluidics[89] have documented how deformation and stiffness characterization can distinguish cancer cells of different metastatic potential. Guck et al. [88] used optical stretchers to probe the optical deformability of human epithelial breast cancer cells, and found that aggressive cell line. They found that non-invasive human breast cancer cells, MCF7, were more compliant, than the normal MCF10A human breast epithelial cells. With the same cell lines, Li et al. [90] found that cancerous MCF7 cells

had an Young's modulus 1.3-1.7 times larger than normal MCF10A. Hence, mechanically phenotyping of cells can possibly reveal underlying pathophysiological changes in normal cell homeostasis.

To perform biomechanical phenotyping, we employ real-time deformability cytometry, which is a high throughput non-invasive approach, which allows label-free analysis of a cells mechanical response to non-destructive forces.

5.2 Method

For this study we used the experimental system known as real-time deformability cytometry (RT-DC), see details in 3.4. Eight different cancer cell lines were investigated, ??(section 2.2.3), and samples were prepared as described in ??(Appendix A.2.2). Cells were measured directly after sample preparation, and measurement time was minimized to approximately 30 min per sample, as it has been observed that cells become stiffer over time. Cell shape morphology was also investigated using fluorescence microscopy (section §3.1). The results are presented in section §5.3.

5.2.1 Acquisition software: Shapeln

Real time deformation cytometry (RT-DC) measures the deformation of cells when flowing through a channel. The channels used in our experiments were 20 μm wide, and flow speeds of 0.04 $\mu\text{l/s}$ and 0.12 $\mu\text{l/s}$ were applied. The different flow speeds were only used as a control of the robustness of the measured deformation changes under varying shear forces. Deformation versus cell area (cross-sectional area) plots comparing flow speeds can be seen in Figure B.2. The force exerted on the cells in the channel has been estimated analytically to be approximately 0.5 μN and 1.5 μN , respectively, for the two flow speeds[69]. For each experiment we register at least 5,000 cells (minimum cell size 10 μm^2) in the channel, and in the reservoir 10,000 cells. An overview of statistical data can be seen in Figure B.1. The reservoir measurement served as a control of prior perturbations not in relation to the shear within the channel.

5.3 Results

5.3.1 Deformability versus cell area

After acquisition, the data was evaluated using the analysis software ShapeOut version 0.7.8¹. We removed cells with irregular shape to limit the counting of damaged/unhealthy cells or out-of-focus blur, by applying the area ratio (parameter defined in section §??(3.4)). In the top right inset of Figure B.3, an image of an excluded cell can be seen. Measured cell contour was not allowed to deviate more than 10% from the convex hull area, when applying this filter. Deformation versus cell area figures from ShapeOut can be seen in

¹Available at <https://github.com/ZELLMCHANIK-DRESDEN/ShapeOut>

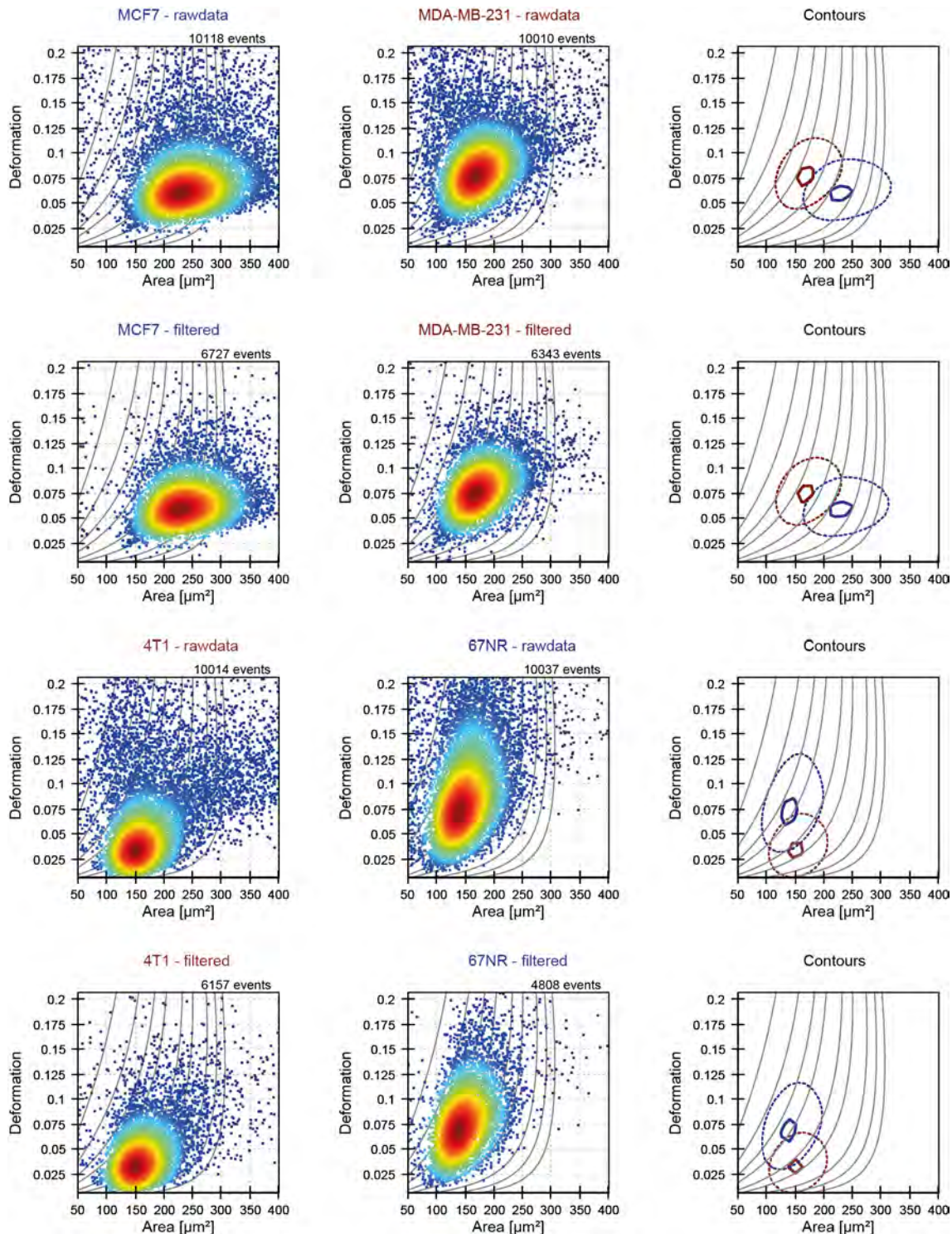


Figure 5.1: RT-DC scatter plots of cell deformation and cell size of different breast cancer cell lines. The scatter plots depict deformation versus cell area (cross-sectional area) measured within a narrow channel. The two first rows depict Shapeout plots for human breast cancer cell lines (MCF7, MDA-MB-231) with all data and gated data, respectively. The bottom two rows depict the corresponding scatter plots for the mouse breast cancer cell lines (67NR, 4T1). Invasive cell lines are depicted in red, while non-invasive cell lines are in blue. Last plot in each row are density contour plots comparing invasive and non-invasive pairs from that row. The solid line marks 50% maximum density and the dashed line is at 95%.

Figure 5.1 for breast cancer cell lines with an area ratio filter set to 10%. The trends observed did not change by this, but minimized our cell count to between 50-80% of the total amount of data. This also holds true for the cell lines. The exact total amount

of counted cells can be seen in Figure B.1. Our approach is robust as the unfiltered data shows the same general trend for the rawdata distributions as for the area ratio limited data.²

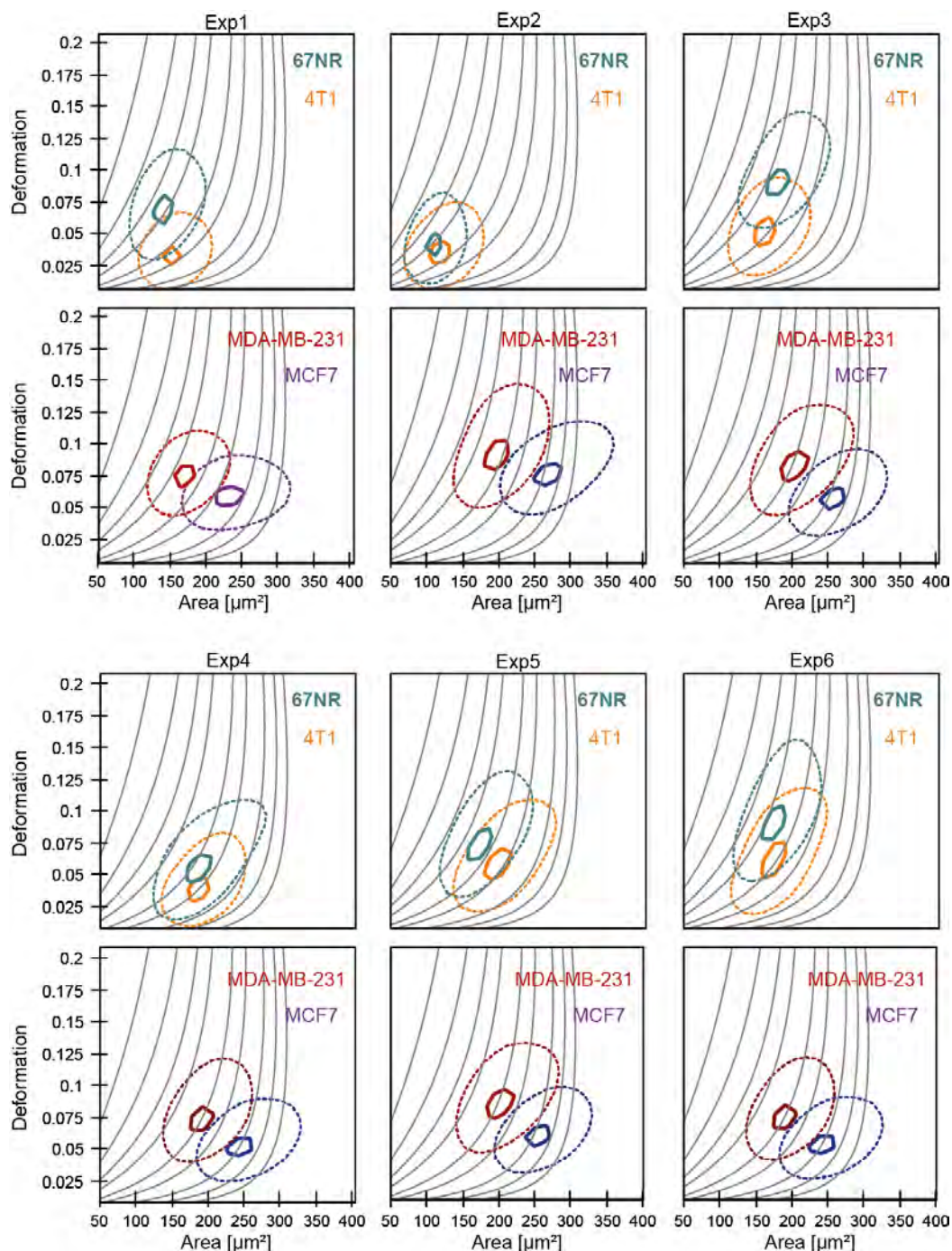


Figure 5.2: Deformation versus cell area plots of breast cancer cell lines. Density contour plots comparing deformations resulting of MCF7 (human, non-invasive), MDA-MB-231 (human, invasive), 67NR (murine, non-invasive), and 4T1 (murine, invasive) cells. The solid line marks 50% maximum density and the dashed line is at 95%. Single day deformation experiments of invasive and non-invasive cancer pairs.

²Knock knock. - Who's there? - A little old lady. - A little old lady who? - All this time, I had no idea you could yodel.

5.3 Breast cancer cell lines

The experimental data consistently showed a higher deformability for non-invasive mouse breast cancer cells, 67NR, than for the invasive mouse breast cancer cells, 4T1. The density contour plots from Shapeout can be seen in Figure 5.2, where invasive cell lines have shades of red color and non-invasive have blue shades. Though day-to-day variations are apparent in the data, the results consistently show a higher deformation for the cells that have an elongated shape; non-invasive 67NR and invasive MDA-MB-231. For the murine cell lines, this means that the less invasive cells, 67NR, deform more than their invasive counterpart, 4T1.

All experimental data was exported and analyzed in Matlab. Probability density histograms of all deformability measurements are plotted for both mouse (a) and human (b) breast cancer cell lines in Figure 5.3. Due to the skewed nature of the distributions, we have used the mode (black line in Figure 5.3) of the probability density function for further analysis. The mode value is the deformation value at which the distribution has the highest count.

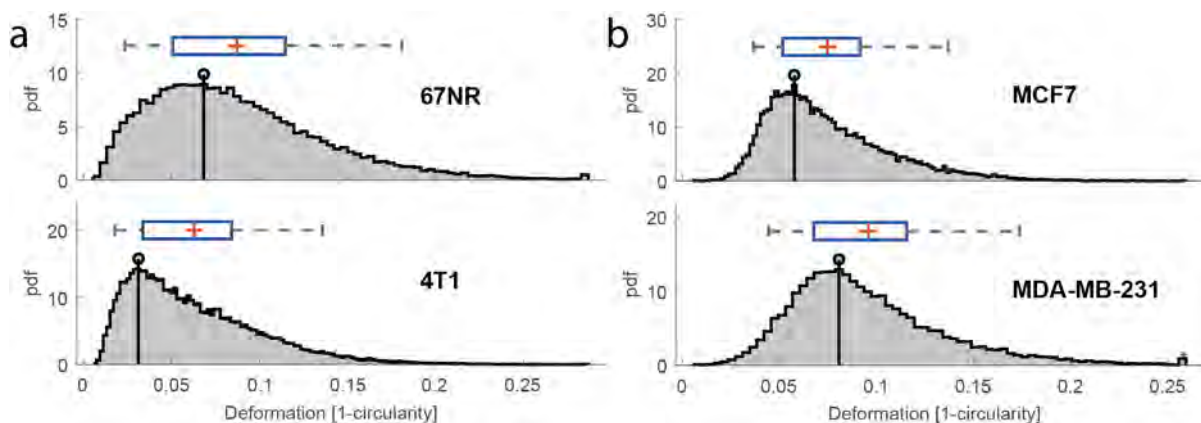


Figure 5.3: Distribution of deformation measurements of single cells from RT-DC experiments of breast cancer cells. Boxplot above the distributions bound the 25 and 75 percentiles, and the whiskers 5% and 95%. The red + indicates the mean, while the vertical black line in the histogram represents the mode value (most common value). (a) Probability density distributions and boxplot distributions of murine cell lines; non-invasive 67NR and invasive 4T1. (b) Probability density distributions and boxplot distributions of human cell lines; non-invasive MCF7 and invasive MDA-MB-231. Errors are SD.

5.3 Colorectal and pancreatic cancer cell lines

We expanded our study to colorectal (epithelial shape) and pancreatic (mesenchymal shape) cancer pairs to elucidate the relation between metastatic potential, shape, and deformation. The cell lines measured were; murine non-invasive pancreatic KPfIC, murine invasive pancreatic KPC, human non-invasive colorectal SW480, and human invasive SW620. The cell lines are grouped by color in the contour density plots of deformation versus cell area in Figure 5.5. Invasive species are depicted in shades of red and non-invasive in shades of blue. Little difference is observed in deformation between the colorectal cancers, but a significant difference between the pancreatic cancers. Since

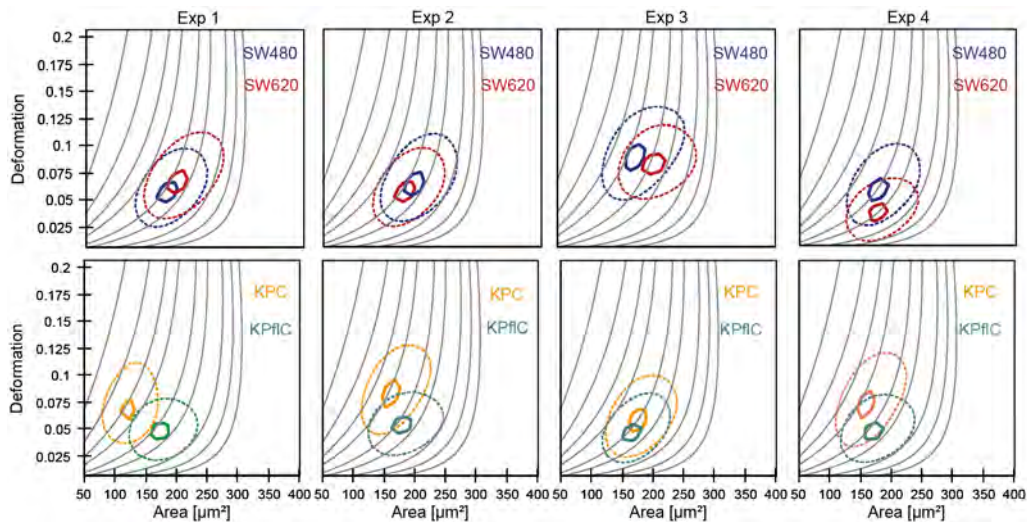


Figure 5.4: Deformation versus cell area plots of breast cancer cell lines. Density contour plots comparing deformations resulting of MCF7 (human, non-invasive), MDA-MB-231 (human, invasive), 67NR (murine, non-invasive), and 4T1 (murine, invasive) cells. The solid line marks 50% maximum density and the dashed line is at 95% Single day deformation experiments of invasive and non-invasive cancer pairs.

both pancreatic cancers are elongated, this can not be attributed to shape properties, but the more deformable pancreatic cell line is also the aggressive KPC.

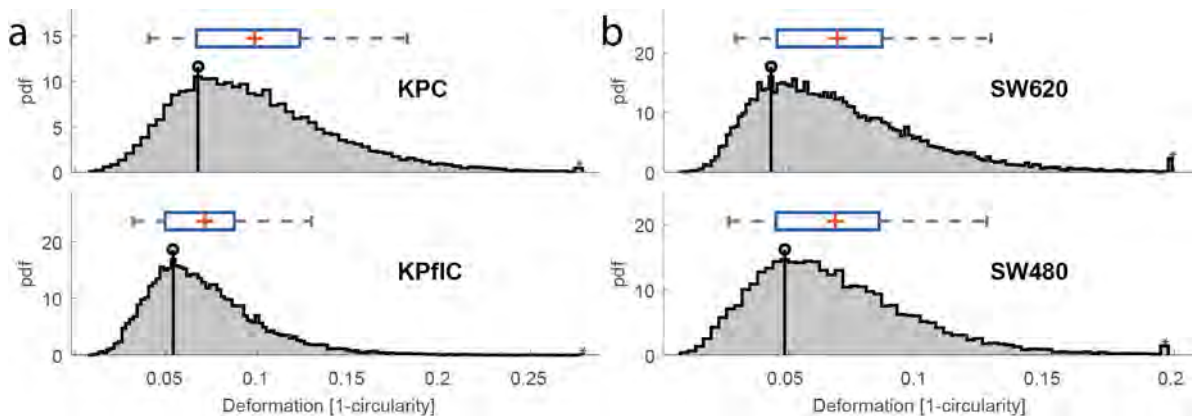


Figure 5.5: Distribution of deformation measurements of single cells from RT-DC experiments of pancreatic (a) and colorectal (b) cancer cells. Boxplot above the distributions bound the 25 and 75 percentiles, and the whiskers 5% and 95%. The red + indicates the mean, while the vertical black line in the histogram represents the mode value (most common value). (a) Probability density distributions and boxplot distributions of pancreatic cell lines; non-invasive KPflC and invasive KPC. (b) Probability density distributions and boxplot distributions of colorectal cell lines; non-invasive SW480 and invasive SW620.

5.3 Comparison of epithelial and mesenchymal cell lines

To see whether there was a trend related to the cell morphologies, we quantified the measured deformation values for all cell lines in relation to their shape. In Figure 5.6 average deformation values (mode values) have been plotted in relation to the previously defined shape of the each cell. Elongated cells are significantly more deformable than rounded cells.

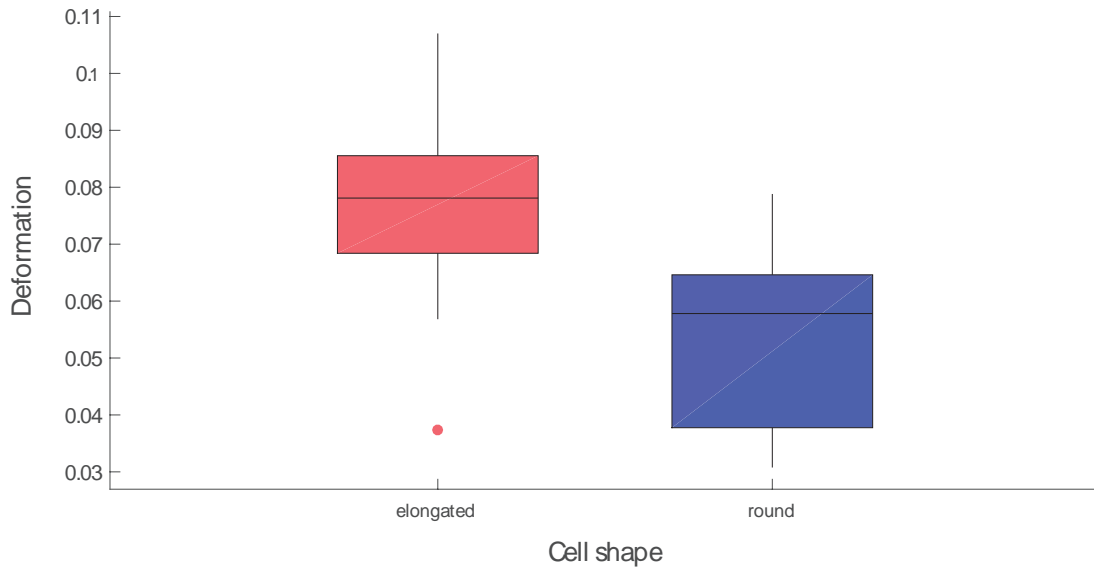


Figure 5.6: Comparison of deformation results for cancer cell types of different morphology. Boxplot of deformation values for elongated cells, 67NR (non-invasive murine breast cancer), MDA-MB-231 (invasive human breast cancer), KPfIC (non-invasive pancreatic), and KPC (invasive pancreatic). Bounding box of 5-95 percentile and SD error bars.

5.3.2 Prior shape perturbations

The deformability measurements inside the channel did not take into account prior perturbations of the cell shape. The circularity of the suspended cell was evaluated in the open reservoir prior to the channel (see Figure 3.5), to account for cell-to-cell variations. All reservoir measurements showed little difference in the unperturbed spherical shape of suspended cells from the different cell lines. Reservoir deformation mode and mean values can be seen in 5.1. We tested the robustness of our data by subtracting the reservoir values from the channel values, which gave us a relative deformation, $D_{rel} = D_{channel} - D_{reservoir}$ (see Figure 5.7). The normalized relative deformation values

Table 5.1: Characteristic values for cancer cells measured in the reservoir of the RT-DC system. Mean and mode deformation for pairs of invasive and non-invasive cell lines from breast, colorectal, and pancreatic cancer. Values were measured when the cell were unperturbed. Standard deviation (SD) is given for the mean.

Cell types	$D_{\text{mean,res}}$	$D_{\text{SD,res}}$	$D_{\text{mode,res}}$
67NR	0.03	0.02	0.01
4T1	0.02	0.02	0.01
MCF7	0.02	0.01	0.01
MDA-MB-231	0.03	0.02	0.01
KPC	0.02	0.02	0.01
KPflC	0.02	0.01	0.01
SW620	0.02	0.01	0.01
SW480	0.02	0.01	0.01

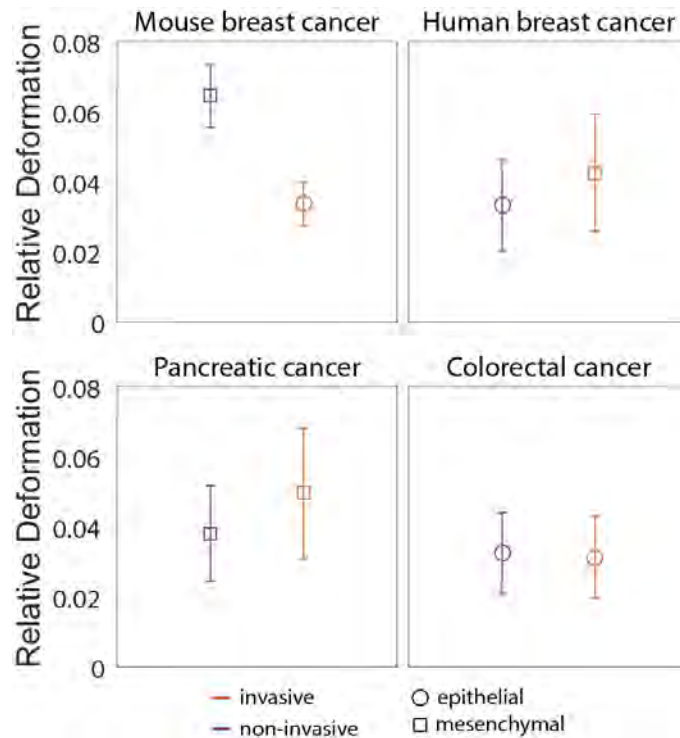


Figure 5.7: Mean relative deformation of cancer pairs. The relative deformation is calculated by subtracting the measured deformation in the channel with the measured deformation in the reservoir. Color indicates invasive potential (purple – noninvasive, red – invasive), and shape phenotype is indicated by marker type (square – elongated/mesenchymal, circle – round/epithelial). Error bars are standard errors of the mean, and the data is an average of data from 4-6 populations.

5.3.3 Young's elastic modulus

Within Shapeout it was possible to convert deformation to Young's elastic modulus. The conversion of deformation values was limited by the analytical model behind as explained in section §???. The conversion was only possible for 25-45% for the MCF7 cell line, due to their large size (see Figure B.4), and KPCs because of their high deformation values. To find the trend of the majority of the cell population we evaluated our distributions

using mode values. Table 5.2 shows the registered deformation values and estimated Young's elastic modulus according to shape and invasive potential of the respective cell lines. Though a significant amount of data could not be converted, we still had 3500 data points in the worst case. For breast cancer cells, we found that non-invasive 67NR and invasive MDA-MB-231 had a lower Young's modulus than their respective counterparts. For pancreatic cells, we generally observed a greater deformability of the invasive KPCs. The results are, as expected, consistent with our observations for the deformability, as the Young's elastic modulus, Y , has an inverse relationship to the deformation, $D = \frac{1}{Y}$.

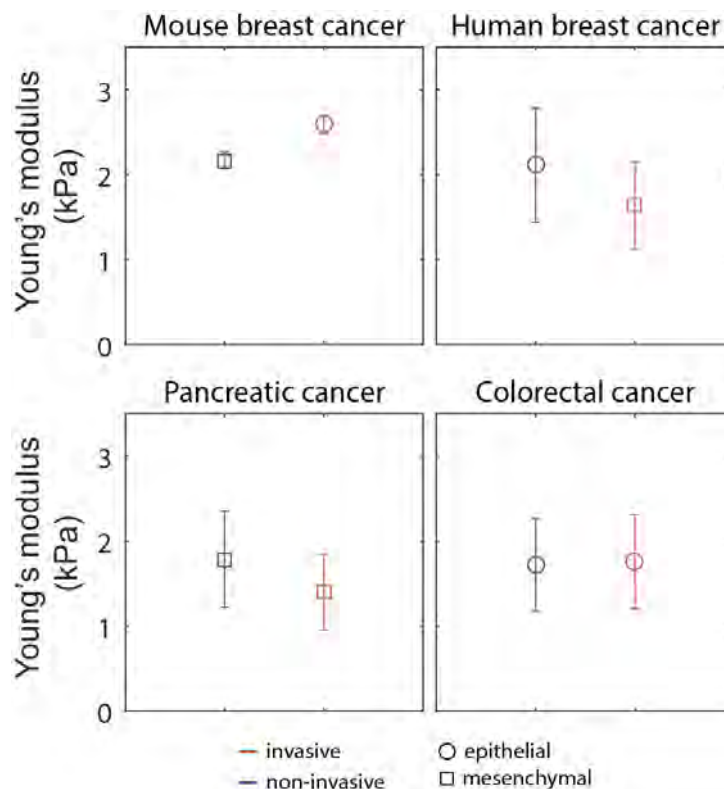


Figure 5.8: The average Young's modulus for metastatic and non-metastatic cancer pairs (4-6 different experiments per cell line). Color indicates invasive potential (purple – noninvasive, red – invasive), and shape phenotype is indicated by marker type (square – elongated, circle – round). Error bars are standard errors of the mean.

5.3.4 Statistical significance

To evaluate the significance in the difference between the deformation distributions of the non-invasive and invasive cell lines, we utilized the resampling technique, bootstrapping. Though the samples themselves approximate lognormal distributions, we have assumed that the sample means and modes have a normal distribution. Assuming a normal distribution is advantageous, as this will allow us to perform a two-sample t-test. We resampled the extracted means from individual distributions 1,000 times, and got a sampling distribution from which we could test the null hypothesis. See resampling distributions in Figure B.5. Across all cell lines, the t-test rejected the null hypothesis at the 5% significance level, indicating a significant difference between the distributions. P-values from

Table 5.2: Overview of significant properties of the 8 different cancer cell lines. Deformation values from RT-DC measurements. Young's modulus values calculated from deformation values. cThe conversion yield for the calculated Young's modulus, as there are size and deformation limits to the analytical model by Mokbel et al. [70]. Shape morphology and invasive potential of the different cell lines.

Cell types	Deformation* (1-circularity)	± SEM	Young's Modulus** (kPa)	± SEM	Conversion Yield (%)	Shape	Invasive Potential
67NR	0.073	0.009	2.167	0.098	76	elongated	-
4T1	0.041	0.006	2.592	0.107	65	round	+
MCF7	0.038	0.013	2.108	0.672	44	round	-
MDA-MB-231	0.052	0.017	1.633	0.517	85	elongated	+
KPC	0.053	0.019	1.400	0.444	24	elongated	+
KPflC	0.041	0.014	1.783	0.565	65	elongated	-
SW620	0.034	0.012	1.758	0.556	59	round	+
SW480	0.036	0.011	1.717	0.544	79	round	-

* Mean of sample mode values.

**Young's modulus calculated from deformation values.

the t-test analysis can be seen in Table 5.3.

Table 5.3: Statistical p-values for deformation distributions of different cancer cell lines. The p-values are calculated for the distributions depicted in Figure 5.3 and Figure 5.5 using a two sample t-test.

	67NR	4T1	MCF7	MDA-MB-231	KPC	KPflC	SW620	SW480
67NR	-	0	0	10^{-239}	10^{-195}	0	0	0
4T1		-	10^{-18}	10^{-94}	10^{-78}	0.001	10^{-73}	10^{-43}
MCF7			-	10^{-114}	10^{-108}	10^{-8}	10^{-12}	10^{-3}
MDA-MB-231				-	0.3	10^{-75}	10^{-176}	10^{-148}
KPC					-	10^{-73}	10^{-163}	10^{-138}
KPflC						-	10^{-35}	10^{-19}
SW620							-	10^{-5}
SW480								-

5.3.5 TGF-beta

We treated a selection of cell types, which expressed a more round cobblestone phenotype, with the transforming growth factor (TGF)- β 1. TGF- β 1 is a cytokine known to induce mesenchymal transition (EMT), and regulates cancer cell motility by altering the actin cytoskeleton[91, 92]. The cells treated were colorectal cancer cell lines SW620 (invasive, human) and SW480 (non-invasive, human). Cells were treated with 2ng/ml and incubated for 48h prior to measurements. Changes in cell shape phenotype were difficult to distinguish, and RT-DC experiments revealed little difference in deformability of the treated and untreated cell, as can be seen in 5.9.

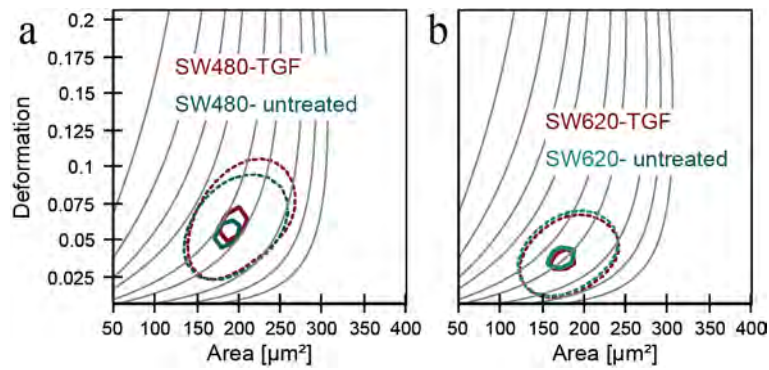


Figure 5.9: Deformation versus shape plots with and without TGF-beta treatment. Cells tested were the colorectal SW480 and SW620. The solid line marks 50% maximum density and the dashed line is at 95% maximum density. Single day deformation experiments of invasive and non-invasive cancer pairs.

5.4 Investigating cell shape

Previously, we observed that there seems to be a shape difference between the cell lines growing in 2D. To make an actual quantification of the difference in cell shape among our cell lines, we seeded cells sparsely in a well for 24h, and treated them with calcein, as described in ??, for 15 min prior to imaging. Calcein is typically used for viability assays, as it is actively metabolized by living cells and becomes fluorescent under the process, hence, lighting up the cytoplasm of the cell. Shape analysis was performed with “ImageJ/Analyze Particles” and the shapedescriptor function within this. One of the properties reported with this analysis, is the circularity defined as $4\pi(\text{area}/\text{perimeter}^2)$. Spherical objects will have a circularity of 1, and deformations will lower the value towards 0. The results can be seen in Figure 5.10, where exemplary images for each cell types are depicted together with a table of the calculated circularity values. The circularity parameter reveals a greater elongation in the non-invasive murine cells, 67NR, than their invasive counterpart, 4T1. For the human cell lines the non-invasive cells, MCF7, are more round than the invasive MDA-MB-231. The new cell lines, which were described in ?? have the same morphology within their invasive and non-invasive pair. The pancreatic cell lines, KPC and KPfIC, have an elongated mesenchymal shape, while the colorectal cell lines, SW620 and SW480, have a round epithelial morphology. All epithelial-like cells are found to have a higher circularity parameter, except for the 4T1 (murine, invasive). It was observed that cells which normally appear rounded in colonies, tend to elongate when sparsely seeded. From the rendered images in Figure 5.10 it is also possible to distinguish morphologies by eye. We have found that there is no correlation between shape morphology and invasive potential.

From another project we have quantified aspect ratios of breast cancer cells in colonies manually by identifying major and minor axis of individual cells. We found the following average values (10 cells/cell line); 2.46 (67NR), 1.59 (4T1), 1.59 (MCF7), and 3.44 (MDA-MB-231). In our manual approach we did choose to selectively exclude rounded MDA-MB-231, which were cells that were not adhered to the surface. The average aspect ratios found cooperate our findings from shape analysis using calcein.

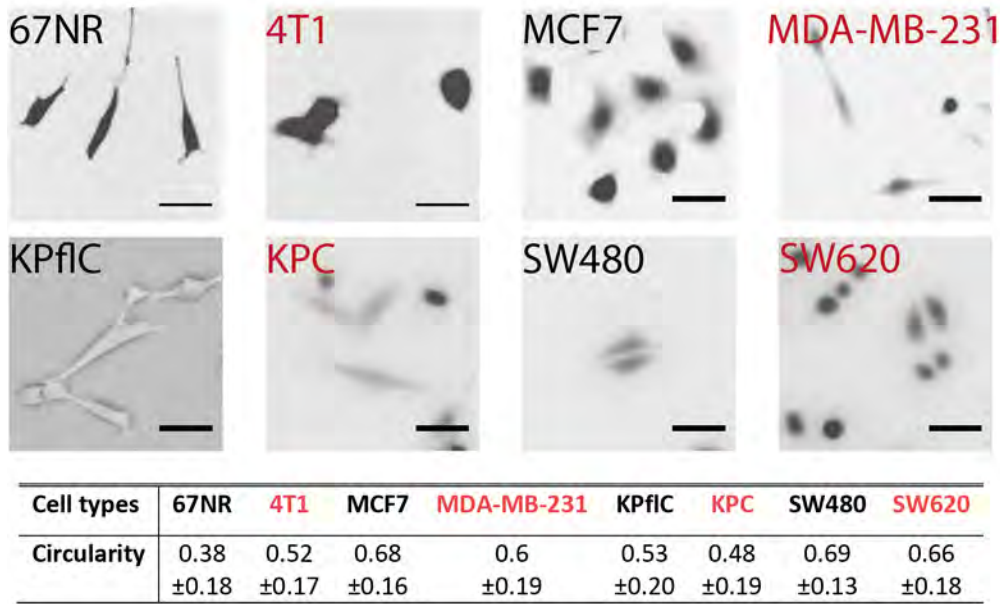


Figure 5.10: Representative images and circularity values of cancer cell morphologies. Fluorescence images of calcein treated murine (67NR & 4T1) and human (MCF7 & MDA-MB-231) breast cancer cells, pancreatic cells (KPC & KPfIC) and colorectal (SW480 & SW620). The red color indicates invasive cell lines, and the average circularity ($C = 4\pi(\text{area}/\text{perimeter}^2)$) is noted in the table below the images for all cell types. Circularity was calculated for ~ 2000 cells per cell type. Errors are SD. Scale bars are $50 \mu\text{m}$.

5.5 Conclusions

RT-DC is a non-invasive high throughput method for mechanical characterization of cells, deemed the new hope for simple pathogen detection in the future[67, 93]. We sought to probe the differences in cytoskeletal rigidity of cancer cells with and without the ability to metastasize using this technique. Previous studies have claimed that metastatic cells are more deformable than non-metastatic and normal cells[94], but it has become apparent that this is substrate dependent[95]. Changing morphology from epithelial to mesenchymal, is reversible and could be more dynamic than previously assumed[94]. A more compliant cell structure could be suitable during invasion, while epithelial-like cells lead growth at tumor sites. Our understanding of membrane mechanics supports a more adaptable cytoskeleton as the elastic moduli is dependent on bending, compression, and shear resistance[96]. We saw that elongated mesenchymal phenotypes were more deformable than round epithelial phenotypes in general, but with no correlation to invasive potential. We observed non-invasive murine breast cancer cells (67NR) that were more deformable than their invasive counterpart (4T1), while the opposite was observed for human breast cancer (non-invasive MCF7 and invasive MDA-MB-231). The latter is the classical hypothesis of deformation grading with metastatic potential, and has previously been reported, for the human breast cancer cells, MCF7 (non-invasive) and MDA-MB-231 (invasive), by Guck et al. [88]. Colorectal cancer lines, which were both epithelial shaped, were found to have similar values. For the pancreatic cancer lines, the invasive, KPC, was found to have a lower mechanical integrity than the non-invasive, KPfIC. We have not found a consistent connection between metastatic phenotypes, deformation,

and shape, but rather a more dynamic and multi-parametric relationship, where morphology and metastatic potential both play an important role in mechanical cell properties. It would be interesting to investigate the mesenchymal pancreatic cancers further for differences in their cytoskeletal properties, since they display the same morphology, but different deformability. Using cytoskeletal mechanical properties to distinguish abnormal cells from healthy ones seems quite possible, but a detection technique with multiple parameters is probably needed. ZellMechaniks have introduced 1D fluorescence imaging together with flow cytometry (RT-FDC)[97] which opens up new possibilities. It would be of great interest to observe nucleus size and deformation during experimentation.

Chapter 6

Mechanosensitivity of cancer cells

The project presented in this chapter concerns the mechanosensitivity of cancers with different invasive potential. The data shown is part of a larger project which was led by my colleague, PhD Lena Wullkopf from Biotech Research Institute Center (University of Copenhagen) with supervision from post doc Natascha Leijnse. We have investigated the viscoelastic properties of cancer cells in matrices of different stiffness using optical tweezers (section §3.2). 3D confocal images were taken of the cells imbedded in collagen, to elucidate the arrangement of collagen fibers in relation to cell protrusions. The data is part of a project in which the adaptability of cancer cells of different invasive potential, was investigated in matrices of various stiffness. The combined work has been prepared for PNAS and a preprint is attached in section §C.3.

6.1 Introduction

Human tumors are stiffer than normal tissues, but prior work using techniques such as atomic force microscopy, optical stretchers, and microfluidic devices have revealed that single cancer cells are softer than healthy cells and even grade with invasive potential[88, 89, 86]. Malignant cancers utilize their ability to dynamically alter the actin cytoskeleton during migration and cancer invasion[98, 99]. The microenvironment is highly connected to tumorigenesis, and local changes in the extracellular matrix, ECM, near the tumor cells contribute to cancer progression[100, 101]. Cells probe their environment using contractile and adhesive molecular machinery, and it has been reported that cancer cells can respond to matrix rigidity and density via cytoskeletal force responses, such as the actin-talin-integrin-fibronectin clutch[102], or actomyosin response[103]. Most notably, matrix stiffness has been shown to drive malignant transformation in breast cancer, and cancerous epithelial tissue was reported to exhibit a 10 fold higher Young's elastic modulus than that of normal epithelial tissue[104, 105].

Most approaches used to characterize cell stiffness measures the overall response of the cell membrane, and thereby get the outer mechanical properties. Material properties within the cell can be probed using optical tweezers, from which one extracts the intra-

cellular viscoelasticity using endogenous granules[66, 56]. We apply optical tweezers to cells in a 3D collagen matrix system, and probe the cellular response of, cancer cells with different invasive potential, to changes in matrix stiffness.

6.2 Method

An optical light trap integrated in a confocal microscope (section §3.2) was used to characterize the viscoelastic properties of cancer cell lines imbedded in collagen matrices of different stiffness. Confocal microscopy (section §3.1) was applied to image the displacement of the surrounding collagen matrix. Optical tweezers were used to measure the motion of intracellular vesicles, which were distinguishable dark spots (200-300nm) during bright field imaging. The granules are highly refractive allowing trapping with optical tweezers, as previously described for fission yeast[106] and endothelial cells (HUVECS)[56]. Data was acquired by a fast data acquisition card (NI PCI-6040E) at a sampling frequency of 22kHz and processed by a custom made LabVIEW programs (LabVIEW 2010, National Instruments). Power spectrum analysis of particle displacement in the optical trap was converted to scaling exponent values, α , that represent viscoelastic properties within the cytoplasm. We assumed that the cells are minimally affected by the laser light when using low laser power and a short measurement time (3s), as temperature increase related to light absorption is expected to be below 1°C [66]. The analysis was done using custom-made Matlab programs developed by Selhuber-Unkel et al. [106] for extracting scaling exponents. The powerspectrum was decorrelated, binned and fitted with a linear fit within the frequency regime of 500Hz-9900Hz. The scaling exponent α was derived from the slope of the linear fit.

6.3 Results

6.3.1 Matrix stiffness

Cells derived from a diverse range of tissues were investigated using viscoelastic characterization with Optical Tweezers. Cell lines studied were breast cancer cells, 67NR (non-invasive murine), 4T1 (invasive murine), MCF7 (non-invasive human), and MDA-MB-231 (invasive human); pancreatic cancer cell lines KPflC (non-invasive), and KPC (invasive); and colorectal cancer cell lines SW480 (non-invasive) and SW620 (invasive). The cells were measured in collagen matrices of 1mg/ml and 4mg/ml (Figure 6.1), which were confirmed to increase in stiffness when probed using rheology, see Figure 6.2. Collagen gels of 1mg/ml resembled the soft tissue of lung or mammary glands with a median Young's modulus of 421Pa (1mg/ml matrix)[100, 107], while the 4mg/ml gels exhibited a Young's modulus of 137Pa., is comparable to stiffening shown to occur during cancer progression in mammary gland[101, 100].

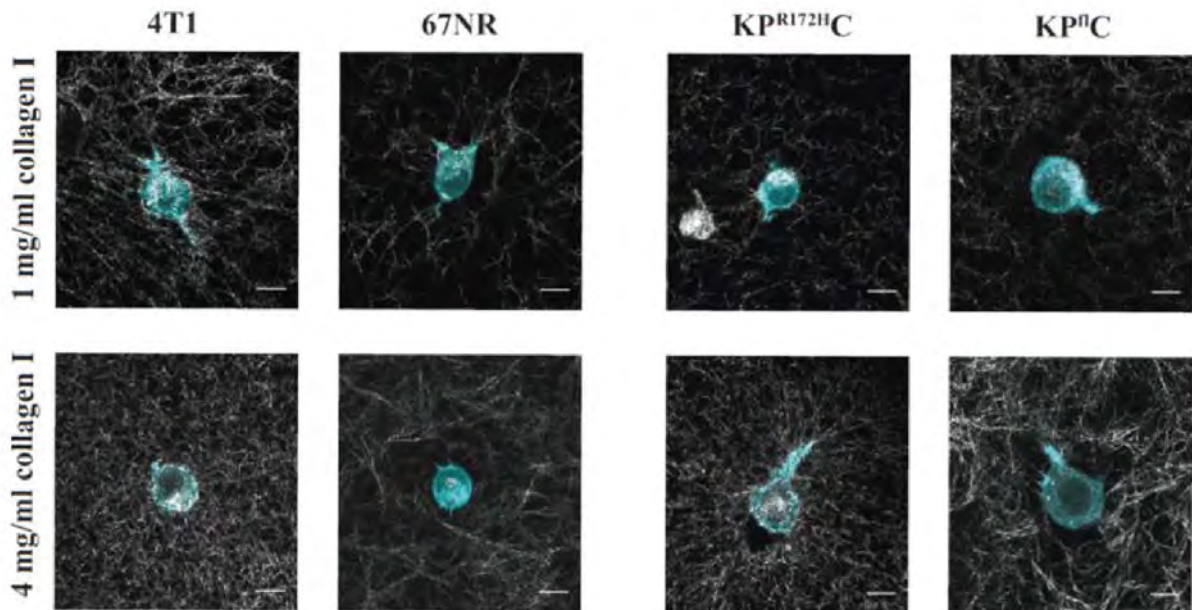


Figure 6.1: Representative images of cancer cells in 3D collagen gels of different stiffness. Murine breast cancer cell lines; 4T1 (invasive) and 67NR), and pancreatic cancer cell lines; KPC (invasive) and KPⁿC (non-invasive) in matrices of either 1mg/ml collagen 1 (top row) or 4mg/ml collagen 1 (bottom row). Figure adapted from manuscript in section §C.3.

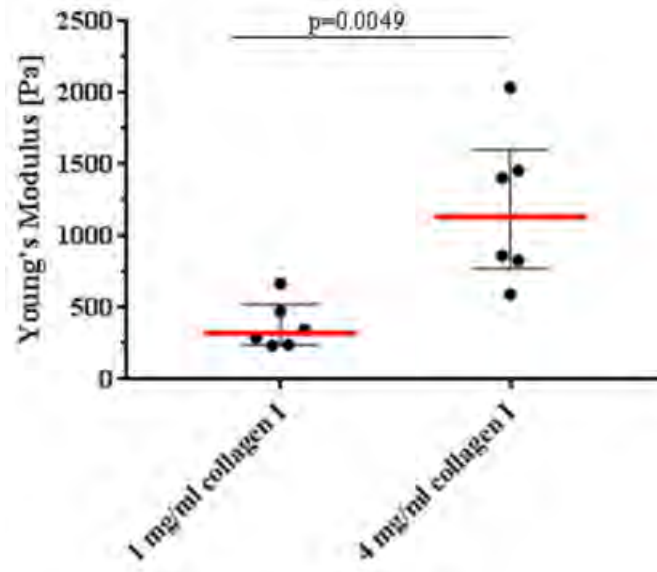


Figure 6.2: Confirmation of matrix stiffness via rheology. Increasing the concentration of collagen I in gels results in a significant increase in the Young's modulus. P-values from Mann-Whitney test (two tailed).

6.3.2 Mechnosensitivity of cancer cells

The scaling exponent measured with optical tweezers is relatable to the viscoelastic properties of cells, as explained in section §3.2. All cell lines were generally found to fluctuate around scaling values of 0.6, but the invasive cell lines were observed to significantly adjust to changes in matrix stiffness, see Figure 6.3. Invasive cell lines MDA-MB-231 (breast cancer) and KPC (pancreatic) were found to reduce their intracellular viscosity

from $\alpha=0.64$ to $\alpha=0.61$, and $\alpha=0.63$ to $\alpha=0.55$ respectively. The opposite response was observed for the other invasive cell lines, 4T1 (breast cancer) and SW620 (colorectal). Scaling exponents measured for these cell lines were found to increase from $\alpha=0.58$ to $\alpha=0.63$ for the 4T1, and from $\alpha=0.53$ to $\alpha=0.57$ for the SW620. The results revealed a mechanosensitivity within the invasive cell lines, which could be related to results seen in previous chapters of this thesis, involving other parameters such as morphology. The cell lines which have a proportional response to matrix stiffness, are also those which have an epithelial morphology. Epithelial cancers are often attributed the role of governing growth within tumors, and this response could be related to this. Likewise, the cells which exhibited an adjustable viscoelasticity of their cytoplasm, are cells which have a mesenchymal phenotype often connected with highly invasive properties.

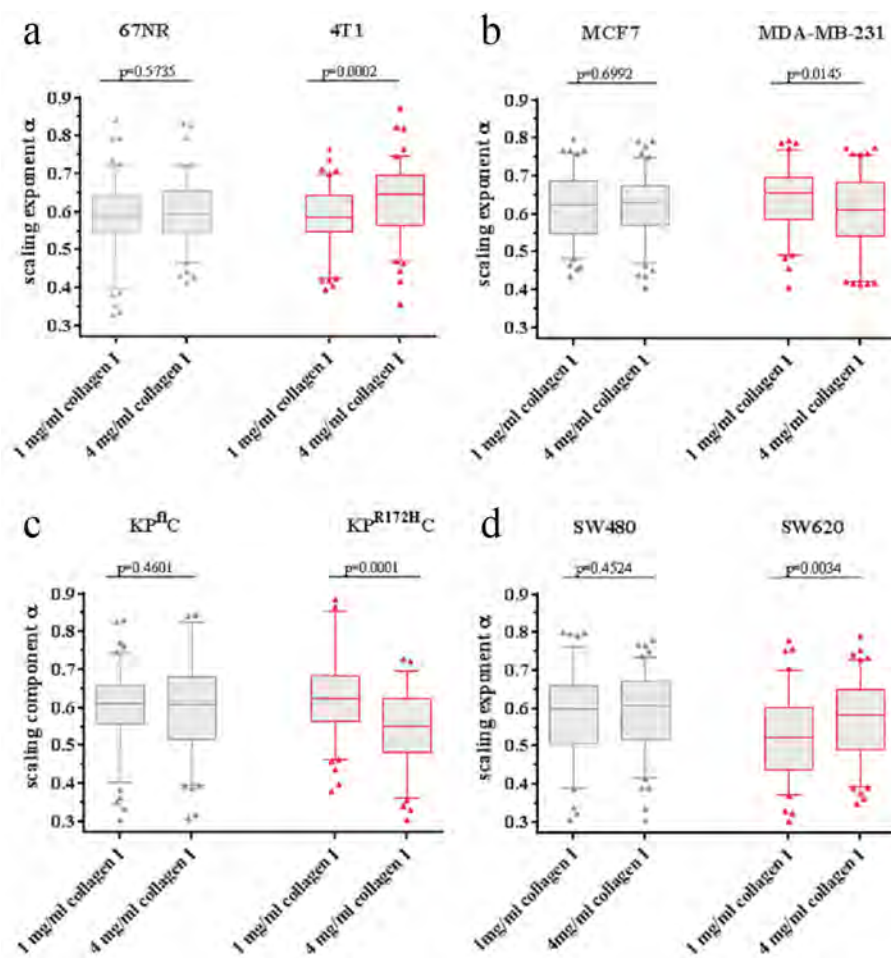


Figure 6.3: Mechanosensitivity of cancer cells imbedded in gels of different stiffness. Scaling exponent, α , from lipid granule diffusion experiments, for cancer cell lines of invasive (red outline) and non-invasive (grey outline) potential; (a) murine breast cancer (non-invasive 67NR, invasive 4T1), (b) human breast cancer (non-invasive MCF7, invasive MDA-MB-231), (c) pancreatic (non-invasive KPflC, invasive KPC), and colorectal (non-invasive SW480, invasive 620). Boxplots of 5-95 percentile, and p-values from Mann-Whitney test (two-tailed). Figure adapted from manuscript in section §C.3.

To study the overall cytoskeletal adjustment of cells in the different matrices, we measured the cell deformability of the cells using RT-DC, section §??, as also done for cells on plastic in chapter 5. All cell lines exhibited a Young's elastic modulus around 2-3kPa. Compared to cells cultured on plastic, the deformation properties of the cell lines have

changes when grown in a matrix. In general, the cells have become more elastic since values were previously found to be 1.4-2.6 kPa, Table 5.2. In those experiments we also observed that elongated cells displayed a higher deformation in general, but now we see that many of the cell pairs have a more similar elasticity, ie. murine breast cancer (67NR,4T1) and pancreatic cancer cells (KPfIC,KPC). Where we previously saw that the mesenchymal cell in these cell lines were more deformable than their counterpart, we now see that they display the same mechanical properties. In relation to the mechanosensitivity of the cell lines, we confirm with this technique that the invasive lines exhibit an adaptability when subjected to stiffer environments, as seen with the intracellular tracking experiments.

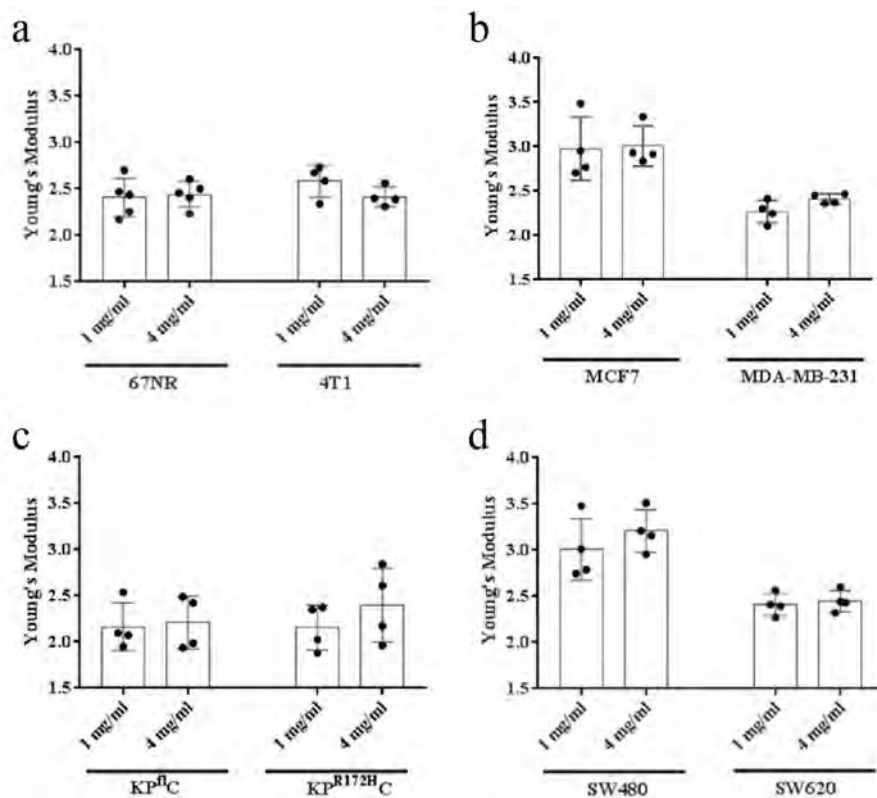


Figure 6.4: Young's elastic modulus values extracted from RT-DC measurements. Boxplots of measured Young's modulus values for murine breast cancer (non-invasive 67NR, invasive 4T1), human breast cancer (non-invasive MCF7, invasive MDA-MB-231), pancreatic (non-invasive KP^{fIC}, invasive KPC), and colorectal (non-invasive SW480, invasive 620) in gels with a concentration of 1mg/ml or 4mg/ml collagen. Figure adapted from manuscript in section §C.3

6.4 Summary

The progression of cancer is believed to be related to pathophysiological changes, which can be attributed to cytoskeletal restructuring [108]. It has been hypothesized there exists a form of “cellular memory” concerning mechanical stimulus, which could affect cell fate. Reported have been made that the cytoskeletal system displays hysteresis, but is still not well understood[29]. Metastasis is a journey of force, where the cancer cells have to disseminate from the primary tumor and colonize secondary sites. The metastatic processes requires a lot of adaptability to mechanical differences during progression.

We have investigated the mechanosensitivity of cancer cells in 3D matrices using optical tweezers. We find that invasive cancer cell lines adjust with the stiffness of their environment while non-invasive cell lines do not. Invasive cell lines from human breast cancer (MDA-MB231) and colorectal (KPC) were found to decrease their intracellular viscosity, while pancreatic (KPC) and murine breast cancer (4T1) increased their viscosity. The mechanical rigidity of the overall cell in changing environment, was analyzed using RT-DC and supported findings from the optical tweezers experiments. Malignant cells were found to adjust their elasticity when in stiffer matrices. All cells exhibited a Young’s elastic modulus between 2-3kPa, in contrast to previous results for cells on plastic (1.4-2.6kPa). This reveals that cancer cells grown on plastic are less elastic than cells in collagen. In addition, we have seen that previously distinguishable cell lines, murine breast cancers and pancreatic cancers, had very similar elastic modulus values when they had been grown in collagen gels. This proves that the very stiff environment of plastic dishes have a significant affect on cell mechanics.

These results are part of a larger project in which also 3D spheroid invasion assays have been examined. The complete study can be seen in the attached manuscript section §C.3.

Chapter 7

Nematic kenotaxis

This chapter describes our study of tissue migration into empty space, kenotaxis[17]. For analysis, we invoke models inspired by liquid crystal theory, and apply them on images acquired using time-lapse microscopy. The project was initiated during my stay in the group of Prof. Julia Yeomans in Oxford, and it has been a close collaboration with post doc Amin Doostmohammadi. Algorithms were developed by Dr. Thuan Saw from Singapore University. The work is ongoing, and analysis of the data has not yet been finalized.

7.1 Introduction

Migration of cell groups is a fundamental process of interconnected cells, and plays an important role in morphogenesis and the reshaping of larger tissues. Collective motion is necessary for epithelial homeostasis and regeneration, as well as during tumor progression and invasion[2]. Mechanical cues within migratory processes have proven to play a pivotal role in coordinated cell motion. Collective migration has been shown to induce coordinated stress patterns within endothelial cell[75], while traction forces measured by Trepats et al. [18] in epithelial tissues, revealed forces generated well behind the leading front of a migrating cell layer. Recent years, the field of statistical physics has lent insight into collective cell behavior. Emerging are models capturing cell dynamics using continuum models of active nematic materials[109]. Singularities within the orientational alignment of a variety of biological systems has been identified including lipid vesicles[110], cell colonies[111], and *Escherichia coli* colonies[47]. Recently, such models have provided insight into how topological defects drive cell death and extrusion within epithelial tissue[45].

Here, we will introduce our current work on the nematic properties of cancer migration. The collective migration of breast epithelial carcinomas was investigated using non-intrusive removable culture inserts, and dynamics were evaluated with techniques from flow dynamics and liquid crystal theory.

7.2 Methods

Four breast cancer cell lines were investigated; 67NR (murine, non-invasive), 4T1 (murine, invasive), MCF7 (human, non-invasive), and MDA-MB-231 (human, invasive). Cells were cultured and prepared as detailed in ???. Cells, with a 500 μm cell free gap (removable culture insert assay), were imaged for approximately 20-24h using the time-lapse system described in section §3.1. Image acquisition area was 1105x1105 μm (1700x1700 px), and the time between images was 10 min, with a few sequences taken at a 15 min interval. Post processing was done in ImageJ and Matlab as described in section §???. The assay is based on kenotaxis into a vacant space between two cell colonies, as shown in Figure 7.1.

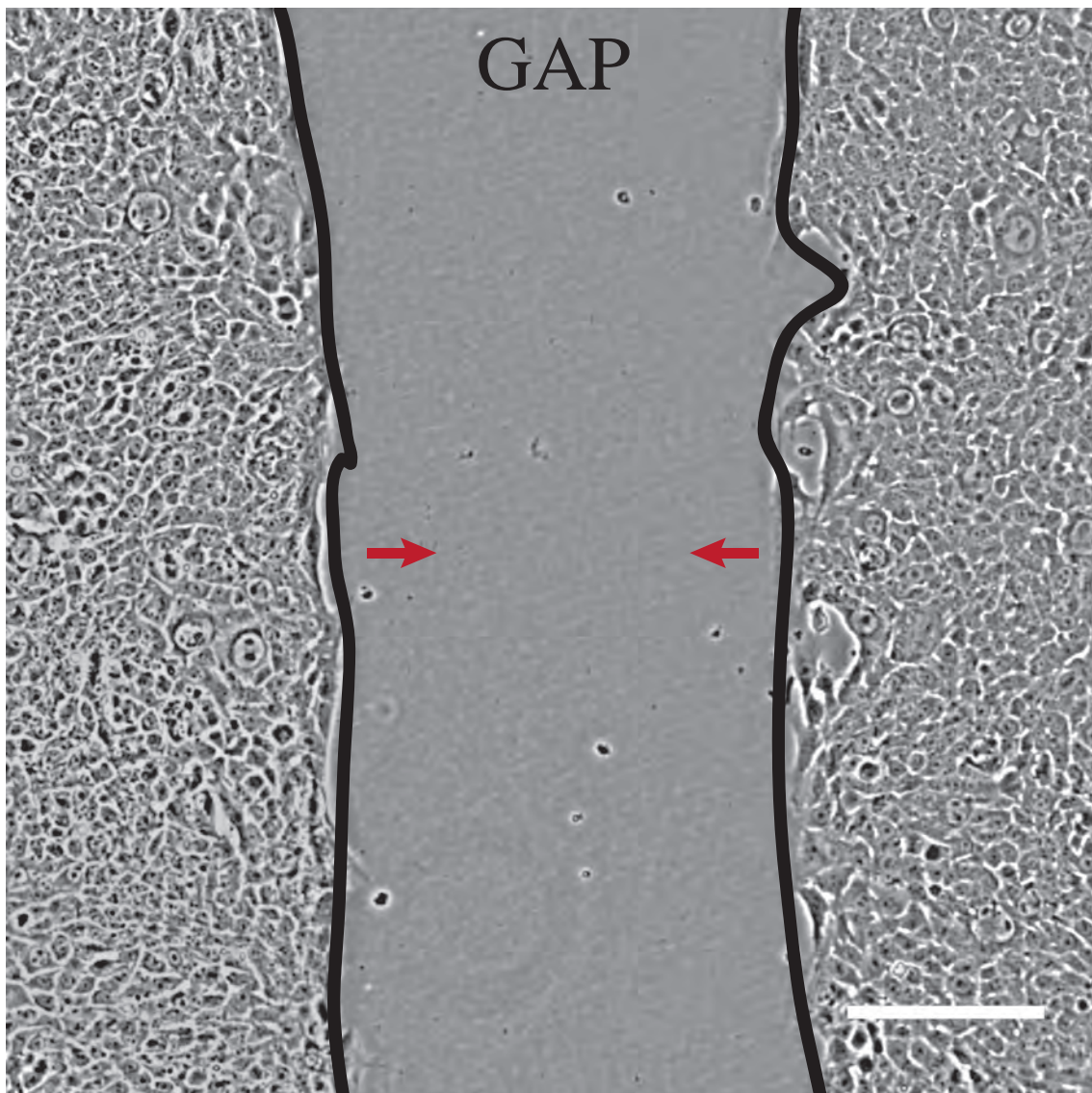


Figure 7.1: Representative image of wound closure assay. Cells have been grown on each side of a 500 μm gap, and after removal of the culture insert, cells freely move into the vacant gap (red arrows). Scale bar, 200 μm .

7.3 Results

Analysis is still ongoing so results presented are primarily for the murine breast cancer cell lines 67NR (non-invasive) and 4T1 (invasive), and is an overview of our current work. All cell lines are depicted in Figure 7.2. Different modes of migration were exhibited. The 67NR and 4T1s advanced in waves, while the MCF7 move as a collective continuous front. The MDA-MB-231 were highly individual in their movement.

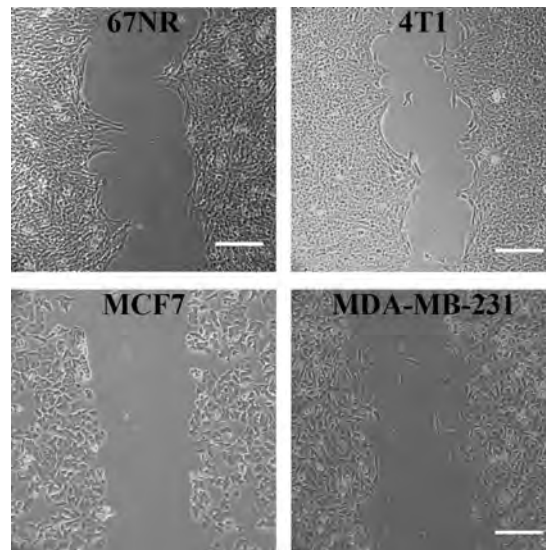


Figure 7.2: Migration front of different cancer cell lines. The images show the migration of breast cancer cell line into open space (10h). Cell depicted are breast cancer cell; murine non-invasive (67NR) and murine invasive (4T1), human non-invasive (MCF7) and human invasive (MDA-MB-231).

7.3.1 Velocity field analysis

We applied PIV, section §3.3, to obtain velocity fields for each time frame of the image sequences. Figure 7.3 contains sample images of results found for invasive mouse breast cancer. In the phase contrast images, Figure 7.3 (a), we observed a gradual closing of the cell free area from both sides of the gap. The cell front moved into the open space move with greater speed than cell speeds deeper within the tissue. The increased motility of the front of the cell monolayer was observable in the hydrodynamic profiles given in Figure 7.3 (b-d). Increased speeds and flow pattern intensities were localized at the cell colony rim in both velocity Figure 7.3 (b), divergence, Figure 7.3 (c), and vorticity fields, Figure 7.3 (d). The migration speeds for the different cell lines were found to be $0.25 \mu\text{m}/\text{min}$ for 67NR (non-invasive), $0.29 \mu\text{m}/\text{min}$ 4T1 (invasive), $0.007 \mu\text{m}/\text{min}$ for MCF7 (non-invasive), and $0.29 \mu\text{m}/\text{min}$ for MDA-MB-231 (invasive). Invasive cell lines migrated at greater speeds than non-invasive cell lines, but for the murine cell lines, the non-invasive 67NR possessed a relatively similar speed. This cell line also exhibits distinct leader-like protrusion, in contrast to the other non-invasive cell line, MCF7.

In the previous study of division dynamics, chapter 4, we observed an overall higher motility in the more aggressive cell lines, as do we here. Aggressive cell lines had a

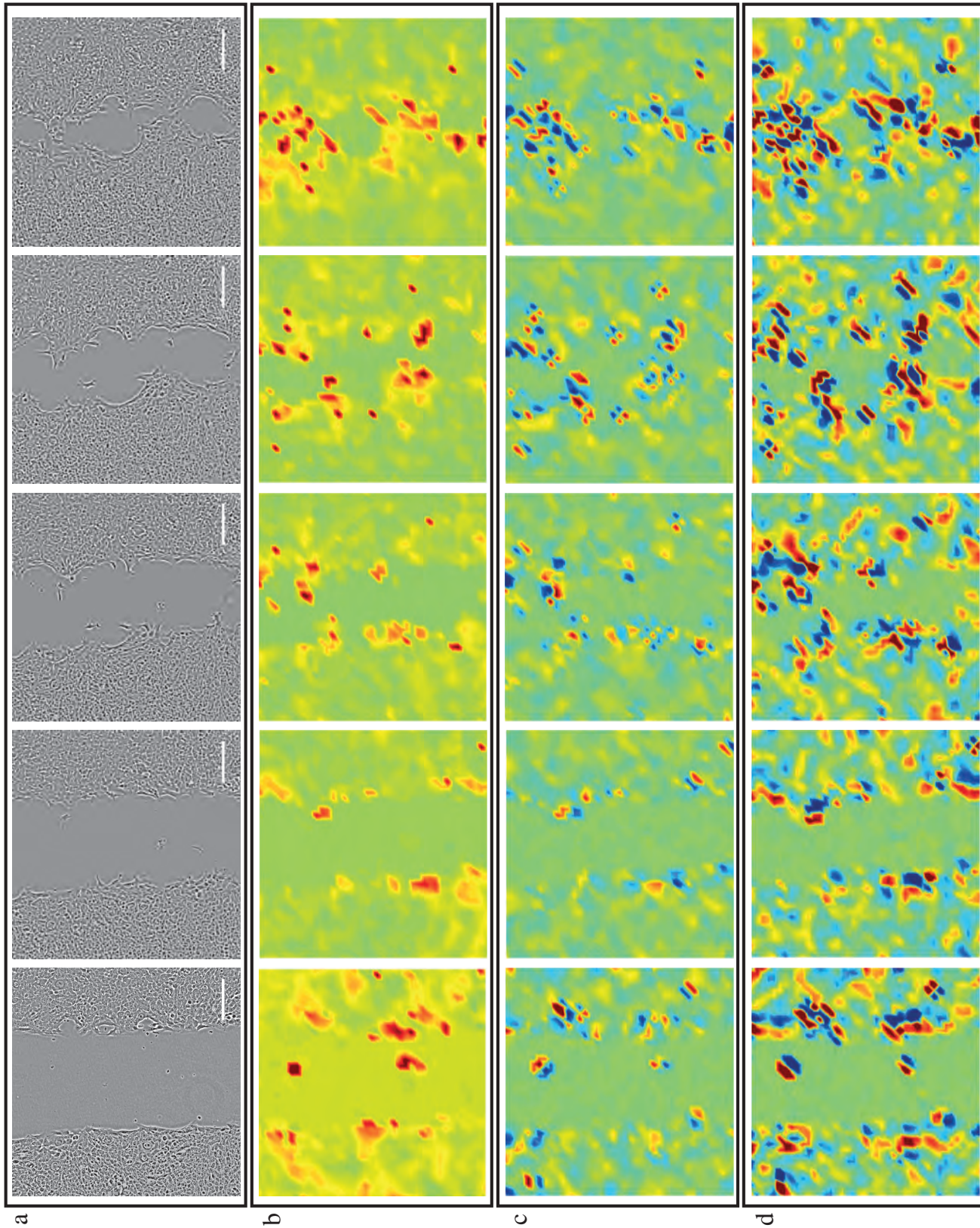


Figure 7.3: Velocity field analysis images murine invasive breast cancer during gap closure migration. (a) phase contrast image sequence with an interval of 3h and 20 min (20 frames) between each depicted frame, and first frame at the onset of imaging ($t=0$). (b) velocity fields of the migrating cell layer, portrayed using a color scale of $[-1, -1] \mu\text{m}/\text{min}$. (c) divergence (contraction and expansion). Color map: $[-0.04, -0.04] \text{min}^{-1}$. (d) vorticity (swirling), with a color map range $[-0.01, -0.01] \text{min}^{-1}$. Data is from invasive murine breast cancer, 4T1. Scale bar, 200 μm .

higher activity than the non-aggressive counterparts, and the cell fronts moved quicker and have greater vorticity patterns. Examples of the vorticity patterns in the expanding tissues can be seen in Figure 7.4 for non-invasive 67NR and invasive 4T1 breast cancer.. As hinted, distinct flow patterns were not obvious, and overlaying multiple images was not possible as the images were too noisy and result in all signals cancelling out. We tried minimizing our region of interest, but dynamics were again averaged out, due to the stochastic variations between samples.

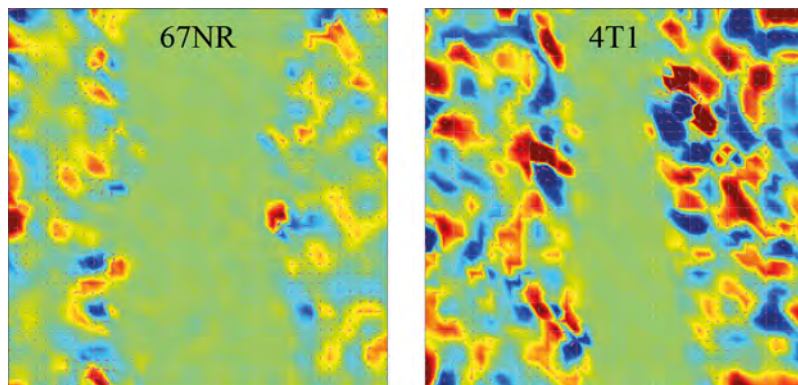


Figure 7.4: Sample vorticity fields of migrating cancer cells in a wound assay. Murine breast cancer cells in a wound closure assay; non-invasive 67NR (left), invasive 4T1 (right). Invasive cell line displays a higher magnitude of vorticity than the non-invasive. Color map range is $[-0.01, 0.01] \text{ min}^{-1}$.

7.3.2 Orientation analysis

A property relevant in nematic studies, is the orientation of constituents within the material, as introduced in ???. We see that during migration most cells tend to extend and display polarity allowing automated orientation detection even though the static cell is approximately spherical. Wound assay images were analyzed using customized ImageJ and Matlab scripts developed by collaborator Dr. Thuan Saw. The algorithms were developed for kidney cells (MDCK)[45], and the scripts had to be customized for our analysis. Compared to normal healthy cells, the boundary of the cancer cells used by us, are not as easy to distinguish using phase contrast microscopy. Hence, the boundary of single cells can be difficult to quantify using available segmentation programs.

From the orientation field analysis we get the director field. A sample image can be seen in Figure 7.5, in which directors are overlaid the image, thus recapitulating the general orientation of the monolayer. It is clear that the overall directionality of the migrating cell front is towards the open space. Multiple cell diameters behind the interphase the coordinated alignment is lost, and orientation becomes more random.

To identify topological defects within the orientation field, we analyzed orientation angle between neighboring director vectors. We distinguish between $+1/2$ and $-1/2$ defects. In Figure 7.5 an image of the director field and defects (plus=green, minus=yellow) can be seen. Compared to tissues originally analyzed using this technique, our blurry cell boundaries makes it difficult to confirm the validity of defect detection. From the images

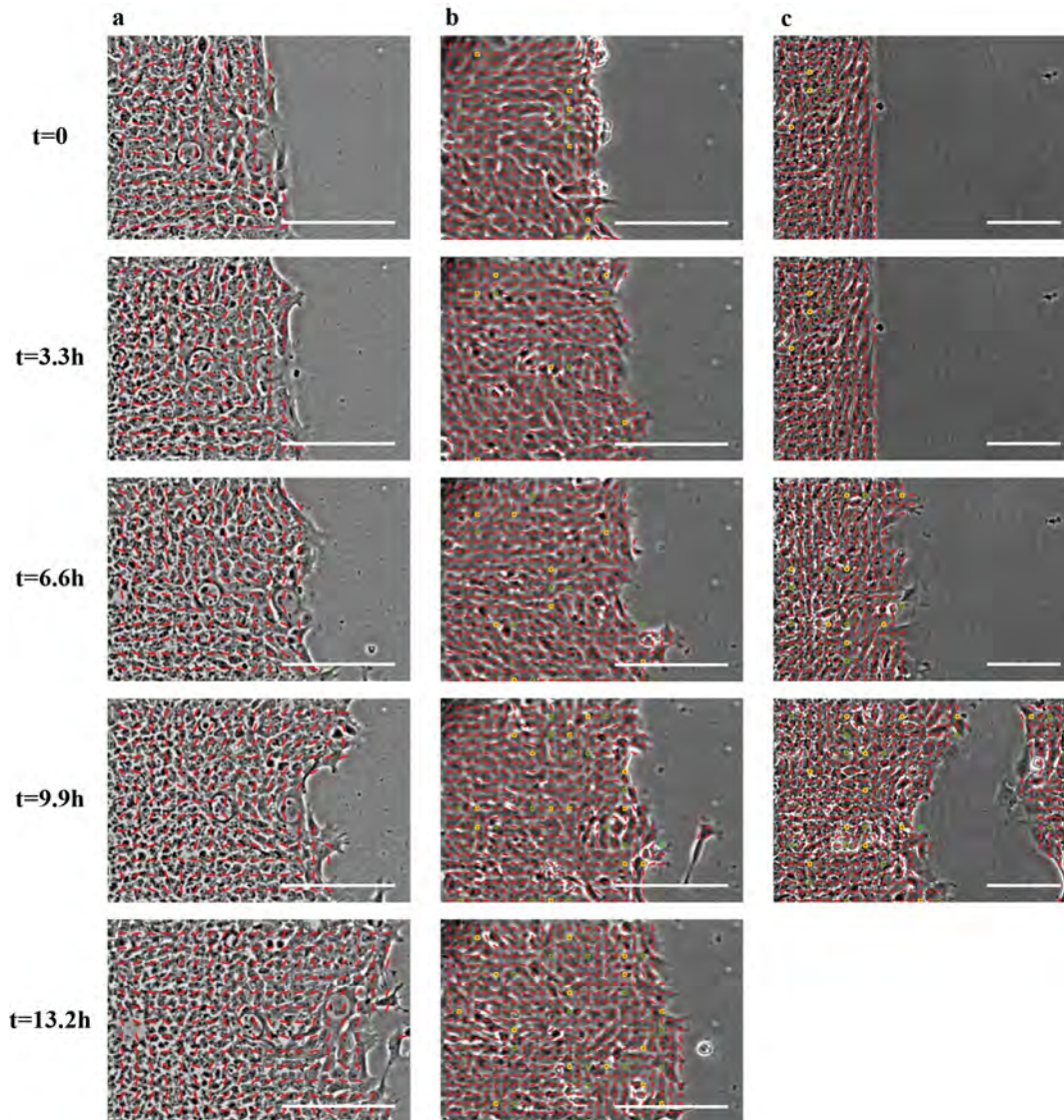


Figure 7.5: Director field overlaid phase contrast images. The director field (red headless arrows) capture the local orientation within the cell layer. (a) 4T1, (b) 4T1 + defects (c) 67NR. Defects occurring in the orientation field of cell layers. Wound assay images overlaid with the calculated director field (red headless vectors). $+1/2$ defects (green) and $-1/2$ defects (yellow) are marked with a circle. Scale bar $200 \mu\text{m}$.

it is apparent that our detection limits are not adjusted properly, as we identify a vast amount of defect. Due to the high amount of We we are still analysing these images, as it is necessary to follow the defects over long time periods, and observe if they in fact annihilate or induce migratory patterns as seen with bacteria. We have observed a possible connection between defects centered within local vacancies within the cell layer, when confluency has not been completely reached. Before the cell colony migrates into open space, it will eliminate such vacancies. The speed at which the wound is closed is also density dependent. Sample data of calculated correlation functions for velocity field, director field and vorticity field can be seen in Figure B.6.

7.3.3 Investigating divisions during kenotaxis

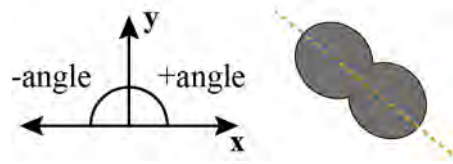


Figure 7.6: Orientation analysis of dividing cells. The orientation angle was defined in the plane of the migrating front, x , resulting in the a division like the one shown, having a negative angle.

We observed by eye what seemed to be a general alignment between the direction of flow and the orientation of dividing cells. Normally one can create an automatic program to register the halo surrounding dividing cells, but the signal-to-noise ratio between dividing and non-dividing cancer cells is too low. Division location and analysis was therefore processed manually in ImageJ. An example of the image analysis can be seen in Figure 7.7. Cells undergoing cytokinesis were identified and the angle at which the two daughter cells were moving was measured. The reference frame for the angle measurement was set to be in the plane of the migration direction, see

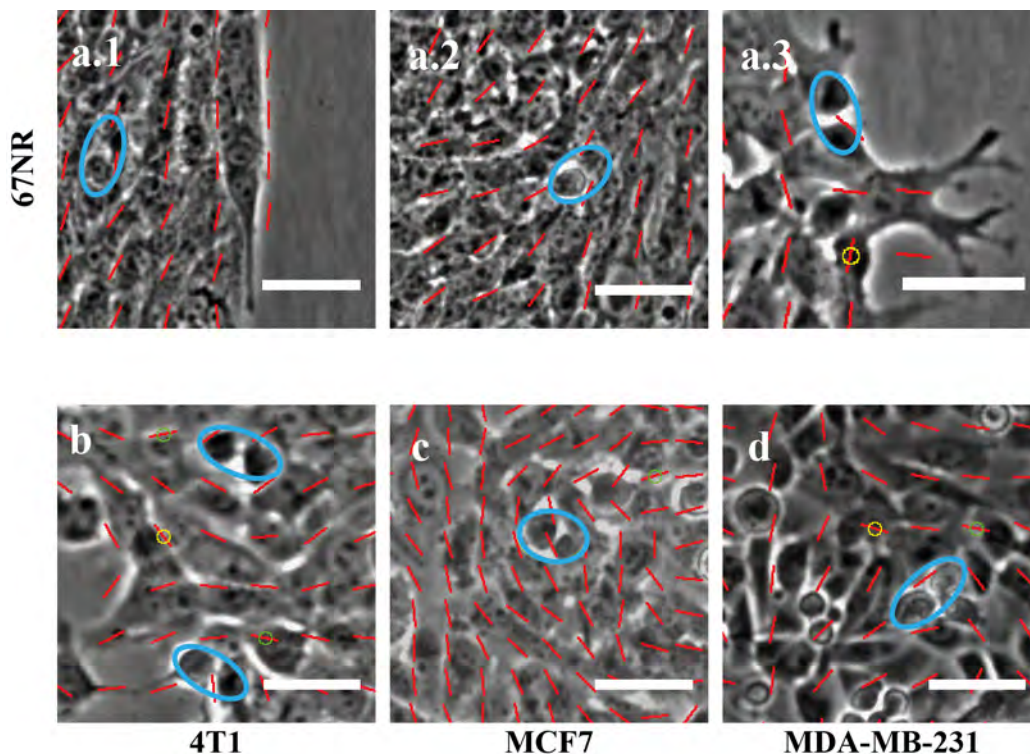


Figure 7.7: Division orientation and location during kenotaxis. Wound assay images overlaid with calculated director field (red headless vectors), $+1/2$ defects (green circle) and $-1/2$ defects (yellow circle). Large blue ovals highlight manually identified divisions. (a) comparison of division orientation close to the rim (a.1,a.3) of the moving cell front and further back (a.2). Divisions oriented predominantly perpendicular to the migration direction. The orientation was found to align perpendicular to images are of breast cancer cells; left image is non-invasive 67NR, right image is invasive 4T1. Scale bar 200 μm .

Analysis of the orientation of divisions showed that there tends to be a general negative orientation in the migratory direction. Average orientation of divisions was found to be; -54° (67NR), -39° (4T1), -39° (MCF7), and -26° (MDA-MB-231) for an average of at

least 30 divisions. Angles were measured from the horizontal direction in which the cell layer is migrating. The meaning of the negative angle is not quite apparent yet. At the interphase it was been observed that cells tend to divide preferably perpendicular to the direction of movement, possibly due to the strains occurring at the migrating cell front.

7.4 Summary & perspective

We have performed wound healing assays with cancer cells of graded invasive potential, and investigated nematic properties of the migrating cell layer. Wound healing is not a natural process in cancer tissues so the gap closure was not vital to our results at present time. The migration modes of the different cell lines were found to be quite distinct, though speeds were correlated to invasiveness. The non-invasive MCF7 migrated as a collected front, while the MDA-MB-231 were highly individual. The murine breast cancer cells, 67NR and 4T1, both were observed to migrate with protruding waves at the front. The 4T1s were not always observed to display this trait, and we believe density factors in to affect the way they initiate migration. Migration in the direction of minimal stress was reported by Trepal et al. [18], and similar mechanics could be behind density driven migration. Mechanical waves have before been observed in migrating cell layers[76], but what induces them is still to be reported. The obtained orientation fields were rich in information, and we are still analyzing data for the 4 breast cancer cell types. Our current hypothesis is that there could be two differently behaving regions in the migrating cell layer. In combination with previous studies, where leading cells guide the movement[20], our hypothesis is that the cells multiple cell diameters away from the front, align and create some forward movement. Coordinated motility in the trailing cells could induce strains that guide the collective motion of the tissue. We have previously found that aggressive cell lines move quicker than their non-aggressive counter parts (4.3), and this holds true for these experiments as well. We observed migration speeds of $0.25 \mu\text{m}/\text{min}$ for 67NR (non-invasive), $0.29 \mu\text{m}/\text{min}$ 4T1 (invasive), $0.007 \mu\text{m}/\text{min}$ for MCF7 (non-invasive), and $0.29 \mu\text{m}/\text{min}$ for MDA-MB-231 (invasive). A subject we have not covered at all, is the meaning of topological defects during kenotaxis. This is yet to come.

Chapter 8

Conclusion

The aim of the thesis was to investigate how invasive potential and morphology affects the dynamics and mechanics of cancer cells.

We found that divisions induced structured hydrodynamic patterns locally, which were short termed, and the magnitude of velocities, vorticity and divergence correlated with the invasive potential of the cell line. An viscoelastic continuum model reproduced observed dynamics. The collective behavior of cells has been found to be predictable in relation to deformation and motion in studies by Merkel and Manning [112]. To study the effect of deformability we used RT-DC, and contrary to previous finding[86, 87, 88, 89], we saw that the deformability of cancerous cells was not always proportional the malignancy. We hypothesis, that the observed deformations are related to morphological parameters which differ between the cell lines, as some invasive strains are round epithelial-like while others are classically elongated mesenchymal.

Following our interest in the mechanical properties of the whole cell, we barked upon an investigation of the significance of matrix rigidity. The intracellular viscoelasticity of cells in a 3D matrix was studied using optical trapping of granules within the cell. The movement of the granules is relatable to a scaling exponent, α , which is a measure of the diffusion mechanics within the cell. Measurements revealed that contrary to benign cancer cells, the invasive cell lines can adjust the viscoelasticity of their cytoplasm, when embedded in collagen matrices of increasing stiffness (1mg/ml and 4mg/ml). We found that within the invasive cell lines there were two different responses to the changes in matrix stiffness. The invasive human breast cancer (MDA-MB231) and colorectal cancer (KPC) cells were found to decrease in viscosity, while the invasive murine breast cancer (4T1) and pancreatic cancer (KPC) increased in intracellular viscosity. To evaluate the overall mechanical response of the cancer cells to matrix stiffness, the cells grown in collagen matrices were investigated using RT-DC. Cells were found to support conclusions from the intracellular viscoelastic measurements. In, addition, comparing the results with cells grown on plastic, we find that the average Young's elastic modulus for all cells changes from between 2-3kPa when in a matrix, to 1.4-2.6kPa for cells grown on plastic. The results show that cancer cells grown on plastic are less elastic than cancer

cells in collagen.

Across all our studies we have found a possible relationship between observed dynamics and either invasiveness or morphological shape properties. These parameters are necessary to evaluate when characterizing cancer cell lines, but this might be increasingly difficult for *in vivo* studies, as it has been found that EMT can be reversible[94].

Our nematics study is still ongoing, but the results here have shown how orientation analysis of migrating monolayers during chemotaxis, can reveal underlying driving forces. We observed distinct orientation properties related to the rim of the migrating cell layer. The cells seem to align to drive forward the collective motion. We hypothesize that there might be two phases in the migrating cell layer. One in the front, where leader cells might occur, but equally important could be collective forces exerted from the trailing cells.

We are at the moment working on an assay in which we can evaluate the migration of cells through a channel. The properties of cells in a channel has been studied previously[113, 114], but it could be of great interest to see if there are distinct features when the cells leave the channel.

Appendix A

Experimental details

A.1 Cell cultures

All cells were cultured at 37 °C and with 5% CO₂. The 4T1 and 67NR murine breast cancer cell lines were a gift from Fred Miller (Wayne State University)[115] and were confirmed through STR testing. The MDA-MB-231 and MCF7 human breast cancer cell lines were purchased from ATCC, as were the colorectal cell lines SW620 and SW480. The pancreatic cell lines, KPC and KPfIC, were a gift from Jennifer Morton (Beatson Institute for Cancer Research)[116].

A.1.1 Growth medium requirements

The 4T1, 67NR, MDA-MB-231, KPC, KPfIC, SW480, and SW620 cells were cultured in Dulbecco's Modified Eagle Medium (DMEM, Gibco) containing high glucose and GlutaMAX™, 10% Fetal Bovine Serum (FBS) and 1% Penicillin Streptomycin (P/S). The MCF7 cell line was cultured in DMEM/F-12 (Gibco) supplemented with 10% FBS and 1% P/S.

A.1.2 Passaging

The cells were passaged following the same protocol in the appropriate growth medium (see section §A.1.1). Cultures were kept in either T25 flask or T75 flask depending on the amount of cells needed. The following protocol is for T25/T75 flask, respectively.

- Cells were washed with 2/5 ml DPBS (1X, [-] CaCl₂, [-] MgCl₂, Gibco).
- 2 ml Trypsin EDTA (Gibco) was added, and the cells were incubated for 3 min to allow detachment.
- The trypsin was inactivated by applying 3 ml of warm (37°C) cell specific growth medium.

- Cells were centrifuged for 4 min at 80 RFC to remove the trypsin, and resuspended in new growth medium.
- The solution was pipetted up and down 8-10 times to create a single cell suspension.
- Generally the cells were passaged into a new culture flask with a dilution factor of 1:5 or 1:10 (cell suspension: growth medium), depending on the desired final cell density, and to a final volume of 5/10 ml.
- This protocol was repeated approximately every 2-4 days depending on cell density, and growth medium was exchanged at least every 3rd day.

A.2 Sample preparation

A.2.1 Confluent 2D monolayers (chapter 4)

Cells were seeded in Nunc Cell-Culture Treated 6-multiwell plates (Thermoscientific) at a density between $7 \cdot 10^5$ to $9 \cdot 10^5$ cells. After seeding they were allowed to settle for approximately 24 h (16–32 h) to create a confluent monolayer.

A.2 Aphidicolin

For control experiments with aphidicolin (Sigma Aldrich), confluent monolayers were incubated for 6h with $2 \mu\text{g/mL}$ aphidicolin in the media.

A.2 Collagen

Collagen mixtures of 1, 4 or 8 mg/mL were prepared by mixing the corresponding volumes of high concentration rat tail type I collagen (Corning), sterile PBS and 5X collagen buffer containing 0.1M HEPES, 2% NaHCO_3 and α -MEM. The gels were allowed to polymerize for 1h before they were washed with PBS and cells were added.

A.2.2 Cells in solution for RT-DC (chapter 5)

The duration of this type of measurement is determined by the concentration of cells in suspension. Hence the cells were grown to a confluency of approximately 90% prior to sample preparation. The following protocol is for T25/T75 flask, respectively

- Cells were washed with 2/5 ml DPBS (1X, [-] CaCl_2 , [-] MgCl_2 , Gibco).
- 1/2 ml Trypsin EDTA (Gibco) was added, and the cells were incubated for 3 min to allow detachment.
- The trypsin was neutralized by applying 4/3 ml of warm (37°C) cell specific growth medium.

- Cells were centrifuged for 4 min at 80 RFC, washed with DPBS, another round of centrifugation, and resuspended in 1 ml Cell Carrier buffer (ZellMechanik). Resuspension was done carefully as the buffer has a higher viscosity than normal growth medium, and bubbles are easily created.
- The cell solution was transferred to a syringe and connected to the experimental setup, as explained in section §??.

A.2.3 Calcein treatment (chapter 5)

Cells were sparsely seeded in Nunc Cell-Culture Treated 6-multiwell plates (Thermoscientific) at a density of $7 \cdot 10^4$ to $9 \cdot 10^5$ cells. Calcein was purchased from Lifetechnologies, and was resuspended in DMSO to a final concentration of 2.5 mM.

- Medium was removed from the wells and 1ml warm (37°C) cell specific growth medium was added to each well.
- $2 \mu\text{l}$ of calcein was added and the cells were incubated for 15 min.

A.2.4 3D collagen gels (chapter 6)

Cells were suspended in the collagen mixtures prepared as described above??. After polymerization at 37°C for 1h the gels were washed once and incubated with normal culture medium for 24h.

A.2.5 Wound assays (chapter 7)

In both approaches, the cells were seeded in Nunc Cell-Culture Treated 6-multiwell plates (Thermoscientific) at a density of $7 \cdot 10^4$ to $9 \cdot 10^5$ cells. For the insert assay, an Ibidi Culture Insert-2 was placed in the middle of a well. The Culture Insert-2 has two reservoirs in which the cells are seeded (50-100 μl per reservoir). The cells were allowed to settle for approximately 24h (16-32h) to create a confluent monolayer. For scratch assays a pipette tip (200 μL) was used to create a gap down the middle of the well, while for experiments using culture inserts, the insert was simply removed carefully using a tweezer.

Appendix B

Figures

B.1 Division study

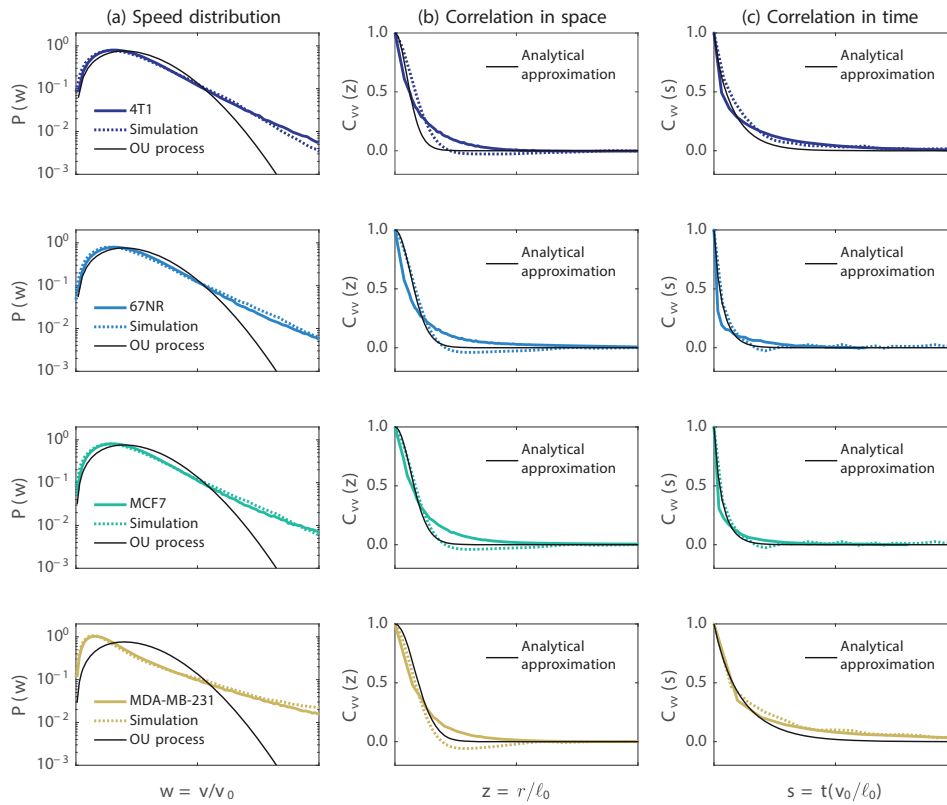


Figure B.1: Statistical characteristics of tissue dynamics. Solid lines represent experimental data, and the dashed lines are the result of a model fit. (a) Speed distribution as a function of the speed v normalized with the mean speed v_0 . Black lines depict the Gaussian tailed speed distribution, that would result from a pure Ornstein-Uhlenbeck process. (b) The spatial velocity correlation as a function of distance r scaled with the correlation length ℓ_0 . The black lines depict the analytical correlation functions in the case of a drag term instead of friction. (c) The temporal velocity correlation as a function of time t scaled with the characteristic time $\ell_0=v_0$. Model fits and analytical solutions agree well with experimental data. Adapted from Christensen [84].

B.2 RT-DC study

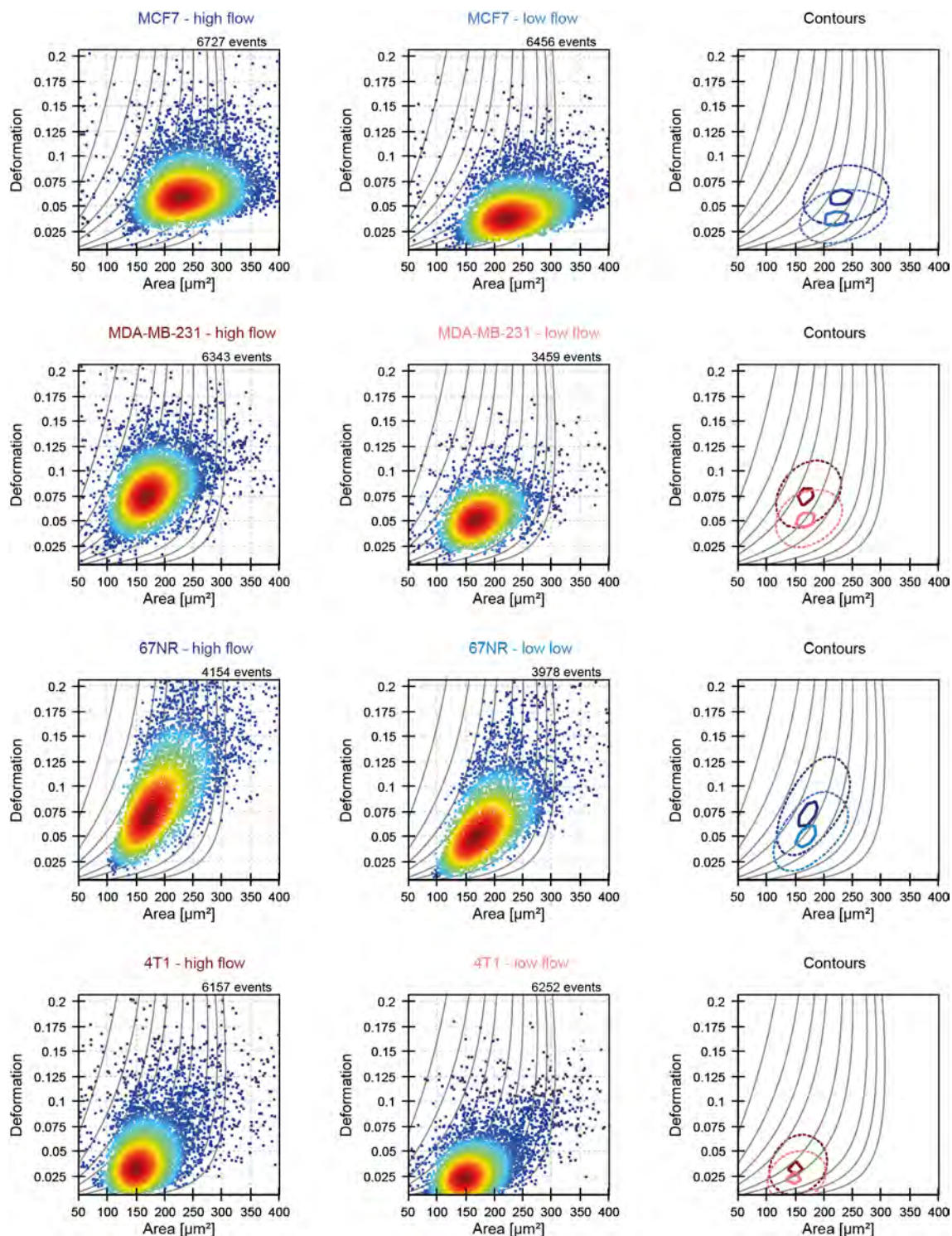


Figure B.2: Comparison of different flow speeds in RT-DC measurements. The scatter plots depict deformation versus cell area (cross-sectional area) measured within a narrow channel. Each row contains plots of one cell type with either high flow speed ($0.12\mu\text{m/s}$) or low flow speed ($0.04\mu\text{m/s}$). The cell lines depicted are all breast cancer cells; MCF7 (human, non-invasive), MDA-MB-231 (human, invasive), 67NR (murine, non-invasive), and 4T1 (murine, invasive). Invasive cell lines are depicted in red shades, while non-invasive cell lines are in shades of blue. Last plot in each row are density contour plots comparing deformations resulting from high and low flow speed. The solid line marks 50% maximum density and the dashed line is at 95%

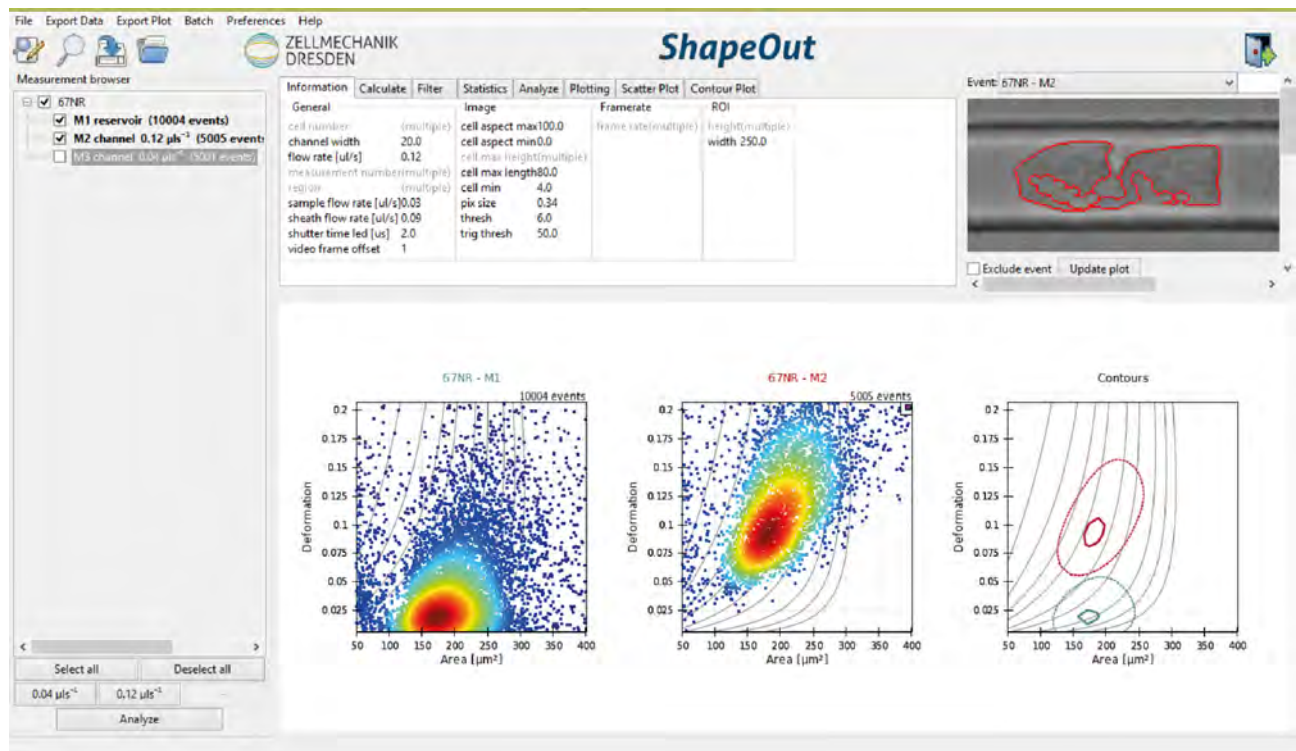


Figure B.3: Screenshot of ShapeOut. Analysis software ShapeOut allows exportation of stored data. The plots show deformation versus cell area data for murine breast cancer cell lines 4T1 (invasive) and 67NR (noninvasive). Single data points can be viewed (top right) and manually eliminated. General filters can also be applied to restrict among others; width, height, area, and aspect ratio. Statistics of the plotted data can also be viewed and exported. A newer feature is the possibility to calculate the Young's modulus.

a

DEFORMATION

Cell type	number of points	mean	std	serror	median	mode
67NR	27260	0.09	0.05	0.00	0.08	0.07
4T1	28020	0.06	0.04	0.00	0.05	0.03
MCF7	17207	0.07	0.03	0.00	0.07	0.06
MDA-MB-231	16641	0.10	0.04	0.00	0.09	0.08
KPC	14901	0.10	0.04	0.00	0.09	0.07
KPflC	18527	0.07	0.03	0.00	0.07	0.05
SW620	17581	0.07	0.03	0.00	0.06	0.04
SW480	15323	0.07	0.03	0.00	0.06	0.05

b

YOUNG'S MODULUS

Cell type	number of points	mean	std	serror	median	mode
67NR	9827	2.49	0.63	0.01	2.37	2.08
4T1	18501	3.03	0.84	0.01	2.87	2.73
MCF7	11494	3.49	0.80	0.01	3.37	3.22
MDA-MB-231	6420	2.66	0.55	0.01	2.57	2.42
KPC	3534	2.45	0.51	0.01	2.35	2.08
KPflC	12033	2.85	0.61	0.01	2.75	2.52
SW620	10410	2.88	0.59	0.01	2.76	2.60
SW480	12064	2.87	0.56	0.01	2.77	2.55

Table B.1: Characteristic values for cancer cells measured in the channel of the RT-DC system. Deformation and Young's modulus values for pairs of invasive and non-invasive cell lines from breast, colorectal, and pancreatic cancer.

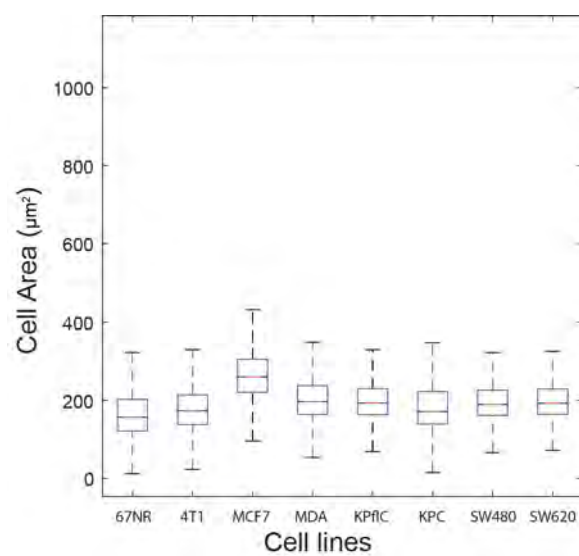


Figure B.4: Cancer cell sizes measured using real-time deformation cytometry. Boxplot of average cell size for different cancer cell lines.

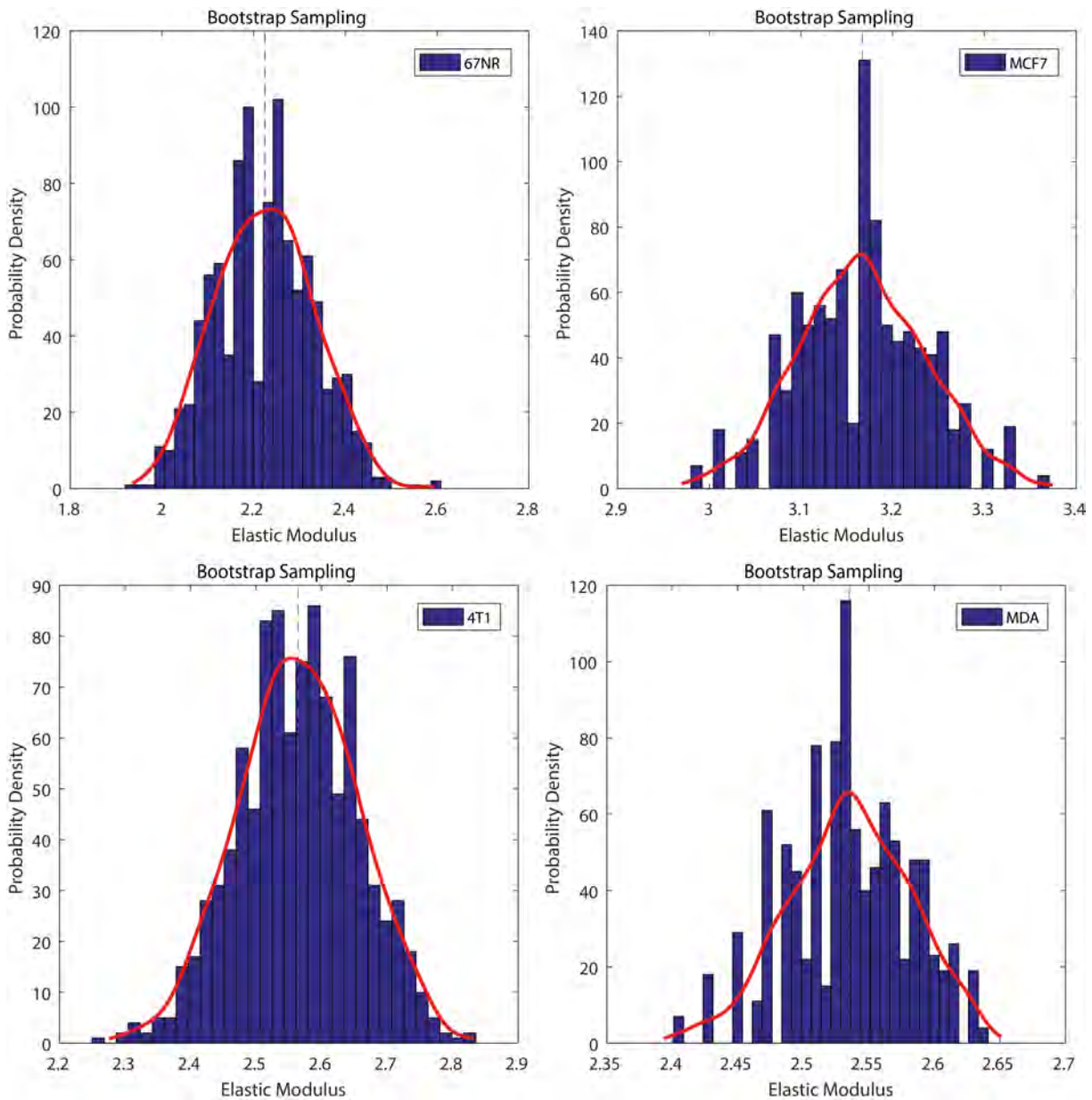


Figure B.5: Bootstrap resampling analysis of Young's elastic modulus values. We assume the mean elastic modulus is normally distributed. Mean values from 4-6 different RT-DC experiments were resampled in order to perform a two-sample t-test between invasive and non-invasive data results. The sample distributions are found to be significantly different, see Table 5.3.

B.3 Nematics of migrating monolayers study

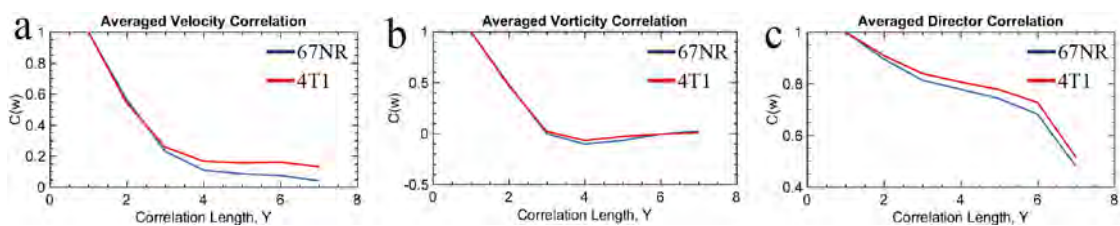


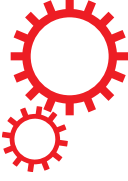
Figure B.6: Characteristic correlation lengths from orientation analysis of wound assays. Average correlation lengths of velocity (a), vorticity (b), and director (c) fields for invasive 4T1 (red) and non-invasive 67NR (blue) mouse breast cancer cells.

Appendix C

Publications and manuscripts

C.1 Dynamics of cancerous tissue correlates with invasiveness

SCIENTIFIC REPORTS



OPEN

Dynamics of cancerous tissue correlates with invasiveness

Ann-Katrine Vransø West¹, Lena Wullkopf², Amalie Christensen¹, Natascha Leijnse¹, Jens Magelund Tarp¹, Joachim Mathiesen¹, Janine Terra Erler² & Lene Broeng Oddershede¹

Received: 10 November 2016

Accepted: 30 January 2017

Published: 06 March 2017

Two of the classical hallmarks of cancer are uncontrolled cell division and tissue invasion, which turn the disease into a systemic, life-threatening condition. Although both processes are studied, a clear correlation between cell division and motility of cancer cells has not been described previously. Here, we experimentally characterize the dynamics of invasive and non-invasive breast cancer tissues using human and murine model systems. The intrinsic tissue velocities, as well as the divergence and vorticity around a dividing cell correlate strongly with the invasive potential of the tissue, thus showing a distinct correlation between tissue dynamics and aggressiveness. We formulate a model which treats the tissue as a visco-elastic continuum. This model provides a valid reproduction of the cancerous tissue dynamics, thus, biological signaling is not needed to explain the observed tissue dynamics. The model returns the characteristic force exerted by an invading cell and reveals a strong correlation between force and invasiveness of breast cancer cells, thus pinpointing the importance of mechanics for cancer invasion.

Cancer is initiated by an uncontrolled cell division, but as long as the inappropriately dividing cells respect the basal membrane as the tissue border, the disease is called non-invasive or benign, and the disease can be treated by surgery. The actual life-threatening systemic disease requires another cellular quality, the ability to infiltrate into healthy tissue and spread to distant organs. Cancer cells can migrate by different modalities; besides the classical single cell migration, collective movements of cell groups and sheets have been observed^{1–3}. Most cancerous tissues are carcinomas, which originate from epithelial cells⁴. Epithelial tissues are characterized by strong inter-cellular interactions, mainly provided by tight junctions, which not only guarantee mechanical support and protection, but also support collective cell behavior. One example is the cooperative cell motility during the closure of wounds. Here, epithelial cells are found to migrate in a collective fashion with long range velocity fields and definable leader cells⁵. Long-range correlation in tissue dynamics has also been observed in endothelial tissue, where well-ordered vortex patterns emerge several cell diameters away from the cell division site⁶. Individual cells need to exert a force in order to initiate tissue migration and it has been shown that local cellular migration follows the local maximum stress⁷, however, with a robust cellular collective drive to fill unfilled space⁸. Mechanical waves guiding such motion have been shown to build up in epithelial monolayers⁹. In collective migration of cancerous tissue the cells are connected via cell-cell junctions, and invasion is initiated and maintained by signaling pathways that control cytoskeletal dynamics and turnover of cell-matrix and cell-cell junctions¹⁰. However, it has proven difficult to define the rate-limiting mechanisms governing invasive migration, and cancer cell invasion is currently regarded as a heterogeneous and adaptive process¹⁰. During invasion cancer cells are subject to considerable forces that have been shown to be large enough to cause nuclear envelope rupture and DNA damage as the cells squeeze through tight interstitial spaces¹¹.

Here, we take an alternative view on cancer tissue dynamics with the goal of understanding which of the observed properties can be understood alone from a materials science point of view, without the need to invoke complex signaling mechanisms, although many such signaling pathways have been identified¹². We characterize the dynamics of cancer tissue of different invasive potential, originating from both mouse and human. As uncontrolled cell division is a hallmark of cancerous tissue, we focus on the dynamics related to cell division and on the forces exerted by the dividing cells on the surrounding tissue. We find a strong correlation between the velocity, divergence and vorticity fields of the cancer and its invasive potential. To understand the dynamics from a mechanical point of view, we formulated a model which considers the tissue as a viscoelastic continuum and reproduces well the velocity field. The model allows for quantification of the force exerted by the dividing cells on

¹Niels Bohr Institute, University of Copenhagen, Blegdamsvej 17, 2100 Copenhagen, Denmark. ²Biotech Research & Innovation Centre (BRIC), University of Copenhagen, Ole Maaløes Vej 5, 2200 Copenhagen, Denmark. Correspondence and requests for materials should be addressed to L.B.O. (email: oddershede@nbi.dk) or J.T.E. (email: janine.erler@bric.ku.dk)

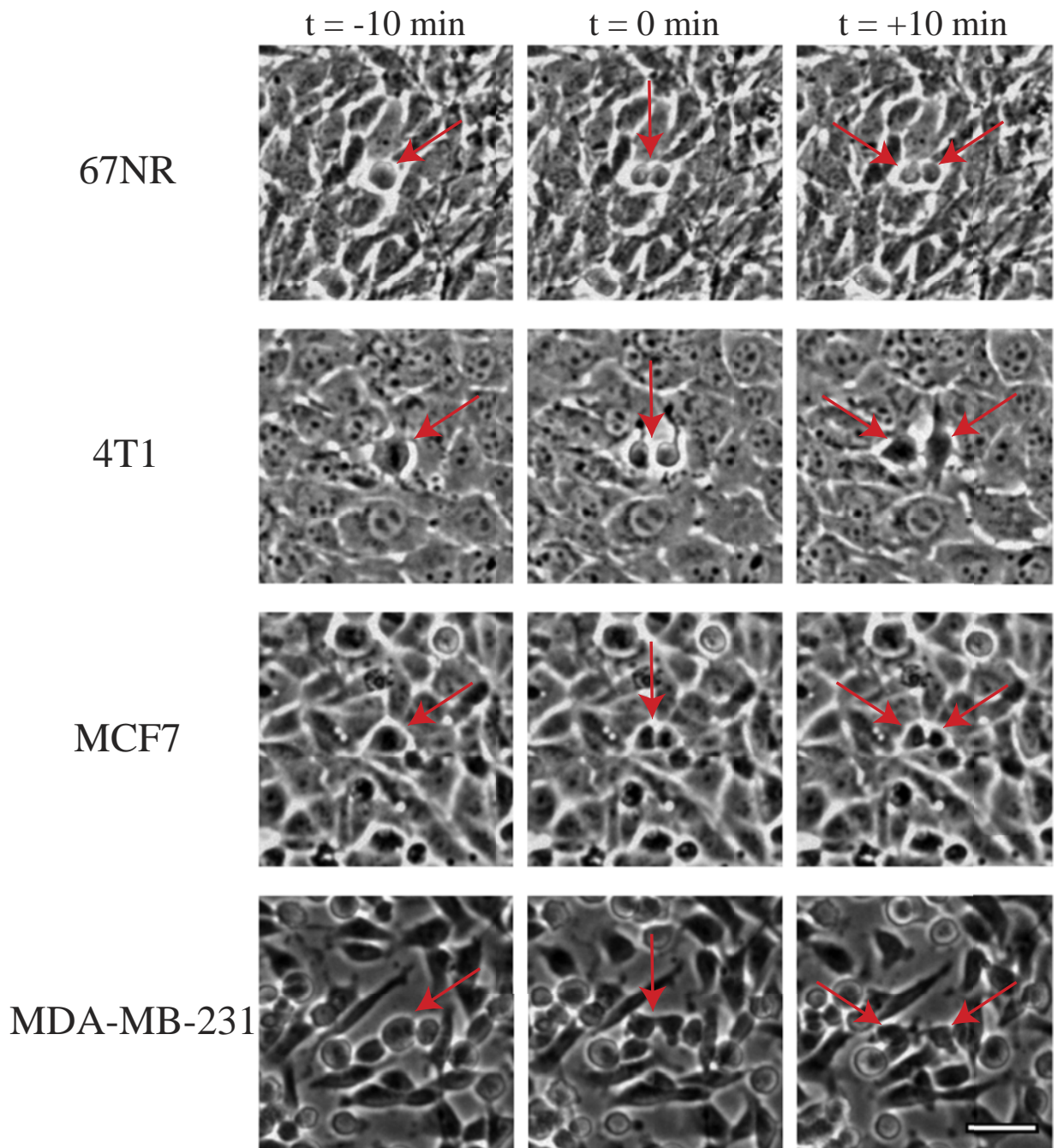


Figure 1. Images of cancer tissue surrounding a cell division site in a confluent monolayer of the breast cancer cell lines 67NR (mouse, non-invasive), 4T1 (mouse, invasive), MCF7 (human, non-invasive), and MDA-MB-231 (human, invasive). The red arrows point to the site of cell division and at the resulting daughter cells. Time zero is defined as the onset of cytokinesis, i.e., the first image where two distinct daughter cells are visible. The dividing cell is centered in the image and the image is rotated so that the daughter cells move in a horizontal direction after cell division. The scalebar is 40 μm and applies to all images.

the surrounding tissue, and this force is found to correlate with the invasiveness of the cancer. These results are useful for understanding the underlying fundamental mechanisms of cancer tissue dynamics.

Results

Characterizing the dynamics of cancerous tissue. All tissue types investigated here originate from epithelial monolayer breast tissue and representative images of these monolayers are shown in Fig. 1. We investigated the human breast cancer cell lines MCF7 (non-invasive) and MDA-MB-231 (invasive). These human cell lines show the classical phenotype with the non-invasive MCF7 retaining an epithelial-like and round shape whereas the highly invasive MDA-MB-231 cells exhibit a more mesenchymal-like and elongated appearance (see

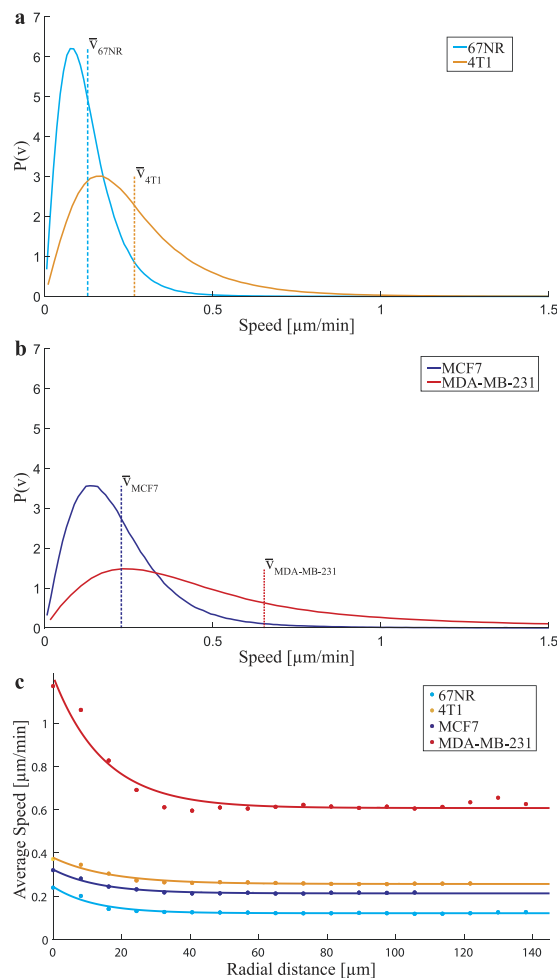


Figure 2. Invasive cancerous tissues move faster than their non-invasive analogue. (a) Probability density functions of the speeds from the complete monolayer velocity field (obtained by PIV analysis) during the entire imaging period (80 min) for the human cells (non-invasive MCF7, invasive MDA-MB-231). The vertical lines depict the mean speed for each tissue type. (b) Same as (a) for the murine cells (non-invasive 67NR, invasive 4T1). (c) The average tissue speeds as a function of distance from the division site, dots denote data points, solid lines are exponential fits. The speed is only elevated compared to the normal tissue speeds ~ 1 cell diameter away from the division site. Also, it is clear from this plot that the most aggressive cell type here investigated, the human MDA-MB-231 cells, move significantly faster than any of the other cell types.

Fig. 1). In addition, we investigated murine cell lines which exhibit the opposite phenotype with the non-invasive 67NR cells showing a more mesenchymal-like phenotype while the malignant 4T1s maintain a round epithelial shape (see Fig. 1). These differences are also reflected in the gene-expression of the classical epithelial marker E-Cadherin: The invasive human breast cancer cell line MDA-MB-231 shows a striking downregulation of the cell adhesion protein E-Cadherin, while the invasive murine 4T1s maintain high E-Cadherin levels. For the non-invasive cell lines, the human MCF7 exhibit high E-Cadherin levels, while the murine 67NR does not.

The dynamics of the cancerous tissue was quantified by particle image velocimetry (PIV). This method tracks the displacements from image to image by finding the maximum correlation between intensity patterns¹³ (more details are given in Methods). The time lapse between two consecutive images was 2 minutes and the division sites were chosen so that no other divisions took place during this time interval within the frame investigated. An example of an extracted velocity field is shown in Supplementary Fig. S1.

Correlation between velocity and invasiveness. From the velocity fields, we calculated the speed distributions of all investigated cell tissue types. These are depicted in Fig. 2a and b for the murine and human cells, respectively. At least 30 independent data sets were used for each tissue and for each data set images were analyzed 40 minutes before and 40 minutes after cytokinesis, i.e., at least 1200 images were analyzed for each tissue type. Figure 2c shows the average speed as a function of distance from the division site. Only within ~ 1 cell diameter from the division site does the average speed exceed the typical tissue speed. Also, cell division is rare and changes in the velocity field around the dividing cell are only visible ~ 4 min before and ~ 4 min after cytokinesis. Therefore, the average speed distributions (Fig. 2a and b) characterize the motion of the entire cancerous tissue, not of the cell division site per se. The murine cell lines showed an average speed of $0.13 \pm 0.03 \mu\text{m}/\text{min}$ for the non-invasive

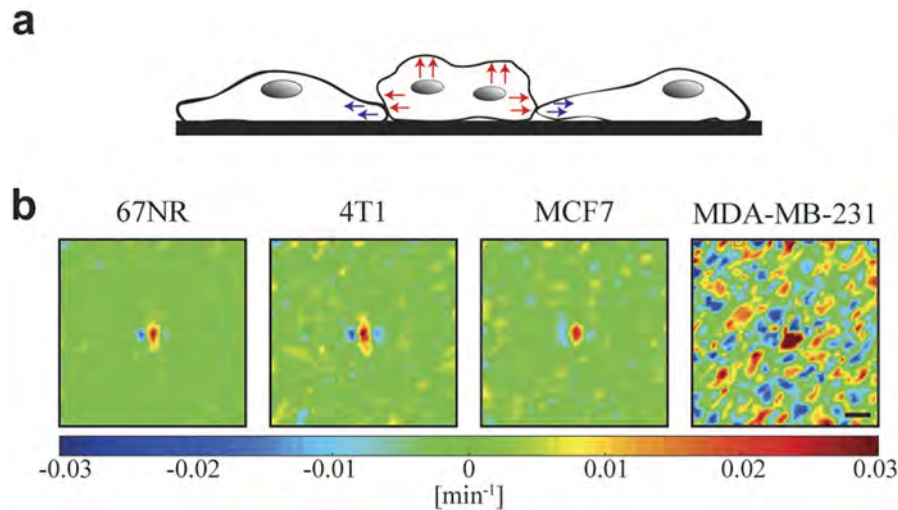


Figure 3. Contraction and expansion in cancer tissue around a cell division site. (a) Illustration of the contraction (blue arrows) and expansion (red arrows) of cells undergoing or neighbouring cell division. (b) Divergence field during cytokinesis around a dividing cell located in the center of each image. The daughter cells move in a horizontal direction after cytokinesis. Each image is $300 \times 300 \mu\text{m}^2$ and is an average of at least 30 data sets. The scalebar is $40 \mu\text{m}$ and applies to all images. The color scale displays the degree of divergence with blue denoting contraction and red expansion. The two invasive tissue types (mouse 4T1 and human MDA-MB-231) exhibit a higher degree of contraction and expansion than their non-invasive counterparts (mouse 67NR and human MCF7).

67NR cells, while the invasive 4T1 cells had an average velocity of $0.27 \pm 0.06 \mu\text{m}/\text{min}$. For the human cell lines, the non-invasive MCF7 cells display a mean velocity of $0.23 \pm 0.02 \mu\text{m}/\text{min}$, while the invasive MDA-MB-231 cells had an average speed of $0.7 \pm 0.2 \mu\text{m}/\text{min}$. For each cell type, the reported error was found as the standard deviation of the mean speeds, calculated for at least 30 independent experiments. Hence, for both the cancerous tissue types, mouse and human, the invasive cells had a significantly higher average speed than the non-invasive counterparts. From Fig. 2a and b it is also apparent that the speed distribution of the most aggressive cells here investigated, the human MDA-MB-231, has a ‘fatter tail’ than the others, this signifies a relatively large number of cells moving extra-ordinarily fast. For the human cell lines, the average velocities here obtained correspond well to those reported in literature in migration assays^{14–17}. For the murine cell lines, there only exists a value for the non-invasive 67NR of $0.03 \mu\text{m}/\text{min}$ ¹⁸, which is somewhat lower than observed here.

Divergence and vorticity around dividing cancer cells. Just before a cancer cell divides it contracts and ‘balls up’ thus becoming higher than the surrounding tissue. At cytokinesis the two daughter cells move in opposite directions away from the cleavage furrow while the adjacent cells contract their cell protrusions (as illustrated in Fig. 3a). These features are visible for all investigated tissue types in the experimentally obtained divergence fields, which are calculated as described in Methods and depicted in Fig. 3b. The invasive cell lines display stronger divergence than the non-invasive counterparts. Also, the human invasive MDA-MB-231 is the tissue type which shows the overall largest degree of divergence throughout the entire tissue (not just around the division site). This is probably because these cells are highly motile and move more independently than other tissue types. To increase the signal to noise ratio, the data shown both in Figs 3b and 4 are averages over at least 30 data sets. Before averaging, the frames were aligned so that the cell division occurs in the center of the image, and rotated so that the two daughter cells move in a horizontal direction immediately following cytokinesis. Similar divergence patterns were previously reported for cell divisions of endothelial cells⁶.

Vorticity is another convenient measure of tissue dynamics, it describes the curl of the velocity field and thereby the swirling induced in the tissue by the dividing cells. After cell division, the two daughter cells expand outward in opposite directions, inducing two pairs of vortices in the tissue, with the center at the division site, see Fig. 4. These two pairs of vortices are visible for at least 4 minutes after cell division in all investigated tissue types. There are, however, important differences between the cell lines: The vorticity around a dividing cell is clearly stronger for the invasive cells (mouse 4T1, human MDA-MB-231) than for their non-invasive counterparts (mouse 67NR, human MCF7). Hence, vorticity correlates with invasiveness. Remarkably, the background level is significantly higher for the most invasive tissue type investigated, the human MDA-MB-231, which was also the case for the divergence (Fig. 3b).

Compared to the vorticity fields surrounding healthy dividing endothelial cells, there are distinct differences to cancer cells. For instance, the vortex pairs induced by cancer cell division are relatively short-lived, they dissipate ~ 6 minutes after division (Supplementary Fig. S2). In contrast the vortex structures surrounding dividing endothelial cells remain detectable for hours⁶. Also, the extent of the vortex structures around dividing cancer cells is relatively short, only ~ 1 cell diameter (Supplementary Fig. S2) corresponding to an induction of only primary vortices. This is quite different from endothelial tissue where the correlation length was significantly

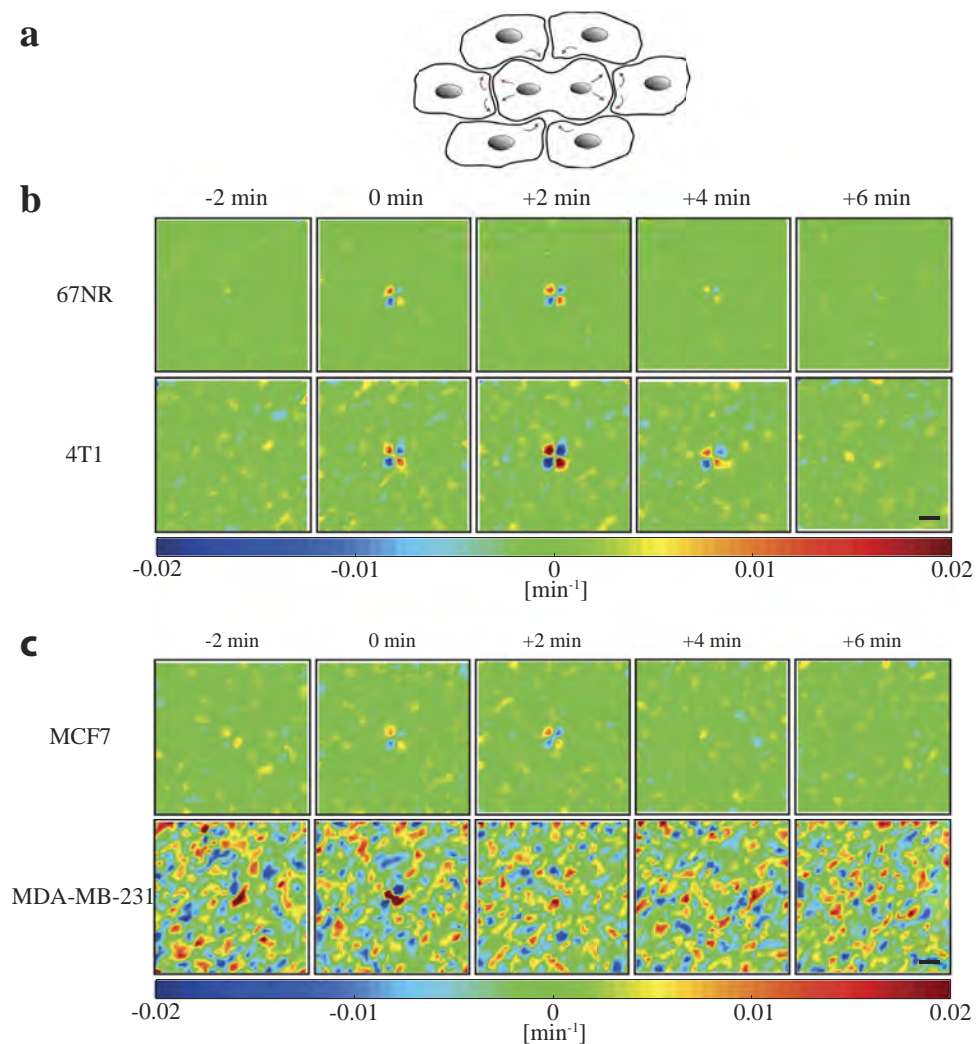


Figure 4. Cell divisions induce ordered vorticity patterns in a confluent monolayer of breast cancer cells. (a) Illustration of the division induced cell movement resulting in the emergence of a central vortex pair. (b) and (c) show the average vorticity fields in an area of $150\ \mu\text{m}$ from a cell division site ($n = 30$) for breast cancer cells with the daughter cells moving in a horizontal direction after cytokinesis. Time zero was defined as onset of cytokinesis. (b) Vorticity fields of murine cell lines (non-invasive 67NR, invasive 4T1). (c) Vorticity fields of human cell lines (non-invasive MCF7, invasive MDA-MB-231). The colorscale displays the vorticity (counterclockwise motion blue, and clockwise motion red). The scalebars are $40\ \mu\text{m}$ and apply to all images.

larger, expanding over 3 cell diameters and where also secondary and tertiary vortices were induced⁶. Such structured dynamics around dividing cancer cells was not observed in control experiments without cell divisions (Supplementary Fig. S3).

Continuum model. Biological matter, from single yeast cells¹⁹ to developing embryos²⁰, has been shown to possess viscoelastic properties^{21,22}. This means that on short time scales, the tissue deforms and relaxes elastically in response to a mechanical loading, whereas loads applied over a longer time will result in an irreversible viscous deformation. Many models of viscoelastic behavior exist and one of the most simple models, which include a crossover from predominantly elastic behavior on short time scales to viscous flow on larger time scales, is the Oldroyd-B model²³. In the limit of small velocity gradients this model is based on the constitutive relation:

$$\sigma + \lambda_1 \frac{\partial \sigma}{\partial t} = 2\eta_0 \left(\gamma + \lambda_2 \frac{\partial \gamma}{\partial t} \right), \quad (1)$$

where σ is the deviatoric stress tensor, $\gamma = \frac{1}{2}[\nabla \mathbf{v} + (\nabla \mathbf{v})^T]$ is the strain rate tensor and the material properties are parametrized by the relaxation time λ_1 , the retardation time λ_2 and the total viscosity η_0 . In contrast to a purely viscous fluid the stress state of an Oldroyd-B fluid has memory of the past and the constitutive relation therefore includes time derivatives of the stress tensor σ . In our model, we go beyond basic viscoelasticity by also including the self-propelling force of individual cells.

The dynamics of the tissue is modeled by the mass and momentum balance equations, where the mass balance is guaranteed by the incompressibility condition $\nabla \cdot \mathbf{v}$ and the momentum balance equation assumes the form

$$0 = -\frac{1}{\rho} \nabla p + \frac{1}{\rho} \nabla \cdot \sigma - \alpha \hat{\mathbf{v}} + \mathbf{m}, \quad (2)$$

where ρ is the mean density, p is the pressure, $\hat{\mathbf{v}} = \mathbf{v}/|\mathbf{v}|$ is the direction of the local mean velocity of the tissue, α is a positive friction constant and \mathbf{m} is a stochastic acceleration term describing the self-propelling forces of the cells. The friction term $\alpha \hat{\mathbf{v}}$ accounts for all the dissipative processes between the cells and the substrate. Similar to the basic Coulomb friction law, we shall here assume that the friction is independent of the speed of the cells. The momentum balance, eq. 2, contains no inertial terms, as the dynamics are assumed to be fully overdamped, i.e., the dissipative forces completely dominate the inertial forces. More details of the model are given under 'Experimental Procedures' and in Supplemental Information. The correlation length, ξ , in the motion of the cancerous cells is relatively short (Supplementary Table S1 and Supplementary Fig. S4) compared with other tissues such as endothelial tissue⁶, probably because the cancer cells are less tightly connected than the endothelial cells. When tissue dynamics exhibit longer correlation lengths the dynamics are better described by higher order models, see, e.g., in refs 6 and 24.

The governing equations of the model, eqs 1 and 2, are valid in both 2D and 3D. However, the cell-substrate friction term would be irrelevant in 3D, where no substrate is present. Also, one could relatively easily implement the presence of chemokines into the model as a scalar concentration field, the gradient of which would lead to a local force affecting the velocity.

Comparison to experimental data. The cells are self-propelling and we expect them to explore their environment in a random fashion, when no interactions are taken into account. The motility term \mathbf{m} in eq. 2 was therefore taken to be the result of an Ornstein-Uhlenbeck process with a noise persistence time λ_m , strength β_m and an imposed characteristic length scale ℓ_m (see Methods). The continuum model described by eqs 1 and 2 was simulated numerically and the speed probability density function $P(v)$, the spatial velocity correlation function $C_r(r)$, and the temporal velocity correlation function $C_t(t)$ were calculated. The model parameters were fitted by measuring the chi-square between the experimental and the simulated $P(v)$, $C_r(r)$, and $C_t(t)$, choosing the parameter set yielding the smallest chi-square value in a parameter grid search. (Details on the numerical implementation of the continuum model and the fitted parameters are given in Methods and Supplementary Information).

Figure 5a shows the speed distributions for the different tissue types returned by the continuum model. It is clear that the model (dotted lines) reproduces the experimental data (full lines) quite well for all tissue types. Even the tails of the speed distributions (see the semi-log inset of Fig. 5b), and the exceptionally 'fat tail' of the human invasive MDA-MB-231 in Fig. 2, are captured well by the continuum model, due to the inclusion of viscoelasticity and friction in the model. If these features were not included, the Ornstein-Uhlenbeck forcing \mathbf{m} would generate a speed distribution with a Gaussian tail. The spatial and temporal correlation functions as well as their fits are shown in Supplementary Fig. S4.

Quantifying the force exerted by a dividing cell. To quantify the mechanical forces exerted by a dividing cell, we include cell division in the continuum model by adding an active stress σ_0 inspired by refs 25–27 to the constitutive relation in eq. 2:

$$\sigma + \lambda_1 \frac{\partial \sigma}{\partial t} = 2\eta_0 \left(\gamma + \lambda_2 \frac{\partial \gamma}{\partial t} \right) + \sigma_0. \quad (3)$$

The active stress has a simple on/off time dependence and is assumed to originate from two equal but opposite constant point forces of magnitude f_0 separated by a small distance $2a$ and centered on the cell division site.

We are interested in the cell layer's response to a division and therefore neglect the noise term \mathbf{m} in eq. 1 since it represents the cells' intrinsic motility, which is not a division-induced effect for the studied cell lines. The friction term $-\alpha \hat{\mathbf{v}}$ is small compared to the force driving the division and is neglected. In the absence of noise and friction, eqs 1 and 3 can be solved analytically. The obtained velocity field is a Stokeslet dipole $\mathbf{v}_{\text{sto}}(\mathbf{x})$ in space multiplied by a time dependent function $h(t)$, (see Methods):

$$\mathbf{v}_{\text{mod}}(\mathbf{x}, t) = \mathbf{v}_{\text{sto}}(\mathbf{x})h(t). \quad (4)$$

The model velocity field $\mathbf{v}_{\text{mod}}(\mathbf{x}, t)$ was fitted to the time-series of averaged experimental \mathbf{v} data using regularized Stokeslets²⁸. For each time series, the magnitude of the point force divided by the viscosity, f_0/η_0 , as well as the retardation time, λ_2 , were extracted (values are given in Table 1). A comparison of the experimentally obtained velocities around a dividing cell with the model's predictions is shown in Fig. 5b. The resulting time dependence of the forcing (defined as force per meter divided by characteristic viscosity) is shown in Fig. 5c and the obtained retardation times, given in Table 1, were similar to the values obtained when fitting the model to the statistical characteristics of the entire velocity field.

As apparent from Fig. 5c and Table 1, the invasive cell lines exerted a larger force to viscosity ratio during cell division than the non-invasive cell lines for both the murine and human model systems. To test the statistical significance of the difference in forcing magnitude f_0/η_0 between invasive and non-invasive cells, a two-sided student's t-test was performed. A sample of 30 values of f_0/η_0 for each cell type was extracted by fitting the model velocity field $\mathbf{v}_{\text{mod}}(\mathbf{x}, t)$ to each of the 30 individual experimental time series making up the averaged experimental velocity time series \mathbf{v} . Comparing the samples of 4T1 and 67NR yielded a p -value less than 10^{-8} whereas the comparison of MCF7 and MDA-MB-231 yielded a p -value less than 10^{-3} , supporting that the invasive cell lines 4T1

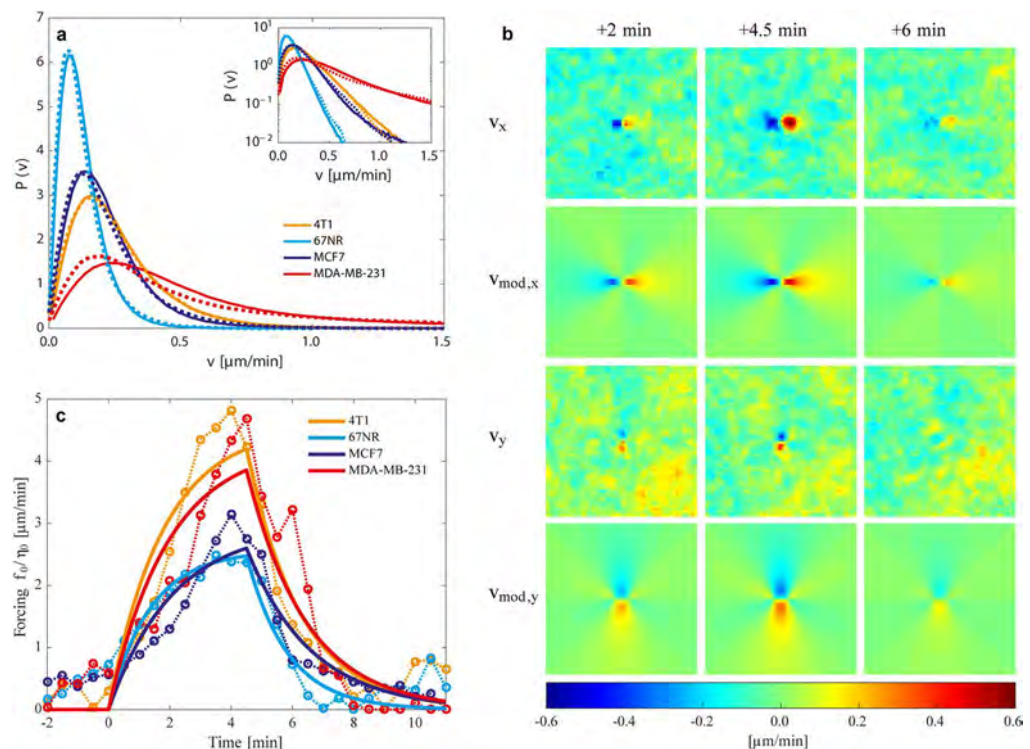


Figure 5. Predictions by the continuum model and comparison to experiments. (a) Probability density of the normalized speed distribution during the whole imaging period (80 min). Experimental data are shown by full lines, the model's predictions by dotted lines. Inset: The speed distributions on a semi-logarithmic scale demonstrating how well the exponential tails are reproduced by the model. (b) The velocity field induced by a single cell division v compares well with a fit of the model velocity field v_{mod} given in eq. 4. The cell division occurs at time $t = 0$ min and the displayed experimental data v , are from an average over at least 30 data sets. The cell line displayed is the invasive murine 4T1 and the three other cell lines are fitted equally well by the model. (c) The force exerted by the expanding daughter cell divided by the viscosity as a function of time. The solid lines are the result of fitting eq. 4 to the experimental velocity time series during division. One value of f_0/η_0 and λ_2 is obtained for each of the four time series. The dotted lines represent fits to the same experimental data, when no time dependence is imposed on the model, i.e., a Stokeslet dipole $v_{sto}(x)$ is fitted to each time frame, thus returning one fitted value of f_0/η_0 per time frame. The time series of f_0/η_0 -values serves as a test of the time dependence predicted by the full time-dependent model. For both the murine and human cells, the invasive cell lines exert the largest force during division and expansion.

Cell type	Forcing f_0/η_0	Retardation time λ_2
4T1	$(4.6 \pm 0.4) \mu\text{m}/\text{min}$	$(1.8 \pm 0.3) \text{min}$
67NR	$(2.6 \pm 0.4) \mu\text{m}/\text{min}$	$(1.3 \pm 0.5) \text{min}$
MCF7	$(2.9 \pm 0.4) \mu\text{m}/\text{min}$	$(2.1 \pm 0.6) \text{min}$
MDA-MB-231	$(4.3 \pm 0.4) \mu\text{m}/\text{min}$	$(1.9 \pm 0.3) \text{min}$

Table 1. Forcing and typical retardation times for the different cancer model systems, numbers are obtained by fitting the theoretical model to the experimental data.

and MDA-MB-231 do exert a significantly larger forcing f_0/η_0 than their non-invasive analogues. The obtained retardation times, λ_2 , did not differ significantly between cell types, signaling a relative similar rheology.

Discussion

Using image analysis, we quantified the velocity fields in cancerous tissue surrounding dividing cells. By invoking different measures for the tissue dynamics, speed, divergence and vorticity, we found that invasive cancer cell lines (mouse 4T1 and human MDA-MB-231) move faster, and display stronger divergence and vorticity, than their non-invasive counterparts (mouse 67NR and human MCF7). Hence, fast intrinsic tissue movements correlates with the aggressiveness of the breast cancer type.

The two metastatic cell lines investigated here represent breast cancer cells with a varying level of physical interaction. The MDA-MB-231 are known to have a downregulated production of the classical epithelial marker

E-Cadherin²⁹, they have a mesenchymal, elongated phenotype, and they primarily migrate and invade as single cells. Although being highly aggressive, 4T1 cells in contrast continue to express the epithelial tight junction marker E-Cadherin³⁰ and accordingly migrate in a collective manner^{30,31}. Despite these striking regulatory differences, our analysis reveals a correlation between invasiveness and all observed parameters characterizing dynamics. In addition, we can exclude a pure correlation between cell shape and dynamics.

All investigated cell lines displayed the emergence of two pairs of vortices around division sites, and the spatial and temporal correlations of these patterns were short compared to similar events in endothelial tissue⁶. This may be attributed to the fact that cancerous tissues have weaker intercellular adhesion than endothelial tissue, and adjacent cells move in a less correlated fashion. Endothelial cells are stress sensitive, tightly packed, and rely on cooperation within the layer to function optimally. Cancer cells, on the other hand, divide at higher rates and their lower cell-to-cell adhesion, compared to normal cells, give rise to high motility.

The continuum model presented here was inspired by the experimental observations, in particular, the relatively short correlation length and the visco-elastic properties of the tissue were crucial for the model's exact formulation. The model captures the experimentally observed velocity fields, and in addition provides important information on the forces exerted by cancerous cells undergoing division. Our discovery that the invasive cells exert a larger forcing (and a larger force, if viscosity is assumed constant) than the non-invasive counterparts in both the human and murine model system, intuitively makes sense as the more aggressive cells should be better able to squeeze through tight interstitial spaces and even be able to cross boundary layers such as blood vessel walls. The present work focuses on 2D migration and does not consider aspects of tumor growth such as tumor morphology, interaction between healthy and cancerous tissue, nor the availability of resources such as oxygen and nutrients^{32,33}. The model regards cancer tissue as a continuum and is solely based on the material properties of the system, no biological signaling is included. In real life, the behavior of cancer tissue will be influenced both by biochemical signaling and material properties^{34–36}. Although the influence of the mechanics, material properties, and the tumor microenvironment is receiving increasing attention, a full understanding of the mechanisms governing collective dynamics is still missing.

By analyzing the dynamics of cancerous tissue, both murine and human, we found a strong correlation between the invasiveness of breast cancer cell lines and the 2D tissue dynamics. Invasive cell lines, murine 4T1 and human MDA-MB-231, showed significantly faster intrinsic tissue movements than their non-invasive counterparts (murine 67NR and human MCF7). Uncontrolled cell division is a hallmark of cancer cells and the divergence and vorticity fields around dividing cells were significantly stronger for the invasive cell lines than for the non-invasive albeit, with shorter correlation lengths than observed around dividing cells in endothelial tissue⁶. The experimental observations led to formulation of a continuum model which incorporated the viscoelastic nature of the tissue. This model nicely reproduced all observed experimental data, for instance the velocity, divergence and vorticity fields. In addition, the model returned the force³⁷ divided by viscosity applied by the dividing cells onto the remainder of the tissue and we found that the forces exerted by the invasive cell lines were significantly larger than by their non-invasive counterparts. These results prove a strong correlation between cancer tissue invasiveness, dynamics and force generation, where the most aggressive cells are the strongest and fastest. This information shows that dynamics are a more reliable parameter for judging aggressiveness than, e.g., cell shape, tissue connectedness, or endothelial marker expression. A natural extension of the current study will be to investigate the dynamics of a tumor embedded in a three dimensional matrix. The theoretical model here presented should still be valid in three dimensions, however, PIV analysis of experimental images would be challenging. *In vivo*, the physical and biological properties of the tumor microenvironment (TME) will influence tumor cell growth³⁴ and migration rate³⁸. For instance, the rigidity and meshwork density of the TME has been shown to influence cellular migration and invasion^{39–41}. Hence, for translation into an *in vivo* or clinical setting, the influence of the TME would need to be assessed.

Methods

Cell culture. All cell lines were cultured at 37 °C and with 5% CO₂. The 4T1 and 67NR murine breast cancer cell lines were a kind gift from Fred Miller (Wayne State University)³⁷ and were confirmed through STR testing. The MDA-MB-231 and MCF7 human breast cancer cell lines were purchased from ATCC. All cell lines were routinely tested negative for mycoplasma. The 4T1, 67NR and MDA-MB-231 cells were cultured in Dulbecco's Modified Eagle Medium (DMEM, Gibco) containing high glucose and GlutaMAXTM, 10% Fetal Bovine Serum (FBS) and 1% Penicillin Streptomycin (P/S). The MCF7 cell line was cultured in DMEM/F-12 (Gibco) supplemented with 10% FBS and 1% P/S.

The cells were seeded in Nunc Cell-Culture Treated 6-multiwell plates (Thermoscientific) at a density between 7·10⁵ to 9·10⁵ cells. After seeding they were allowed to settle for approximately 24 h (16–32 h) to create a confluent monolayer.

Time lapse microscopy and image analysis. Phase contrast images were taken of the monolayer for a duration of 6–12 h using a Nikon Eclipse Ti-E microscope system. The majority of the data was taken using a 10x air objective (CFI Plan Fluor DLL, 10x, N.A. 0.30, W.D. 16.0 mm, Ph1, Nikon), acquiring an image every 2 min. To increase spatial and temporal resolution, imaging was repeated with a 20x objective (CFI Plan Fluor DLL, 20x, N.A. 0.50, W.D. 2.1 mm, Ph1, Nikon) taking an image every 0.5 min (see Supplementary Methods for discussion on this).

Dividing cells with a distance of at least 150 μm from other dividing cells during the duration of the observation period were identified manually in the phase contrast images. The dividing cell was centered in the 300 × 300 μm² frame and the frame was rotated so that the daughter cells would move along a horizontal axis away from the site of division (Fig. 1 and Supplementary Fig. S1). The image sequence spanned from +/- 40 min from the site of cell division.

Particle Image Velocimetry, divergence and vorticity. The image processing was performed using particle image velocimetry, more precisely the GUI based open-source tool called PIVlab¹³. This method allows us to perform the analysis of tissue dynamics using Matlab routines. It uses cross correlation algorithms to measure space- and time-resolved flow velocities, and enhances signal-to-noise and vector resolution by applying multiple rounds of displacement analysis to offset the following rounds. These multiple rounds are known as passes. For the PIV analysis, 3 passes were used and final interrogation areas of 15.6 μm for the 10x experiments and 7.8 μm for the 20x experiments, respectively.

From the velocity vectors, it is possible to calculate contraction and expansion of the vector field (divergence), and the swirling tendency (vorticity). These were calculated using the equations below.

Divergence [min^{-1}]:

$$d = \frac{\partial}{\partial x} v_x + \frac{\partial}{\partial y} v_y = \sum_{r \in 0} \frac{v_x(\mathbf{r})r_x - v_y(\mathbf{r})r_y}{A} \quad (5)$$

Vorticity [min^{-1}]:

$$\omega = \frac{\Gamma}{A} = \frac{\oint \mathbf{v}(\mathbf{r}) \cdot d\mathbf{r}}{A} = \sum_{r \in 0} \frac{v_x(\mathbf{r})r_y - v_y(\mathbf{r})r_x}{A} \quad (6)$$

To increase the signal-to-noise ratio, the velocity fields and all subsequent analyses were averaged over at least 30 (for 10x) or 50 (for 20x) data sets, deriving from at least 4 individual experiments. Analysis of the velocities was performed with custom made Matlab scripts.

The continuum model. The proposed model aims at describing cell-cell interaction, cell-substrate dissipation and intrinsic motility of the cells in a mechanical framework. A continuum description is therefore natural, as it renders mechanical properties such as local stresses and forces easily accessible. The cell-cell interactions are in the continuum described by the material rheology eq. 1, the cell-substrate interactions are accounted for by the friction term $-\alpha \hat{\mathbf{v}}$ and the intrinsic cell motility is incorporated through the noisy acceleration term \mathbf{m} .

The acceleration term, representing cell motility, was taken to be the result of an Ornstein-Uhlenbeck process:

$$\frac{\partial \mathbf{m}}{\partial t} + (\mathbf{v} \cdot \nabla) \mathbf{m} = -\frac{1}{\lambda_m} \mathbf{m} + \varphi(\mathbf{x}, t), \quad (7)$$

where λ_m is the noise persistence time and $\varphi(\mathbf{x}, t)$ is a white Gaussian noise field $\zeta(\mathbf{x}, t)$ of strength $\langle \zeta(\mathbf{x}, t) \cdot \zeta(\mathbf{x}', t') \rangle = 2\beta_m \delta(\mathbf{x} - \mathbf{x}') \delta(t - t')$, filtered in space with a Gaussian function of width l_m and zero mean to impose a characteristic length scale on the noise. The imposed length scale reflects the fact that a cell is coherent and the velocity field should not fluctuate on scales smaller than the cell size.

Numerical simulation. The model described by eqs 1 and 2 was simulated numerically in a two-dimensional box with periodic boundaries using a pseudo-spectral method. Non-linear terms were evaluated in real space and then transformed back to Fourier space using the Fast Fourier Transform. An exponential time differencing scheme⁴², was used for the time integration of the stress tensor and the motility term. The velocity field and pressure were found in each time step by a relaxation procedure. A grid of size 256 by 256 and a time step of the order $\Delta t \sim 10^{-4}$ were used. In physical dimensions this corresponds to a box of length $\sim 200 \mu\text{m}$ and a time step $\sim 0.01 \text{ min}$.

The velocity field of a single dividing cell. When friction and motility are ignored, the model described by eqs 1 and 3 can be solved analytically using Laplace transform techniques, since the transformed equations have the same structure as Newtonian Stokes flow driven by point forces. If the active stress σ_0 is turned on at time $t=0$ and turned off at time $t=t_{\text{off}}$ then the velocity solution $\mathbf{v}_{\text{mod}}(\mathbf{x}, t) = \mathbf{v}_{\text{sto}}(\mathbf{x})h(t)$ has the time dependence:

$$h(t) = 1 - e^{-\frac{t}{\lambda_2}} - \left[1 - e^{-\frac{(t-t_{\text{off}})}{\lambda_2}} \right] \theta(t - t_{\text{off}}), \quad (8)$$

where $\theta(t)$ is the Heaviside step function. We take σ_0 to be the stress resulting from two point forces located at $\mathbf{x} = \pm \mathbf{a}$ respectively with equal but opposite force strengths $\pm f_0$. The spatial part of the velocity field is then a sum of the two Stokeslets²⁸ corresponding to the two point forces:

$$\mathbf{v}_{\text{sto}}(\mathbf{x}, t) = \frac{1}{4\pi\eta_0} \left\{ f_0 \cdot (\mathbf{x} - \mathbf{a}) \frac{(\mathbf{x} - \mathbf{a})}{r_+^2} - f_0 \cdot (\mathbf{x} + \mathbf{a}) \frac{(\mathbf{x} + \mathbf{a})}{r_-^2} - f_0 \ln \left(\frac{r_+}{r_-} \right) \right\}, \quad (9)$$

where $r_{\pm} = |\mathbf{x} \mp \mathbf{a}|$ is the distance from the point force located at $\mathbf{x} = \pm \mathbf{a}$, respectively.

References

1. Friedl, P. & Gilmour, D. Collective cell migration in morphogenesis, regeneration and cancer. *Nature reviews. Molecular cell biology* **10**, 445–457, doi: 10.1038/nrm2720 (2009).
2. Deisboeck, T. S. *et al.* Pattern of self-organization in tumour systems: complex growth dynamics in a novel brain tumour spheroid model. *Cell Prolif* **34**, 115–134 (2001).

3. Deisboeck, T. S. & Couzin, I. D. Collective behavior in cancer cell populations. *Bioessays* **31**, 190–197, doi: 10.1002/bies.200800084 (2009).
4. Weinberg, R. *The Biology of Cancer, Second Edition*. (Garland Science, 2013).
5. Poujade, M. *et al.* Collective migration of an epithelial monolayer in response to a model wound. *Proceedings of the National Academy of Sciences of the United States of America* **104**, 15988–15993, doi: 10.1073/pnas.0705062104 (2007).
6. Rossen, N. S., Tarp, J. M., Mathiesen, J., Jensen, M. H. & Oddershede, L. B. Long-range ordered vorticity patterns in living tissue induced by cell division. *Nature Communications* **5**, 5720–5720, doi: 10.1038/ncomms6720 (2014).
7. Tambe, D. T. *et al.* Collective cell guidance by cooperative intercellular forces. *Nature Materials* **10**, 469–475, doi: 10.1038/nmat3025 (2011).
8. Kim, J. H. *et al.* Propulsion and navigation within the advancing monolayer sheet. *Nature Materials* **12**, 856–863, doi: 10.1038/nmat3689 (2013).
9. Serra-Picamal, X. *et al.* Mechanical waves during tissue expansion. *Nature Physics* **8**, 628–U666, doi: 10.1038/nphys2355 (2012).
10. Friedl, P. & Alexander, S. Cancer Invasion and the Microenvironment: Plasticity and Reciprocity. *Cell* **147**, 992–1009, doi: 10.1016/j.cell.2011.11.016. (2011).
11. Denais, C. M. *et al.* Nuclear envelope rupture and repair during cancer cell migration. *Science* **352**, 353–358 (2016).
12. Yang, S. Y., Zhang, J. J. L. & Huang, X. Y. Orai1 and STIM1 Are Critical for Breast Tumor Cell Migration and Metastasis. *Cancer Cell* **15**, 124–134, doi: 10.1016/j.ccr.2008.12.019 (2009).
13. Thielicke, W. & Stamhuis, E. J. PIVlab - Towards User-friendly, Affordable and Accurate Digital Particle Image Velocimetry in MATLAB. *Journal of Open Research Software* **2**, e30, doi: http://dx.doi.org/10.5334/jors.bl (2014).
14. Carey, S. P. *et al.* Comparative mechanisms of cancer cell migration through 3D matrix and physiological microtracks. *Am J Physiol Cell Physiol* **308**, C436–447, doi: 10.1152/ajpcell.00225.2014 (2015).
15. Mendoz, E. & Lim, C. T. Collective Migration Behaviors of Human Breast Cancer Cells in 2D. *Cellular and Molecular Bioengineering* **4**, 411–426, doi: 10.1007/s12195-011-0193-8 (2011).
16. Angelucci, C. *et al.* Stearoyl-CoA desaturase 1 and paracrine diffusible signals have a major role in the promotion of breast cancer cell migration induced by cancer-associated fibroblasts. *British Journal of Cancer* **112**, 1675–1686, doi: 10.1038/bjc.2015.135 (2015).
17. Gligorijevic, B., Bergman, A. & Condeelis, J. Multiparametric Classification Links Tumor Microenvironments with Tumor Cell Phenotype. *Plos Biology* **12**, doi: 10.1371/journal.pbio.1001995 (2014).
18. Tse, J. M. *et al.* Mechanical compression drives cancer cells toward invasive phenotype. *Proceedings of the National Academy of Sciences of the United States of America* **109**, 911–916, doi: 10.1073/pnas.1118910109 (2012).
19. Mas, J., Richardson, A. C., Reihani, S. N. S., Oddershede, L. B. & Berg-Sorensen, K. Quantitative determination of optical trapping strength and viscoelastic moduli inside living cells. *Physical Biology* **10**, doi: 10.1088/1478-3975/10/4/046006 (2013).
20. Forgacs, G., Foty, R. A., Shafirir, Y. & Steinberg, M. S. Viscoelastic properties of living embryonic tissues: a quantitative study. *Biophysical Journal* **74**, 2227–2234, doi: 10.1016/S0006-3495(98)77932-9 (1998).
21. Beysens, D. A., Forgacs, G. & Glazier, J. A. Cell sorting is analogous to phase ordering in fluids. *Proceedings of the National Academy of Sciences of the United States of America* **97**, 9467–9471, doi: 10.1073/pnas.97.17.9467 (2000).
22. Guevorkian, K., Colbert, M. J., Durth, M., Dufour, S. & Brochard-Wyart, F. Aspiration of Biological Viscoelastic Drops. *Physical Review Letters* **104**, doi: 10.1103/PhysRevLett.104.218101 (2010).
23. Spagnolie, S. E. *Complex Fluids in Biological Systems. Biological and Medical Physics, Biomedical Engineering*. (Springer New York, 2015).
24. Wensink, H. H. *et al.* Meso-scale turbulence in living fluids. *Proceedings of the National Academy of Sciences of the United States of America* **109**, 14308–14313, doi: 10.1073/pnas.1202032109 (2012).
25. Ranft, J. *et al.* Fluidization of tissues by cell division and apoptosis. *Proceedings of the National Academy of Sciences of the United States of America* **107**, 20863–20868, doi: 10.1073/pnas.1011086107 (2010).
26. McMahon, T. A. *Muscles, Reflexes, and Locomotion*. (Princeton University Press, 1984).
27. Tlili, S. *et al.* Colloquium: Mechanical formalisms for tissue dynamics (vol 38, 33, 2015). *European Physical Journal E* **38**, doi: 10.1140/epje/i2015-15033-4 (2015).
28. Cortez, R. The method of regularized Stokeslets. *Siam Journal on Scientific Computing* **23**, 1204–+, doi: 10.1137/S106482750038146X (2001).
29. Frixen, U. H. *et al.* E-cadherin-mediated cell-cell adhesion prevents invasiveness of human carcinoma cells. *J Cell Biol* **113**, 173–185 (1991).
30. Westcott, J. M. *et al.* An epigenetically distinct breast cancer cell subpopulation promotes collective invasion. *J Clin Invest* **125**, 1927–1943, doi: 10.1172/JCI77767 (2015).
31. Cheung, K. J., Gabrielson, E., Werb, Z. & Ewald, A. J. Collective invasion in breast cancer requires a conserved basal epithelial program. *Cell* **155**, 1639–1651, doi: 10.1016/j.cell.2013.11.029 (2013).
32. Macklin, P. *et al.* Multiscale modelling and nonlinear simulation of vascular tumour growth. *J Math Biol* **58**, 765–798 (2009).
33. Rejniak, K. A. An immersed boundary framework for modelling the growth of individual cells: an application to the early tumor development. *Journal of theoretical biology* **247**, 186–204, doi: 10.1016/j.jtbi.2007.02.019 (2007).
34. Eaves, G. The invasive growth of malignant tumours as a purely mechanical process. *J Pathol* **109**, 233–237, doi: 10.1002/path.1711090308 (1973).
35. Plodinec, M. *et al.* The nanomechanical signature of breast cancer. *Nat Nano* **7**, 757–765, doi: http://www.nature.com/nnano/journal/v7/n11/abs/nnano.2012.167.html#supplementary-information (2012).
36. Gordon, V. D. *et al.* Measuring the mechanical stress induced by an expanding multicellular tumor system: a case study. *Exp Cell Res* **289**, 58–66 (2003).
37. Aslakson, C. J. & Miller, F. R. Selective events in the metastatic process defined by analysis of the sequential dissemination of subpopulations of a mouse mammary tumor. *Cancer Res* **52**, 1399–1405 (1992).
38. Kaufman, L. J. *et al.* Glioma expansion in collagen I matrices: analyzing collagen concentration-dependent growth and motility patterns. *Biophys J* **89**, 635–650 (2005).
39. Wolf, K. *et al.* Physical limits of cell migration: control by ECM space and nuclear deformation and tuning by proteolysis and traction force. *J Cell Biol* **201**, 1069–1084, doi: 10.1083/jcb.201210152 (2013).
40. Lang, N. R. *et al.* Biphasic response of cell invasion to matrix stiffness in three-dimensional biopolymer networks. *Acta Biomater* **13**, 61–67, doi: 10.1016/j.actbio.2014.11.003 (2015).
41. Shebanova, O. & Hammer, D. A. Biochemical and mechanical extracellular matrix properties dictate mammary epithelial cell motility and assembly. *Biotechnol J* **7**, 397–408, doi: 10.1002/biot.201100188 (2012).
42. Cox, S. M. & Matthews, P. C. Exponential Time Differencing for Stiff Systems. *Journal of Computational Physics* **176**, 430–455, doi: 10.1006/jcph.2002.6995 (2002).

Acknowledgements

The authors acknowledge financial support from the Danish Research Council grant DFF-4002-00099, the Danish National Research Foundation grant DNR116, the Villum Foundation grant ‘Earth Patterns’, and from a Novo Nordisk Foundation Hallas Møller stipend. We thank H. Frost for proofreading.

Author Contributions

A.V.W., L.W., J.T.E. and L.B.O. designed the experimental study. A.V.W., N.L., and L.W. performed the experiments. A.C., J.T., and J.M. constructed the theoretical model. A.C. performed the simulations. L.B.O., J.T.E., and J.M. supervised the project. A.V.W., L.W., A.C., J.T.E., and L.B.O. wrote the paper. All authors agreed with the submitted version of the paper.

Additional Information

Supplementary information accompanies this paper at <http://www.nature.com/srep>

Competing Interests: The authors declare no competing financial interests.

How to cite this article: West, A.-K. V. *et al.* Dynamics of cancerous tissue correlates with invasiveness. *Sci. Rep.* 7, 43800; doi: 10.1038/srep43800 (2017).

Publisher's note: Springer Nature remains neutral with regard to jurisdictional claims in published maps and institutional affiliations.



This work is licensed under a Creative Commons Attribution 4.0 International License. The images or other third party material in this article are included in the article's Creative Commons license, unless indicated otherwise in the credit line; if the material is not included under the Creative Commons license, users will need to obtain permission from the license holder to reproduce the material. To view a copy of this license, visit <http://creativecommons.org/licenses/by/4.0/>

© The Author(s) 2017

C.2 Quantifying Cell Motility and Division Processes in Tissue by a Mechanical Continuum Model

Quantifying Cell Motility and Division Processes in Tissue by a Mechanical Continuum Model

Amalie Christensen¹, Ann-Katrine Vransø West¹, Lena Wullkopf², Janine Terra Erler², Lene Broeng Oddershede¹ and Joachim Mathiesen^{1*}

1 Niels Bohr Institute, University of Copenhagen, Copenhagen, Denmark

2 Biotech Research & Innovation Centre (BRIC), University of Copenhagen, Copenhagen, Denmark

* mathies@nbi.dk

Abstract

The collective dynamics of cells play a significant role in diverse biological processes such as wound healing, cancer metastasis and morphogenesis. It is becoming more and more clear that not only biochemical signaling but also mechanical forces and material properties are important factors in the development, coordination and collective motion of cells. Here, we present a mechanical model of living tissue, which accounts for cell motility, cell-cell interactions, cell-substrate interaction, and cell division. The model describes the velocity field of a cell monolayer and is tested on experimental data of endothelial and cancer cells. In particular, the model captures the exponential tails of the bulk speed distributions as well as the motion around cell division sites. Finally, our model quantifies measurable physical tissue parameters such as effective viscosity and forces between cells from simple recordings of the velocity field.

Author Summary

The collective motion of tissue cells is important during diverse processes such as wound closure, embryonic development and the invasion of healthy tissue by cancer cells. The cell interactions orchestrating the motion, however, are not easily measured and in many cases not well understood. To better understand the collective motion of cells, we propose a continuum-scale model, which takes into account the mechanical interaction between cell neighbors, the friction with the substrate and the self-propelling forces of the cells. The model is capable of describing the observed motion of several cell types.

Introduction

The collective motion of cells have been described by a broad range of models including particle based models, which consider (often point-like or undeformable) particles with various interactions [1–4], cellular Potts models [5–7], vertex models [8], phase field models [9], as well as continuum-scale models with cell polarization [10–16] and without cell polarization [17, 18]. Here, we will follow the latter class of models by treating the cells as a continuous monolayer, while borrowing the self-propelling forces often used in particle type models. The self-propelling force will in our approach take the shape of a structured noise term with a finite persistence time. Overall, the model will be formulated in terms of the velocity field of the tissue and will therefore be directly

1

2

3

4

5

6

7

8

9

10

comparable to experimentally acquired Particle-Image Velocimetry (PIV) data. Finally, an advantage of continuum-scale models is that analytical derivations often become more tractable than in particle based model. We use this to derive analytically the flow field and stresses in the tissue surrounding a cell-division.

Individual cells have been observed to behave viscoelastically in response to mechanical stimuli [19,20], i.e. on short time scales a cell deforms and relaxes elastically in response to a mechanical loading, whereas loads applied over a longer time will result in viscous flow and thus irreversible deformation. Several rheological models, using the viscous dashpot and the elastic spring as basic building blocks, have been employed to describe viscoelastic behavior of single cells [21]. The Maxwell fluid element (Fig 1A), consisting of a dashpot in *series* with a spring, and the Kelvin-Voigt solid element (Fig 1B), consisting of dashpot in *parallel* with a spring, are the simplest fluid and solid models from which most other rheological models are derived. Depending on the coupling of the basic building blocks, both fluid-like and solid-like behavior can be obtained. One prominent example of a rheological model is the standard linear solid, where the dashpot in the Kelvin-Voigt element is coupled in series with a spring. When subjected to a sudden strain, the stress in the standard linear solid model decays exponentially towards a constant non-zero value.

On length scales beyond individual cells, tissues are also observed to behave viscoelastic [22]. Based on stress relaxation experiments on freely suspended cell monolayers, Harris et al. [23] used the standard linear solid model to estimate an apparent viscosity for Madine-Darby Canine Kidney cell monolayers. Guevorkian et al. [24] obtained an apparent viscosity for murin sarcoma cell aggregates using a micropipette aspiration technique and the standard linear solid model in series with a dashpot. Forgacs et al. [25] performed parallel plate compression experiments on chicken cell aggregates and estimated the viscosity using a rheological model of two parallel coupled Maxwell fluid elements. Also the viscosity of breast cancer tumors has been measured using ultrasonic shear-wave imaging experiments combined with a Maxwell model [26].

Results

Continuum model of collective motion

We consider tissue comprised of motile cells, which on time scales longer than approximately the cell size ($\sim 20 \mu\text{m}$) divided by the typical cell speed ($\sim 1 \mu\text{m}/\text{min}$), experiences irreversible deformation. We are interested in modeling the behavior of a tissue over the course of hours and due to the irreversible deformation present at this time scale, we will consider the tissue as a viscoelastic fluid. One of the simplest models describing a viscoelastic fluid is the Oldroyd-B model [27], which is often thought of as the result of dissolving a Maxwell fluid of viscosity η_1 and shear modulus G in a Newtonian fluid of viscosity η_2 (Fig 1C). Defining the total viscosity $\eta_0 = \eta_1 + \eta_2$, the relaxation time $\lambda_1 = \eta_1/G$ and the retardation time $\lambda_2 = (\eta_2/\eta_0)\lambda_1$, the Oldroyd-B constitutive relation is:

$$\sigma + \lambda_1 \overset{\nabla}{\sigma} = 2\eta_0 \left(\gamma + \lambda_2 \overset{\nabla}{\gamma} \right), \quad (1)$$

where $\overset{\nabla}{\sigma}$ and $\overset{\nabla}{\gamma}$ are the upper convected derivatives of the deviatoric stress tensor σ and the strain rate tensor $\gamma = \frac{1}{2}(\nabla\mathbf{v} + (\nabla\mathbf{v})^T)$ respectively and \mathbf{v} is the local mean velocity. The upper convected derivative ensures objectivity of the constitutive relation and corresponds to the rate of change of γ or σ in a small fluid volume stretching with the flow.

Experiments measuring the stress relaxation of tissue after a sudden compression, have found the stress to relax exponentially with one or two characteristic time scales depending on the initial loading strain rate [23, 25]. The Oldroyd-B model only captures exponential stress relaxation with a single characteristic time scale λ_1 under the same experimental conditions. More rheological elements could have been added to account for the second stress relaxation time scale observed in experiments, but aiming at simplicity, we have chosen not to.

Fig 1. Rheological diagrams. Details on the relation between constitutive equations and the rheological diagrams are given in Methods. (A) *Maxwell fluid*. Under sudden stress, the spring of elastic modulus E deforms instantaneously whereas the dashpot deforms at a constant rate like a fluid of viscosity η . When the Maxwell element is released, the spring regains its original length, but irreversible deformation has happened due to the dashpot. (B) *Kelvin-Voigt solid*. Under sudden stress, the Kelvin-Voigt solid deforms with a characteristic time scale η/G . The deformation is reversible and when released, the Kelvin-Voigt solid regains its original shape. (C) *Oldroyd-B fluid*. When subjected to a sudden strain ϵ_0 , the stress decays exponentially with a timescale η_1/G towards zero.

Dynamics

We consider a confluent monolayer of cells residing on a substrate. The tissue is taken to be incompressible, such that the divergence of the local mean velocity vanishes $\nabla \cdot \mathbf{v} = 0$, and the projected area of each cell is conserved. Frictional forces completely dominate inertia for tissue dynamics, and the momentum balance equation is therefore modeled as:

$$0 = -\frac{1}{\rho}\nabla p + \frac{1}{\rho}\nabla \cdot \sigma - \alpha\hat{\mathbf{v}} + \mathbf{m}, \quad (2)$$

where ρ is the mean density, p is pressure, σ is the deviatoric stress tensor, $-\alpha\hat{\mathbf{v}}$ is a friction term with $\hat{\mathbf{v}} = \mathbf{v}/|\mathbf{v}|$ being the velocity direction and \mathbf{m} accounts for the cell motility.

Friction

The friction term $-\alpha\hat{\mathbf{v}}$ in Eq (2) models the dissipative processes between cells and substrate and is inspired by dry kinetic Coulomb friction between two solid objects. Coulomb friction does not depend on speed, only on the velocity direction $\hat{\mathbf{v}}$ and the constant friction coefficient α .

From a microscopic point of view, the friction force can be motivated by considering a single cell of area A_c which adheres to the substrate with N_c contacts. The average contact density is $n_c = N_c/A_c$ and we assume that new contacts are established as the cell moves, such that the contact density stays constant. Taking the energy cost of breaking or establishing contacts to be constant, the energy spent as the cell moves is only dependent on the distance traveled, not on the speed at which the cell moved. The cell therefore experiences an opposing force of constant magnitude. As the friction acts against any motion breaking adhesion contacts, we expect the friction force to point in the opposite direction of the velocity.

The friction term $-\alpha\hat{\mathbf{v}}$ can also be motivated from the experimental observation that the cell layers show speed distributions with exponential tails (Fig 2A). If the cell motion had been a pure Ornstein-Uhlenbeck process with a linear damping term proportional to $-\mathbf{v}$:

$$\frac{d\mathbf{v}}{dt} = -\frac{1}{\lambda_v}\mathbf{v} + \boldsymbol{\xi}(t), \quad (3)$$

where $\boldsymbol{\xi}$ is a white Gaussian noise field of strength $\langle \xi_i(t)\xi_j(t') \rangle = \omega_v \delta(t-t')\delta_{ij}$, then the resulting stationary probability density for the speed v would have a Gaussian tail:

$$P(v) = \frac{2v}{\lambda_v \omega_v} \exp\left(-\frac{v^2}{\lambda_v \omega_v}\right). \quad (4)$$

Let us instead consider a generic version of Eq (3) with a different damping term:

$$\frac{d\mathbf{v}}{dt} = -\boldsymbol{\psi}(\mathbf{v}) + \boldsymbol{\xi}(t). \quad (5)$$

Demanding that the process in Eq (5) should result in a stationary probability distribution with an exponential tail:

$$P(v) = \frac{v}{a^2} \exp\left(-\frac{v}{a}\right), \quad (6)$$

where a is some constant, then the stationary Fokker-Planck equation takes the form:

$$[\psi_x \hat{v}_x + \psi_y \hat{v}_y] - a \left[\frac{\partial \psi_x}{\partial v_x} + \frac{\partial \psi_y}{\partial v_y} \right] = \omega_v \left[\frac{1}{a} - \frac{1}{v} \right], \quad (7)$$

where subscripts denote x or y -components. The simplest choice of $\boldsymbol{\psi}(\mathbf{v})$ fulfilling Eq (7) is given by $\boldsymbol{\psi}(\mathbf{v}) = (\omega_v/a)\hat{\mathbf{v}}$ where $\hat{\mathbf{v}} = \mathbf{v}/|\mathbf{v}|$ is the velocity direction.

The friction term linear in the velocity, has commonly been used in the literature on tissue dynamics [1, 10, 17, 18, 28, 29]. Such a term resembles the drag of a viscous fluid flowing over a solid surface for low Reynolds numbers. In the proposed model, we do treat the cells as a viscoelastic fluid, but we do not stretch the fluid analogy to also describe the cell-substrate interaction and we therefore use the friction term proportional to the velocity direction.

Motility

Non-interacting motile cells perform persistent random motion, where the velocity \mathbf{v} changes on a characteristic time scale λ_m [30, 31]. This persistent random motion is frequently modeled as an Ornstein-Uhlenbeck process, which produces an exponentially decaying temporal velocity autocorrelation [32]. We will employ a motility model closely related to the Ornstein-Uhlenbeck process:

$$\frac{\partial \mathbf{m}}{\partial t} + (\mathbf{v} \cdot \nabla)\mathbf{m} = -\frac{1}{\lambda_m}\mathbf{m} + \boldsymbol{\phi}(\mathbf{x}, t), \quad (8)$$

where $\mathbf{m}(\mathbf{x}, t)$ is the local forcing accounting for cell motility, λ_m is the persistence time and $\boldsymbol{\phi}$ is filtered white Gaussian noise. In a pure Ornstein-Uhlenbeck process, $\boldsymbol{\phi}$ is white Gaussian noise. However, as each cell is a coherent body moving at a single velocity, there is a minimum length scale - similar to the cell size - below which the velocity field is constant. We therefore impose a length scale ℓ_m on the random forcing by filtering a white Gaussian noise field $\boldsymbol{\xi}$ with a Gaussian function of width ℓ_m and zero mean to obtain the filtered noise field $\boldsymbol{\phi}(\mathbf{x}, t)$:

$$\boldsymbol{\phi}(\mathbf{x}, t) = \frac{1}{2\pi\ell_m^2} \int \boldsymbol{\xi}(\mathbf{x}', t) \exp\left(-\frac{|\mathbf{x} - \mathbf{x}'|^2}{2\ell_m^2}\right) d\mathbf{x}'. \quad (9)$$

The strength of the white Gaussian noise field was taken to be $\langle \xi_i(\mathbf{x}, t)\xi_j(\mathbf{x}', t') \rangle = \beta_m \delta^{(2)}(\mathbf{x} - \mathbf{x}')\delta(t-t')\delta_{ij}$ where the indices i, j run over the spatial directions x, y . The filtered noise field has an exponentially decaying spatial correlation:

$$\langle \phi_i(\mathbf{x}, t)\phi_j(\mathbf{x}', t') \rangle = \frac{\beta_m}{4\pi\ell_m^2} \exp\left(-\frac{|\mathbf{x} - \mathbf{x}'|^2}{4\ell_m^2}\right) \delta(t-t')\delta_{ij}. \quad (10)$$

The model captures statistical characteristics of experimental data

The velocity field of bulk motion in epithelial and endothelial tissue experiments as reported in [?, 14] allows for quantification of statistical characteristics such as the speed distribution $P(v)$, the spatial velocity correlation function $C_{vv}(r)$ and the temporal velocity correlation function $C_{vv}(t)$. These three fingerprints of tissue dynamics can be compared quantitatively to the proposed model (Fig 2).

The model described by Eq (1-9) and the incompressibility condition has seven parameters listed in Table 1. Since the main constituent of biological tissue is water, the density ρ will not be considered a parameter of the model. The model was simulated numerically in the limit of small deformations where the upper-convected derivative can be replaced by a partial time derivative using a pseudo-spectral method on a 2D periodic domain (see Methods). The model was fitted to the experiments by performing a parameter grid search and choosing the parameters resulting in the smallest chi-squared between the experimental and simulated statistical characteristics $P(v)$, $C_{vv}(r)$ and $C_{vv}(t)$. An example of a simulated velocity field is shown in Fig 3.

Table 1. Model parameters.

Symbol	Units	Description
λ_1	time	Relaxation time
λ_2	time	Retardation time
λ_m	time	Motility persistence time
ℓ_m	length	Motility length scale
β_m	length ⁴ /time ²	Motility noise strength
η_0	mass/(length·time)	Total viscosity
α	length/time ²	Friction coefficient

Exponential tail of the speed distribution

The model successfully reproduces the spatial and temporal velocity correlations and it captures the exponentially decaying tail of the speed distribution (Fig 2A). A similar exponential tail has been observed for dilute suspensions of the MDA-MB-231 cell line [33], and non-Gaussian tails have been observed experimentally for other types of tissue [30, 31, 34].

Correlation functions

The proposed model accurately reproduces the temporal correlation observed in the experiments (Fig 2C). It also captures the characteristic length scale of the spatial velocity correlation but shows a negative dip, which signals the presence of vortices, which are absent in the data (Fig 2B).

Numerical simulations of the model with the friction term $-\alpha\hat{v}$ replaced by a drag term $-\alpha\mathbf{v}$ revealed, that the correlation functions are almost identical in the case of friction and the case of drag. The choice of a drag or friction term thus mainly affects the speed distribution. The velocity correlation functions can be calculated analytically when advection of the noise field is neglected and when a drag term is used instead of a friction term (S1 Appendix). The resulting analytical correlation functions are displayed as black lines in Fig 2 and closely resembles the simulations. The negative dip of the spatial velocity correlation functions is not present in the analytical correlation function, and is thus a result of the advection and the friction term.

Fig 2. Statistical characteristics are well described by the model.

Experimentally measured statistical characteristics are plotted as solid colored lines, whereas statistical characteristics of the model fits are displayed as dashed lines. Speed, distance and time are rescaled by the mean speed v_0 , the spatial correlation length ℓ_0 and the time scale ℓ_0/v_0 respectively. (A) The exponential tails of the speed distributions are captured by the model. We note, that the experimental and simulated speed distributions are very different from the result of an Ornstein-Uhlenbeck process (full black line), which results in a Gaussian tail. (B) The spatial correlation function of the model shows a negative dip which is not present in the data, but otherwise matches the experiments. The analytical correlation functions in the case of a drag term (S1 Appendix) are displayed as black solid lines and closely resemble the simulations. (C) The temporal correlation functions are closely matched by the model.

Fig 3. Bulk velocity fields. (A) *Experiment.* Human MCF7 cells during bulk motion. (B) *Simulation.* Velocity field of a simulation, where the speed distribution $P(v)$, the temporal velocity correlation $C_{vv}(t)$ and the spatial velocity correlation $C_{vv}(r)$ have been fitted to the experimentally measured data of the MCF7 cells.

Mechanical forces during cell division

The flow fields generated by the proposed model are the result of an interplay between the energy injection caused by the intrinsic cell motility and the dissipative processes of the cell-cell and cell-substrate interactions. Another source of energy injection is cell divisions, which have not been included in the model, since the effect on the bulk flow was found to be negligible in the considered experiments. However, cell division can play a role in tissues where division events are more frequent.

A single cell exerts forces on the surrounding tissue and generates flow as it divides. The flow fingerprint of such a single cell division can be found analytically within the proposed model. Since we are only interested in the effect of the cell division, motility is neglected in the momentum balance equation. Experimentally, this condition can be obtained by aligning a number of cell division flow fields along the division direction and taking the average. Also friction is discarded, as the friction force should be small compared to the forces exerted by the dividing cell in order of cell division to be feasible. In absence of motility and friction, the momentum balance Eq (2) reduces to:

$$\nabla p = \nabla \cdot \sigma. \quad (11)$$

We incorporate the forces caused by the division process by adding an active stress term σ_0 inspired by [12, 35, 36] in parallel with the viscous dashpot representing the cells in the Oldroyd-B model (see Methods, Fig 6). The resulting constitutive relation in the limit of small deformation is:

$$\sigma + \lambda_1 \frac{\partial \sigma}{\partial t} = 2\eta_0 \left(\gamma + \lambda_2 \frac{\partial \gamma}{\partial t} \right) + \sigma_0, \quad (12)$$

where the active stress $\sigma_0(\mathbf{x}, t) = c(t)g(\mathbf{x})$ is a simple function of space and time. We take the active stress to have a simple square pulse time dependence describing the onset ($t = 0$) and finalization ($t = t_{\text{off}}$) of the division process:

$$c(t) = \theta(t) - \theta(t - t_{\text{off}}), \quad (13)$$

where $\theta(t)$ is the Heaviside step function. We assume that a dividing cell located at $\mathbf{x} = 0$ during division exerts two equal but opposite point forces $\pm \mathbf{f}_0$ on its environment. The point forces are separated by a distance $2a$ and located at $\mathbf{x} = \pm \mathbf{a}$ respectively, such that:

$$\nabla \cdot g(\mathbf{x}) = \mathbf{f}_0 \left[\delta^{(2)}(\mathbf{x} - \mathbf{a}) - \delta^{(2)}(\mathbf{x} + \mathbf{a}) \right]. \quad (14)$$

The separation $2a$ is taken to be smaller than the cell scale. Laplace transforming Eq (12) and substituting into the Laplace transformed Eq (11) yields:

$$\nabla \tilde{p}(\mathbf{x}, s) = \frac{(1 + \lambda_2 s)}{(1 + \lambda_1 s)} \eta_0 \nabla^2 \tilde{\mathbf{v}}(\mathbf{x}, s) + \frac{\tilde{c}(s)}{(1 + \lambda_1 s)} \nabla \cdot g(\mathbf{x}), \quad (15)$$

where tilde denotes a Laplace transformed function and s is the transform variable. Eq (15) describes a Stokes flow in space driven by two point forces, which can be made clear by defining a time dependent viscosity $\tilde{\eta}(s) = \eta_0(1 + \lambda_2 s)/(1 + \lambda_1 s)$ and forcing $\tilde{d}(s) = \tilde{c}(s)/(1 + \lambda_1 s)$ such that Eq (15) takes the form:

$$\nabla \tilde{p}(\mathbf{x}, s) = \tilde{\eta}(s) \nabla^2 \tilde{\mathbf{v}}(\mathbf{x}, s) + \tilde{d}(s) \mathbf{f}_0 \left[\delta^{(2)}(\mathbf{x} - \mathbf{a}) - \delta^{(2)}(\mathbf{x} + \mathbf{a}) \right]. \quad (16)$$

The solution to the two dimensional Stokes equation driven by a point force is well known [37], and for the force dipole in Eq (16) we obtain:

$$\tilde{\mathbf{v}}(\mathbf{x}, s) = \frac{\tilde{d}(s)}{\tilde{\eta}(s)} \frac{1}{4\pi} \left\{ [\mathbf{f}_0 \cdot (\mathbf{x} - \mathbf{a})] \frac{(\mathbf{x} - \mathbf{a})}{r_+^2} - [\mathbf{f}_0 \cdot (\mathbf{x} + \mathbf{a})] \frac{(\mathbf{x} + \mathbf{a})}{r_-^2} - \mathbf{f}_0 \ln \left(\frac{r_+}{r_-} \right) \right\} \quad (17)$$

$$= \frac{\tilde{d}(s)}{\tilde{\eta}(s)} \mathbf{v}_{\text{sto}}(\mathbf{x}). \quad (18)$$

The time dependence can be found by transforming $\tilde{h}(s) = \tilde{d}(s)/\tilde{\eta}(s)$ to the time domain: 189

$$h(t) = 1 - e^{-t/\lambda_2} - \left[1 - e^{-(t-t_{\text{off}})/\lambda_2}\right]\theta(t - t_{\text{off}}). \quad (19) \quad 190$$

So the velocity field resulting from a single cell division: 191

$$\mathbf{v}(\mathbf{x}, t) = \mathbf{v}_{\text{sto}}(\mathbf{x}) h(t), \quad (20) \quad 192$$

is simply a Stokesflow in space $\mathbf{v}_{\text{sto}}(\mathbf{x})$ given by Eq (17-18) multiplied by a time-dependent function $h(t)$ given by Eq (19). The time dependence in Eq (19) is intimately related to the rheological model. If the tissue for instance had been treated as a pure Maxwell fluid instead of an Oldroyd-B fluid, then the time dependence would have been completely governed by the active stress time dependence $c(t)$ in Eq (13). 193
194
195
196

A flow field resembling that of a force dipole flow was also observed and modeled in dividing Madin-Darby canine kidney cells [13]. The time dependence of the division induced flow field was however not reported. 197
198
199

Extracting forces at play from experimental flow fields 200

Eq (20) relates the velocity field during division to the forces exerted by the dividing cell on its environment. Given an experimentally observed flow field, Eq (20) can be used to estimate the forces at play. 201
202
203

For each breast cancer cell type, at least 30 individual experimental cell division time series were centered, aligned and overlaid (see Methods). The resulting time series of the averaged velocity field (Fig 4) show the fingerprint of a cell division with the effect of motility averaged out. We fitted the velocity field in Eq (20) to the averaged experimental velocity fields and obtained good agreement between the time dependence in Eq (19) and the experimental velocity fields (Fig 4,5). The fitted values of the point force strength f_0 and the retardation time λ_2 are listed in Table 4. 204
205
206
207
208
209
210

Fig 4. Averaged velocity field during division. The experimental velocity component fields are obtained as an average over 30 individual division events for the MCF7 cell line. Time zero is defined as the onset of cytokinesis, i.e., the first image where two distinct daughter cells are visible. The model prediction in Eq (20) was fitted to the experimental data and the model captures the spatial structure and the temporal evolution of the velocity field well. The depicted domains are $200 \times 200 \mu\text{m}$.

Fig 5. Averaged normalized velocity field during division in the center region. The velocity field components $\langle v_x(\mathbf{x}, t) \rangle$ and $\langle v_y(\mathbf{x}, t) \rangle$, which resulted from an average over at least 30 experiments, were normalized at each spatial point with the local maximal occurring velocity component $\langle v_{x,\text{max}}(\mathbf{x}) \rangle$ and $\langle v_{y,\text{max}}(\mathbf{x}) \rangle$ respectively. The figure shows the mean evolution of the normalized velocity components close to the cell division center during the division process. The observed velocity evolution is qualitatively well captured by the analytically calculated model time dependence function $h(t)$ in Eq (19). The shading indicates the standard deviation of the mean evolution.

Discussion

211

A large number of models have been employed to describe various aspects of collective tissue motion, but few allowed for quantification of mechanical quantities such as forces and stresses. In this paper, we developed a continuum model for tissue, which successfully captured the statistical characteristics of bulk tissue velocity fields for a range of epithelial and endothelial cell types and provided a natural framework for assessing stresses and forces in the tissue. Furthermore, the proposed model allowed for an analytical solution of the velocity field induced by a single cell division, and the possibility to extract physical parameters such as retardation and relaxation times as well as the cell division force.

212
213
214
215
216
217
218
219
220

The proposed model differs from many previous works in the inclusion of the Coulomb like cell-substrate friction term. Existing continuum and particle models of collective tissue motion frequently include a drag term linear in the velocity field to describe dissipation caused by cell-substrate adhesion contacts being broken [1, 10, 17, 18, 28, 29]. To our knowledge, little is known about the cell-substrate dissipation process on the tissue scale, and it could be interesting to obtain firmer experimental knowledge on the appropriateness of either a linear drag or a Coulomb type friction. We note, that the Coulomb type friction term is responsible for the model being able to produce a speed distribution with an exponential tail, but a speed distribution with a Gaussian tail as observed experimentally in [1] is also possible within the parameter space of the model.

221
222
223
224
225
226
227
228
229
230
231

The self-propulsion of cells in the proposed model incorporates a length scale and a persistence time of the local motility force field, which accounts for the finite extend of a single cell and for the tendency of a single cell to change its velocity on a certain time scale. Several papers have used related but more elaborate approaches, where the motility force field evolves in time due to some specified dynamics. Basan et al. [38] proposed that the local motility force tends to align with the tissue velocity and combined with an assumption of cell locomotion being suppressed by neighbors, Zimmermann et al. [39] were able to model the traction patterns observed experimentally in spreading epithelial tissue [40, 41]. Other authors have envisioned the polarization field as a two-dimensional nematic liquid crystal [10, 13, 29], which allows for complex flow patterns with vortices and jets. In contrast to these existing models, the proposed motility evolution contains no assumptions of velocity-motility alignment or nematic behavior.

232
233
234
235
236
237
238
239
240
241
242
243
244

Including a motility force explicitly, as done in this paper, has the advantage that the local velocity need not be aligned with the local motility force. This behavior has been observed in an expanding monolayer, where the velocity and the local motility (traction) force under certain circumstances were anti parallel [41]. A natural next step is therefore to incorporate tissue boundaries in the proposed model, such that monolayer expansion and the generated tractions can be studied. This would also allow the model to be compared with and used to study the classical scratch-wound assay experiment [42–44], the observed fingering of tissue edges [44, 45] and the propagation of strain rate waves in spreading tissue [46].

245
246
247
248
249
250
251
252
253

Materials and Methods

Constitutive relations resulting from rheological diagrams

As an illustration of the relationship between constitutive equations and rheological diagrams, consider the rheological diagram for the active Oldroyd-B fluid in Figure 6. The total stress and strain are:

$$\sigma = \sigma_a + \sigma_b \quad \epsilon = \epsilon_a + \epsilon_b \quad (21)$$

where:

$$\sigma_a = G\epsilon_a = \eta_1 \frac{\partial \epsilon_b}{\partial t} + \sigma_0 \quad \sigma_b = \eta_2 \frac{\partial \epsilon}{\partial t}. \quad (22)$$

We wish to eliminate all references to part a and b and only work with the total stress σ and strain ϵ :

$$\sigma = \eta_1 \frac{\partial \epsilon_b}{\partial t} + \eta_2 \frac{\partial \epsilon}{\partial t} + \sigma_0 = -\eta_1 \frac{\partial \epsilon_a}{\partial t} + \eta_0 \frac{\partial \epsilon}{\partial t} + \sigma_0 = -\frac{\eta_1}{G} \frac{\partial \sigma_a}{\partial t} + \eta_0 \frac{\partial \epsilon}{\partial t} + \sigma_0. \quad (23)$$

Resulting in:

$$\sigma + \frac{\eta_1}{G} \frac{\partial \sigma}{\partial t} = \eta_2 \frac{\eta_1}{G} \frac{\partial^2 \epsilon}{\partial t^2} + \eta_0 \frac{\partial \epsilon}{\partial t} + \sigma_0 \quad (24)$$

Identifying $\gamma = \partial \epsilon / \partial t$ and using the definitions $\lambda_1 = \eta_1 / G$ and $\lambda_2 = (\eta_2 / \eta_0) \lambda_1$, we obtain Eq (12) of the main text. A similar approach relates the other rheological diagrams of Fig 1 to constitutive equations.

Fig 6. Rheological diagram for the Oldroyd-B fluid when division processes are included. The active stress σ_0 models the force exerted by dividing cells and is a simple function of time and space. Stresses in parallel add up, the same is true for strains in series.

Cell cultures and experiments

The data presented here have previously been published in references [?, 14]. The experiments, the cell culturing methods and the data analysis are described in detail in these two references.

In short, the part of the experiments concerning cell division were performed using two invasive breast cancer cell lines, the murine 4T1 and the human MDA-MB-231 cells, and two non-invasive breast cancer cell lines, the murine 67NR and the human MCF7 [?]. The cells were seeded in multi-well plates and were allowed to settle for ~ 24 hours in appropriate media to create a confluent monolayer. The monolayer was imaged in phase-contrast microscopy for a duration of 6 to 12 hours acquiring an image every 2 minutes. The sequences of images were analyzed by Particle Image Velocimetry (PIV) [47] which returned the velocity fields of the monolayer.

Also, we here describe data from experiments performed on human umbilical vein endothelial cells (HUVEC) [14]. These cells were seeded in collagen IV coated dishes and cultured for 3 days in a CO_2 atmosphere and with relevant media which was exchanged every 24 hours. For the endothelial tissue, images were acquired every 10th minute and the images were analyzed by the PIV routines to return the velocity fields.

The mean speed and velocity correlation length observed in bulk motion experiments are listed in Table 2.

Table 2. Measured characteristics of experimental velocity fields in bulk experiments.

Cell line	Mean speed v_0	Correlation length ℓ_0
4T1	$(0.27 \pm 0.06) \mu\text{m}/\text{min}$	$(25.8 \pm 0.9) \mu\text{m}$
67NR	$(0.13 \pm 0.03) \mu\text{m}/\text{min}$	$(26.5 \pm 1.1) \mu\text{m}$
MCF7	$(0.23 \pm 0.02) \mu\text{m}/\text{min}$	$(19.6 \pm 0.7) \mu\text{m}$
MDA-MB-231	$(0.7 \pm 0.2) \mu\text{m}/\text{min}$	$(13.7 \pm 0.4) \mu\text{m}$
HUVEC	$(0.5 \pm 0.1) \mu\text{m}/\text{min}$	$(28.0 \pm 0.1) \mu\text{m}$

The correlation length ℓ_0 was found by fitting a single exponential $C_{vv}(r) = e^{-r/\ell_0}$ to the spatial correlation functions displayed in Fig 2.

The limit of small deformations

For the considered cell types, the upper convected derivative can be approximated by a partial time derivative. To see this, consider the upper convected derivative of a tensor ψ is defined as:

$$\overset{\nabla}{\psi} = \frac{\partial \psi}{\partial t} + (\mathbf{v} \cdot \nabla) \psi - [\psi \cdot (\nabla \mathbf{v}) + (\nabla \mathbf{v})^T \cdot \psi] \quad (25)$$

Defining a characteristic time t_ψ on which ψ changes, a characteristic flow velocity U_v and length scale L_v , the upper convected derivative can be cast in dimensionless form:

$$\overset{\nabla}{\psi} = \frac{\partial \psi}{\partial t} + \frac{t_\psi U_v}{L_v} \left\{ (\mathbf{v} \cdot \nabla) \psi - [\psi \cdot (\nabla \mathbf{v}) + (\nabla \mathbf{v})^T \cdot \psi] \right\} \quad (26)$$

In the limit of small velocity gradients U_v/L_v compared to the characteristic time t_ψ , the quantity $(t_\psi U_v/L_v)$ is small and the upper convected derivative reduces to a partial derivative with respect to time. The cell lines considered have a characteristic flow velocity $U_v \sim 1 \mu\text{m}/\text{min}$ and a characteristic size of $L_v \sim 20 \mu\text{m}$ (Table 2). The characteristic viscoelastic time can be estimated as the retardation time $t_\psi \sim \lambda_2$ obtained from the cell division process (Table 4), such that the deformation is small $(t_\psi U_v/L_v) \sim 0.05$ and the upper convected derivative can be replaced by a partial time derivative.

Numerical simulations

The dynamics of the bulk velocity field described by Eq (1-9) and the incompressibility condition was simulated numerically using a pseudo-spectral method on a 2D box with periodic boundaries. Fourier- and inverse Fourier transforms were performed using the Fast Fourier Transform algorithm, and non-linear terms were evaluated in real space. Time integration of the stress tensor and the noise term was performed using an exponential time differencing scheme [48]. In each time step, the velocity field and the pressure was found by a relaxation procedure.

The periodic 2D domain consisted of 256×256 grid points corresponding to a box of length $\sim 200 \mu\text{m}$ in physical units. The time step was ~ 0.01 min in physical units.

Model parameters

The viscosity η_0 , along with the density ρ , a characteristic velocity U and a characteristic length L were used to non-dimensionalize the equations and η_0, ρ were thus not subjected to fitting. The dimensionless simulation parameters were converted

to parameters with physical units for each cell type by identifying the simulation mean speed v_0 with the experimental mean speed and the simulation velocity correlation length ℓ_0 with the experimental velocity correlation length.

The speed distribution $P(v)$, the spatial velocity correlation function $C_{vv}(r)$ and the temporal velocity correlation function $C_{vv}(t)$ were calculated for both experiments and simulations. The model was fitted to an experiment, by minimizing the chi squared of $P(v)$, $C_{vv}(r)$, $C_{vv}(t)$ between simulation and experiment. The set of parameters obtained for each cell type is listed in Table 3.

Table 3. Fitted parameters for bulk cell motion.

Cell type	λ_1 (min)	λ_2 (min)	λ_m (min)	ℓ_m (μm)	$\alpha (\rho/\eta_0)$ ($\mu\text{m}\cdot\text{min}$) ⁻¹	$\beta_m (\rho/\eta_0)^2$ (min) ⁻³
4T1	1.6	0.4	7.8	10	0.002	0.003
67NR	2.9	0.7	7.1	12	0.001	0.001
MCF7	1.2	0.3	3.0	9	0.003	0.010
MDA-MB-231	2.2	0.2	4.3	7	0.015	0.125
HUVEC	1.6	0.4	7.8	10	0.002	0.003

Table 4. Fitted parameters for cell division processes.

Cell line	Force/viscosity f_0/η_0	Retardation time λ_2
4T1	(4.6 ± 0.4) $\mu\text{m}/\text{min}$	(1.8 ± 0.3) min
67NR	(2.6 ± 0.4) $\mu\text{m}/\text{min}$	(1.3 ± 0.5) min
MCF7	(2.9 ± 0.4) $\mu\text{m}/\text{min}$	(2.1 ± 0.6) min
MDA-MB-231	(4.3 ± 0.4) $\mu\text{m}/\text{min}$	(1.9 ± 0.3) min

Supporting Information

S1 Appendix. Analytical calculation of velocity correlation functions.

When the non-linear friction term $-\alpha\hat{v}$ in the model is replaced by a linear drag term $-\alpha v$ and advection of the motility term is neglected, then the velocity correlation functions can be calculated analytically. The velocity correlation functions are almost identical in the case of drag and friction.

Acknowledgments

The authors acknowledge financial support from the Danish Research Council DFF-4002-00099, from the Danish National Research Foundation DNRF116 and from the Villum Foundation grant Earth Patterns.

References

1. Sepúlveda N, Petitjean L, Cochet O, Grasland-Mongrain E, Silberzan P, Hakim V. Collective Cell Motion in an Epithelial Sheet Can Be Quantitatively Described by a Stochastic Interacting Particle Model. *PLOS Comput Biol.* 2013;9(3):e1002944. doi:10.1371/journal.pcbi.1002944.
2. Arboleda-Estudillo Y, Krieg M, Stühmer J, Licata NA, Muller DJ, Heisenberg CP. Movement Directionality in Collective Migration of Germ Layer Progenitors. *Current Biology.* 2010;20(2):161–169. doi:10.1016/j.cub.2009.11.036.

-
3. Szabó B, Szöllösi GJ, Gönci B, Jurányi Z, Selmeczi D, Vicsek T. Phase transition in the collective migration of tissue cells: Experiment and model. *Physical Review E*. 2006;74(6):061908. doi:10.1103/PhysRevE.74.061908.
 4. Méhes E, Vicsek T. Collective motion of cells: from experiments to models. *Integr Biol*. 2014;6(9):831–854. doi:10.1039/C4IB00115J.
 5. Graner F, Glazier JA. Simulation of biological cell sorting using a two-dimensional extended Potts model. *Physical Review Letters*. 1992;69(13):2013–2016. doi:10.1103/PhysRevLett.69.2013.
 6. Szabó A, Ünneper R, Méhes E, Twal WO, Argraves WS, Cao Y, et al. Collective cell motion in endothelial monolayers. *Physical Biology*. 2010;7(4):046007. doi:10.1088/1478-3975/7/4/046007.
 7. Albert PJ, Schwarz US. Dynamics of Cell Ensembles on Adhesive Micropatterns: Bridging the Gap between Single Cell Spreading and Collective Cell Migration. *PLOS Comput Biol*. 2016;12(4):e1004863. doi:10.1371/journal.pcbi.1004863.
 8. Farhadifar R, Röper JC, Aigouy B, Eaton S, Jülicher F. The Influence of Cell Mechanics, Cell-Cell Interactions, and Proliferation on Epithelial Packing. *Current Biology*. 2007;17(24):2095–2104. doi:10.1016/j.cub.2007.11.049.
 9. Aland S, Hatzikirou H, Lowengrub J, Voigt A. A Mechanistic Collective Cell Model for Epithelial Colony Growth and Contact Inhibition. *Biophysical Journal*. 2015;109(7):1347–1357. doi:10.1016/j.bpj.2015.08.003.
 10. Lee P, Wolgemuth CW. Crawling Cells Can Close Wounds without Purse Strings or Signaling. *PLOS Comput Biol*. 2011;7(3):e1002007. doi:10.1371/journal.pcbi.1002007.
 11. Bittig T, Wartlick O, Kicheva A, González-Gaitán M, Jülicher F. Dynamics of anisotropic tissue growth. *New Journal of Physics*. 2008;10(6):063001. doi:10.1088/1367-2630/10/6/063001.
 12. Ranft J, Basan M, Elgeti J, Joanny JF, Prost J, Jülicher F. Fluidization of tissues by cell division and apoptosis. *Proceedings of the National Academy of Sciences*. 2010;107(49):20863–20868. doi:10.1073/pnas.1011086107.
 13. Doostmohammadi A, Thampi SP, Saw TB, Lim CT, Ladoux B, Yeomans JM. Celebrating Soft Matter's 10th Anniversary: Cell division: a source of active stress in cellular monolayers. *Soft Matter*. 2015;11(37):7328–7336. doi:10.1039/C5SM01382H.
 14. Rossen NS, Tarp JM, Mathiesen J, Jensen MH, Oddershede LB. Long-range ordered vorticity patterns in living tissue induced by cell division. *Nature Communications*. 2014;5:5720. doi:10.1038/ncomms6720.
 15. Köpf MH, Pismen LM. A continuum model of epithelial spreading. *Soft Matter*. 2013;9(14):3727. doi:10.1039/c3sm26955h.
 16. Banerjee S, Utuje KJC, Marchetti MC. Propagating Stress Waves During Epithelial Expansion. *Physical Review Letters*. 2015;114(22):228101. doi:10.1103/PhysRevLett.114.228101.
 17. Arciero JC, Mi Q, Branca MF, Hackam DJ, Swigon D. Continuum Model of Collective Cell Migration in Wound Healing and Colony Expansion. *Biophysical Journal*. 2011;100(3):535–543. doi:10.1016/j.bpj.2010.11.083.

-
18. Cochet-Escartin O, Ranft J, Silberzan P, Marcq P. Border Forces and Friction Control Epithelial Closure Dynamics. *Biophysical Journal*. 2014;106(1):65–73. doi:10.1016/j.bpj.2013.11.015.
 19. Lim CT, Zhou EH, Quek ST. Mechanical models for living cells—a review. *Journal of Biomechanics*. 2006;39(2):195–216. doi:10.1016/j.jbiomech.2004.12.008.
 20. Kasza KE, Rowat AC, Liu J, Angelini TE, Brangwynne CP, Koenderink GH, et al. The cell as a material. *Current Opinion in Cell Biology*. 2007;19(1):101–107. doi:10.1016/j.ceb.2006.12.002.
 21. Zhu C, Bao G, Wang N. Cell Mechanics: Mechanical Response, Cell Adhesion, and Molecular Deformation. *Annual Review of Biomedical Engineering*. 2000;2(1):189–226. doi:10.1146/annurev.bioeng.2.1.189.
 22. Verdier C, Etienne J, Duperray A, Preziosi L. Review: Rheological properties of biological materials. *Comptes Rendus Physique*. 2009;10(8):790–811. doi:10.1016/j.crhy.2009.10.003.
 23. Harris AR, Peter L, Bellis J, Baum B, Kabla AJ, Charras GT. Characterizing the mechanics of cultured cell monolayers. *Proceedings of the National Academy of Sciences*. 2012;109(41):16449–16454. doi:10.1073/pnas.1213301109.
 24. Guevorkian K, Colbert MJ, Durth M, Dufour S, Brochard-Wyart F. Aspiration of Biological Viscoelastic Drops. *Physical Review Letters*. 2010;104(21):218101. doi:10.1103/PhysRevLett.104.218101.
 25. Forgacs G, Foty RA, Shafrir Y, Steinberg MS. Viscoelastic Properties of Living Embryonic Tissues: a Quantitative Study. *Biophysical Journal*. 1998;74(5):2227–2234. doi:10.1016/S0006-3495(98)77932-9.
 26. Wang Y, Insana MF. Viscoelastic Properties of Rodent Mammary Tumors Using Ultrasonic Shear-Wave Imaging. *Ultrasonic Imaging*. 2013;35(2):126–145. doi:10.1177/0161734613477321.
 27. Larson RG. *The Structure and Rheology of Complex Fluids*. 1st ed. New York: Oxford University Press; 1998.
 28. Galle J, Loeffler M, Drasdo D. Modeling the Effect of Deregulated Proliferation and Apoptosis on the Growth Dynamics of Epithelial Cell Populations In Vitro. *Biophysical Journal*. 2005;88(1):62–75. doi:10.1529/biophysj.104.041459.
 29. Doostmohammadi A, Adamer MF, Thampi SP, Yeomans JM. Stabilization of active matter by flow-vortex lattices and defect ordering. *Nature Communications*. 2016;7:10557. doi:10.1038/ncomms10557.
 30. Selmeczi D, Mosler S, Hagedorn PH, Larsen NB, Flyvbjerg H. Cell Motility as Persistent Random Motion: Theories from Experiments. *Biophysical Journal*. 2005;89(2):912–931. doi:10.1529/biophysj.105.061150.
 31. Takagi H, Sato MJ, Yanagida T, Ueda M. Functional Analysis of Spontaneous Cell Movement under Different Physiological Conditions. *PLOS ONE*. 2008;3(7):e2648. doi:10.1371/journal.pone.0002648.
 32. Bressloff PC. *Stochastic Processes in Cell Biology*. vol. 41 of *Interdisciplinary Applied Mathematics*. Cham: Springer International Publishing; 2014. Available from: <http://link.springer.com/10.1007/978-3-319-08488-6>.

-
33. Czirók A, Schlett K, Madarász E, Vicsek T. Exponential Distribution of Locomotion Activity in Cell Cultures. *Physical Review Letters*. 1998;81(14):3038–3041. doi:10.1103/PhysRevLett.81.3038.
 34. Upadhyaya A, Rieu JP, Glazier JA, Sawada Y. Anomalous diffusion and non-Gaussian velocity distribution of Hydra cells in cellular aggregates. *Physica A: Statistical Mechanics and its Applications*. 2001;293(3–4):549–558. doi:10.1016/S0378-4371(01)00009-7.
 35. McMahon TA. *Muscles, Reflexes, and Locomotion*. Princeton, N.J: Princeton University Press; 1984.
 36. Tlili S, Gay C, Graner F, Marcq P, Molino F, Saramito P. Colloquium: Mechanical formalisms for tissue dynamics. *The European Physical Journal E*. 2015;38(5):1–31. doi:10.1140/epje/i2015-15033-4.
 37. Pozrikidis C. *Introduction to Theoretical and Computational Fluid Dynamics*. OUP USA; 2011.
 38. Basan M, Elgeti J, Hannezo E, Rappel WJ, Levine H. Alignment of cellular motility forces with tissue flow as a mechanism for efficient wound healing. *Proceedings of the National Academy of Sciences*. 2013;110(7):2452–2459. doi:10.1073/pnas.1219937110.
 39. Zimmermann J, Camley BA, Rappel WJ, Levine H. Contact inhibition of locomotion determines cell–cell and cell–substrate forces in tissues. *Proceedings of the National Academy of Sciences*. 2016;113(10):2660–2665. doi:10.1073/pnas.1522330113.
 40. Treppe X, Wasserman MR, Angelini TE, Millet E, Weitz DA, Butler JP, et al. Physical forces during collective cell migration. *Nature Physics*. 2009;5(6):426–430. doi:10.1038/nphys1269.
 41. Kim JH, Serra-Picamal X, Tambe DT, Zhou EH, Park CY, Sadati M, et al. Propulsion and navigation within the advancing monolayer sheet. *Nature Materials*. 2013;12(9):856–863. doi:10.1038/nmat3689.
 42. Rosen P, Misfeldt DS. Cell density determines epithelial migration in culture. *Proceedings of the National Academy of Sciences*. 1980;77(8):4760–4763.
 43. Farooqui R, Fenteany G. Multiple rows of cells behind an epithelial wound edge extend cryptic lamellipodia to collectively drive cell-sheet movement. *Journal of Cell Science*. 2005;118(1):51–63. doi:10.1242/jcs.01577.
 44. Poujade M, Grasland-Mongrain E, Hertzog A, Jouanneau J, Chavrier P, Ladoux B, et al. Collective migration of an epithelial monolayer in response to a model wound. *Proceedings of the National Academy of Sciences*. 2007;104(41):15988–15993. doi:10.1073/pnas.0705062104.
 45. Reffay M, Petitjean L, Coscoy S, Grasland-Mongrain E, Amblard F, Buguin A, et al. Orientation and Polarity in Collectively Migrating Cell Structures: Statics and Dynamics. *Biophysical Journal*. 2011;100(11):2566–2575. doi:10.1016/j.bpj.2011.04.047.
 46. Serra-Picamal X, Conte V, Vincent R, Anon E, Tambe DT, Bazellieres E, et al. Mechanical waves during tissue expansion. *Nature Physics*. 2012;8(8):628–634. doi:10.1038/nphys2355.

-
47. Thielicke W, Stamhuis E. PIVlab – Towards User-friendly, Affordable and Accurate Digital Particle Image Velocimetry in MATLAB. *Journal of Open Research Software*. 2014;2(1). doi:10.5334/jors.bl.
 48. Cox SM, Matthews PC. Exponential Time Differencing for Stiff Systems. *Journal of Computational Physics*. 2002;176(2):430–455. doi:10.1006/jcph.2002.6995.

C.3 The ability of cancer cells to mechanically adjust to their matrix correlates with their invasive potential

Manuscript Wullkopf et al.

The ability of cancer cells to mechanically adjust to their matrix correlates with their invasive potential

Lena Wullkopf^{1,2}, Ann-Katrine V West², Natascha Leijnse², Thomas R Cox^{1,3}, Chris Madsen^{1,4}, Lene B Oddershede^{2}, Janine T Erler^{1*}*

1 Biotech Research and Innovation Centre (BRIC), University of Copenhagen, Denmark

2 Niels-Bohr Institute, University of Copenhagen, Denmark

3 Garvan Institute of Medical Research, The Kinghorn Cancer Centre, Sydney, Australia

4 Lund University, Sweden

**Corresponding authors*

Significance (other PNAS papers: 100-150 words)

Cancer cells proliferate, expand and migrate in a microenvironments of highly varying nature. Understanding the intracellular mechanical response of cancer cells to changes in their microenvironment is essential to understanding how cancer spreads and why certain cancer types are more prone to invade and form metastasis than others. Our data uncovers a differential intracellular visco-elastic landscape of malignant and benign cancer cells with only the invasive cancer cells exhibiting the ability to sense and adjust to the stiffness of their microenvironment. In addition, we show that the cancer cells belonging to the edge of a colony increase their viscosity during the process of invasion into the surrounding dense three-dimensional matrix, possibly with the goal of more easily being able to squeeze through narrow channels. These findings show that the biomechanical interplay between cells and their microenvironment plays an important role in cancer progression.

Abstract (other PNAS papers: ~200 words)

The metastatic cascade is a physically highly demanding process for cancer cells. They have to resist mechanical forces as compression, tension and high shear stresses in the blood stream and need to apply forces on the environment while squeezing through the dense network of extracellular matrix or the endothelial lining of blood vessels. In addition, the ability to adapt to different physical conditions is essential for a successful metastatic colonization, as secondary tumor sites often exhibit vastly different biomechanical conditions than the organ of tumor origin. Here, we probed the adaptability of cancer cell lines of different invasive potential changes in their microenvironment. Optical tweezers based micro-rheology and real time deformability cytometry of cells cultured in collagen matrices of variant stiffness revealed striking differences in their intracellular visco-elasticity. The cytoplasmic viscoelasticity of the invasive cells changes significantly following a change in matrix stiffness. In contrast, the non-invasive cells has a much smaller response, or no response, to changes in matrix stiffness. Furthermore, using a 3D spheroid invasion assay we revealed significant changes of the intracellular viscoelasticity between the non-invading cells and the invading cells of the spheroid. Inhibition of the focal adhesion kinase (FAK) could abrogate the visco-elasticity of the cancer cells in different positions of the spheroid, suggesting that the FAK based mechanosensing pathway is involved. Thus, cancer cells with a high invasive potential are characterized by the ability to mechanically adjust to their matrix and a more viscous cytoplasm seems beneficial for the cells to squeeze through narrow channels and potentially metastasize. Insight into these mechanisms may pave the way for novel type of cancer drugs prohibiting biomechanical adjustments of the cytoplasm in response to the matrix.

Key words

Viscoelasticity – Optical Tweezers – Micro-rheology – Invasion – Cancer progression – Stiffness –intracellular plasticity

Introduction (other PNAS papers: 400-1000 words)

Metastatic spread is responsible for more than 90% of cancer-related deaths (1). The progression from a primary tumor to a disseminated metastatic disease is a complex process and cancer cells are shown to interact with their non-cellular surroundings, the extracellular matrix (ECM), at each step of the metastatic process (2). The expression and deposition of many ECM proteins is significantly altered during the progression of tumors, leading to both biochemical and biomechanical changes of the tumor microenvironment (TME).

Despite the fact that the ECM comprises over 500 components, its physical properties are vastly determined by fibrillar collagens, elastin, glycosaminoglycans (GAGs) and proteoglycans (PGs) (3). The family of collagens is the most prevalent protein in human tissues with type I collagen being the most abundant. Fibrillar collagen I builds a physical scaffold providing tensile strength and stiffness to the tissue (4). The density and alignment of collagen fibrils varies in different tissues to provide distinct mechanical and biological functions of an organ. Hence, alteration of collagen deposition or posttranslational modifications and crosslinking observed in pathological settings as fibrosis and cancer change the physical properties of tissues vastly and can contribute to disease manifestation and progression (4–6). A prominent example is breast cancer with cancerous tissues exhibiting an elastic modulus that is around tenfold stiffer than normal mammary tissue (7). Moreover, increased matrix stiffness is shown to drive a malignant transformation in the breast (6,7).

In this study we focus on cellular responses to changes of the density of type I collagen in their environment. Although it is well established that an increased deposition and crosslinking of type I collagen promotes the metastatic progression of tumors (7–9), little is known of the intracellular mechanical changes in reaction to increased collagen density. Baker et al. performed micro-rheological studies on endocytosed particles inside prostate cancer cells cultured in 3D matrices or on 2D matrices of varying stiffness. They found the intracellular creep compliance to be dependent on matrix stiffness, but only in 3D assays (cite Baker2009). Using endocytosed beads in mammary epithelial cells (MECs) the same group found that MECs possessing ErbB2 transforming potential stiffen in response to matrix stiffness while non-transformed MECs do not (Baker2010). However, these studies both used endocytosed polystyrene particles for the micro-rheological studies and thereby they only probed the endocytotic pathway, which may not be representative for the entire cytoplasm. Also, they did not relate invasive potential to the ability to respond to the matrix' stiffness. In the current study, we focus on the relation between the cytoplasmic visco-elasticity, the stiffness of the surrounding matrix and the invasive potential of the cells. To probe the cytoplasmic viscoelasticity we use a tightly focused laser beam, an optical trap, capable of tracking the mobility of endogenously occurring lipid granules. This technique is well established for extracting intracellular viscoelasticity and has the advantages that it does not need externally injected tracers or endocytosed particles and can probe at any site within the cytoplasm or nucleus of living cells (cite Tolic PRL 2004, Jeon2011 PRL, Leijnse 2012). Our studies reveal a clear correlation between the invasive potential and the ability to mechanically adjust to the surrounding matrix of a variety of families of cancer cells. In addition, we show that within a colony, or a spheroid, the leader-cells which extend out from the colony to invade the adjacent tissue are more viscous than those cells forming the center. These results point towards a much-overlooked influence of the biomechanical properties of cells and their microenvironment on the metastatic process.

Results

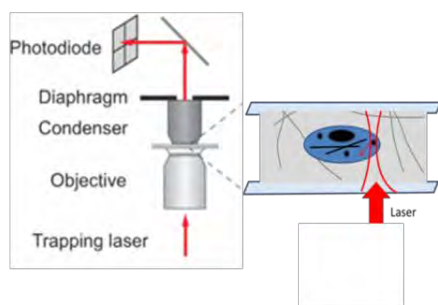
Optical tweezers micro-rheological measurements in 3D cultured cancer cells

Extracellular stiffness was shown to drive breast cancer progression (7). Nevertheless the mechanism and intracellular mechanical response to the changes in the microenvironment have not been revealed yet. Performing micro-rheology measurements in 3D cultured cancer cells in matrices of different collagen I concentrations, our aim was to measure the intracellular response of cancer cells to extracellular stiffness.

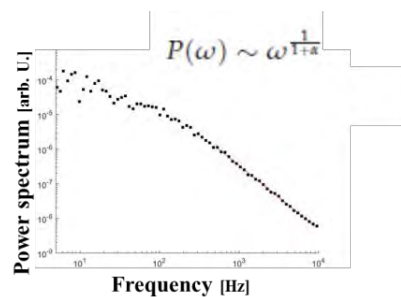
We combined a 3D collagen culture system with optical tracking of the intracellular diffusion of lipid granules in cancer cell lines of various invasive potential.

Lipid granules were reported to occur naturally in eukaryotic cells (15). They exhibit a diameter of 200-300nm and are highly refractive allowing trapping with optical tweezers. Tracking the movement of the lipid granules using a tightly focused laser and a quadrant photodiode (**Fig. 1A**) therefore allows intracellular diffusion studies as described for fission yeast (16) and human umbilical vein endothelial cells (HUVEC) (14).

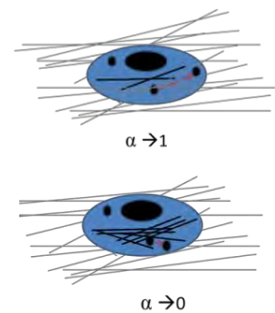
A custom-made Matlab program was used to calculate the power spectra by fourier transforming the time series of the granule's position. The slope of a linear fit in the high frequency region ($9900\text{Hz} > f > 500\text{Hz}$) gives a very precise measurement of the cytoplasmic viscoelasticity, namely the scaling exponent α (**Fig 1B**, in detail in the Method section and Selhuber et al. (16)). A scaling exponent $\alpha=1$ indicates Brownian motion of a particle, whereby $\alpha < 1$ describes sub-diffusive behavior of a tracked granule which is typical for particles moving in viscoelastic media. This implies that the closer α is approaching 1, the more viscous is the cytoplasm of a cell, while small scaling exponents describe a dense cytoplasm (**Fig 1C**). To modulate the stiffness of different microenvironments, cancer cells were cultured in gels containing either a concentration of 1 or 4 mg/ml rat-tail collagen I (Corning Inc.) (**Fig. 1D**). Representative images of the cancer cells after 24h in the different 3D gels are shown in **Fig. 1E** and **S. 1**.



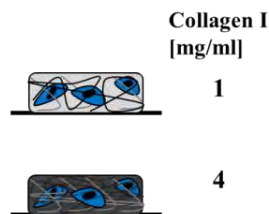
(A)



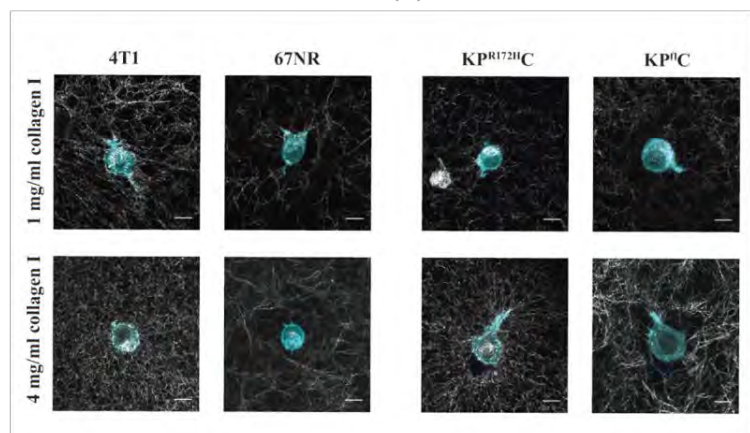
(B)



(C)



(D)



(E)

Fig. 1 Optical tweezer microrheology experiments in 3D cultured cancer cells.

Illustration of the optical trapping setup (A). Exemplary power spectrum analysis of the time series of a trapped lipid granule (B). Interpretation of different values of the scaling exponent α . $\alpha \rightarrow 1$ describes a freely moving particle in a more viscous cytoplasm, $\alpha \rightarrow 0$ describes a slower moving particle in a densely packed more elastic cytoplasm (C). Illustration of the 3D culture system of variant collagen I concentration (D). Exemplary pictures of actin-labelled 4T1 and 67NR breast cancer as well as KP^{R172H}C and KP^IC pancreatic cancer cells cultured in matrices of 1 or 4 mg/ml rat-tail collagen I (E).

The intracellular mechanical plasticity correlates with the invasive potential of cancer cells

We applied this method to cancer cell pairs of different invasive potential that were derived from diverse tissues. These were the breast cancer cell lines 4T1 and 67NR as well as MDA-MB-231, MCF-7; colorectal cancer lines SW620 and SW480 and the pancreatic cancer cell lines KP^{R172H}C and KP^IC (Fig. 2A). The increase in stiffness by changing the collagen concentration in the matrices was confirmed by rheology (Fig. 2B). A median Young's modulus of 421Pa (1mg/ml matrix) corresponds to soft tissues as the lung or mammary gland (5,17).

The gel of 4 mg/ml collagen I (E=1137Pa) resembles a stiffening of these tissues during cancer progression as shown for the mammary gland (4,7) and other stiffer tissue types as the liver that are sites for colonization of metastasis (18).

While all cancer cells tested showed viscoelastic properties with a scaling exponent fluctuating around $\alpha=0.6$ when cultured within three-dimensional matrices, we could report a striking difference in the intracellular plasticity of malignant and benign cell lines. Non-invasive cell lines did not show significant changes in the scaling exponent when cultured in collagen gels of different concentrations (MCF7 $p=0.6992$, KP^IC $p=0.4601$, 67NR $p=0.5735$, SW480 $p=0.4524$). In contrast, all invasive cell lines showed strong intracellular adjustments when cultured within the different collagen I matrices (Fig. 2C-F; Table 1).

Cell lines with a relatively high scaling exponent in the soft matrix of 1 mg/ml collagen I as the MDA-MB-231 and KP^{R172H}C cells showed a reduced intracellular viscosity in response to higher collagen concentrations with a scaling exponent decreasing from $\alpha=0.64$ to $\alpha=0.61$ and from $\alpha=0.63$ to $\alpha=0.55$ respectively (Fig. 2C-D; Table 1). We also observed an opposite response, namely an increase in cytoplasmic viscosity as a response to matrix stiffness with a change in the scaling exponent from $\alpha=0.58$ to $\alpha=0.63$ in the breast cancer cell line 4T1 and from $\alpha=0.53$ to $\alpha=0.57$ in the colorectal cancer line SW620 cultured in matrices of 1 and 4 mg/ml collagen I (Fig. 2E, F; Table 1). Both of these cell lines showed a relatively high elastic component when cultured in soft gels, which was proportionally decreased in matrices of higher collagen content.

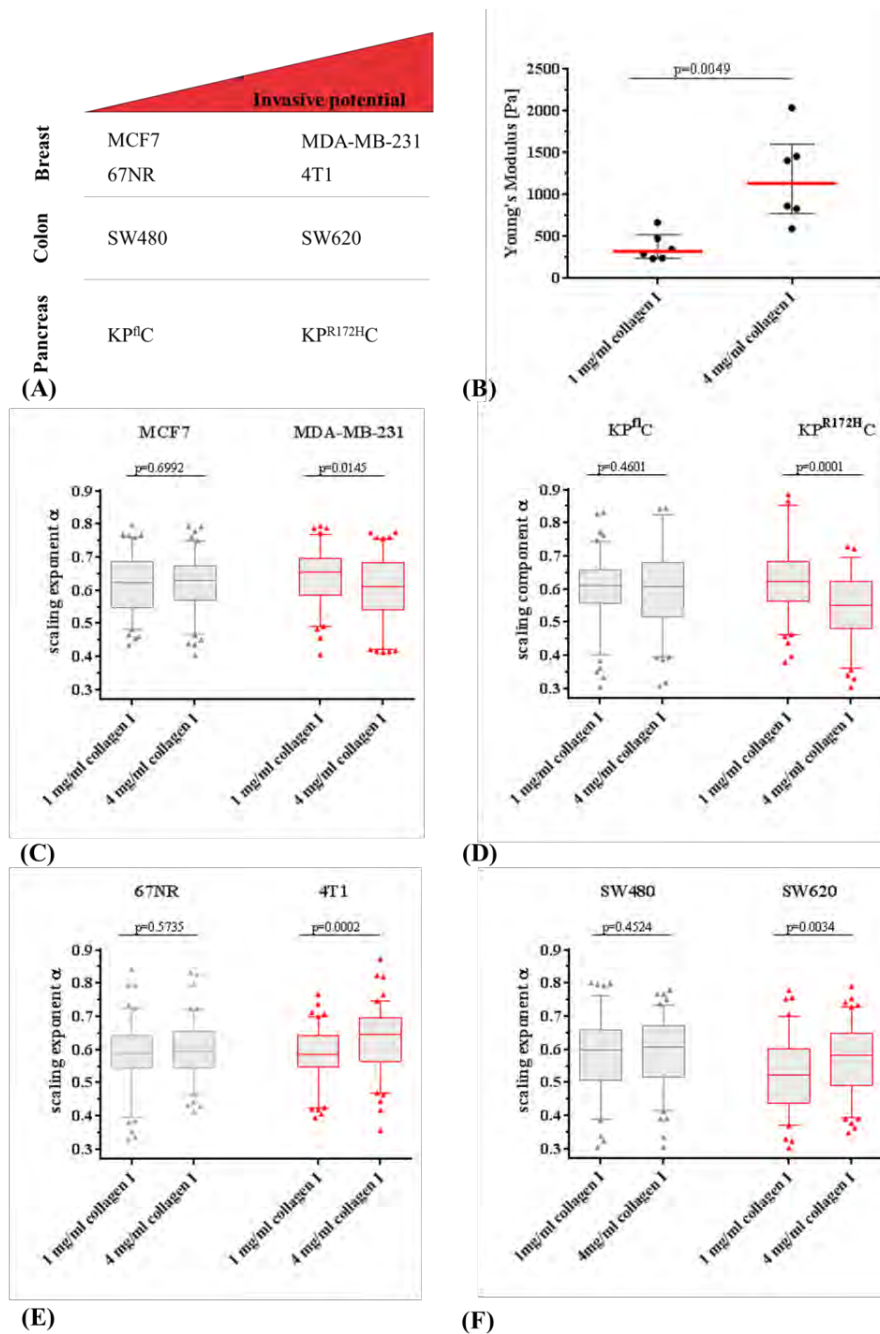


Fig. 2 The scale of intracellular adjustments to cues in the environment correlates with cancer cell invasiveness.

Summary of the cancer cell pairs used in the optical tweezers micro-rheological measurements (A). The young's modulus of 1 mg/ml or 4 mg/ml collagen I matrices was determined by shear-rheology (B). Scaling exponent of the intracellular lipid granule diffusion in human breast cancer cell lines MDA-MB-231, MCF7 and MCF10A (C); pancreatic cancer cell lines KP^{R172H}C, KP^dC (D); mouse breast cancer cell lines 4T1, 67NR (E) and colorectal cancer cell lines SW620, SW480 (F). Highly invasive cell lines are shown in red, non-invasive cancer cell lines in grey. Box plot of 5-95 percentile, Mann-Whitney test (two-tailed).

	Invasive		Non-invasive	
	1 mg/ml collagen I	4 mg/ml collagen I	1 mg/ml collagen I	4 mg/ml collagen I
MDA-MB-231	0.6416 ± 0.08599	0.607 ± 0.09391		
MCF7			0.6197 ± 0.08603	0.622 ± 0.08232
KP^{R172H}C	0.6327 ± 0.1118	0.5501 ± 0.1072		
KPⁿC			0.6051 ± 0.09252	0.599 ± 0.1222
4T1	0.5857 ± 0.07676	0.6275 ± 0.09017		
67NR			0.588 ± 0.09011	0.5983 ± 0.08017
SW620	0.5287 ± 0.1074	0.5714 ± 0.1003		
SW480			0.5776 ± 0.1106	0.5881 ± 0.1025

Table 1 Overview of the scaling exponent for cancer cells cultured within three dimensional collagen matrices.

Data is shown as mean ± SD, n=100.

The stiffness of invasive cancer cell lines changes with their microenvironment

In order to investigate if the overall elasticity of the cells is affected in the same way as the locally measured intracellular viscoelasticity, we studied the stiffness of cancer cells cultured on matrices of variant concentration of collagen I using Real-Time (RT-) Deformability Cytometry (**Fig. 3A**).

RT-Deformability Cytometry is a high throughput technique that probes the deformation of cells streamed through a microfluidic channel. High shear stresses at the 20µm constriction of the microfluidic chips deform the spherical cells into a bullet-like shape. The degree of deformation ($D = 1 - \text{circularity}$) is dependent on cell size and mechanical phenotype of the cell (19). To focus solely on the mechanical properties of the cancer cells, the cell size dependent deformation values (**S 2**) were converted into size independent values of the Young's modulus based on the numerical simulation work by Mokbel et al. (20). This linear elasticity model for fully elastic spheres was integrated in the software ShapeOut enabling us to extract cancer cell stiffness after 24h culture on the different substrates.

Overall the cancer cell lines showed a Young's modulus around 2-3kPa (**Fig. 3 B-E**). Focusing on the cellular response to the collagen gels of different stiffness we could observe the same trends as in the optical tweezer based viscoelasticity measurements described above. While non-invasive cancer cell lines did not show significant differences in their deformation or elasticity, invasive lines revealed changes in their stiffness after being cultured on collagen I gels of different concentrations (**Fig. 3B-D and S 2**). An exception was the pair of colorectal cancer cell lines with the invasive SW620 showing no differential response to the matrices (**Fig. 3E and S 2E**). However, due to the high variability within the measurements, the distributions of the deformability values were not significantly different when the cells were cultured on matrices of different collagen concentrations. Nevertheless they appear clearly distinct of the distributions in non-invasive cell lines (**S 2B**).

Again we recorded the correlation of cellular and extracellular stiffness for the invasive MDA-MB-231 and the KP^{R172H}C, while the breast cancer cell line 4T1 also showed a lower young's modulus of the cell in response to a stiffer substrate.

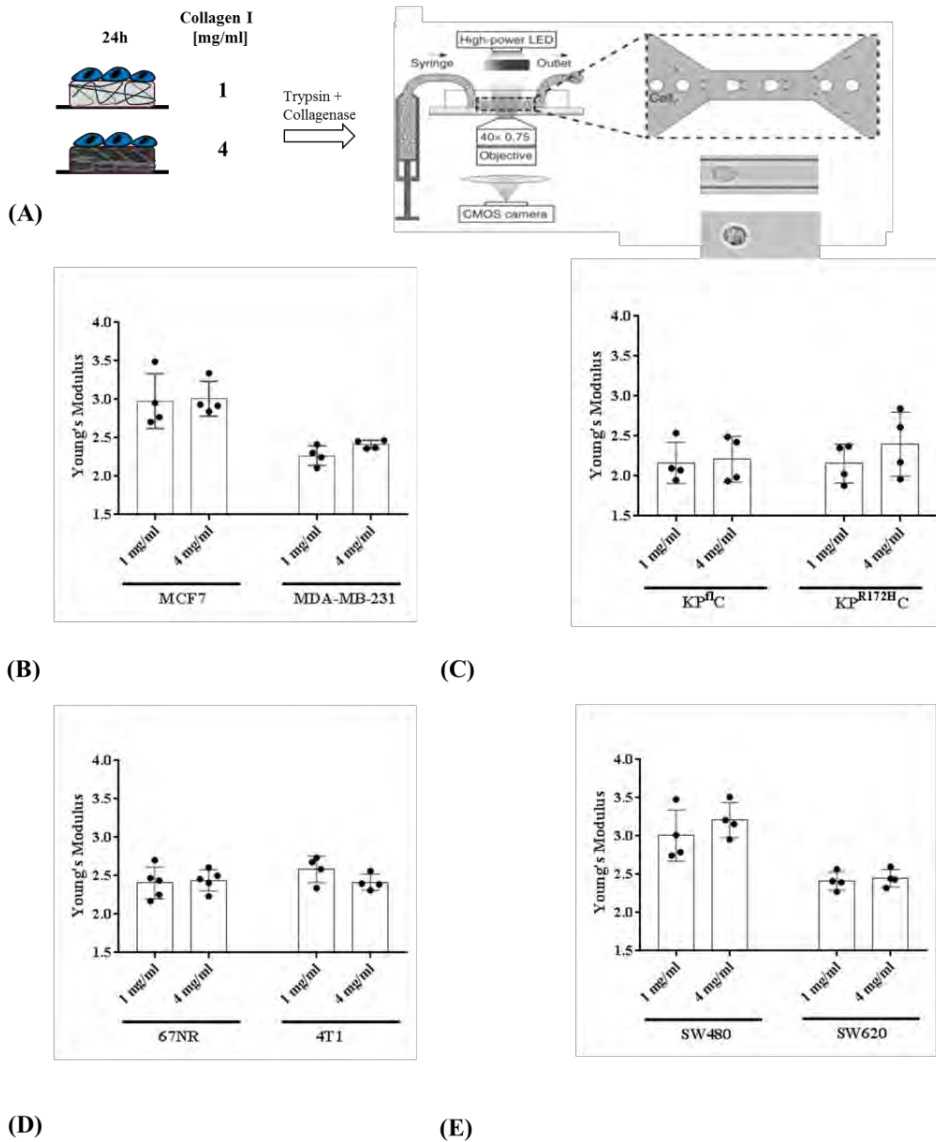


Fig. 3 Real-Time Deformability Cytometry of cancer cell lines cultured on matrices of variant stiffness.

Schematic of Real-Time Deformability Cytometry of cancer cells cultured on matrices of different type I collagen concentration. After detachment, suspended cells experience high shear forces when entering a 20 μ m channel. The resulting deformation is captured by a high speed camera (Illustration of the RT-Deformability Cytometer adapted from Otto et al. (19)) (A). Overview of the median Young's modulus of a pair of human breast cancer (B), pancreatic cancer (C), mouse breast cancer (D) and colorectal cancer (E) cell lines after 24h culture on different collagen type I matrices. Error bars are SD, n=4.

Cancer cells become more viscous during the process of invasion

To investigate mechanical cellular changes during the invasion of cancer cells, we combined the optical tweezers micro-rheology with the 3D spheroid invasion assay into collagen matrices of different stiffness. Hereby lipid granule diffusion in cells remaining in the center of the spheroid, at the tip as well as in the stalk of invading branches was examined (Fig. 4A). This experimental setup allows the comparison of the intracellular viscoelasticity of cells of the same origin during the process of invasion. We utilized the highly invasive pancreatic cancer cell line KP^{R172H}C and breast cancer cell line 4T1 showing differential intracellular responses to changes in their microenvironment.

Both cell lines showed significant mechanical intracellular adjustments during the invasive process. Cells that invaded the matrices exhibited significantly higher scaling exponents than cells that remained at the surface of the spheroids. 4T1 cells at the tip of an invading branch in a collagen matrix of 1mg/ml showed a mean scaling exponent of $\alpha=0.60$ in comparison to $\alpha=0.56$ of cells in the center ($p=0.04$). Cells in the stalk of the invasive branch following the tip cell showed a trend of a higher viscosity ($\alpha=0.58$) than their non-invasive counterparts.

KP^{R172H}C at the invasive front showed a mean scaling exponent of $\alpha=0.62$. The following cells in the stalk revealed a reduced exponent of $\alpha=0.61$ and cells remaining in the center of the sphere $\alpha=0.59$. Both cell lines did also show this effect in collagen matrices of higher concentration (Fig. 4B, C; Table 2).

Regarding the intracellular mechanical status of the cells in the matrices of different collagen concentrations, we observed the same trend as in the single cell micro-rheological measurements with an opposing overall stiffness response of the cell lines regardless of their position in the sphere. While 4T1 cells became more viscous in collagen gels of higher concentration, KP^{R172H}Cs showed a reduced mean scaling exponent in response to a stiffer substrate (Fig. 4B, C; Table 2).

All in all, the optical tweezer based micro-rheology data in the spheroid invasion setup suggested an increasing viscosity of the cells invading three-dimensional matrices. Nevertheless, the cells did still show a differential mechanical status in differing microenvironments.

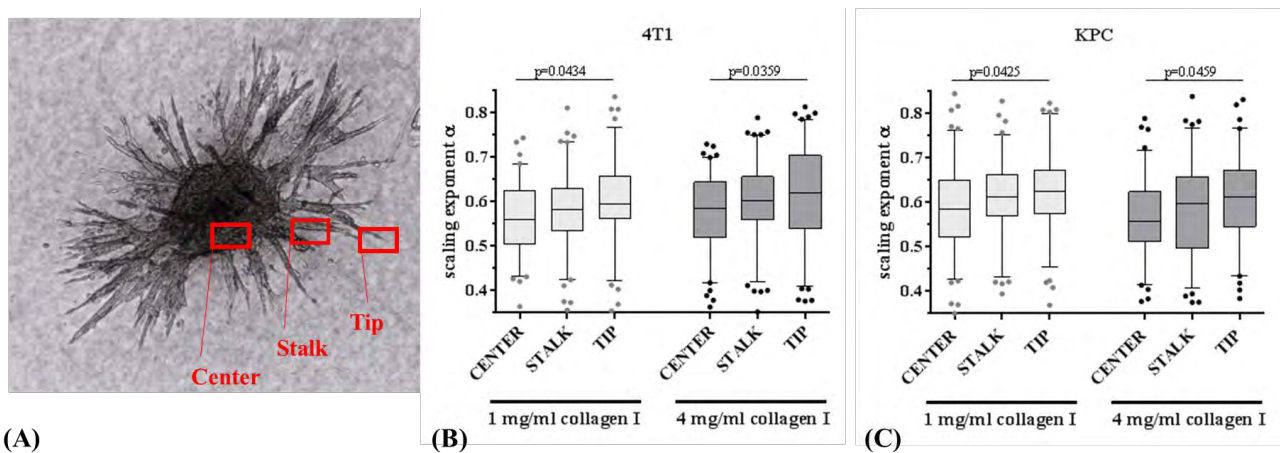


Fig. 4 Cancer cells become more viscous during the process of invasion.

Illustration of the experimental setup. The image depicts a 4T1 spheroid 72h after embedding within a matrix of 4 mg/ml collagen I. The different regions 'Center', 'Stalk' and 'Tip' are indicated in red (A). Assessment of the scaling exponent of the intracellular lipid granule diffusion in 4T1 (B) and KP^{R172H}C (C) either in the center, out-moving stalk or tip of an invading branch of a spheroid embedded in a matrix of 1 or 4mg/ml collagen I. Box plot of 5-95 percentile, ordinary one-way ANOVA followed by a Holm-Sidak's multiple comparisons test.

	1 mg/ml collagen I			4 mg/ml collagen I		
	CENTER	STALK	TIP	CENTER	STALK	TIP
4T1	0.5642 ± 0.08007	0.5816 ± 0.08568	0.6013 ± 0.09252	0.579 ± 0.08237	0.6015 ± 0.08431	0.6167 ± 0.1054
KP^{R172H}C	0.5855 ± 0.09727	0.6087 ± 0.08464	0.6244 ± 0.09194	0.567 ± 0.08617	0.5842 ± 0.1058	0.6055 ± 0.0944

Table 2 Overview of the scaling exponent of cells in different positions of the spheroid.

Data is shown as Mean ± SD, n=100.

To demonstrate the sensitivity of the setup to mechanical changes in the cell, i.e. due to changes in the cytoskeleton, we short-term treated spheroids that had invaded into the collagen matrices with Latrunculin B (LatB), a marine toxin inhibiting actin polymerization and disrupting the microfilament organization of the actin cytoskeleton of a cell.

Cancer cells incubated with the toxin changed cell shape into a round phenotype accompanied by an increase in intracellular viscosity in cells in all positions of the spheroid compared to control cells. The effect was visible in both the 1 and 4mg/ml collagen matrices (**Fig. 6, Table 3**). Especially cells in the center that exhibited the lowest scaling exponent in control spheroids showed a pronounced increase in viscosity (4T1 $p < 0.0001$ in both the 1 mg/ml and 4 mg/ml matrices; KP^{R172H}C $p = 0.35$ in a 1mg/ml matrix, $p = 0.0003$ in a 4 mg/ml collagen gel).

The toxin levelled out any differential mechanical status associated to the different position of the cells in the sphere or the different microenvironments.

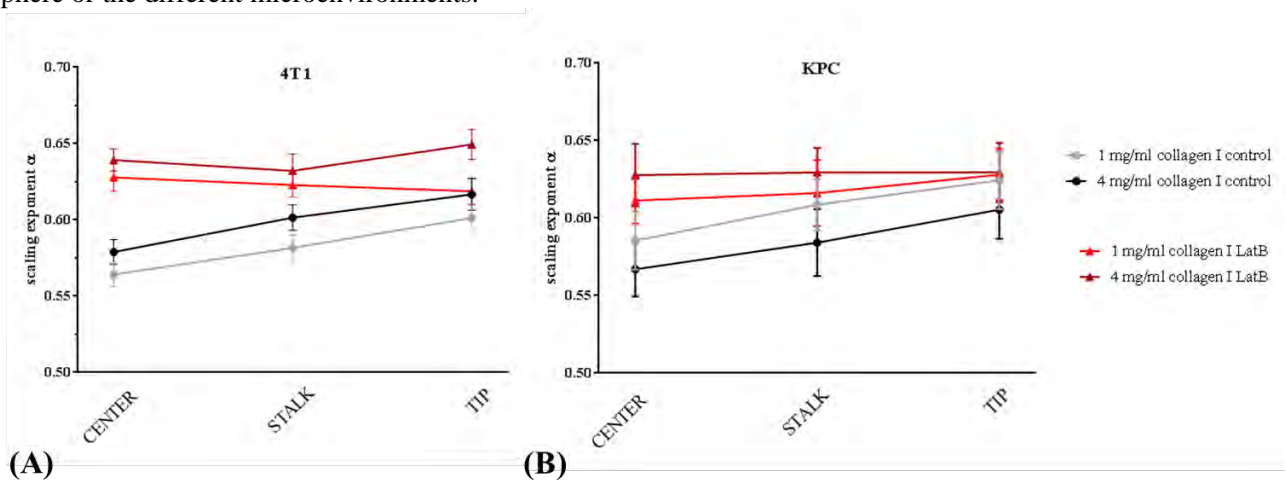


Fig. 5 Latrunculin B levels out mechanical differences of invasive and non-invasive cells.

Comparison of the mean scaling exponent of trapped lipid granules in 4T1 (A) and KP^{R172H}C (B) cells in different positions of the spheroid after 72h of invasion into collagen matrices of 1 and 4 mg/ml. While control cells show an increasing viscosity with their invasive phenotype (grey and black line), LatB treated cells show a higher and rather constant scaling exponent in all position of the sphere (light and dark red line). Data is shown as mean ± SEM.

	1 mg/ml collagen I			4 mg/ml collagen I		
	CENTER	STALK	TIP	CENTER	STALK	TIP
4T1	0.6278± 0.09103	0.6229± 0.07874	0.6188± 0.08723	0.6392± 0.07176	0.6321± 0.1045	0.6494± 0.09695
KP^{R172H}C	0.6114 ± 0.07256	0.6162± 0.1027	0.628± 0.0796	0.6277± 0.09979	0.6295± 0.08006	0.6295± 0.09469

Table 3 Overview of the scaling exponent of Latrunculin B treated cells in different positions of the spheroid.

Data is shown as Mean ± SD, n=100.

Focal adhesion kinase signalling is essential for intracellular biomechanical adaptations during cancer cell invasion

As extracellular stiffness was shown to induce focal adhesion kinase (FAK) activation, we wanted to study the role of FAK in rigidity sensing and adjustments of the mechanical status of the cancer cells during the invasive process.

The broadly used inhibitor of the FAK Inhibitor 14 was able to reduce the levels of phosphorylated FAK in a concentration dependent manner and blocked invasion of both cell lines into the different matrices.

KP^{R172H}C and 4T1 spheroids were allowed to invade into collagen matrices for ~2.5 days before they were treated with FAK Inhibitor 14. Inhibiting FAK signalling made the cancer cells insensitive to changes in the microenvironment and diminished any differential mechanical status in dependence of the position of the cells in the spheroid. For 4T1 cells the scaling exponent levelled out at $\alpha=0.60$. KP^{R172H}Cs plateaued around $\alpha=0.61$ (Fig. 6, Table). These findings suggest that FAK is critical for the observed intracellular biomechanical adaptations of invading cancer cells.

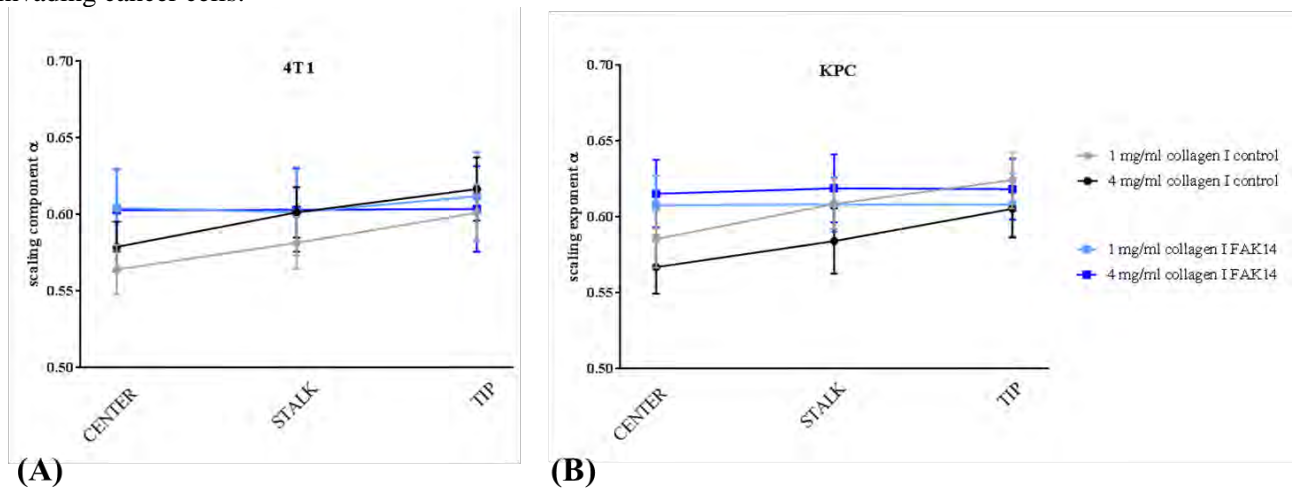


Fig. 6 FAK Inhibition abrogates a differential mechanical state during invasion.

Assessment of the viscoelasticity of 4T1 (A) and KP^{R172H}C (B) cells in different positions of the spheroid after 72h of invasion into collagen matrices of 1 and 4 mg/ml. While control cells show an increase in the scaling exponent with their invasive phenotype (grey and black line), FAK inhibitor 14 treated cells show a plateau in α in all position of the sphere (light and dark blue line). Data is shown as mean ± SEM.

	1 mg/ml collagen I			4 mg/ml collagen I		
	CENTER	STALK	TIP	CENTER	STALK	TIP
4T1	0.6044 ± 0.1284	0.6015 ± 0.1348	0.612 ± 0.1394	0.6029 ± 0.1341	0.6031 ± 0.1392	0.6038 ± 0.1383
KP^{R172H}C	0.6079 ± 0.1019	0.6083 ± 0.08791	0.6082 ± 0.1014	0.615 ± 0.1153	0.619 ± 0.1129	0.6185 ± 0.1049

Table 4 Overview of the scaling exponent of FAK inhibitor 14 treated cancer cells in different positions of the spheroid.

Data is shown as Mean ± SD, n=100.

Discussion

Cancer research is still most of all focused on the biochemical changes during disease progression. Although much progress has been made in the last decade to uncover the physical changes of cancer cells and tissues, there are still many open questions regarding the interplay of biomechanics and biochemical signaling in the progression of cancer. Metastatic spread is physically a very challenging process that requires tumor cell motility in a dense and rigid stromal tissue, a survival of high shear stresses in the circulation, but also a great adaptability to colonize a secondary organ that exhibits vastly different mechanical properties than the organ of tumor origin.

Cancer progression is accompanied by an increased ECM deposition, especially collagens, a process termed desmoplasia. This increased abundance of proteins is highly correlated with an increase in stromal stiffness (4,5,21). It has been demonstrated that physical properties of the ECM vastly influence cancer cell behavior as aberrant cell proliferation, migration, invasion and survival (22,7,23–29). Tumor stiffness has even been associated with poor prognosis and metastasis (4,30).

In this study we combined 3D cultures with state of the art biophysical tools allowing us to study mechanical changes of cancer cells not only in dependence of cancer progression but also the microenvironment.

Particle tracking micro-rheology in 3D cultured cells revealed a conventional sub-diffusive behavior of the trapped lipid granules that was described earlier (12,13,14). The scaling exponent fluctuated around $\alpha=0.6$ indicating a slightly lower value of the intracellular viscoelasticity than reported for other cells in 2D ($\alpha=0.74$ for fission yeast (13) and $\alpha=0.75$ for HUVECs (14)). The sub-diffusive motion of the granules can hereby be explained by the restricted movement of the particle within a cytoplasm densely packed with polymers as the components of the cytoskeleton. Particles embedded in F-Actin networks *ex vivo* were also shown to undergo sub-diffusion with a scaling exponent of $\alpha=0.76$ (31).

Interestingly, we found a striking difference in the ability of invasive and non-invasive cancer cell lines to adjust their cytoplasmic viscoelasticity in response to changes in the surrounding. Only cancer cells of an advanced tumor stage were capable to sense and adapt to changing collagen concentrations.

Despite this overall correlation of intracellular plasticity and invasive potential of the cells, we could detect two different adjustment strategies. While KPC and MDA-MB-231 cells showed a correlating intra- and extracellular viscoelasticity, 4T1 breast cancer cells as well as SW620 colorectal cancer cells showed an increasing intracellular viscosity when cultured in a stiffer environment.

Our findings do strongly support two previous publications by Baker et al. (10,11). The authors combined intracellular micro-rheology with three-dimensional cultures in collagen matrices of variant stiffness. Tracking endocytosed tracer beads with optical tweezers they could also find both types of intracellular changes. While ErbB2 transformed mammary epithelial cells (MECs) showed a corresponding intra- and extra-cellular stiffness (11), PC-3 prostate cancer cells revealed a decreasing apparent intracellular elastic modulus in response to increased matrix stiffness (10). In accordance with our overall association of the invasive potential and the magnitude of intracellular adjustment to changes in the ECM the authors could observe a more pronounced intracellular response in the more motile transformed MECs than in control MECs (11).

Baker et al. concluded that there may be a correlation of intracellular stiffness sensitivity and cell motility in breast cancer (11). Our data strongly supports this increased stiffness sensitivity not only in breast cancer cells but as a general concept of cancer progression. We hypothesize that this intracellular flexibility might aid colonization at a physical different secondary site of the body. The outgrowth of cancer cells on very soft substrates as in the soft agar colony formation assay is a hallmark of carcinogenesis (32). We postulate that the intracellular physical adjustments of aggressive cancer demonstrated here may play a role in this process.

In current literature it is still highly debated if cancer cells have to become more compliant or stiffer during the progression of the disease. Both adjustments strategies have advantages for invasion into a dense matrix. A more viscous cytoplasm allows higher deformation and hence migration through small pores (33–38). On the other hand,

a higher elasticity is associated with a stronger cytoskeleton and linked to higher force generation which was also shown to correlate with cancer cell invasion (39–41).

We could not detect an overall increase in the viscosity when comparing cell lines of diverse invasive potential cultured in three-dimensional matrices. For example did MDA-MB-231 and KPC cells show a significant higher viscosity in the soft gels than their non-invasive counterparts MCF7 and KP^{fl}C, but showed the reverse behavior with a significant more elastic cytoplasm of the highly aggressive cells in the collagen gels of higher concentration.

Nevertheless, we could detect a consistent increase in intracellular viscosity by looking at the actual process of invasion in the elegant optical tweezer based micro-rheology experiments in the spheroid invasion assay. While the cancer cells moved away from the cell sphere and invaded the dense collagen matrices, they showed an increasing value for the scaling exponent α . This confirms the hypothesis that an increasing compliance allows the cells to squeeze through a confined environment which is especially important for degradation free invasion (34).

With our data we therefore confirm previously performed studies using different techniques as the optical stretcher (33) , AFM (37) or magnetic tweezers (35). Swaminathan et al. did find the same adverse correlation of intracellular stiffness and invasiveness looking either at ovarian cancer cell lines of different invasive potential or patient-derived cell lines (35). Nevertheless these previous studies were performed by comparing different cell lines that were cultured on glass or plastic, thus very stiff surfaces.

The information encoded by ECM stiffness is translated into changes of cellular signaling, behavior and phenotype by a multi-step process that can also alter the intracellular stiffness. In large part, cells feel the rigidity of their microenvironment by constantly pulling against the extracellular matrix (42). Although there has been a lot of progress elucidating the signalling components that regulate this probing of the microenvironment and the final responses of the cells to it, the complex network is not fully understood.

It has been demonstrated that matrix rigidity can induce FAK phosphorylation and activation at the focal adhesions of cells (7,23,42–46). FAK is involved in numerous intracellular signaling circuits including cytoskeletal remodeling and focal adhesion turnover (46–50). Both processes are not only involved in force sensing and transduction but also in the invasion of cancer cells and metastasis (51,52–56). A recent study on the role of FAK in 3D migration and cellular mechanics could show that FAK knockout fibroblasts displayed an impaired invasiveness into 3D matrices of 2.4 mg/ml collagen type I. Furthermore the knockout cells showed a reduced cell adhesion strength and a lower cellular stiffness determined by magnetic tweezer experiments in 2D cultures (56).

By targeting FAK in the optical tweezer based micro-rheology experiments during cancer sphere invasion we add proof that cancer cells of an advanced stage indeed sense and respond to the mechanical environment in a FAK-dependent manner. Inhibiting FAK signaling made the cancer cells not only insensitive to stiffness in their surrounding but did also level out any differential mechanical status in dependence of the position of the cells in the spheroid. As the concentration of the inhibitor chosen for the experiments is able to block any invasion of the cells, one can interpret the results as cells losing their differentially elevated viscosity when losing their invasive status. Nevertheless it remains unclear if this mechanical effect of FAK inhibition is one of the mechanisms in which FAK inhibition is able to abrogate invasion, or just a consequence and bystander effect of the treatment. It would be very exciting to study the physical properties of cancer tissues derived from patients treated with the FAK inhibitors of the first clinical trials in advanced solid tumors (57).

The ECM is a complex network of proteins. We are aware that the chosen 3D collagen culture system therefore does not fully resemble a tumor microenvironment. A further limitation is that an increasing collagen concentration does not only alter the stiffness of the matrices but also pore size and importantly it increases the concentration of

integrin ligands simultaneously. Hence all effects observed in this study cannot be solely attributed as mechanically mediated but as a combined response to biochemical and biophysical stimuli.

To avoid this mixed influence many previous publications used polyacrylamide gels of variant stiffness coated with the same amount of ECM protein. While this is a good way around changing ligand densities it does not allow 3D as the precursor components of the cells are highly toxic (58).

However, it has been previously demonstrated that while cells respond strongly to increasing collagen concentrations when cultured on stiff matrices, one can hardly see an influence of the collagen density in “soft cell cultures” that is comparable to our stiffness range (59).

Taken together, our data suggests that the intracellular mechanical plasticity is an important physical factor strongly associated to invasiveness of cancer cells across tumor types. As the differential (intra-)cellular mechanical plasticity of malignant cancer cells is independent of cancer type and biochemical signaling it could be utilized as an additional characteristic for cancer staging. Furthermore, to our knowledge, we are the first to demonstrate the increase of cancer cell viscosity during the invasion in a true three-dimensional invasion assay. Hereby, the differential mechanical state in the diverse microenvironments is maintained during the process of invasion and is dependent on FAK signaling.

Methods

Cell culture

The 4T1 and 67NR murine breast cancer cell lines were a kind gift from Fred Miller (Wayne State University) and were confirmed through STR testing. The KP^{R172H}C and KP^{fl}C murine pancreatic cancer cell lines were derived from Jennifer Morton (CRUK Beatson Institute). The MDA-MB-231 and MCF7 human breast cancer cell lines as well as the SW620 and SW480 human colorectal cancer cell lines were purchased from ATCC. All cell lines were cultured at 37 °C and with 5% CO₂ and routinely tested negative for mycoplasma. The 4T1, 67NR, MDA-MB-231, KP^{R172H}C and KP^{fl}C, SW620 and SW480 cell lines were cultured in Dulbecco's Modified Eagle Medium (DMEM, Gibco) containing high glucose and GlutaMAXTM, 10% Fetal Bovine Serum (FBS) and 1% Penicillin Streptomycin (P/S). The MCF7 cell line was cultured in DMEM/F-12 (Gibco) supplemented with 10% FBS and 1% P/S.

Culturing cells on type I collagen gels (2.5D)

Collagen mixtures of 1, 4 or 8 mg/mL were prepared by mixing the corresponding volumes of high concentration rat tail type I collagen (Corning), sterile PBS and 5X collagen buffer containing 0.1M HEPES, 2% NaHCO₃ and α -MEM. The gels were allowed to polymerize in 6-wells on 37 °C for 1h before they were washed with PBS. 3×10^5 cells were added and incubated for 24h before RT-Deformability Cytometry or immunoblot analysis.

Three-dimensional type I collagen cell culture

Cells were suspended in the collagen mixtures prepared as described above. After polymerization at 37°C for 1h the gels were washed once and incubated with normal culture medium for 24h.

Cell transfections

The different cancer cell lines were transfected with mEmerald-lifeAct-7 (a kind gift of the Ivaska Lab) using Lipofectamine 2000 (Thermo Fisher Scientific) and incubated for ~12h before embedding in 3D collagen matrices as described above.

Spheroid invasion assay

Cancer cell spheroids of 2×10^4 4T1 or KP^{R172H}C cells were generated by hanging drop technique as described previously (60). The next day the spheroids were embedded in type I collagen matrices as described for single cells above. The spheroids were allowed to invade the collagen gels for 72h before optical tweezer measurements. Treatment with FAK Inhibitor 14 (Sigma, 50 μ M) was performed 24h, Latrunculin B (Sigma, 1 μ M) 1-2h before measurement.

Intracellular Micro-rheology/ Particle Tracking microscopy

In order to study the intracellular viscoelasticity of cancer cells in dependence on their microenvironment particle tracking microscopy of endogenous lipid granules was performed. Optical tweezers were used to track precisely the position of the granules in single 3D cultured cancer cells or cells in different positions of a sphere invading a collagen matrix (indicated as tip, stalk and center cells). All cells analyzed were at least 30 μ m away from the glass surface to ensure they were fully embedded in the collagen matrices.

The optical trap was implemented in an inverted Leica DMIRBE microscope and described before (14). In brief, the laser beam (Nd : YVO4 (5W Spectra Physics BL106C, $\lambda = 1064$ nm, TEM $_{\infty}$)) was tightly focused by a water objective (Leica, HCX, PL APO, 63x, NA = 1.4, water). The scattered laser light passing the sample was collected by a condenser (Leica, PI 1.40 oil S1) and focused onto a quadrant photodiode (S5981, Hamamatsu). A low laser power and a short measurement time of 3s made it highly unlikely that the cells would be physiologically affected by the laser light as temperature increase related to absorption of the laser light is expected to be below 1°C (61). Data was acquired by a fast data acquisition card (NI PCI-6040E) at a sampling frequency of 22kHz and processed by a custom made LabVIEW programs (LabVIEW 2010, National Instruments). For the short distances travelled by a trapped granule, the voltage output from the photodiode is linearly related to particle displacement with respect to the laser focus (citation) allowing the extraction of the scaling exponent from the photodiode measurements. The time series of the position of the granule recorded in LabVIEW

$$\vec{r}(t) = (x(t), y(t))$$

were analyzed by a Matlab script (The MathWorks Inc., USA) described in (16). In brief, a powerspectrum was calculated by a fourier transform of the x and y directions of the granule displacement.

with $(P_x(f), P_y(f))$

$$\text{and } P_x(f) \equiv \langle |\bar{x}(f)|^2 \rangle \quad P_y(f) \equiv \langle |\bar{y}(f)|^2 \rangle.$$

The powerspectrum was decorrelated, binned and fitted with a linear fit within the frequency regime of 500Hz-9900Hz. The scaling exponent α is derived from the slope of the linear fit.

$$P_i(f) = kf^{-(1+\alpha)}; \quad i = x, y,$$

Lipid granules in living cells have been found to undergo subdiffusion ($0 < \alpha < 1$) (13,14). The relative contribution of the elastic and viscous components to the mechanical state of the cytoplasm is reflected by the scaling exponent α . The closer α is to 1 the more viscous is the cytoplasm, while a small value reflects a very crowded cytoplasm that allows little movement of the lipid granule.

Confocal Imaging

LifeAct-7 transfected cancer cells cultured in 3D collagen matrices were imaged on an inverted Leica SP5confocal microscope with a 63X water objective (1.2~NA, COR R CS, Leica) and a heated stage. Before imaging, most of the growth medium was removed from the MatTek dish to ensure that the collagen matrices did not detach from the glass surface. For both, the cell and the collagen signals, PMTs were used. mEmerald-lifeAct-7 was excited at 488~nm and the collagen fibres were imaged using the 633~nm laser in fluorescence mode without enhanced dynamics. Images were acquired with 1024x1024~px, 700~Hz, 2 line averages, and at zoom 3. All imaged cells were at least 20 μ m away from the glass surface to ensure they were fully embedded in the gels.

Real-Time (RT-) Deformation Cytometry

Cancer cells cultured on type I collagen matrices were washed with PBS twice followed by trypsinization for 20min on 37°C. The cell solution was collected in Falcon tubes and a collagenase mixture containing 0.05% trypsin, 4mM collagenase II and 4mM collagenase IV (Worthington) was added to the gels for 5 min 37°C. The mixture was added to falcon tubes and incubated for another 5min on 37°C to prevent collagen fragments in the samples. The enzymatic reaction was stopped using DMEM GlutaMAXTM containing 20% FBS and 1% P/S. Cell solutions were washed in PBS and re-suspended in a final volume of 600 μ l Cell Carrier Buffer. The samples were analyzed in a RT-Deformability Cytometer (Zellmechanik Dresden) as described before (19). In brief, deformation of the cells in a microfluidic chip with a constricted channel of 20 μ m was recorded at a flow rate of 0.12 μ l/s. The data was analyzed using the analysis software ShapeOut version X.X.X (available at

<https://github.com/ZELLMCHANIK-DRESDEN/ShapeOut>). Following filters were applied: Range Area 50-400 μ m, Range Area Ratio 1-1.05 allowing a relative difference of 5% between convex hull area and cell area. From the filtered deformation data the apparent Young's Modulus E of the cells was extracted allowing a cell size independent comparison of cellular stiffness after cultivation on different collagen matrices (62).

Determination of F-/G-Actin Ratios/ Change to tubulin

F-/G-Actin ratios were investigated by western blotting as described before (63). Briefly, cancer cells cultures on type I collagen matrices were washed with PBS and lysed in actin stabilization buffer (50mM PIPES [pH 6.9], 50mM NaCl, 5mM MgCl₂, 5mM EGTA, 2mM ATP, 5% glycerol, 0.1% Nonidet P-40, 0.1% Triton X-100, 0.1% Tween 20, 0.1% β -mercaptoethanol) for 10 min at 37°C followed by scraping. Protein concentrations were determined by the Bradford method and adjusted using the actin stabilization buffer. An aliquot was taken (total actin) before the remaining samples were transferred into ultracentrifugation tubes (...type, company). F-Actin and G-Actin fractions were separated by ultracentrifugation at 100,000g for 40min at 37°C (ULTACENTRIFUGE). The supernatant containing the G-Actin was collected in a fresh tube, while the pelleted F-Actin was re-suspended in 1mM cytochalasin D (Sigma-Aldrich) and incubated on ice for 45 min. Laemmli buffer was added to all samples followed by 10min incubation at 95°C and standard immune blotting using an antibody against β -actin (Abcam) (64). Fraction intensities were determined using the Fiji gel analysis tool.

Shear rheology

Relative stiffness of type I collagen I gels of variant concentration were measured by shear rheology using a DHR-2 controlled strain rotational rheometer (TA Instruments) as described previously (65).

In brief, type I collagen matrices of different concentrations were prepared as described above and incubated on 37C for 24h prior measurements. Discs of 8mm diameter were prepared using a disposable biopsy punch (KAI). Measurements were performed at a temperature of 21°C using an 8 mm sand-blasted parallel plate geometry (TA Instruments), a fixed frequency of 1Hz and an increasing strain from 0.2% to 1.2%. The samples were found to be only minimally frequency dependent within the range of testing and showed a linear viscoelastic response within the strain range evaluated. Storage moduli (G') at 0.3% strain were extracted and the elastic moduli (E) were determined the following:

$$E = 2 \times G' (1 + \nu) \quad \text{where, } \nu = 0.5 \text{ for hydrogels (65).}$$

Statistics

All statistical tests were performed as indicated in the figure legends. Normal distribution was tested in a D'Agostino-Pearson omnibus normality test. If a Gaussian distribution was given groups were compared using the One-way ANOVA followed by a Holm-Sidak's multiple comparison test.

For differently distributed samples the Mann-Whitney test or the Kruskal Wallis test with Dunn's multiple comparisons test was applied.

P < 0.05, **P < 0.01, *P < 0.001.*

Acknowledgements

The authors acknowledge financial support from the Danish Research Council grant DFF-4002-00099, the Danish National Research Foundation grant DNRF116, the Villum Foundation grant 'Earth Patterns', and from a Novo Nordisk Foundation Hallas Møller stipend.

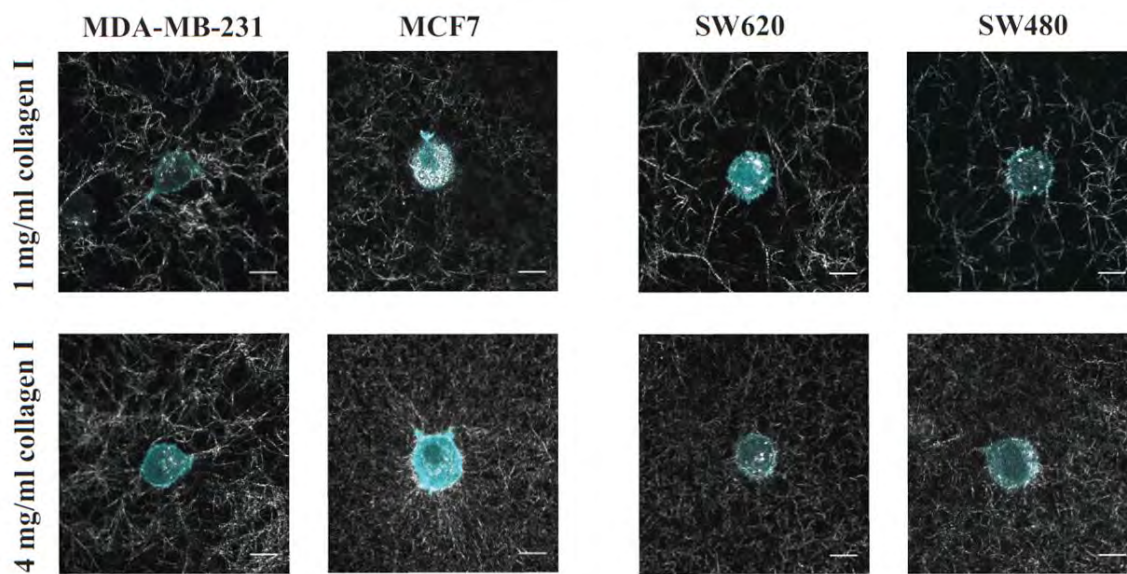
Conflict of Interest Statement

The authors declare no conflict of interest.

Authors Information

L.W., J.T.E. and L.B.O. designed the experimental study. L.W., N.L. and A.V.W. performed the experiments. L.W., J.T.E., and L.B.O. wrote the paper. All authors agreed with the submitted version of the paper. To whom correspondence may be addressed: E-mail Janine.erler@bric.ku.dk

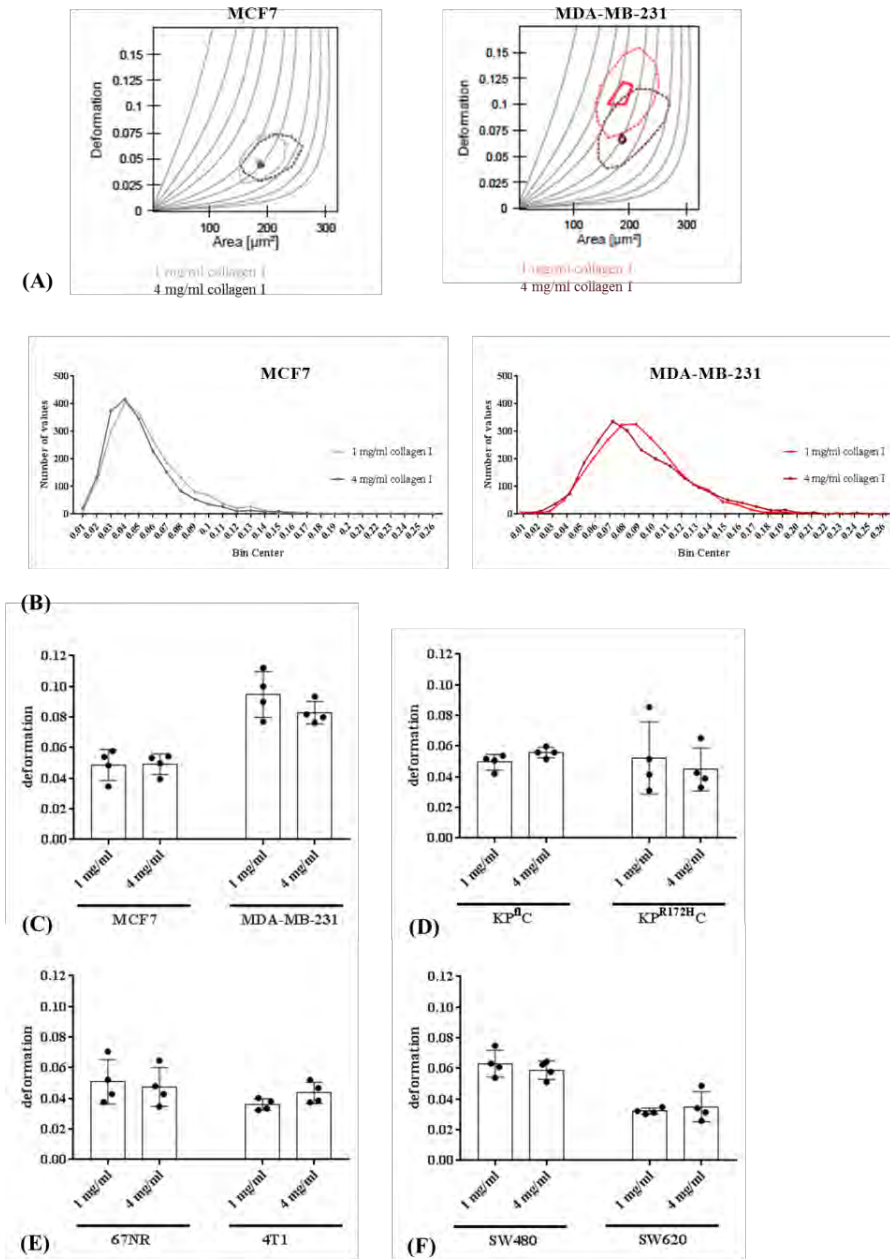
Supplements



Sup.

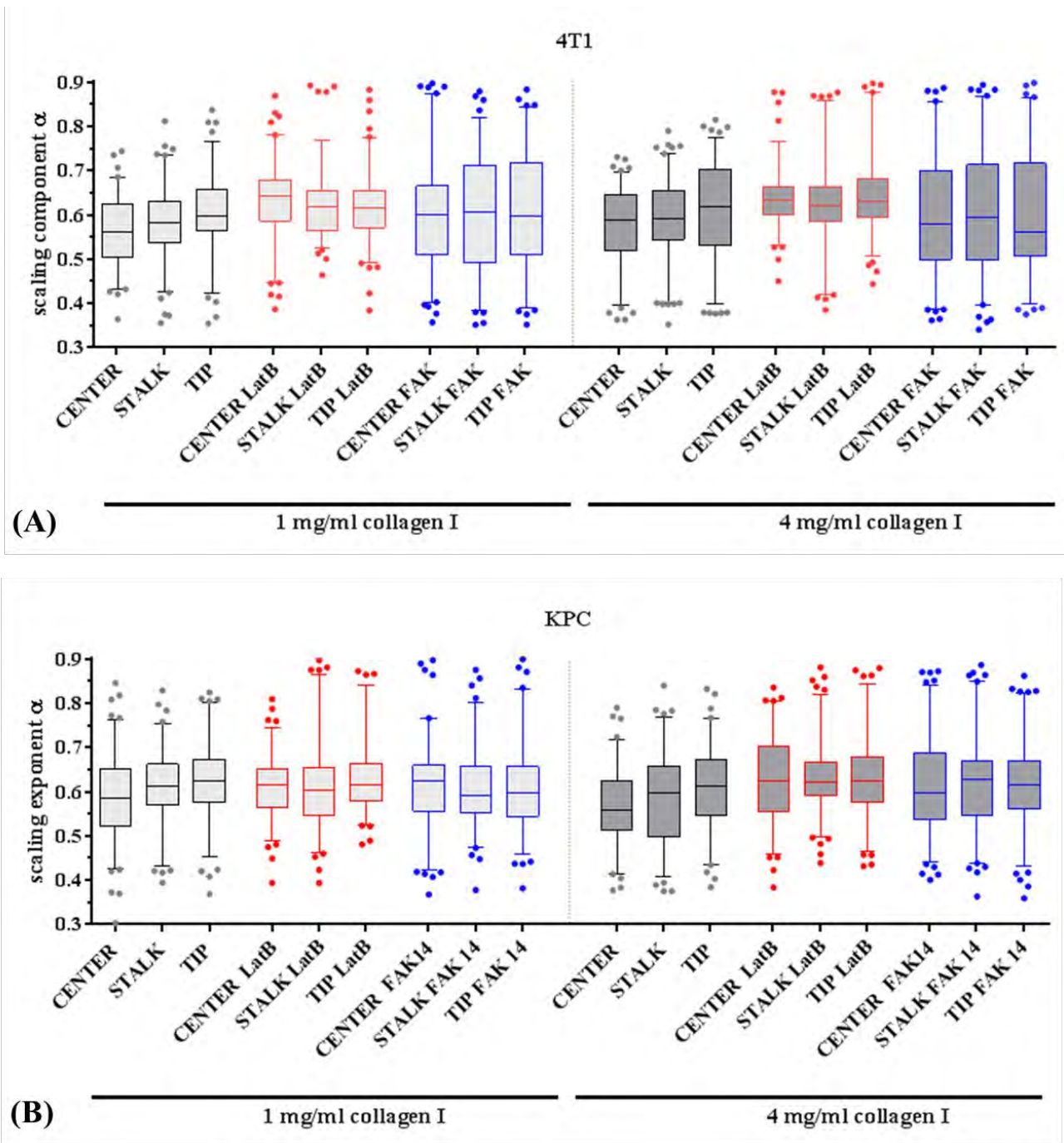
Fig. 1 Three dimensional culture of cancer cells.

Exemplary pictures of actin-labeled MDA-MB-231 and MCF7 breast cancer as well as SW620 and SW480 colorectal cancer cells cultured in matrices of 1 or 4 mg/ml rat-tail collagen I.



Sup. Fig. 2 Deformability of cancer cells cultured on matrices of different collagen I concentration.

Exemplary scatter plot of deformability and cell size of non-invasive MCF7 and invasive MDA-MB-231 cells after 24h culture on matrices of 1 or 4 mg/ml collagen I (A). Histogram of the overall distribution of deformation values of non-invasive MCF7 and invasive MDA-MB-231 cells after 24h culture on matrices of 1 or 4 mg/ml collagen I (n=2000) (B). Quantification of the median deformability of human breast cancer cell lines (C), pancreatic cancer cell lines (D), mouse breast cancer cell lines (E) and colorectal cancer cell lines after 24h of culture on matrices of 1 or 4mg/ml collagen I. Non-invasive cell lines are displayed left and invasive lines on the right side of each graph. Error bars are SD, n=4.



Sup. Fig. 3 Overview of the optical tweezer based microrheology in the spheroid invasion assay.

Overview of the box plots of 5-95 percentile of the scaling exponent of the intracellular lipid granule diffusion in 4T1 (A) and KPR^{172H}C (B) control or either Latrunculin (500nM, 2h) or FAK 14 (50 μ M, 16h) treated spheroids.

Supplementary tables

	1 mg/ml collagen I			4 mg/ml collagen I		
	CENTER	STALK	TIP	CENTER	STALK	TIP
Control	0.5642 ± 0.08007	0.5816 ± 0.08568	0.6013 ± 0.09252	0.579 ± 0.08237	0.6015 ± 0.08431	0.6167 ± 0.1054
LatB	0.6278± 0.09103	0.6229± 0.07874	0.6188± 0.08723	0.6392± 0.07176	0.6321± 0.1045	0.6494± 0.09695
FAK 14	0.6044 ± 0.1284	0.6015 ± 0.1348	0.612 ± 0.1394	0.6029 ± 0.1341	0.6031 ± 0.1392	0.6038 ± 0.1383

Sup. Table 1 Overview of the mean scaling exponent in control, LatB and FAK14 treated 4T1 spheroids.
Data shown as mean ± SD.

	1 mg/ml collagen I			4 mg/ml collagen I		
	CENTER	STALK	TIP	CENTER	STALK	TIP
Control	0.5855 ± 0.09727	0.6087 ± 0.08464	0.6244 ± 0.09194	0.567 ± 0.08617	0.5842 ± 0.1058	0.6055 ± 0.0944
LatB	0.6114 ± 0.07256	0.6162± 0.1027	0.628± 0.0796	0.6277± 0.09979	0.6295± 0.08006	0.6295± 0.09469
FAK 14	0.6079 ± 0.1019	0.6083 ± 0.08791	0.6082 ± 0.1014	0.615 ± 0.1153	0.619 ± 0.1129	0.6185 ± 0.1049

Sup. Table 2 Overview of the mean scaling exponent in control, LatB and FAK14 treated K^{PR172H}C spheroids.
Data shown as mean ± SD.

1. Sporn MB. The war on cancer. *The Lancet*. 1996 May 18;347(9012):1377–1381.
2. Venning FA, Wullkopf L, Erler JT. Targeting ECM disrupts cancer progression. *Front Oncol*. 2015 Oct 20;5:224.
3. Humphrey JD, Dufresne ER, Schwartz MA. Mechanotransduction and extracellular matrix homeostasis. *Nat Rev Mol Cell Biol*. 2014 Dec;15(12):802–812.
4. Erler JT, Weaver VM. Three-dimensional context regulation of metastasis. *Clin Exp Metastasis*. 2009;26(1):35–49.
5. Cox TR, Erler JT. Remodeling and homeostasis of the extracellular matrix: implications for fibrotic diseases and cancer. *Dis Model Mech*. 2011 Mar;4(2):165–178.
6. Butcher DT, Alliston T, Weaver VM. A tense situation: forcing tumour progression. *Nat Rev Cancer*. 2009 Feb;9(2):108–122.
7. Levental KR, Yu H, Kass L, Lakins JN, Egeblad M, Erler JT, et al. Matrix crosslinking forces tumor progression by enhancing integrin signaling. *Cell*. 2009 Nov 25;139(5):891–906.
8. Provenzano PP, Inman DR, Eliceiri KW, Knittel JG, Yan L, Rueden CT, et al. Collagen density promotes mammary tumor initiation and progression. *BMC Med*. 2008 Apr 28;6:11.
9. Conklin MW, Eickhoff JC, Riching KM, Pehlke CA, Eliceiri KW, Provenzano PP, et al. Aligned collagen is a prognostic signature for survival in human breast carcinoma. *Am J Pathol*. 2011 Mar;178(3):1221–1232.
10. Baker EL, Bonnecaze RT, Zaman MH. Extracellular matrix stiffness and architecture govern intracellular rheology in cancer. *Biophys J*. 2009 Aug 19;97(4):1013–1021.
11. Baker EL, Lu J, Yu D, Bonnecaze RT, Zaman MH. Cancer cell stiffness: integrated roles of three-dimensional matrix stiffness and transforming potential. *Biophys J*. 2010 Oct 6;99(7):2048–2057.
12. Berg-Sørensen K, Flyvbjerg H. Power spectrum analysis for optical tweezers. *Review of Scientific Instruments*. 2004;75(3):594.
13. Tolić-Nørrelykke IM, Munteanu E-L, Thon G, Oddershede L, Berg-Sørensen K. Anomalous diffusion in living yeast cells. *Phys Rev Lett*. 2004 Aug 13;93(7):078102.
14. Leijnse N, Jeon J-H, Loft S, Metzler R, Oddershede LB. Diffusion inside living human cells. *The European Physical Journal Special Topics*. 2012 Apr;204(1):75–84.
15. Robinow CF, Hyams JS. General cytology of fission yeasts. *Molecular biology of the fission yeast*. Elsevier; 1989. p. 273–330.

16. Selhuber-Unkel C, Yde P, Berg-Sørensen K, Oddershede LB. Variety in intracellular diffusion during the cell cycle. *Phys Biol*. 2009 Jul 1;6(2):025015.
17. Barnes JM, Przybyla L, Weaver VM. Tissue mechanics regulate brain development, homeostasis and disease. *J Cell Sci*. 2017 Jan 1;130(1):71–82.
18. Yeh W-C, Li P-C, Jeng Y-M, Hsu H-C, Kuo P-L, Li M-L, et al. Elastic modulus measurements of human liver and correlation with pathology. *Ultrasound Med Biol*. 2002 Apr;28(4):467–474.
19. Otto O, Rosendahl P, Mietke A, Golfier S, Herold C, Klaue D, et al. Real-time deformability cytometry: on-the-fly cell mechanical phenotyping. *Nat Methods*. 2015 Mar;12(3):199–202, 4 p following 202.
20. Mokbel M, Mokbel D, Mietke A, Träber N, Girardo S, Otto O, et al. Numerical Simulation of Real-Time Deformability Cytometry To Extract Cell Mechanical Properties. *ACS biomaterials science & engineering*. 2017 Jan 30;
21. Oudin MJ, Weaver VM. Physical and chemical gradients in the tumor microenvironment regulate tumor cell invasion, migration, and metastasis. *Cold Spring Harb Symp Quant Biol*. 2016;81:189–205.
22. Discher DE, Janmey P, Wang Y-L. Tissue cells feel and respond to the stiffness of their substrate. *Science*. 2005 Nov 18;310(5751):1139–1143.
23. Paszek MJ, Zahir N, Johnson KR, Lakins JN, Rozenberg GI, Gefen A, et al. Tensional homeostasis and the malignant phenotype. *Cancer Cell*. 2005 Sep;8(3):241–254.
24. Schrader J, Gordon-Walker TT, Aucott RL, van Deemter M, Quaas A, Walsh S, et al. Matrix stiffness modulates proliferation, chemotherapeutic response, and dormancy in hepatocellular carcinoma cells. *Hepatology*. 2011 Apr;53(4):1192–1205.
25. Zaman MH, Trapani LM, Sieminski AL, Mackellar D, Gong H, Kamm RD, et al. Migration of tumor cells in 3D matrices is governed by matrix stiffness along with cell-matrix adhesion and proteolysis. *Proc Natl Acad Sci U S A*. 2006 Jul 18;103(29):10889–10894.
26. Chen CS. Mechanotransduction - a field pulling together? *J Cell Sci*. 2008 Oct 15;121(Pt 20):3285–3292.
27. Cassereau L, Miroshnikova YA, Ou G, Lakins J, Weaver VM. A 3D tension bioreactor platform to study the interplay between ECM stiffness and tumor phenotype. *J Biotechnol*. 2015 Jan 10;193:66–69.
28. Klein EA, Yin L, Kothapalli D, Castagnino P, Byfield FJ, Xu T, et al. Cell-cycle control by physiological matrix elasticity and in vivo tissue stiffening. *Curr Biol*. 2009 Sep 29;19(18):1511–1518.
29. Tang X, Kuhlenschmidt TB, Zhou J, Bell P, Wang F, Kuhlenschmidt MS, et al. Mechanical force affects expression of an in vitro metastasis-like phenotype in HCT-8 cells. *Biophys J*. 2010 Oct 20;99(8):2460–2469.
30. Schedin P, Keely PJ. and Tumor Progression. 2011;

31. Gittes F, Schnurr B, Olmsted PD, MacKintosh FC, Schmidt CF. Microscopic Viscoelasticity: Shear Moduli of Soft Materials Determined from Thermal Fluctuations. *Phys Rev Lett*. 1997 Oct 27;79(17):3286–3289.
32. Borowicz S, Van Scoyk M, Avasarala S, Karuppusamy Rathinam MK, Tauler J, Bikkavilli RK, et al. The soft agar colony formation assay. *J Vis Exp*. 2014 Oct 27;(92):e51998.
33. Guck J, Schinkinger S, Lincoln B, Wottawah F, Ebert S, Romeyke M, et al. Optical deformability as an inherent cell marker for testing malignant transformation and metastatic competence. *Biophys J*. 2005 May;88(5):3689–3698.
34. Wolf K, Mazo I, Leung H, Engelke K, von Andrian UH, Deryugina EI, et al. Compensation mechanism in tumor cell migration: mesenchymal-amoeboid transition after blocking of pericellular proteolysis. *J Cell Biol*. 2003 Jan 20;160(2):267–277.
35. Swaminathan V, Mythreye K, O'Brien ET, Berchuck A, Blobel GC, Superfine R. Mechanical stiffness grades metastatic potential in patient tumor cells and in cancer cell lines. *Cancer Res*. 2011 Aug 1;71(15):5075–5080.
36. Wolf K, Te Lindert M, Krause M, Alexander S, Te Riet J, Willis AL, et al. Physical limits of cell migration: control by ECM space and nuclear deformation and tuning by proteolysis and traction force. *J Cell Biol*. 2013 Jun 24;201(7):1069–1084.
37. Xu W, Mezencev R, Kim B, Wang L, McDonald J, Sulchek T. Cell stiffness is a biomarker of the metastatic potential of ovarian cancer cells. *PLoS ONE*. 2012 Oct 4;7(10):e46609.
38. Lekka M, Laidler P, Gil D, Lekki J, Stachura Z, Hryniewicz AZ. Elasticity of normal and cancerous human bladder cells studied by scanning force microscopy. *Eur Biophys J*. 1999;28(4):312–316.
39. Solon J, Levental I, Sengupta K, Georges PC, Janmey PA. Fibroblast adaptation and stiffness matching to soft elastic substrates. *Biophys J*. 2007 Dec 15;93(12):4453–4461.
40. Koch TM, Münster S, Bonakdar N, Butler JP, Fabry B. 3D Traction forces in cancer cell invasion. *PLoS ONE*. 2012 Mar 30;7(3):e33476.
41. Mekhdjian AH, Kai F, Rubashkin MG, Prahls LS, Przybyla LM, McGregor AL, et al. Integrin-mediated traction force enhances paxillin molecular associations and adhesion dynamics that increase the invasiveness of tumor cells into a three-dimensional extracellular matrix. *Mol Biol Cell*. 2017 Jun 1;28(11):1467–1488.
42. Schedin P, Keely PJ. Mammary gland ECM remodeling, stiffness, and mechanosignaling in normal development and tumor progression. *Cold Spring Harb Perspect Biol*. 2011 Jan 1;3(1):a003228.
43. Pathak A, Kumar S. Independent regulation of tumor cell migration by matrix stiffness and confinement. *Proc Natl Acad Sci U S A*. 2012 Jun 26;109(26):10334–10339.

44. Provenzano PP, Inman DR, Eliceiri KW, Keely PJ. Matrix density-induced mechanoregulation of breast cell phenotype, signaling and gene expression through a FAK-ERK linkage. *Oncogene*. 2009 Dec 10;28(49):4326–4343.
45. Seong J, Tajik A, Sun J, Guan J-L, Humphries MJ, Craig SE, et al. Distinct biophysical mechanisms of focal adhesion kinase mechanoactivation by different extracellular matrix proteins. *Proc Natl Acad Sci U S A*. 2013 Nov 26;110(48):19372–19377.
46. Bae YH, Mui KL, Hsu BY, Liu S-L, Cretu A, Razinia Z, et al. A FAK-Cas-Rac-lamellipodin signaling module transduces extracellular matrix stiffness into mechanosensitive cell cycling. *Sci Signal*. 2014 Jun 17;7(330):ra57.
47. Schlaepfer DD, Hauck CR, Sieg DJ. Signaling through focal adhesion kinase. *Prog Biophys Mol Biol*. 1999;71(3-4):435–478.
48. Mitra SK, Schlaepfer DD. Integrin-regulated FAK-Src signaling in normal and cancer cells. *Curr Opin Cell Biol*. 2006 Oct;18(5):516–523.
49. Ren XD, Kiosses WB, Sieg DJ, Otey CA, Schlaepfer DD, Schwartz MA. Focal adhesion kinase suppresses Rho activity to promote focal adhesion turnover. *J Cell Sci*. 2000 Oct;113 (Pt 20):3673–3678.
50. Wang HB, Dembo M, Hanks SK, Wang Y. Focal adhesion kinase is involved in mechanosensing during fibroblast migration. *Proc Natl Acad Sci U S A*. 2001 Sep 25;98(20):11295–11300.
51. Gabarra-Niecko V, Schaller MD, Dunty JM. FAK regulates biological processes important for the pathogenesis of cancer. *Cancer Metastasis Rev*. 2003 Dec;22(4):359–374.
52. Lahlou H, Sanguin-Gendreau V, Zuo D, Cardiff RD, McLean GW, Frame MC, et al. Mammary epithelial-specific disruption of the focal adhesion kinase blocks mammary tumor progression. *Proc Natl Acad Sci U S A*. 2007 Dec 18;104(51):20302–20307.
53. Provenzano PP, Inman DR, Eliceiri KW, Beggs HE, Keely PJ. Mammary epithelial-specific disruption of focal adhesion kinase retards tumor formation and metastasis in a transgenic mouse model of human breast cancer. *Am J Pathol*. 2008 Nov;173(5):1551–1565.
54. Baker A-M, Bird D, Lang G, Cox TR, Erler JT. Lysyl oxidase enzymatic function increases stiffness to drive colorectal cancer progression through FAK. *Oncogene*. 2013 Apr 4;32(14):1863–1868.
55. Sulzmaier FJ, Jean C, Schlaepfer DD. FAK in cancer: mechanistic findings and clinical applications. *Nat Rev Cancer*. 2014 Sep;14(9):598–610.
56. Mierke CT, Fischer T, Puder S, Kunschmann T, Soetje B, Ziegler WH. Focal adhesion kinase activity is required for actomyosin contractility-based invasion of cells into dense 3D matrices. *Sci Rep*. 2017 Feb 16;7:42780.

57. Infante JR, Camidge DR, Mileskin LR, Chen EX, Hicks RJ, Rischin D, et al. Safety, pharmacokinetic, and pharmacodynamic phase I dose-escalation trial of PF-00562271, an inhibitor of focal adhesion kinase, in advanced solid tumors. *J Clin Oncol*. 2012 May 1;30(13):1527–1533.
58. Caliarì SR, Burdick JA. A practical guide to hydrogels for cell culture. *Nat Methods*. 2016 Apr 28;13(5):405–414.
59. Engler A, Bacakova L, Newman C, Hategan A, Griffin M, Discher D. Substrate compliance versus ligand density in cell on gel responses. *Biophys J*. 2004 Jan;86(1 Pt 1):617–628.
60. Chang J, Lucas MC, Leonte LE, Garcia-Montolio M, Singh LB, Findlay AD, et al. Pre-clinical evaluation of small molecule LOXL2 inhibitors in breast cancer. *Oncotarget*. 2017 Apr 18;8(16):26066–26078.
61. Jeon J-H, Tejedor V, Burov S, Barkai E, Selhuber-Unkel C, Berg-Sørensen K, et al. In vivo anomalous diffusion and weak ergodicity breaking of lipid granules. *Phys Rev Lett*. 2011 Jan 28;106(4):048103.
62. Mietke A, Otto O, Girardo S, Rosendahl P, Taubenberger A, Golfier S, et al. Extracting Cell Stiffness from Real-Time Deformability Cytometry: Theory and Experiment. *Biophys J*. 2015 Nov 17;109(10):2023–2036.
63. Qiao Y, Chen J, Lim YB, Finch-Edmondson ML, Seshachalam VP, Qin L, et al. YAP Regulates Actin Dynamics through ARHGAP29 and Promotes Metastasis. *Cell Rep*. 2017 May 23;19(8):1495–1502.
64. Cox TR, Bird D, Baker A-M, Barker HE, Ho MW-Y, Lang G, et al. LOX-mediated collagen crosslinking is responsible for fibrosis-enhanced metastasis. *Cancer Res*. 2013 Mar 15;73(6):1721–1732.
65. Cox T, Madsen C. Relative Stiffness Measurements of Cell-embedded Hydrogels by Shear Rheology in vitro. *Bio-protocol*. 2017;7(1).

C.4 Florentsen et al. preprint

Quantification of loading and laser assisted release of siRNA from single gold nanoparticles

Christoffer Dam Florentsen, Ann-Katrine Vransø West, Jes Norberg Clausen, Szabolcs Semsey, Poul Martin Bendix, Lene B. Oddershede

January 3, 2018

Abstract

Short interfering silencing RNA (siRNA) provides an avenue of possibilities to control the regulation of gene expression in cells. To realize the full potential of siRNA therapy in the human body efficient delivery vehicles and novel strategies for triggering release from carrier vehicles have to be developed. Delivery of siRNA into specific target cells can be dramatically increased by using nanocarriers like gold nanoparticles (AuNPs) carrying both oligonucleotides and specific ligands of receptors specifically expressed in target cells. Additionally, AuNPs with sizes of ~ 50 -100 nm have the ability to extravasate into tumor tissue and become transported across the membrane by endocytosis, therefore, a laser controlled oligonucleotide release from such particles is of particular interest. Here, we quantify the loading of specifically attached siRNA onto single gold nanoparticles with diameters of 80, 150 and 200 nm and show that AuNPs with higher surface curvature can accommodate higher densities of siRNA. Moreover, we demonstrate how the sense strand on the siRNA can be dehybridized, and hence released from the AuNP, by irradiation with a near infrared (NIR) laser. Together, these findings show that plasmonic nanoparticles of sizes ~ 50 -100 nm are ideal carriers of oligonucleotides into cells and also allow their cargo to be released in a controlled manner by a thermoplasmonic mechanism. Importantly, this remotely controlled release strategy can be applied to any cargo attached to a plasmonic nanocarrier either on the single particle or ensemble level.

Introduction

Nanoscale therapeutics holds immense potential for treatment of diseases with minimal side effects. Development of novel nanoscale drug delivery systems has reached an advanced level with many sophisticated approaches for attaching and releasing a drug.¹⁻⁵ In particular, gold nanoparticles have received significant attention as a nanocarrier system for the following reasons: i) The gold surface facilitates easy conjugation of ligands, drugs or oligonucleotides, ii) AuNPs are readily taken up by cells,^{6,7} and iii) AuNPs interact strongly with light of specific wavelengths and the absorption and scattering by AuNPs can be exploited for thermoplasmonics and imaging, respectively. AuNPs release the absorbed energy in the form of heat in their local environment.⁸ The absorbance of AuNPs is tunable in the optical spectrum and the shape and composition of AuNPs can be designed to shift the plasmonic band into the NIR region which coincides with the biological transparency window.^{9,10} The prospect of a more efficient cancer treatment using these attractive features of gold nanoparticles for targeted delivery has expanded the field significantly in recent years.¹¹

Of special interest for targeted delivery are small interfering RNA (siRNA), which can be used as a silencer of disease-causing genes.¹² Central to the RNA interference (RNAi)

Bibliography

- [1] Lecuit, T.; Lenne, P.-F. *Nat Rev Mol Cell Biol* **2007**, *8*, 633–644.
- [2] Friedl, P.; Locker, J.; Sahai, E.; Segall, J. E. *Nature Cell Biology* **2012**, *14*, 777–.
- [3] Alberts, B. *Molecular Biology of the Cell: Reference edition*; Garland Science, 2008.
- [4] Chaffer, C. L.; Weinberg, R. A. *Science* **2011**, *331*, 1559.
- [5] Gandalovicová, A.; Vomastek, T.; Rosel, D.; Brábek, J. *Oncotarget* **2016**, *7*, 25022–25049.
- [6] Ball, D. W.; Hill, J. W.; Scott, R. J. *The Basics of General, Organic, and Biological Chemistry*; Flatworld, 2011; ISBN: 978-1-4533-1110-3.
- [7] Steward, J., R.; Tambe, D.; Hardin, C. C.; Krishnan, R.; Fredberg, J. J. *Am J Physiol Cell Physiol* **2015**, *308*, C657–64.
- [8] Hunt, T.; Nasmyth, K.; NovÅ;k, B. *Philosophical Transactions of the Royal Society B: Biological Sciences* **2011**, *366*, 3494–3497.
- [9] Rossen, N. S.; Tarp, J. M.; Mathiesen, J.; Jensen, M. H.; Oddershede, L. B. *Nature Communications* **2014**, *5*, 5720–5720.
- [10] Hynes, R. O. *Cell* **113**, 821–823.
- [11] Weinberg, R. *The Biology of Cancer, Second Edition*; Garland Science, 2013; pp 960–960.
- [12] Deisboeck, T. S.; Berens, M. E.; Kansal, A. R.; Torquato, S.; Stemmer-Rachamimov, A. O.; Chiocca, E. A. *Cell Prolif* **2001**, *34*, 115–34.
- [13] Deisboeck, T. S.; Couzin, I. D. *Bioessays* **2009**, *31*, 190–7.
- [14] Friedl, P.; Alexander, S. *Cell* **2011**, *147*, 992–1009.
- [15] Nieto, M. A.; Huang, R. Y.; Jackson, R. A.; Thiery, J. P. *Cell* **2016**, *166*, 21–45.

- [16] Susanto, O.; Muinonen-Martin, A. J.; Nobis, M.; Insall, R. H. In *Chemotaxis: Methods and Protocols*; Jin, T., Hereld, D., Eds.; Springer New York: New York, NY, 2016; pp 217–228.
- [17] Kim, J. H.; Serra-Picamal, X.; Tambe, D. T.; Zhou, E. H. H.; Park, C. Y.; Sadati, M.; Park, J. A.; Krishnan, R.; Gweon, B.; Millet, E.; Butler, J. P.; Trepac, X.; Fredberg, J. J. *Nature Materials* **2013**, *12*, 856–863.
- [18] Trepac, X.; Wasserman, M. R.; Angelini, T. E.; Millet, E.; Weitz, D. A.; Butler, J. P.; Fredberg, J. J. *Nature Physics* **2009**, *5*, 426–.
- [19] Collins, C.; Nelson, W. J. *Current opinion in cell biology* **2015**, *36*, 62–70.
- [20] Poujade, M.; Grasland-Mongrain, E.; Hertzog, A.; Jouanneau, J.; Chavrier, P.; Ladoux, B.; Buguin, A.; Silberzan, P. *Proceedings of the National Academy of Sciences of the United States of America* **2007**, *104*, 15988–93.
- [21] Haeger, A.; Wolf, K.; Zegers, M. M.; Friedl, P. *Trends in Cell Biology* *25*, 556–566.
- [22] Hulkower, K. I.; Herber, R. L. *Pharmaceutics* **2011**, *3*, 107–124.
- [23] Hayflick, L. *Biochemistry. Biokhimiia* **1997**, *62* (11), 1180–90.
- [24] Albert, P. J.; Schwarz, U. S. *PLOS Computational Biology* **2016**, *12*, e1004863.
- [25] Behrens, J.; Mareel, M. M.; Van Roy, F. M.; Birchmeier, W. *The Journal of Cell Biology* **1989**, *108*, 2435–2447.
- [26] GEY, G. *Cancer Res.* **1952**, *12*, 264–265.
- [27] Scherer, W. F.; Syverton, J. T.; Gey, G. O. *Journal of Experimental Medicine* **1953**, *97*, 695–710.
- [28] zur Hausen H.; de Villiers EM, *Annu Rev Microbiol.* **1994**, *48*, 427–47.
- [29] Fletcher, D. A.; Mullins, R. D. *Nature* **2010**, *463*, 485–92.
- [30] Behrens, J. *Breast Cancer Research and Treatment* **1993**, *24*, 175–184.
- [31] Cavallaro, U. G. O.; Christofori, G. *Annals of the New York Academy of Sciences* **2004**, *1014*, 58–66.
- [32] Foulkes, W. D.; Smith, I. E.; Reis-Filho, J. S. *New England Journal of Medicine* **2010**, *363*, 1938–1948.
- [33] Johnstone, C. N. et al. *Dis Model Mech* **2015**, *8*, 237–51.
- [34] Lou, Y.; Preobrazhenska, O.; auf dem Keller, U.; Sutcliffe, M.; Barclay, L.; McDonald, P. C.; Roskelley, C.; Overall, C. M.; Dedhar, S. *Developmental Dynamics* **2008**, *237*, 2755–2768.

- [35] El-Bahrawy, M.; Poulson, S. R.; Rowan, A. J.; Tomlinson, I. T.; Alison, M. R. *International Journal of Experimental Pathology* **2004**, *85*, 65–74.
- [36] Torres, M. P.; Rachagani, S.; Soucek, J. J.; Mallya, K.; Johansson, S. L.; Bhatra, S. K. *PLoS ONE* **2013**, *8*, e80580.
- [37] Graner, F.; Glazier, J. A. *Physical Review Letters* **1992**, *69*, 2013–2016.
- [38] Angelini, T. E.; Hannezo, E.; Trepas, X.; Marquez, M.; Fredberg, J. J.; Weitz, D. A. *Proc Natl Acad Sci U S A* **2011**, *108*, 4714–9.
- [39] Arciero, J. C.; Mi, Q.; Branca, M. F.; Hackam, D. J.; Swigon, D. *Biophysical Journal* **2011**, *100*, 535–543.
- [40] Cochet-Escartin, O.; Ranft, J.; Silberzan, P.; Marcq, P. *Biophysical Journal* **2014**, *106*, 65–73.
- [41] Rejniak, K. A. *Journal of theoretical biology* **2007**, *247*, 186–204.
- [42] Cortez, R.; Fauci, L.; Medovikov, A. *Physics of Fluids* **2005**, *17*, 031504.
- [43] De Gennes, P. G.; Prost, J. *The physics of liquid crystals; 2nd ed.*; International series of monographs on physics; Oxford Univ. Press: London, 1997.
- [44] Doostmohammadi, A.; Adamer, M. F.; Thampi, S. P.; Yeomans, J. M. *Nat Commun* **2016**, *7*, 10557.
- [45] Saw, T. B.; Doostmohammadi, A.; Nier, V.; Kocgozlu, L.; Thampi, S.; Toyama, Y.; Marcq, P.; Lim, C. T.; Yeomans, J. M.; Ladoux, B. *Nature* **2017**, *544*, 212–216.
- [46] Doostmohammadi, A.; Thampi, S. P.; Saw, T. B.; Lim, C. T.; Ladoux, B.; Yeomans, J. M. *Soft Matter* **2015**, *11*, 7328–36.
- [47] Doostmohammadi, A.; Thampi, S. P.; Yeomans, J. M. *Phys Rev Lett* **2016**, *117*, 048102.
- [48] Genkin, M. M.; Sokolov, A.; Lavrentovich, O. D.; Aranson, I. S. *Phys. Rev. X* **2017**, *7*, 011029.
- [49] Giomi, L.; Bowick, M. J.; Ma, X.; Marchetti, M. C. *Phys. Rev. Lett.* **2013**, *110*, 228101.
- [50] Pismen, L. M. *Phys. Rev. E* **2013**, *88*, 050502.
- [51] Ramaswamy, S. *Annual Review of Condensed Matter Physics* **2010**, *1*, 323–345.
- [52] Jonkman, J.; Brown, C. M. *Journal of Biomolecular Techniques : JBT* **2015**, *26*, 54–65.

- [53] Stephens, D. J.; Allan, V. J. *Science* **2003**, *300*, 82–6.
- [54] Webb, R. H. *Reports on Progress in Physics* **1996**, *59*, 427.
- [55] Richardson, A. C.; Reihani, S.; Oddershede, L. B. *Proc.SPIE* **2006**, *6326*, 6326 – 6326 – 10.
- [56] Leijnse, N.; Jeon, J. H.; Loft, S.; Metzler, R.; Oddershede, L. B. *The European Physical Journal Special Topics* **2012**, *204*, 75–84.
- [57] Bosanac, L.; Aabo, T.; Bendix, P. M.; Oddershede, L. B. *Nano Letters* **2008**, *8*, 1486–1491, PMID: 18386911.
- [58] Cherney, D. P.; Bridges, T. E.; Harris, J. M. *Analytical Chemistry* **2004**, *76*, 4920–4928, PMID: 15373424.
- [59] Barak, P.; Rai, A.; Rai, P.; Mallik, R. *Nature Methods* **2012**, *10*, 68–.
- [60] Uchida, M.; Sato-Maeda, M.; Tashiro, H. *Current Biology* **1995**, *5*, 380 – 382.
- [61] Ashkin, A. *Biophysical Journal* *61*, 569–582.
- [62] Bohren, C. F.; Huffman, D. R. *New York: Wiley, 1983; 1983.*
- [63] Norregaard, K.; Jauffred, L.; Berg-Sorensen, K.; Oddershede, L. B. *Phys. Chem. Chem. Phys.* **2014**, *16*, 12614–12624.
- [64] Neuman, K. C.; Block, S. M. *Review of Scientific Instruments* **2004**, *75*, 2787–2809.
- [65] Coffey, V. *Optics & Photonics News* **2013**,
- [66] Jeon, J.-H.; Tejedor, V.; Burov, S.; Barkai, E.; Selhuber-Unkel, C.; Berg-Sørensen, K.; Oddershede, L.; Metzler, R. *Phys. Rev. Lett.* **2011**, *106*, 048103.
- [67] Otto, O. et al. *Nature Methods* **2015**, *12*(3), 199–202.
- [68] Adan, A.; Alizada, G.; Kiraz, Y.; Baran, Y.; Nalbant, A. *Critical Reviews in Biotechnology* **2017**, *37*, 163–176.
- [69] Mietke, A.; Otto, O.; Girardo, S.; Rosendahl, P.; Taubenberger, A.; Golfier, S.; Ulbricht, E.; Aland, S.; Guck, J.; Fischer-Friedrich, E. *Biophys J* **2015**, *109*, 2023–36.
- [70] Mokbel, M.; Mokbel, D.; Mietke, A.; Träber, N.; Girardo, S.; Otto, O.; Guck, J.; Aland, S. *ACS Biomaterials Science & Engineering* **2017**,
- [71] Kocgozlu, L.; Saw, T. B.; Le, A. P.; Yow, I.; Shagirov, M.; Wong, E.; Mege, R. M.; Lim, C. T.; Toyama, Y.; Ladoux, B. *Curr Biol* **2016**, *26*, 2942–2950.
- [72] Ravasio, A.; Le, A. P.; Saw, T. B.; Tarle, V.; Ong, H. T.; Bertocchi, C.; Mege, R. M.; Lim, C. T.; Gov, N. S.; Ladoux, B. *Integr Biol (Camb)* **2015**, *7*, 1228–41.

- [73] Püspöki, Z.; Storath, M.; Sage, D.; Unser, M. In *Focus on Bio-Image Informatics*; De Vos, W. H., Munck, S., Timmermans, J.-P., Eds.; Springer International Publishing: Cham, 2016; pp 69–93.
- [74] West, A. V.; Wullkopf, L.; Christensen, A.; Leijnse, N.; Tarp, J. M.; Mathiesen, J.; Erler, J. T.; Oddershede, L. B. *Sci Rep* **2017**, *7*, 43800.
- [75] Tambe, D. T.; Hardin, C. C.; Angelini, T. E.; Rajendran, K.; Park, C. Y.; Serra-Picamal, X.; Zhou, E. H. H.; Zaman, M. H.; Butler, J. P.; Weitz, D. A.; Fredberg, J. J.; Trepap, X. *Nature Materials* **2011**, *10*, 469–475.
- [76] Serra-Picamal, X.; Conte, V.; Vincent, R.; Anon, E.; Tambe, D. T.; Bazellieres, E.; Butler, J. P.; Fredberg, J. J.; Trepap, X. *Nature Physics* **2012**, *8*, 628–U66.
- [77] Paszek, M. J.; Zahir, N.; Johnson, K. R.; Lakins, J. N.; Rozenberg, G. I.; Gefen, A.; Reinhart-King, C. A.; Margulies, S. S.; Dembo, M.; Boettiger, D.; Hammer, D. A.; Weaver, V. M. *Cancer Cell* **2005**, *8*, 241–54.
- [78] Ranft, J.; Basan, M.; Elgeti, J.; Joanny, J. F.; Prost, J.; Julicher, F. *Proceedings of the National Academy of Sciences of the United States of America* **2010**, *107*, 20863–20868.
- [79] Carey, S. P.; Rahman, A.; Kraning-Rush, C. M.; Romero, B.; Somasegar, S.; Torre, O. M.; Williams, R. M.; Reinhart-King, C. A. *Am J Physiol Cell Physiol* **2015**, *308*, C436–47.
- [80] Mendoz, E.; Lim, C. T. *Cellular and Molecular Bioengineering* **2011**, *4*, 411–426.
- [81] Angelucci, C.; Maulucci, G.; Colabianchi, A.; Iacopino, F.; D’Alessio, A.; Maiorana, A.; Palmieri, V.; Papi, M.; De Spirito, M.; Di Leone, A.; Masetti, R.; Sica, G. *British Journal of Cancer* **2015**, *112*, 1675–1686.
- [82] Gligorijevic, B.; Bergman, A.; Condeelis, J. *Plos Biology* **2014**, *12*.
- [83] Tse, J. M.; Cheng, G.; Tyrrell, J. A.; Wilcox-Adelman, S. A.; Boucher, Y.; Jain, R. K.; Munn, L. L. *Proceedings of the National Academy of Sciences of the United States of America* **2012**, *109*, 911–916.
- [84] Christensen, A. Stress-driven pattern formation in living and non-living matter. Thesis, The Niels Bohr Institute, University of Copenhagen, 2017.
- [85] Sepúlveda, N.; Petitjean, L.; Cochet, O.; Grasland-Mongrain, E.; Silberzan, P.; Hakim, V. *PLOS Computational Biology* **2013**, *9*, e1002944.
- [86] Lekka, M. *Bionanoscience* **2016**, *6*, 65–80.
- [87] Swaminathan, V.; Mythreye, K.; O’Brien, E. T.; Berchuck, A.; Blobel, G. C.; Superfine, R. *Cancer Res* **2011**, *71*, 5075–80.

- [88] Guck, J.; Schinkinger, S.; Lincoln, B.; Wottawah, F.; Ebert, S.; Romeyke, M.; Lenz, D.; Erickson, H. M.; Ananthakrishnan, R.; Mitchell, D.; Kas, J.; Ulvick, S.; Bilby, C. *Biophys J* **2005**, *88*, 3689–98.
- [89] Hou, H. W.; Li, Q. S.; Lee, G. Y.; Kumar, A. P.; Ong, C. N.; Lim, C. T. *Biomed Microdevices* **2009**, *11*, 557–64.
- [90] Li, Q. S.; Lee, G. Y.; Ong, C. N.; Lim, C. T. *Biochem Biophys Res Commun* **2008**, *374*, 609–13.
- [91] Teng, Y.; Pang, M.; Huang, J.; Xiong, C. *Sensors and Actuators B: Chemical* **2017**, *240*, 158 – 167.
- [92] Brown, K. A.; Aakre, M. E.; Gorska, A. E.; Price, J. O.; Eltom, S. E.; Pietenpol, J. A.; Moses, H. L. *Breast Cancer Research* **2004**, *6*, R215–R231.
- [93] Golfier, S.; Rosendahl, P.; Mietke, A.; Herbig, M.; Guck, J.; Otto, O. *Cytoskeleton (Hoboken)* **2017**,
- [94] Diepenbruck, M.; Christofori, G. *Current Opinion in Cell Biology* **2016**, *43*, 7–13.
- [95] Rianna, C.; Radmacher, M. *European Biophysics Journal* **2017**, *46*, 309–324.
- [96] Boal, D. *Mechanics of the Cell*; Cambridge University Press, 2002.
- [97] Rosendahl, P.; Plak, K.; Jacobi, A.; Kraeter, M.; Toepfner, N.; Otto, O.; Herold, C.; Winzi, M.; Herbig, M.; Ge, Y.; Girardo, S.; Wagner, K.; Baum, B.; Guck, J. *bioRxiv* **2017**,
- [98] Lee, S. H.; Dominguez, R. *Molecules and cells* **2010**, *29*, 311–325.
- [99] Azatov, M.; Goicoechea, S. M.; Otey, C. A.; Upadhyaya, A. *Scientific Reports* **2016**, *6*, 28805.
- [100] Cox, T. R.; Erler, J. T. *Disease Models & Mechanisms* **2011**, *4*, 165–178.
- [101] Erler, J. T.; Weaver, V. M. *Clinical & experimental metastasis* **2008**, *26*, 35–49.
- [102] Elosegui-Artola, A.; Oria, R.; Chen, Y.; Kosmalka, A.; Pérez-González, C.; Castro, N.; Zhu, X., C and Trepant; Roca-Cusachs, P. *Nat Cell Biol* **2016**, *18*(5), 540–8.
- [103] Fouchard, J.; Mitrossilis, D.; Asnacios, A. *Cell Adh Migr.* **2011**, *5*(1), 16–9.
- [104] Levental, K. R.; Yu, H.; Kass, L.; Lakins, J. N.; Egeblad, M.; Erler, J. T.; Fong, S. F.; Csiszar, K.; Giaccia, A.; Weninger, W.; Yamauchi, M.; Gasser, D. L.; Weaver, V. M. *Cell* **2009**, *139*, 891–906.
- [105] Butcher, D. T.; Alliston, T.; Weaver, V. M. *Nature reviews. Cancer* **2009**, *9*, 108–122.

- [106] Selhuber-Unkel, C.; Yde, P.; Berg-Sørensen, K.; Oddershede, L. B. *Physical Biology* **2009**, *6*, 025015.
- [107] Barnes, J. M.; Przybyla, L.; Weaver, V. M. *Journal of Cell Science* **2017**, *130*, 71–82.
- [108] Suresh, S. *Acta Biomaterialia* **2007**, *3*, 413 – 438.
- [109] Thampi, S. P.; Golestanian, R.; Yeomans, J. M. *Philosophical Transactions of the Royal Society of London Series A* **2014**, *372*, 20130366–20130366.
- [110] Hirst, L. S.; Ossowski, A.; Fraser, M.; Geng, J.; Selinger, J. V.; Selinger, R. L. B. *Proceedings of the National Academy of Sciences of the United States of America* **2013**, *110*, 3242–3247.
- [111] Duclos, G.; Erlenkämper, C.; Joanny, J.-F.; Silberzan, P. *Nature Physics* **2016**, *13*, 58–.
- [112] Merkel, M.; Manning, M. L. *Seminars in cell & developmental biology* **2017**, *67*, 161–169.
- [113] Marel, A.-K.; Podewitz, N.; Zorn, M.; Oskar Radler, J.; Elgeti, J. *New Journal of Physics* **2014**, *16*, 115005.
- [114] Vedula, S. R. K.; Leong, M. C.; Lai, T. L.; Hersen, P.; Kabla, A. J.; Lim, C. T.; Ladoux, B. *Proceedings of the National Academy of Sciences* **2012**, *109*, 12974–12979.
- [115] Aslakson, C. J.; Miller, F. R. *Cancer Res* **1992**, *52*, 1399–405.
- [116] Morton, J. P.; Timpson, P.; Karim, S. A.; Ridgway, R. A.; Athineos, D.; Doyle, B.; Jamieson, N. B.; Oien, K. A.; Lowy, A. M.; Brunton, V. G.; Frame, M. C.; Evans, T. R. J.; Sansom, O. J. *Proceedings of the National Academy of Sciences of the United States of America* **2010**, *107*, 246–251.